Final Report

SUBMITTED TO
U.S. Department of Energy
National Energy Technology Laboratory

DOE AWARD NUMBER: DE-FE0026423

A HIGH EFFICIENCY, ULTRA-COMPACT PROCESS FOR PRE-COMBUSTION CO_2 CAPTURE

PRINCIPAL INVESTIGATOR
Theodore T. Tsotsis
213-740-2069
tsotsis@usc.edu

SUBMITTED BY
University of Southern California
Los Angeles, CA, 90089-1211
DUNS Number: 072933393

REPORTING PERIOD: October 1, 2015 – March 31, 2019

SUBMISSION DATE: April 30, 2019

SIGNATURE:

I. DISCLAIMER

This report was prepared as an account of work sponsored by an agency of the United States Government. Neither the United States Government nor any agency thereof, nor any of their employees, makes any warranty, express or implied, or assumes any legal liability or responsibility for the accuracy, completeness, or usefulness of any information, apparatus, product, or process disclosed, or represents that its use would not infringe privately owned rights. Reference herein to any specific commercial product, process, or service by trade name, trademark, manufacturer, or otherwise does not necessarily constitute or imply its endorsement, recommendation, or favoring by the United States Government or any agency thereof. The views and opinions of authors expressed herein do not necessarily state or reflect those of the United States Government or any agency thereof.

II. EXECUTIVE SUMMARY

The overarching objective of this lab-scale study was to prove the technical feasibility of the membrane- and adsorption-enhanced water gas shift (WGS) process that employs a carbon molecular sieve (CMS) membrane reactor (MR) followed by an adsorption reactor (AR) for pre-combustion carbon dioxide (CO_2) capture while demonstrating progress towards achievement of the overall fossil energy performance goals of 90% CO_2 capture rate with 95% CO_2 purity at a cost of electricity (COE) of 30% less than the baseline capture approaches. Such a WGS system combining a MR and an AR in tandem can produce an ultra-pure hydrogen (H_2) product (without the need for using a post-processing step) continuously until the adsorbent (hydrotalcite-based) in the AR unit is saturated for regeneration via a pressure swing (PSA) and/or temperature swing adsorption (TSA) operation. The research effort was led by the University of Southern California (USC) with assistance from the University of California – Los Angeles (UCLA) and Media and Process Technology, Inc. (M&PT).

The project was carried-out in two different phases: In Phase I (during Budget Period 1 (BP1) of the project), the team designed, constructed and tested the lab-scale experimental MR-AR system; prepared and characterized appropriate membranes and adsorbents, and also

upgraded and experimentally validated an in-house mathematical model that describes system behavior. In Phase II (during BP2), the team experimentally tested the proposed novel MR-AR process in the lab-scale apparatus using simulated fuel gas (gasifier off-gas), and completed the initial technical and economic feasibility study.

All project milestones and success criteria were met. Specifically, the team: (i) prepared CMS membranes for use in the MR-AR studies that displayed high performance that exceeded all the original project performance targets: H_2 permeance (1 to 1.5 $m^3/m^2/hr/bar$, or 370.3 to 555.5 GPU) and a H_2/CO selectivity >80 at the relevant temperature (up to 300°C) and pressure conditions (up to 25 bar); (ii) prepared hydrotalcite adsorbents with large CO_2 uptake capacities (>10wt%), and working capacities under cyclic AR conditions (3wt%, the targeted value in the project) and characterized them under high (up to 30 bar) pressure conditions; (iii) experimentally evaluated in multicycle experiments the integrated MR-AR system for the WGS reaction in the context of the IGCC power generation application. The CMS membranes, HTC adsorbents and catalysts employed all exhibited very robust and stable performance during the long-term run (over a >500 hr run of H_2S exposure at 25 bar of pressure). Furthermore, the proposed MR-AR IGCC system achieved a COE of 86.3 $/MWh, with a N_2 sale price of $30/ton, which represents a 36% reduction in the baseline IGCC w/CCS COE of 135.4 $/MWh. As a result, the overall project objective of a 30% reduction in the baseline COE was surpassed. Thus, the proposed MR-AR IGCC system delivers a cost of 5.1 $/ton of CO_2 captured, versus a cost of 63.20 $/ton of CO_2 captured for the baseline. The MR-AR based IGCC plant also showed a 9% increase in power output over the baseline IGCC w/CCS (593 MWe from 543 MWe).

III. ABSTRACT

The key objective of this lab-scale study was to prove the technical feasibility of the membrane- and adsorption-enhanced water gas shift (WGS) reaction process that employs a carbon molecular sieve (CMS) membrane reactor (MR) followed by an adsorption reactor (AR) for pre-combustion carbon dioxide (CO_2) capture, while demonstrating progress towards achievement of the overall fossil energy performance goals of 90% CO_2 capture rate with 95% CO_2 purity, at a cost of electricity of 30% less than the baseline capture approaches. Such a WGS system combining a MR and an AR in tandem can produce an ultra-pure hydrogen (H_2) product (without the need for using a post-processing step) continuously, until the adsorbent (hydrotalcite-based) in the AR unit is saturated for regeneration via a pressure swing adsorption (PSA) and/or temperature swing adsorption (TSA) operation. The project effort was led by the University of Southern California (USC) with assistance from the University of California - Los Angeles (UCLA) and Media and Process Technology, Inc. (M&PT).

The project was divided into two Budget Periods (BP). During Budget Period 1 (BP1) of the project, the key focus was to: (i) design, construct and test the lab-scale experimental MR-AR system, (ii) select and characterize appropriate membranes, adsorbents and catalysts, and (iii) upgrade and experimentally validate an in-house mathematical model. The key focus during BP2 was to experimentally test the proposed novel process in the lab-scale apparatus using simulated fuel gas (gasifier off-gas), and to complete the initial technical and economic feasibility study. In each Budget Period, there were a number of milestones and success criteria, which were all met by their due dates. Specifically, during BP1, the team: (i) completed the construction of the lab-scale MR-AR experimental system; (ii) prepared and characterized CMS membranes at the anticipated process conditions; (iii) prepared and characterized adsorbents at the anticipated process conditions, and generated global rate expressions for the catalyst; (iv) began testing of the MR and AR individual subsystems; and (v) developed mathematical models and began validating their ability to fit the experimental data. During BP2, the team: (i) experimentally tested the proposed novel process in the lab-scale apparatus using simulated fuel gas (gasifier off-gas), and (ii) completed the initial technical and economic

feasibility study. Additional details on some of these key technical accomplishments are provided below.

The team prepared high-performance CMS membranes for use in the membrane reactor testing activities. These membranes displayed very high performance and met all the original project performance targets: H_2 permeance (1 to 1.5 $m^3/m^2/hr/bar$, or 370.3 to 555.5 GPU) and a H_2/CO selectivity >80 at the relevant temperature (up to 300°C) and pressure conditions (up to 25 bar). They have been shown to be stable in intermediate-term thermal stability testing (consistent with our past experience). Further, the team had success in developing very highly H_2/CO_2 selective membranes (H_2/CO_2 selectivity >>200) using our higher quality tubular substrates in conjunction with modification of the pyrolysis conditions.

Hydrotalcite (HTC) adsorbent materials were also prepared and characterized under both atmospheric and high (up to 30 bar) pressure conditions at M&PT and at higher pressures at USC. These materials have shown large CO_2 uptake capacities (>10 wt%) and working capacities under cyclic AR conditions (3 wt%, the targeted value in the project). They have also been stable during CO_2 cycling in various atmospheres, including a >500-hour MR-AR run. A commercial sour-shift catalyst was utilized in the experiments. Global rate expressions based on the experimental data generated were formulated and used in the models developed for simulating the behavior of the lab-scale MR-AR system as well as in the generation of a preliminary process TEA.

A key focus during the initial phase of the project was to modify an existing lab-scale test unit at USC to permit operation at higher pressures (up to 25 bar) and to incorporate a dedicated AR subsystem. This new lab-scale system consisted of: (i) the gas delivery system; (ii) the MR system containing the CMS membrane packed with WGS catalyst in its annulus; (iii) the AR subsystem, consisting of two adsorbent beds for continuous cycling between adsorption and desorption, and containing the adsorbent and catalyst with its appropriate valves and control hardware; (iv) overall system control hardware; and (v) the analysis section equipped with the appropriate analytical equipment. Graphite O-rings were employed as seals between the membrane and housing. GC-TCD and GC-FID were used in concert with MFM to study the performance of the MR subsystem by measuring the total molar flow rates and

analyzing the permeate and feed/reject side gas compositions. Since the AR subsystem operated under transient conditions, mass analyzers were used to track its performance, together with GC analysis at preset intervals (for validation of the mass analyzer's readings).

Initial testing focused on the individual components (i.e., MR and AR) of the MR-AR lab-scale system. Key experimental parameters investigated for the MR subsystem included: (i) the membrane permeation characteristics; (ii) reactor temperature, feed and permeate pressures, contact time, catalyst weight to CO molar flow rate (W/F_{CO}), and the permeate side (steam) purge rate. For the AR subsystem, key parameters studied included: (i) the catalyst and adsorbent weights; (ii) the operating envelope (i.e., temperature and pressure) of the adsorption/reaction cycle; and (iii) the desorption/regeneration mode. The dependent variables monitored included exit stream compositions and flow rates, and based on such data we quantified the CO conversion, H_2 recovery and purity, CO_2 recovery and purity, and degree of adsorbent regeneration. The experimental data were then used to validate a mathematical model developed as part of this project.

Upon construction of the lab-scale system and validation of the performance of its individual subsystems, the integrated MR-AR system, which consisted of a MR followed by two ARs, was investigated. This integrated MR-AR system was experimentally evaluated for the WGS reaction in the context of the IGCC power generation application. The CMS membrane exhibited very robust and stable performance during the long-term run (over a >500 hr run of H_2S exposure at 25 bar of pressure) and maintained high He/N_2 (~126) and H_2/CO (~100) selectivities over a total of 742-hour of H_2S exposure during the MR-AR run.

The combined MR-AR lab-scale system was tested during numerous multiple-cycle runs and displayed superior performance to that of a conventional PBR with high purities for the hydrogen product, which can be directly usable in a hydrogen turbine for power generation. During the MR-AR multiple-cycle run, the team continued to monitor MR subsystem performance with respect to MR CO conversion, H_2 purity and recovery in order to verify both membrane and catalyst stability. The membrane and catalyst in the MR both displayed stable performance during the long-period run. To properly characterize and monitor the AR behavior, the team has defined the "AR effect time" in two different ways, and during the MR-

AR multiple-cycle run, the team found that the "AR effect time" takes a few cycles to settle to its eventual "steady-state" value. The team also monitored the "pseudo-steady state" CO conversion in the AR prior to being switched into the regeneration mode by allowing for the sorption-enhanced WGS reaction time to be long enough so that the adsorbent becomes saturated with CO_2. The team also found that it takes again a few cycles before the conversion settles down to its eventual steady state value. Further, the catalyst in the AR demonstrated very robust and stable performance during a continuous 18-cycle experiment under various regeneration treatment. Thus, one concludes that the membrane, catalyst and adsorbent are very robust and stable under the large concentration H_2S, high-temperature and high-pressure IGCC-like environment during the long-period MR-AR multiple-cycle run.

The aforementioned experimentally validated mathematical model was used to carry out a preliminary TEA of the MR-AR-based IGCC plant, which delivered the following key results: (i) 92% CO_2 capture with a net power output of 593 MWe. This corresponds to a 9% increase in power output, while delivering greater CO_2 capture, over the baseline IGCC plant which features a 90% CO_2 capture with a net power output of 543 MWe; (ii) a COE of 113.1 $/MWh (86.3 $/MWh) corresponding to a $39.3/ton ($5.10/ton) CO_2 capture cost, when Nitrogen is not sold (sold at $30/ton) and the MR membrane lifespan is considered to be 10 years. This represents a 16% (36%) reduction in the baseline IGCC w/CCS COE of 135.4 $/MWh and a 37.8% (91.9%) reduction in the baseline IGCC w/CCS CO_2 capture cost of $63.2/ton; (iii) a MR-AR IGCC COE increase of 0.2% and 0.6% (from 86.3 $/MWh to 86.5 $/MWh and 86.8 $/MWh) if the MR membrane lifespan is reduced to 5 years and 2 years, respectively; (iv) a baseline IGCC w/CCS COE decrease of 16%, 17%, 36%, and over 100% (from 135.4 $/MWh to 113.1$/MWh, 112.2 $/MWh, 86.3 $/MWh, and -255.8 $/MWh) for N_2 sale prices of $0/ton, $1/ton, $30/ton, and $414/ton, respectively.

Table of Contents

I. DISCLAIMER i
II. EXECUTIVE SUMMARY i
III. ABSTRACT iii
List of Figures ix
List of Tables xv
1. INTRODUCTION AND OVERAL PROJECT STRUCTURE 1
1.1 Major Goals of the Project 1
1.2 Project Structure 2
1.3 Project Administration 3
2. MATERIALS PREPARATION AND CHARACTERIZATION 12
2.1 - Preparation and Characterization of the CMS Membranes 12
2.2 - Preparation and Characterization of Adsorbents 26
2.3. Catalyst Activity Testing 36
2.4 Summary and Conclusions 40
3.0. CONSTRUCTION OF THE LAB-SCALE SYSTEM AND INITIAL TESTING AND VALIDATION 42
3.1. Design and Construction of the Lab-Scale Experimental System 42
3.2. Initial Testing of the Individual MR and AR Subsystems 46
3.3. Summary and Conclusions 66
4.0 LAB-SCALE TESTING AND VALIDATION OF THE ULTRA-COMPACT MR-AR PROCESS 67
4.1 Overview 67
4.2 Preliminary Experiments with no Steam Sweep 68
4.2.1 Experimental Section 68
4.2.1.1 Materials 68
4.2.2 Results and Discussion 74
4.3 Long-Term MR-AR Experiments 82
4.3.1 Experimental Section 84
4.3.2 Results and Discussion 88
4.4. Summary and Conclusions 98
5.0 MODEL SIMULATIONS AND DATA ANALYSIS 100
6.1 – Process Design/Optimization 115

6.3 Sensitivity Analysis 136
6.4. Summary and Conclusions 137
NOMENCLATURE 139
REFERENCES 142
STATE POINT DATA TABLE 144
APPENDIX 146

List of Figures

Figure 1.1. The MR-AR process 1

Figure 2.1. SEM photomicrograph of defects in the carbon precursor layer 17

Figure 2.2. Thermal stability at 250°C in the presence of He and N_2 of the CMS membrane HMR-52(10") before and after installation (dotted vertical line) in the USC MR module 24

Figure 2.3. Thermal stability at 250°C in the presence of He and N_2 of the CMS membrane HMR-41(10") 24

Figure 2.4. Thermal stability at 250°C in the presence of He and N_2 of HMR-67 (top) and HMR-72 (bottom) in M&PT standard testing module. Both membranes were transferred to the USC reactor modules for membrane reactor testing 25

Figure 2.5. In-situ TGA-MS study of the Mg-Al-CO_3 HTC as a function of temperature 27

Figure 2.6. Fraction of the species removed from the Mg-Al-CO_3 HTC vs. temperature 27

Figure 2.7. Thermal evolution of the structure of Mg-Al-CO_3 LDH 28

Figure 2.8. TGA of M&PT hydrotalcite samples: Starting from Top Left: (i) Alcoa TSO-1091-2. (ii) HT-3MgAl-121415-A1, the original M&PT prepared material. And two of the recently prepared samples as part of the large-batch preparation: (iii) HT-3MgAl-20g#1 and (iv) HT-3MgAl-G-20g-#4 30

Figure 2.9. Long-term CO_2 adsorption profile at 400°C for HT-3MgAl-20g-#1 pre-calcined at 650°C in N_2 31

Figure 2.10. (a) CO_2 adsorption of M&PT hydrotalcite sample HT-3MgAl-20g-#1 at room temperature and atmospheric pressure. (b) The test was conducted after the final adsorption cycle at 200°C to confirm the original CO_2 adsorption capacity at RT (see also Table 2.8) 34

Figure 2.11. Photograph of the hydrotalcite sample after (left) and before (right) exposure to naphthalene in a cyclic CO_2 adsorption/regeneration study (17 cycles) 36

Figure 2.12. CO_2 capacity determination of the naphthalene exposed hydrotalcite sample (HT-20g-#31 Post-Naphthalene) compared with the unexposed virgin material (HT-20g-#31 Pre-Naphthalene) and a previously prepared hydrotalcite (HT-20g-#1). All samples were pre-calcined at 450°C in CO_2 prior to capacity measurement at 200°C. Testing was conducted at ambient pressure 36

Figure 2.13. The iso-conversion graph 39

Figure 3.1. Experimental MR-Ar lab-scale system.....44

Figure 3.2. The schematic of the AR 45

Figure 3.3. The photograph of the AR 45

Figure 3.4. The photograph of the AR with coiled tubing installed in the GC oven 46

Figure 3.5. The experimental set-up used for the CO_2 breakthrough experiments.....47

Figure 3.6. Experimental CO_2 breakthrough curves obtained with the HTC adsorbent provided by M&PT using a feed of 74.2 vol% of CO_2 in N_2 (Reactor pressure = 10 bar, Oven temperature = 400°C, Flow rate = 500 sccm); blank experiment using only the quartz particles also carried out under the same experimental conditions 49

Figure 3.7. A summary of the experimental CO_2 breakthrough curves obtained with the HTC adsorbent provided by M&PT using a feed of 74.2 vol% CO_2 in N_2 at various reactor pressures (5, 10, 15, 20, 25 bar), (Oven temperature = 400°C, Flow rate = 500 sccm).....50

Figure 3.8. A summary of the experimental CO_2 breakthrough curves obtained with the HTC adsorbent provided by M&PT using a feed of 74.2 vol% CO_2 in N_2 and various oven temperatures (300, 350, 400°C), (Reactor pressure = 25 bar, Flow rate = 500 sccm).....50

Figure 3.9. A summary of the experimental CO_2 breakthrough curves obtained with the HTC adsorbent provided by M&PT using a feed of 74.2 vol% CO_2 in N_2 and a feed of 74.2 vol% of CO_2 in N_2 with 1000 ppm H_2S (Reactor pressure = 25 bar, Oven

temperature= 300ºC, Total flow rate = 500 sccm). (Insert: H_2S breakthrough curve) 51

Figure 3.10. A summary of experimental CO_2 adsorption and desorption profiles of M&PT HTC adsorbent using a feed of 74.2 vol% of CO_2 in N_2 at various reactor pressures (e.g. 5, 15, 25 bar), (oven temperature = 250ºC, flow rate = 500 sccm) 54

Figure 3.11. Schematic diagram of the static experimental set-up 55

Figure 3.12. Excess and Absolute Adsorption Isotherm data and Langmuir Isotherm fit 59

Figure 3.13. Experimental set-up of the SEWGSR experiments 60

Figure 3.14. Dynamic experiments at 15 bar and 400°C with 240 s injection time and 500 sccm flow rate 62

Figure 3.15. The dynamic diagram of the AR system 63

Figure 3.16. Conversion vs. W/F_{CO} for MR (feed pressure 14.5 bar, reactor temperature 250ºC, no sweep) 64

Figure 3.17. H_2 Recovery vs. W/F_{CO} for MR (feed pressure 14.5 bar, reactor temperature 250°C, no sweep) 65

Figure 4.1. Experimental set-up used in the MR-AR experiments (red lines are heat-traced to prevent water from condensing; **MR:** Membrane Reactor; **AR:** Adsorptive Reactor; **MFC:** Mass Flow Controller; **BFM:** Bubble Flow-meter; **RGA:** Residue Gas Analyzer; **GC:** Gas Chromatography; **BPR:** Back Pressure Regulator) 70

Figure 4.2. Conversion vs. W/F_{CO} for the membrane reactor and packed-bed reactor at 250°C 76

Figure 4.3. Hydrogen purity vs. W/F_{CO} for the MR and PBR at 250°C 77

Figure 4.4. Hydrogen recovery vs. W/F_{CO} for the membrane reactor at 250°C 77

Figure 4.5. CO conversion in the AR and total MR-AR conversion, and molar flow rates of CO_2, H_2, CO in the two AR's. (Left) AR I, and (Right) AR II. Temperature of 250°C, pressure of 25 bar, H_2O/CO ratio of 2.8, with the MR operated with a W/F_{CO} of 33 g·h/mol 79

Figure 4.6. CO conversion in the AR and total MR-AR conversion, and molar flow rates of CO_2, H_2, CO in the two AR's. (Left) AR I, and (Right) AR II. Temperature of 250°C, pressure of 25 bar, H_2O/CO ratio of 2.8, with the MR operated with a W/F_{CO} of 77 g·h/mol 80

Figure 4.7. CO conversion in the AR and total MR-AR conversion, and molar flow rates of CO_2, H_2, CO in the two AR's. (Left) AR I, and (Right) AR II. Temperature of 250°C, pressure of 15 bar, H_2O/CO ratio of 2.8, with the MR operated with a W/F_{CO} of 33 g·h/mol 80

Figure 4.8. CO conversion in the AR and total MR-AR conversion, and molar flow rates of CO_2, H_2, CO in the two AR's. (Left) AR I, and (Right) AR II. Temperature of 250°C, pressure of 15 bar, H_2O/CO ratio of 2.8, with the MR operated with a W/F_{CO} of 55 g·h/mol 81

Figure 4.9. CO conversion in the AR and total MR-AR conversion, and molar flow rates of CO_2, H_2, CO in the two AR's. (Left Top) AR I, first cycle, (Right Top) AR II, first cycle, (Left Bottom) AR I, second cycle, (Right Bottom) AR II, second cycle. Temperature of 250°C, pressure of 25 bar, H_2O/CO ratio of 2.8, with the MR operated with a W/F_{CO} of 55 g·h/mol 82

Figure 4.10. Experimental set-up used in the MR-AR experiments (red lines are heat-traced to prevent water from condensing; **MR:** Membrane Reactor; **AR:** Adsorptive Reactor; **MFC:** Mass Flow Controller; **BFM:** Bubble Flow-meter; **RGA:** Residue Gas Analyzer; **GC:** Gas Chromatography; **BPR:** Back Pressure Regulator) 85

Figure 4.11. Single-gas permeances vs. H_2S exposure time during the >500-hour run 92

Figure 4.12. He/N_2 and H_2/CO selectivities vs. H_2S exposure time during the >500-hour run 93

Figure 4.13. The MR properties during a multi-cycle run. Experimental conditions: T=250°C, feed pressure=25 bar, permeate-side pressure 3 bar, with steam sweep ratio=0.49, H_2O/CO ratio of 4.3, W/F_{CO}= 66 g·h/mol, air-blown gasifier model syngas (CMS#23)..... 94

Figure 4.14. The AR effect time w.r.t 95 % CO conversion during multi-cycle run. Experimental conditions: T=250°C, feed pressure=25 bar, permeate-side pressure 3 bar, with steam sweep, W/FCO= 66 g·h/mol, air-blown gasifier model syngas (CMS#23).....95

Figure 4.15. The AR effect time w.r.t 5 % CO_2 composition during multi-cycle run. Experimental conditions: T=250°C, feed pressure=25 bar, permeate-side pressure 3 bar, with steam sweep, W/F_{CO}= 66 g·h/mol, air-blown gasifier model syngas (CMS#23) 95

Figure 4.16. The AR steady-state CO conversion during a multi-cycle run. Experimental conditions: T=250 °C, feed-side pressure=25 bar, permeate-side pressure 3 bar, with steam sweep, W/F_{CO}= 66 g·h/mol, air-blown gasifier model syngas (CMS#23) 96

Figure 4.17. AR pseudo-steady conversion after adsorbent saturation for various regeneration protocols, as shown on the Figure. Temp=250°C, pressure=5 bar, Wc/F_{CO}=121 g·h/mol, W_{Ad}/W_c= 6.9:1 97

Figure 4.18. Temperature profiles of AR operated at 250°C and 25 bar using W/F_{CO} = 66 and H_2O/CO =3.22, steam sweep ratio=0.5, permeate side pressure=3 bar.....98

Figure 5.1. CO Conversion vs. W_{cat}/F_{CO}.....100

Figure 5.2. H_2 recovery vs. W_{cat}/F_{CO} 101

Figure 5.3. MR exit H_2O/CO ratio vs. W_{cat}/F_{CO} 102

Figure 5.4. MR total molar flow rates vs. W_{cat}/F_{CO} 102

Figure 5.5. MR outlet species mole fractions vs. W_{cat}/F_{CO}.....103

Figure 5.6. Switch time vs. W_{cat}/F_{CO} 104

Figure 5.7. AR CO_2 loading axial profiles for 4 switch times and 5 operating cycles 104

Figure 5.8. Effectiveness factor axial profiles for various pellet sizes (Conventional PBR-Up and MR-Down).....106

Figure 5.9. Catalyst-pellet effectiveness factor AR axial profiles for various pellet sizes (523 K, 25 bar and W_{cat}/F_{CO}=88 g*h/mol) 107

Figure 5.10. Adsorbent-pellet effectiveness factor AR axial profiles for various pellet sizes (523 K, 25 bar and W_{cat}/F_{CO}=88 g*h/mol).....108

Figure 5.11. Adsorbent-pellet local effectiveness factor AR axial-temporal profiles for various pellet sizes (523 K, 25 bar and W_{cat}/F_{CO}=88 g*h/mol) 108
Figure 5.12. Adsorbent-pellet effectiveness factor AR axial profiles for various cycles (523 K, 25 bar and W_{cat}/F_{CO}=88 g*h/mol) 109
Figure 5.13. MR experimental vs. model for various W_{cat}/F_{CO} 111
Figure 5.14. AR profiles corresponding to the MR operating with W_{cat}/F_{CO} = 55 and H_2O/CO = 1.1 111
Figure 5.15. AR profiles corresponding to the MR operating with W_{cat}/F_{CO} = 66 and H_2O/CO = 1.1 112
Figure 6.1. AR CO_2 breakthrough time (Left) and AR maximum operation time (Right) vs. AR- $W_{cat}/F_{CO,0}$ values for various MR exit compositions. W_{ad}/Wcat=6 115
Figure 6.2. Exit-average total (MR+AR) CO conversion vs. AR- $W_{cat}/F_{CO,0}$ values for MR exit compositions. (Left- The minimum time of operation and Right- The maximum time of operation). W_{ad}/W_{cat}=6 116
Figure 6.3. AR CO_2 breakthrough time (Left) and AR maximum operation time (Right) vs. AR-$W_{cat}/F_{CO,0}$ values for various W_{ad}/W_{cat} values. MR $W_{cat}/F_{CO,0}$ =60.....117
Figure 6.4. Exit-average total (MR+AR) CO conversion vs AR- $W_{cat}/F_{CO,0}$ values for various W_{ad}/W_{cat} values. MR $W_{cat}/F_{CO,0}$ =60.....117
Figure 6.5. CO conversion vs. W_{cat}/F_{CO}.....120
Figure 6.6. H_2 Recovery vs. W_{cat}/F_{CO} 121
Figure 6.7. Exit H_2O/CO ratio vs. W_{cat}/F_{CO} (all cases).....121
Figure 6.8. CO_2 recovery vs. W_{cat}/F_{CO}.....122
Figure 6.9. CO conversion vs. W_{cat}/F_{CO}.....123
Figure 6.10. H_2 Recovery vs. W_{cat}/F_{CO} 124
Figure 6.11 26. Exit H_2O/CO ratio vs. W_{cat}/F_{CO} (all cases).....124
Figure 6.12. CO_2 recovery vs. W_{cat}/F_{CO}.....125
Figure 6.13. AR CO_2 switch times vs. time for various W_{cat}-W_{ad}/F_{CO}.....126
Figure 6.14. CO conversion vs. time for various W_{cat}-W_{ad}/F_{CO} 126
Figure 6.15. CO Conversion vs. time for various W_{cat}-W_{ad}/F_{CO}.....127
Figure 6.16: MR-AR process within IGCC plant 128

List of Tables

Table 1.1. Milestone status report 4

Table 1.2. Success criteria status 6

Table 2.1. Permeance and selectivity of three early 10" (25.4 cm) candle-filter style CMS membranes and a typical 30" membrane at 250°C and 20 psig 12

Table 2.2. Performance at 300°C of several of the 30" CMS parts and the 10" parts generated from them (1 m^3/m^2.hr.bar= 370.3 GPU) 15

Table 2.3. Performance of the 10'' M-19 part as measured at USC (1 m^3/m^2.hr.bar= 370.3 GPU) 16

Table 2.4. Performance at 300°C of various 10" CMS membranes prepared during the 4th Quarter 18

Table 2.5. Performance at 250°C of various CMS parts. The high H_2/CO_2 data noted with * here have been confirmed in repeated tests. (The H_2/CO values are inferred based on typical CO/N_2 permeance ratios) 19

Table 2.6. Summary performance at 250°C of various CMS parts prepared during this project. Several parts have been supplied to USC for MR testing, as noted. The extraordinarily high H_2/CO_2 data noted with * here have been confirmed in repeated tests 21

Table 2.7. Summary performance at 250°C of various CMS parts prepared during this project. Several parts have been supplied to USC for MR testing as noted 22

Table 2.8. Summary of TGA results for CO_2 adsorption on variously prepared and calcined samples of HTC prepared by M&PT, and one commercial sample obtained from Alcoa 32

Table 2.9. Summary of TGA results for CO_2 adsorption on variously prepared and pre-treated (calcined) samples of hydrotalcite prepared by M&PT 33

Table 2.10. Physical and chemical properties of the Co-Mo/Al_2O_3 sour-shift catalyst 37

Table 2.11. Fitted kinetic parameters for the power-law rate model 39

Table 2.12. Results for RMSD for each kinetic model 40

Table 3.1. CO_2 mass balance for different adsorption pressures at 250ºC (flow rate = 500 sccm) 53

Table 3.2. Values of the Langmuir Isotherm parameters 58

Table 4.1. Pure-gas permeances of He and N_2 and corresponding ideal selectivity at various temperatures and pressures measured in the empty module 74

Table 4.2. Single-gas permeances and ideal selectivities before and after the MR-AR experiments 78

Table 4.3. Single- gas permeances of N_2 and He at various temperatures and pressures measured in the empty module 89

Table 4.4. Single- gas permeances of N_2 and He at 250°C and 25 bar measured in the module after loading the catalyst 90

Table 4.5. Single- gas permeances of He, N_2, H_2, N_2, A_r, CO, CO_2 and methane at 250°C and 25 bar after the catalyst activation 90

Table 4.6. Single- gas permeances of He, N_2, H_2, N_2, CO, at 250°C and 25bar during the 500-hr run 91

Table 4.7. Single- gas permeances of A_r, CO_2 and methane before and after the 500 hr run .91

Table 4.8. Single- gas permeances of He, N_2 at 250°C and 15 bar after a total of 742 hr exposure to H_2S.....92

Table 6.1. MR simulation cases vs. design parameters.....119

Table 6.2: MR simulation cases vs. design parameters 123

Table 6.3: Metric comparison of baseline pre-combustion CCS IGCC with IGCC MR-AR 129

Table 6.4. Metric comparison of IGCC MR-AR with performance targets 130

Table 6.5: Cost comparison of baseline pre-combustion CCS IGCC with IGCC MR-AR..130

Table 6.6: Performance summary of pre-combustion IGCC with CCS and IGCC MR-AR 131

Table 6.7. Capital cost summary of IGCC MR-AR.....133

Table 6.8. Operating cost summary for IGCC MR-AR 134

Table 6.9. Sensitivity Analysis for Membrane Reactor Lifespan 135

Table 6.10: Sensitivity Analysis for Nitrogen Sale Price..... 136

1. INTRODUCTION AND OVERAL PROJECT STRUCTURE

1.1 Major Goals of the Project

The major goal of this lab-scale study was to prove the technical feasibility of the membrane- and adsorption-enhanced water gas shift (WGS) reaction process that employs a carbon molecular sieve (CMS) membrane reactor (MR) followed by an adsorption reactor (AR) for pre-combustion carbon dioxide (CO_2) capture (for a schematic of the proposed process, see Fig. 1.1), while demonstrating progress towards achievement of the overall fossil energy performance goals of 90% CO_2 capture rate with 95% CO_2 purity, at a cost of electricity of 30% less than the baseline capture approaches. Such a WGS system combining a MR and an AR in tandem can produce an ultra-pure hydrogen (H_2) product (without the need for using a post-processing step) continuously, until the adsorbent (hydrotalcite-based) in the AR unit is saturated for regeneration via a pressure swing adsorption (PSA) and/or temperature swing adsorption (TSA) operation. The project effort was led by the University of Southern California (USC) with assistance from the University of California - Los Angeles (UCLA) and the Media and Process Technology, Inc. (M&PT).

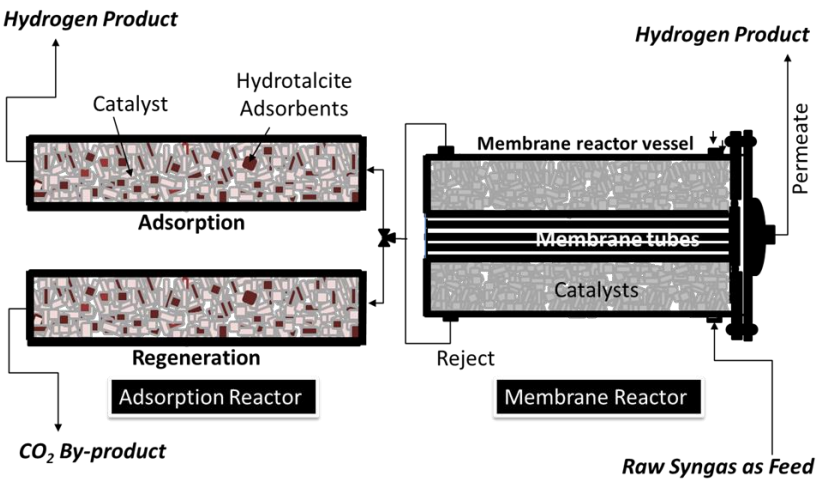

Figure 1.1. The MR-AR Process

1.2 Project Structure

The project was divided into two Budget Periods (BP). During Budget Period 1 (BP1) of the project, the key objective was to design, construct and test the lab-scale experimental MR-AR system, to select and characterize appropriate membranes, adsorbents and catalysts; and to also upgrade and experimentally validate an in-house mathematical model. The reactor system originally in operation at USC was to be modified by decoupling the MR and AR components (with the AR following the MR). The flow system was to be augmented with control valves and other hardware that permit the experimental testing of more elaborate adsorption/desorption protocols for the AR subsystem. The key objective during BP2 was to experimentally test the proposed novel process in the lab-scale apparatus using simulated fuel gas (gasifier off-gas), and to complete the initial technical and economic feasibility study.

In each Budget Period, there were a number of milestones and success criteria, as shown in Tables 1.1 and 1.2 below. These were all met by their due dates, as indicated in Tables 1.1 and 1.2. Specifically, during BP1 we (i) completed the construction of the lab-scale MR-AR experimental system; (ii) prepared and characterized CMS membranes at the anticipated process conditions; (iii) prepared and characterized adsorbents at the anticipated process conditions, and generated global rate expressions for the catalyst; (iv) began testing of the MR and AR individual subsystems; and (v) developed mathematical models and began validating their ability to fit the experimental data. During BP2 (i) we experimentally tested the proposed novel process in the lab-scale apparatus using simulated fuel gas (gasifier off-gas), and (ii) we completed the initial technical and economic feasibility study.

The project consisted of a number of Tasks, as outlined below:

Task 1.0 - Project Management and Planning

Task 2.0 - Materials Preparation and Characterization

Subtask 2.1 - Preparation and Characterization of the CMS Membranes

Subtask 2.2 - Preparation and Characterization of Adsorbents and Catalysts

Task 3.0 - Design and Construction of the Lab-Scale Experimental System

Task 4.0 - Initial Testing and Modeling of the Lab-Scale Experimental System

Subtask 4.1 - Unit Operation Testing

Subtask 4.2 - Mathematical Model Development and Simulations

Task 5.0 – Integrated Testing and Modeling of the Lab-Scale Experimental System

Subtask 5.1 – Materials Optimization and Scale-up

Subtask 5.2 - Integrated Testing

Subtask 5.3 - Model Simulations and Data Analysis

Task 6.0 - Preliminary Process Design/Optimization and Economic Evaluation

Subtask 6.1 – Process Design/Optimization

Subtask 6.2 – Sensitivity Analysis

1.3 Project Administration

As part of "Task 1.0 - Project Management and Planning", the PI carried-out the management of the technical, budgetary and scheduling activities. The PI provided monthly technical briefings/reports to the Project Manager (PM) of DOE/NETL. During regular biweekly conferences/meetings, and on as needed basis, the co-PIs provided input to the PI on technical and financial progress. In the start of the project, the team worked with the DOE/NETL PM to finalize the Project Management Plan (PMP) – a project milestone, which was completed prior to the planned completion date (see Table 1.1). The PI and both co-PIs participated in a Kick-off Meeting with the DOE/NETL PM and his team in Pittsburgh, PA. The presentation file (a project milestone) was delivered to the DOE/NETL PM prior to the planned completion date (see Table 1). The PI (and at least one of the other co-PIs) participated in the Annual CO_2 Capture Technology Meetings, during the month of August, in Pittsburgh, PA. The slide-decks of their presentation were delivered to the DOE/NETL PM after the conclusion of the meeting. The team completed and delivered on time all quarterly Research Performance Progress Reports (RPPR) and worked with the DOE/NETL PM to incorporate his revisions into these reports.

Table 1.1. Milestone status report

Budget Period	ID	Task	Description	Planned Completion Date	Actual Completion Date	Verification Method
1	a	1	Updated PMP submitted	10/31/2015	10/31/2015	PMP document
1	b	1	Kick-off meeting convened	12/31/2015	12/31/2015	Presentation file/report documents
1	c	3	Construction of the lab-scale MR-AR experimental system (designed for pressures up to 25 bar) completed	3/31/2016	3/31/2016	Description and photographs provided in the quarterly report
1	d	2	Preparation/characterization of the CMS membranes at the anticipated process conditions (up to 300ºC and 25 bar total pressure) completed	6/30/2016	6/30/2016	Results reported in the quarterly report
1	e	2	Preparation/characterization of the HT-based adsorbents at the anticipated process conditions (300-450ºC and up to 25 bar total pressure) completed. Adsorbent working capacity, adsorption/desorption kinetics determined. Global rate expression for Co/Mo-based sour shift catalysts at the anticipated process conditions (up to 300ºC and 25 bar total pressure) generated	12/31/2016	12/31/2016	Results reported in the quarterly report
1	f	4	MR subsystem testing and reporting of key parameters (permeance, selectivity, catalyst weight, temperature, pressures, residence time, CO conversion, effluent stream compositions, etc.) completed	3/31/2017	3/31/2017	Results reported in the quarterly report
1	g	4	AR subsystem testing and reporting of key parameters (adsorbent and catalyst weight, temperatures, pressures, residence time, desorption mode, working capacity, energy demand, effluent stream compositions, etc.) completed	3/31/2017	3/31/2017	Results reported in the quarterly report
	h	4	Mathematical model modifications to simulate the hybrid MR-AR process and validate model using experimental	3/31/2017	3/31/2017	Results reported in the quarterly report

1			MR and AR subsystem test results completed			
2	i	5	Parametric testing of the integrated, lab-scale MR-AR system and identification of optimal operating conditions for long-term testing completed	9/30/2017	9/30/2017	Results reported in the quarterly report
2	j	5	Short-term (24 hr for initial screening) and long-term (>100 hr) hydrothermal and chemical stability (e.g., NH_3, H_2S, H_2O, etc.) materials evaluations at the anticipated process conditions completed	3/31/2018	3/31/2018	Results reported in the quarterly report
2	k	5	Integrated system modeling and data analysis completed	3/31/2018	3/31/2018	Results reported in the quarterly report
2	l	5	Materials optimization with respect to membrane permeance/selectivity and adsorbent working capacity at the anticipated process conditions (up to 300ºC for membranes and 300-450ºC for adsorbents, and up to 25 bar total pressure) completed	12/31/2018	12/31/2018	Results reported in the quarterly report
2	m	5	Operation of the integrated lab-scale MR-AR system for at least 500 hr at the optimal operating conditions to evaluate material stability and process operability completed	12/31/2018	12/31/2018	Results reported in the quarterly report
2	n	6	Preliminary process design and optimization based on integrated MR-AR experimental results completed	3/31/2019	12/31/2018	Results reported in quarterly and in the Final Report
2	o	6	Initial technical and economic feasibility study and sensitivity analysis completed	3/31/2019	12/31/2018	Results reported in quarterly and in the Final Report
1,2	QR	1	Quarterly report	Each quarter		Quarterly Report files
2	FR	1	Draft Final report	4/30/2019	4/30/2019	Draft Final Report file

Table 1.2. Success criteria status

Success Criteria for BP1	Status/Comments
Successful completion of all work proposed in Budget Period 1 (up to 12/31/2016).	Achieved, see Final Report
Measurements of membrane permeance for H_2, CH_4, CO, CO_2 both in the absence and presence of H_2O, NH_3, H_2S for full-range of operating temperatures (up to 300ºC) and total pressures (10-25 bar). Target range for H_2 permeance 1-1.5 m^3/m^2.hr.bar; Target range for H_2/CO selectivity 80-100	Achieved, see Sect. 2.1 in Final Report.
Measurement of adsorption/desorption kinetics and working capacity at relevant conditions (300˚C<T<450˚C, pressures up to 25 bar). Measurement of catalytic kinetics, and the development of global rate expression at relevant conditions (temperatures up to 300ºC and pressures up to 25 bar). Target for working capacity >3 wt%	Achieved, see Sect. 2.2 in Final Report.
Complete fabrication of the lab-scale apparatus and testing of the individual units (MR or AR) at relevant experimental conditions. Measurements of CO conversion (%), H_2 recovery (%) and purity (%), CO_2 capture ratio/purity (%) and energy demand for regeneration (kJ/mol CO_2). Generation of experimental data sufficient to validate the model.	Achieved, see Sect. 2.3 and Sect. 3.0 of Final Report
Completion of simulations of the MR-AR system that indicate its ability to meet the targets for CO conversion >95%, for H_2 purity >95%, for H_2 recovery >90%, for CO_2 purity >95%, for CO_2 recovery >90%.	Achieved, see Sect. 5.0 in Final Report
Success Criteria for BP2	
Successful completion of all work proposed in Budget Period 2.	Achieved, see Final Report
Completion of short-term (24 hr) and long-term (>100 hr) hydrothermal/chemical stability evaluations. Membranes/adsorbents are stable towards fuel gas constituents (e.g., NH_3, H_2S, H_2O) at the anticipated process operating conditions. Target <10% decline in performance over 100 hr of testing.	Achieved, see Sect. 4.2 in Final Report.
Completion of integrated testing and system operated for >500 hr at optimal process conditions.	Achieved, see Sect. 4.3 in Final Report.
Results of the initial technical and economic feasibility study show significant progress toward achievement of the overall fossil energy performance goals of 90% CO_2 capture rate with 95% CO_2 purity at a cost of electricity 30% less than baseline capture approaches	Achieved, see Sect. 6.0 in Final Report.
Submission of updated membrane and adsorbent state-point data tables based on the results of integrated lab-scale MR-AR testing	Achieved, see Final Report
Submission of a Final Report	Achieved, Report Submitted

Technical Presentations

We have presented a number of technical papers at various meetings, as indicated below.

1. Tsotsis, T., Manousiouthakis, V., Ciora, R., "A High Efficiency, Ultra-Compact Process for Pre-Combustion CO_2 Capture," Project Kick-off Presentation, Pittsburgh, PA, Nov. 16, 2015.

2. Tsotsis, T., Manousiouthakis, V., Ciora, R., "A High Efficiency, Ultra-Compact Process for Pre-combustion CO_2 Capture (FE0026423), Presented at the CO_2 Capture Technology Meeting, August 8-12, 2016, Pittsburgh, PA.

3. Lowd, J., Tsotsis, T., Manousiouthakis, V., Ciora, R., "Experimental and Theoretical Studies of CO_2 Adsorption on Hydrotalcite," Presentation at 2016 AICHE Conference, November 13-18, San Francisco, California.

4. Karagoz S., Tsotsis, T., Manousiouthakis, V., "Study of Adsorptive Reactor (AR): Dynamic Multi-Scale (Catalyst/Adsorbent/Reactor Scale) Modeling and Simulation", Presentation at 2016 AICHE Conference, November 13-18, San Francisco, California.

5. Karagoz S., Tsotsis, T., Manousiouthakis, V., "Multi-Scale (Pellet-Reactor Scale) Membrane Reactor Modeling and Simulation: Low Temperature and High Pressure Water-Gas Shift Reaction," Presentation at 2016 AICHE Conference, November 13-18, San Francisco, California.

6. Tsotsis, T., Manousiouthakis, V., Ciora, R., "A High Efficiency, Ultra-Compact Process for Pre-Combustion CO_2 Capture," BP1 Project Review Meeting Presentation, Pittsburgh, PA, March 2, 2017.

7. Garshasbi, A., Chen, H., Cao, M., Karagöz, S., Ciora, R.J., Liu, P.K.T, Manousiouthakis, V.I., and Tsotsis, T.T., "Membrane-Based Reactive Separations for Process Intensification During Power Generation," Key-note Presentation at the ICCMR13, Houston, TX, July 10-13, 2017.

8. Garshasbi, A., Chen, H., Cao, M., Karagöz, S., Ciora, R.J., Liu, P.K.T, Manousiouthakis, V.I., and Tsotsis, T.T., "Membrane-Based Reactive Separations in Power Generation," Presentation at the ICOM 2017, San Francisco, CA, July 29- August 4, 2017.

9. Tsotsis, T., Manousiouthakis, V., Ciora, R., "A High Efficiency, Ultra-Compact Process for Pre-combustion CO_2 Capture (FE0026423)," Presented at the CO_2 Capture Technology Meeting, August 2017, Pittsburgh, PA.

10. Karagoz S., Tsotsis, T., Manousiouthakis, V., "Modeling and Simulation of a Hybrid Adsorptive-Membrane Reactor (HAMR) for Intensification of the Water-Gas Shift (WGS) Reaction Process", Presentation at 2017 AIChE Conference, October 29 - November 3, Minneapolis, MN.

11. Karagoz S., Tsotsis, T., Manousiouthakis, V., "A Parametric Study of the Adsorption/Desorption Steps for an Adsorptive Reactor (AR) Intensifying the Water Gas Shift (WGS) Reaction" Presentation at 2017 AIChE Conference, October 29 - November 3, Minneapolis, MN.

12. Karagoz S., Tsotsis, T., Manousiouthakis, V., "Comparative Study of a Hybrid Adsorptive-Membrane Reactor (HAMR) with a Membrane Reactor/Adsorptive Reactor Sequence", Presentation at the 2017 AIChE Conference, October 29 - November 3, Minneapolis, MN.

13. Pichardo, P., Karagoz, S., Tsotsis, T.T., Ciora, R., Manousiouthakis, V. "Technical Economic Analysis of an Intensified Integrated Gasification Combined Cycle Plant Design Featuring Membrane and Adsorptive Reactors", Presentation at 2017 AIChE Conference, October 29 - November 3, Minneapolis, MN.

14. Chen, H., Cao, M., Karagoz, S., Manousiouthakis, V., and Tsotsis, T.T., "Experimental and Numerical Study of an Intensified Water-Gas Shift (WGS) Reaction Process Using a Membrane Reactor (MR)/Adsorptive Reactor (AR) Sequence", Presentation at the 2017 AIChE Conference, October 29 - November 3, Minneapolis, MN.

15. Garshasbi, A., Karagöz**,** S**.,** Chen, H., Cao, M., Pichardo, P., Ciora, R., Liu, P.K.T, Manousiouthakis, V., and Tsotsis, T.T., "Membrane-Based Reactive Separations for Process Intensification During the Power Generation", Presentation at the 25th International Symposium on Chemical Reaction Engineering, May 20 - 23, 2018, Florence, Italy.

16. Chen, H., Garshasbi, A., Karagöz**,** S**.,** Cao, M., Pichardo, P., Ciora, R., Liu, P.K.T, Manousiouthakis, V., and Tsotsis, T.T., "Carbon Molecular Sieve-Based Reactive Separations for Power Generation Applications," Presentation at the 15th International Conference on Inorganic Membranes, June 18 - 22, 2018, Dresden, Germany

17. Tsotsis, T., Manousiouthakis, V., Ciora, R., "A High Efficiency, Ultra-Compact Process for Pre-combustion CO_2 Capture (FE0026423)," Presented at the CO_2 Capture Technology Meeting, August 13-17, 2018, Pittsburgh, PA.

18. Karagoz S., Tsotsis, T., Manousiouthakis, V.I., "Process Intensification of Hydrogen Production Systems", Session 185ag Interactive Session: Systems and Process Design, presented at AIChE Annual Meeting, Pittsburgh, PA, 10-29-2018.

19. Karagoz S., Tsotsis, T., Manousiouthakis, V.I., "Effectiveness Factor Phenomena for the Transition between PBR and MR via Coupled Heat and Mass Transfer", Session 360g Process Intensification by Enhanced Heat and Mass Transfer, presented at AIChE Annual Meeting, Pittsburgh, PA, 10-30-2018.

20. Chen, H., Cao, M., Karagoz, S., Zhao, L., Manousiouthakis, V., and Tsotsis, T.T., "Experimental and Numerical Study of an Intensified Water-Gas Shift (WGS) Reactor Process Using a Membrane Reactor (MR)/Adsorptive Reactor (AR) Sequence," Paper 464b, presented at the AIChE Annual Meeting, Pittsburgh, PA, 10-31-2018.

Technical Publications

We have published seven papers in peer-reviewed journals. One other paper is currently under review. These papers are listed below. Several other papers are also currently under preparation.

1. Karagöz, S., Da Cruz, F.E., Tsotsis, T.T., and Manousiouthakis, V.I., "Multi-Scale Membrane Reactor (MR) Modeling and Simulation for the Water Gas Shift Reaction," *Chemical Engineering & Processing: Process Intensification*, 133, 245, 2018.

2. Chen, H., Cao, M., Manousiouthakis, V.I., and Tsotsis, T.T., "An Experimental Study of an Intensified Water-Gas Shift Reaction Process Using a Membrane Reactor/Adsorptive Reactor Sequence," *Ind. Eng. Chem. Res.*, 57, 13650, 2018.

3. Karagöz, S., Tsotsis, T.T., and Manousiouthakis, V.I., "Multi-scale Modeling and Simulation of a Novel Membrane Reactor (MR)/Adsorptive Reactor (AR) Process," In Press, *Chemical Engineering & Processing: Process Intensification*, 137, 146, 2019.

4. Karagöz, S., Tsotsis, T.T., and Manousiouthakis, V.I., "Energy Intensification of H_2 Generation and CO_2 Capture/Utilization by Carrying-out the Water Gas Shift Reaction in an Adsorptive Reactor: Multiscale Dynamic Modeling and Simulation," *AIChE J.,* 2019.doi: 10.1002/aic.16608.

5. Pichardo, P., Karagöz, S., Ciora, R., Tsotsis, T.T., and Manousiouthakis, V.I., "Technical Economic Analysis of an Intensified Integrated Gasification Combined Cycle (IGCC) Power Plant Featuring a Sequence of Membrane Reactors," *J. Membrane Sci.,* 579, 266, 2019.

6. Garshasbi, A., Chen, H., Cao, M., Karagöz, S., Ciora, R.J., Liu, P.K.T, Manousiouthakis, V.I., and Tsotsis, T.T., "Membrane-based Reactive Separations for Process Intensification during Power Generation", Catalysis Today, 331, 18, 2019.

7. Karagöz, S., Tsotsis, T.T., and Manousiouthakis, V.I., "Multi-scale Model based Design of Membrane Reactor/Separator Processes for Intensified Hydrogen Production through the Water Gas Shift Reaction," in Press, *Int. J. Hydrogen Energy.*

8. Pichardo, P., Karagöz, S., Ciora, R., Tsotsis, T.T., and Manousiouthakis, V.I., "Techno-Economic Analysis of an Intensified Integrated Gasification Combined Cycle (IGCC) Power Plant Featuring a Combined Membrane Reactor - Adsorptive Reactor (MR-AR) System," Under Review, *Ind. Eng. Chem. Res.*

Student Training

The project trained four graduate students, one at USC and three at UCLA, as well as a post-doctoral student at USC. Their names and current academic status are indicated below:

Mr. Mingyuan Cao, USC: Graduating with his PhD Degree in Chemical Engineering in August 2019.

Dr. Huanhao Chen, USC: Completed his post-doctoral assignment in 2018.

Mr. Sec Karagöz, UCLA: Graduating with his PhD Degree in Chemical Engineering in May 2019.

Ms. Patricia Pichardo, UCLA: Graduating with his PhD Degree in Chemical Engineering in May 2019.

Mr. Jack Lowd, UCLA: Graduating with his PhD Degree in Chemical Engineering in 2020.

In the remainder of the report, we describe activities and key accomplishments of the project that have resulted from the performance of the various Tasks as outlined in Sec. 1.2 above. Only the key activities and findings are described in this Final Report, and for the technical details the reader is referred to the various RPPR's or the technical papers in Sect. 1.3.

2. MATERIALS PREPARATION AND CHARACTERIZATION

Our activities here focus on the preparation and characterization of the key classes of materials involved in this research project, specifically the carbon molecular sieve membranes, the adsorbent, and the sour-shift WGS catalyst. The findings reported in this section were generated as part of the efforts in Task 2.0 (BP1) and Task 5.1 (BP2). M&PT was the lead organization in these activities, tasked with the preparation of membranes and adsorbents. USC assisted with the characterization of the materials, and was also responsible for the testing of the catalyst activity. UCLA assisted with the analysis of the kinetic data. The following discussion describes activities and accomplishments as they pertain to each of these materials:

2.1 - Preparation and Characterization of the CMS Membranes

The primary focus here was to prepare CMS membranes for the membrane reactor testing part of the project (see Sect. 4 below). The target was to prepare CMS membrane tubes with high H_2 permeance (1 to 1.5 $m^3/m^2/hr/bar$, or 370.3 to 555.5 GPU) and a H_2/CO selectivity >80 at the relevant temperature (up to 300°C) and pressure conditions (up to 25 bar). We have succeeded in preparing membranes that meet these targets. Below, we briefly summarize our efforts, while additional details can be found in the quarterly RPPRs.

Table 2.1. Permeance and selectivity of three early 10” (25.4 cm) candle-filter style CMS membranes and a typical 30” membrane at 250°C and 20 psig

Part ID	He Permeance [GPU]	Selectivity He/N_2 [-]	Selectivity He/CO_2 [-]
HAMR-CMS-10”-001	585	62	35
HAMR-CMS-10”-002	491	68	38
HAMR-CMS-10”-003	604	55	32
30” CMS Candle-Filter Tube Performance			
HAMR-CMS-006	571	147	119

The key technical challenge we (M&PT) faced is "down-scaling" the method of preparing closed-end, candle-filter membranes at the 25.4 cm (10 in) size appropriate for testing in the USC lab-scale MR apparatus. Prior to the initiation of the project, the team (M&PT) had substantial experience in preparing longer 76.2 cm (30 in) CMS membranes. However, initial efforts that followed the same preparation procedure employed for the longer membranes did not prove successful in preparing the shorter (25.4 cm) candle-filter (closed-end) membranes, as Table 2.1 above indicates, which compares the properties of three early 25.4 cm membranes with the corresponding properties of a 76.2 cm membrane prepared during the same period. (Note, that throughout this study He is frequently used as a safe model test-gas in place of H_2. Measurements, side-by-side, of He and H_2 permeation rates through the same membrane both at USC and M&PT indicate that for the great majority of cases - with the occasional outlier - the He and H_2 permeabilities are within +-5% from each other. In this report, therefore, we mostly report He single gas permeances, and only occasionally H_2 permeances for some of these membranes. M&PT was not equipped, for most of the project, to do CO measurements with their membranes, so in their facility N_2 was used as a surrogate gas, instead. Measurement of the CO permeances of the membranes sent to USC (and very recently at M&PT as well) indicate, e.g., see RPPR 3, that they are ~15 - 20% higher than those of N_2).

To address this issue, we (M&PT) followed two approaches: the first (stop-gap) measure was to prepare 76.2 cm membranes and cut from them 25.4 cm long pieces, so that they are sent to USC for further testing and verification of their properties, and for the preliminary MR studies. This approach prepared moderately successful membrane parts, as Table 2.2 below indicates. Though the original 76.2 cm (30") parts had good permeation properties, the 25.4 cm parts prepared from the larger parts had distinctly inferior properties, particularly their slow gas (e.g., N_2) permeance increased substantially.

The M-19 part in Table 2.2 was shipped to USC for additional performance testing and evaluation. At USC, the M-19 part was characterized by measurements of its He, N_2, H_2 and CO permeances. The values are shown in Table 2.3 (Note that the permeances in Table 2.3 are reported at S.T.P conditions, while the values reported in Tables 2.1 and 2.2 represent the raw permeation data at the temperature and barometric conditions prevailing at the M&PT

laboratories at the time of the experiments). The first two rows in Table 2.3 represent the permeation data measured at M&PT prior to shipping the membrane to USC, while the other rows are values measured at USC. Comparing the values in row 1, measured at M&PT, with those in row 5, measured at USC under the same conditions (300ºC and 20 psig), the He permeance measured at USC is 7.2% less than the value measured at M&PT, while the H_2 permeance is 2.6% less. These differences, most likely, reflect experimental uncertainties in the measurements made in two different laboratories, which are quite common. The N_2 permeance, on the other hand, measured at USC is 16.6% higher, which is probably due to the development of micro-cracks during the shipping process, probably in the graphite gaskets sealing the membrane to the reactor body. (It should be noted that improvements in better packing of the modules for shipping have, subsequently, eliminated this problem, with the N_2 permeances of membranes shipped since to USC being, generally, close to those measured at M&PT, e.g., see some of the measurements reported in Sect. 4). Such micro-cracks, however, are nm in size (probably<2-4 nm) as the N_2 permeance shows no dependence on pressure (compare permeance values between rows 5 and 6). That is also the general observation at both M&PT and USC, namely that for these nanoporous CMS membranes pressure has no impact on the slow gas (e.g., CO) permeance. The increase in pressure causes a slight decrease in the permeance of the fast gases (3.2% for He and 2.2% for H_2) which, however, is not far from the experimental uncertainty in making some of these measurements. The H_2 permeance of the M-19 10" CMS membrane significantly exceeds (by ~50%) the upper limit of the target range (1 to 1.5 $m^3/m^2/hr/bar$). The (H_2/CO) selectivity is, however, somewhat lower than the target (66-68 vs. >80). The selectivity of the original 30" part (see Table 2.2) was most likely significantly larger. Though not measured by M&PT, the CO permeance (based on the values for N_2 and CO with the 10" CMS part measured at USC – see Table 2.3) most likely averaged ~0.013 $m^3/m^2/hr/bar$, which means that its (H_2/CO) selectivity was >160.

Table 2.2. Performance at 300°C of several of the 30" CMS parts and the 10" parts generated from them (1 m^3/m^2.hr.bar= 370.3 GPU)

Part ID	Temperature	Permeance [m3/m2/hr/bar]				Selectivity		
	[°C]	He	N_2	H_2	CO_2	He/N_2	H_2/N_2	H_2/CO_2
M-19	300°C	2.17	0.011	2.14	0.034	197	195	62.9
	+24 hours	2.14	0.0117			183		
	+48 hours	2.05	0.0102			201		
	+120 hours	2.24	0.0122			184		
	Cut part to length and install in USC reactor module.							
	+120 hours	2.54	0.0312	2.51	0.032	81	80	78.4
	+264 hours	2.42	0.0267			91		
	+288 hours	2.59	0.0287			90		
	+312 hours	2.54	0.028			91		
	Shipped to USC for evaluation.							
		He	N_2	H_2	CO_2	He/N_2	H_2/N_2	H_2/CO_2
M-17	300°C	2.44	0.0178	2.56	0.065	137	144	39.4
	+24 hours	2.5	0.020			125		
	+48 hours	2.38	0.0196			121		
	+120 hours	2.47	0.0229			108		
	+144 hours	2.61	0.022			119		
	+168 hours	2.51	0.0235			107		
	+192 hours	2.58	0.0268			96		
	+312 hours	2.59	0.0345			75		
	Bubble test shows seam leaking between the closed glass tip and the CMS layer.							
		He	N_2	H_2	CO_2	He/N_2	H_2/N_2	H_2/CO_2
M-8	300°C	1.67	0.0152	1.71	0.044	110	113	38.9
	+24 hours	1.57	0.0151			104		
	+96 hours	1.51	0.0147			103		
	Cut part to length and install in USC reactor module.							
	300°C	1.89	0.0202	2.19		94		
	+24 hours		0.0241					
	+96 hours	1.99	0.0256			78		
	+120 hours	2.04	0.0255			80		
	+144 hours	2.10	0.0250			84		
	+168 hours	2.05	0.0263			78		
	+288 hours	2.11	0.0276			77		
	+312 hours	2.09	0.0272			77		
	+336 hours	2.14	0.0263			81		
	+432 hours	2.13	0.0265			80		
	+456 hours	2.15	0.0262			82		

In parallel, M&PT undertook a systematic study to understand the reasons why they were not, initially, able to prepare 25.4 cm membranes with comparable properties with those of the 76.2 cm membranes. In the past (prior to the start of this project), the main source of problems responsible for the preparation of low-quality CMS membranes was found to be flaws in the substrate. To investigate whether this was also a problem with these 25.4 cm substrate tubes, several substrates from the original batch were deposited with the carbon precursor material, and were examined for potential flaws. The carbon precursor "stains" the membrane

and often reveals preliminary flaws in the part that often (though not always) translate into poor CMS membrane performance. Visual inspection showed a far higher number of "spots" on the tube, generally attributable to pinholes in the surface layer. SEM investigation of these parts revealed pinhole development in the 40Å surface layer. Figure 2.1 shows the morphology of the typical defect. The spherical shape and edging of the defects is again attributable to bubbles in the slip. Fortunately, this is a relatively straightforward problem to resolve, since it is the outcome of mishandling the ceramic slip used in the preparation of the 40Å top-coating on the support tubes. Subsequently, several additional sets of 10" ceramic tubular substrates were prepared with a focus on overcoming this problem, so that high-quality 10" glass end-sealed parts could be prepared.

Table 2.3. Performance of the 10'' M-19 part as measured at USC (1 m^3/m^2.hr.bar= 370.3 GPU)

Part ID: M-19	T (^{0}C)	P (psi)	He [m^3/m^2*hr*bar]	N_2 [m^3/m^2*hr*bar]	H_2 [m^3/m^2*hr*bar]	CO [m^3/m^2*hr*bar]	Selectivity
M&PT-STP	300	20	2.34	0.024	2.31	-	97(He/N_2) 96(H_2/N_2)
M&PT-STP	300	160		0.024	-	-	
USC	24	20	0.39	0.029	-	-	13(He/N_2)
USC	24	200	0.34	0.032	-	-	10(He/N_2)
USC	300	20	2.17	0.028	2.25	0.033	76(He/N_2) 68(H_2/CO)
USC	300	200	2.10	0.028	2.20	0.033	76(He/N_2) 66(H_2/CO) 80(H_2/ N_2)

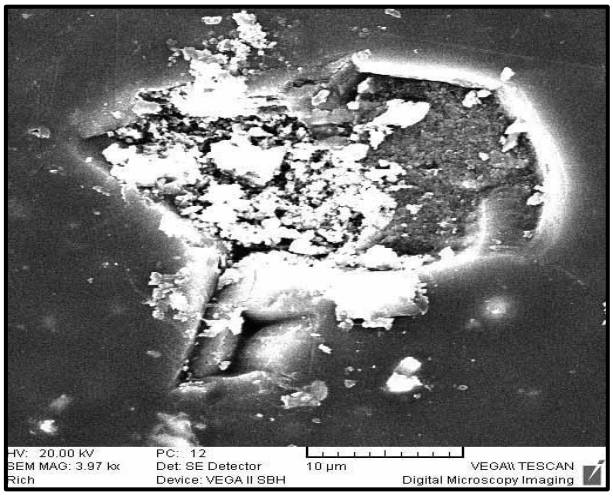

Figure 2.1. SEM photomicrograph of defects in the carbon precursor layer

Table 2.4 shows the initial performance data for the CMS membranes prepared using this new batch of substrates. As can be seen in this Table, several high performance parts have been prepared that meet the desired performance criteria. However, the scatter in the data is relatively high and several parts prepared (including several not shown in this table) displayed poor selectivity ($He/N_2 < 50$). Bubble-testing of these parts revealed obvious defects in the substrate, which under microscopy revealed micro-cracking in the CMS layer as a result of "mud cracking" in the intermediate layer. This flaw is, generally, due to too rapid drying of the intermediate layer during post-deposition annealing. A new set of substrates were then prepared and quality control (QC) analysis shows no similar defects.

These new substrates were utilized to prepare quality 25.4 cm membranes, and the properties of a number of these membranes are shown in Table 2.5. The Table also includes three membranes, specifically, the HMR-39, -47, and -49 parts, that were prepared from previous CMS membranes that had developed flaws in the layer (scratches or other mechanical damage). These membranes were calcined in air to burn-off the carbon layer then re-deposited with the CMS coating. Although the HMR-39 part is not quite as good (we attribute this to the first attempt), the HMR-47 and -49 membranes clearly show high performance and demonstrate that the membranes can be recovered, if necessary. All membranes in Table 2.5 (other than the aforementioned HMR-39 part) surpass the membrane performance targets, as set in the original PMP.

Table 2.4. Performance at 300°C of various 10" CMS membranes prepared during the 4th Quarter						
Part ID	***He [GPU]***	***N_2 [GPU]***	***H_2 [GPU]***	***CO_2 [GPU]***	***He/N_2 [-]***	***H_2/CO_2 [-]***
HMR-23 (10")	732	8.7	727	16.4	84	45
HMR-24 (10")	871	5.6	780	9.5	154	81
3Q2016 Membranes						
HMR-29 (10")	359	0.8	-	-	508	-
HMR-31 (10")	892	4.5	-	-	199	-
HMR-32 (10")	584	4.1	-	14	144	41
HMR-34 (10")	329	3.9	-	-	84	-
HMR-36 (10")	862	15	-	-	59	-
HMR-38 (10")	497	6.1	-	-	81	-
HMR-46 (10")	684	4.1	-	12.0	165	57

A secondary objective under this task was the development of CMS membranes with higher H_2/CO_2 selectivity, their use potentially permitting higher H_2 recovery levels in the WGS reactor as well as a higher CO_2 content in the high-pressure reject stream that is fed to the AR subsystem, where it can be more appropriately segregated and sequestered. As Table 2.5 indicates, we have successfully prepared several membranes, whose ideal H_2/CO_2 selectivities are well above the typical values of ~35-45 associated with CMS membranes previously prepared by our team. As Table 2.5 below shows, membranes with H_2/CO_2 selectivities values from the mid-60's to over 500 have been prepared. Further, these values have been demonstrated in repeated tests on several systems to confirm that we are not observing anomalies due to equipment error.

It is not entirely clear, at this point, what is the exact mechanism that is responsible for the very high H_2/CO_2 selectivity of these membranes. As part of this project, we have had significant success in preparing higher quality substrates (intermediate and final ceramic layers), as validated by repeated QC tests for membrane flaws (visual inspection, bubble-testing and dye-staining). However, this development alone does not account for the dramatic

improvement in the H_2/CO_2 selectivity that has been observed. Though not possible without high quality substrates, it appears that the rate and time of pyrolysis as well as the atmosphere control during pyrolysis are also critical to the fabrication of CMS membranes with ultra-high H_2/CO_2 selectivity. In particular, longer pyrolysis times appear to be necessary to develop higher selectivities at the pyrolysis temperature (>600°C), and this generally translates into high selectivities at the desired gas separation operating temperature (typically 250°C – 300°C). However, high quality substrates are a key pre-requisite, since when using lower quality substrates the selectivity will quickly plateau, and extended deposition times will lead simply to reduced H_2 permeances.

Table 2.5. Performance at 250°C of various CMS parts. The high H_2/CO_2 data noted with * here have been confirmed in repeated tests. (The H_2/CO values are inferred based on typical CO/N_2 permeance ratios)

Part ID	*He [GPU]*	*N_2 [GPU]*	*H_2 [GPU]*	*CO_2 [GPU]*	*H_2/N_2 [-]*	*H_2/CO [-]*	*H_2/CO_2 [-]*
HMR-41(10”)	482	5.7	367	5.7	145	121-126	65
HMR-44(10”)	645	4.2	722	11.3	172	143-150	64
HMR-45(10”)	366	0.85	400	3.2	471	392-410	126*
HMR-46(10”)	684	4.7	-	12.0	-		-
HMR-52(10”)	556	3.8	539	14.3	148	123-129	38
HMR-39(10”)	381	4.4	-	-	86	72-75	-
HMR-47(10”)	846	4.5	819	4.9	179	149-156	167*
HMR-49(10”)	434	1.7	427	8.3	249	207-216	51
HMR-48(10”)	418	4.4	451	6.8	102	85-89	68
HMR-42(10”)	368	1.0	364	0.7	361	301-314	540*

Tables 2.6 and 2.7 below provide a overall summary of all the CMS membranes that M&PT prepared throughout this project that meet and, typically, far exceed the original project performance targets. As the project progressed, M&PT overcame problems with layer delamination and microcracking in sections of the CMS membrane tubes, as reported above.

With these problems resolved, H_2/CO_2 selectivities in the range of 300 to >600, and He/N_2 selectivity >>120 are now readily obtained. As noted in Table 2.7, several membranes were damaged during long-term thermal stability testing at 250°C in N_2, as a result of exposure to air during loss of in-house N_2 over a weekend. Although the damage was not sufficient to render the parts unusable (the He/N_2 selectivity generally dropped into the 100 to 150 range), these parts were nevertheless calcined in air at 550°C to remove the carbon layer, and the CMS layer was then re-deposited on two of these parts. As can be seen in Table 2.7, for the HMR -107 and HMR -108 membranes after this re-deposition step the performance is very good and consistent with the highest quality parts made during the same period. Hence, it is clear that membranes damaged in service can be repaired.

Table 2.6. Summary performance at 250°C of various CMS parts prepared during this project. Several parts have been supplied to USC for MR testing, as noted. The extraordinarily high H_2/CO_2 data noted with * here have been confirmed in repeated tests

Part ID	*He [GPU]*	*N_2 [GPU]*	*H_2 [GPU]*	*CO_2 [GPU]*	*H_2/N_2 [-]*	*H_2/CO_2 [-]*
HMR-23 (10”)	732	8.7	727	16.4	84	45
HMR-24 (10”)[USC]	871	5.6	780	9.5	154	81
3Q2016 Membranes						
HMR-29 (10”)[USC]	359	0.8	-	-	508	-
HMR-31 (10”)	892	4.5	-	-	199	-
HMR-32 (10”)[USC]	584	4.1	-	14	144	41
HMR-34 (10”)	329	3.9	-	-	84	-
HMR-37 (10”)	437	1.9	467	12.5	241	37
HMR-36 (10”)	862	15	-	-	59	-
HMR-38 (10”)	497	6.1	-	-	81	-
4Q2016 Membranes						
HMR-41(10”)	482	5.7	367	5.7	145	65
HMR-44(10”)	645	4.2	722	11.3	172	64
HMR-45(10”)	366	0.85	400	3.2	471	126*
HMR-46(10”)[USC]	684	4.7	-	12.0	-	-
HMR-52(10”)[USC]	556	3.8	539	14.3	148	38
HMR-39(10”)[USC]	381	4.4	-	-	86	-
HMR-47(10”)	846	4.5	819	4.9	179	167*
HMR-43(10”)[USC 15]	434	1.7	427	8.3	249	51
HMR-42(10”)[USC 14]	368	1.0	364	0.7	361	540*
3Q2017 Membranes						
HMR-53(10”) [USC 16]	343	1.9	239	0.5	176	478
HMR-54(10”)	335	5.0		0.7	66	
(retest for steam)	323	5.3	H_2O: 91			He/H_2O: 3.5
HMR-55(10”)	573	5.0	460	0.9	114	525
HMR-56(10”)	507	2.5	510	1.1	202	486
HMR-57(10”)	771	7.9	992	15	97	64

Table 2.7. Summary performance at 250°C of various CMS parts prepared during this project. Several parts have been supplied to USC for MR testing, as noted

Part ID	*He [GPU]*	*N_2 [GPU]*	*H_2 [GPU]*	*CO_2 [GPU]*	*H_2/N_2 [-]*	*H_2/CO_2 [-]*
4Q2017Membranes						
HMR-60 (10”) [USC 20]	381	2.3	449	1.6	192	284
HMR-61 (10”) [USC 17]	578	2.5	550	1.0	219	558
HMR-62 (10”)	392	3.6	487	6.9	135	71
(retest for CO)	388	3.1	CO: 4.0	7.4	-	-
HMR-66 (10”) [USC 18]	433	0.8	384	0.5	499	751
HMR-67 (10”) [USC 21]	450	1.6	581	2.8	354	211
HMR-68 (10”) [USC 19]	591	3.0	675	2.7	227	248
HMR-70 (10”)	445	1.5	502	0.7	344	738
HMR-71 (10”)	313	0.5	292	0.5	549	549
(retest for steam)			H_2O: 193			He/H_2O: 2.2
HMR-72 (10”) [USC 22]	500	1.7	602	2.5	359	246
1Q2018 Membranes	Note: * indicate membrane damaged on exposure to high temperature air.					
HMR-92 (10”)	377	5.5	-	-	-	-
HMR-99 (10”)*	518	1.9	-	-	-	-
2Q2018 Membranes	Note: * indicate membrane damaged on exposure to high temperature air.					
HMR-100 (10”)*	409	0.82	377	0.55	459	681
HMR-101 (10”)*	363	1.1	249	0.37	235	667
HMR-102 (10”)	408	3.6	-	-	-	-
HMR-103 (10”)	512	1.3	249	0.37	235	667
HMR-104 (10”)	542	1.5	540	2.0	361	270
HMR-105 (10”)	515	2.6	461	0.92	178	458
HMR-106 (10”)	513	1.6	471	1.0	299	458
HMR-107 (10”)*	576	6.1				
Redeposit after damage	437	1.4				
HMR-108* (10”)	476	1.2	462	1.4	382	317
Redeposit after damage	518	1.9				
HMR-109 (10”)	434	0.57				
Part ID	*He [GPU]*	*N_2 [GPU]*	*H_2 [GPU]*	*CO_2 [GPU]*	*H_2/N_2 [-]*	*H_2/CO_2 [-]*
HMR-110 (10”)	506	1.9				

HMR-111 (10”)	483	1.1				
HMR-112 (10”)	508	1.2				
HMR-113 (10”)	440	0.93				
HMR-114 (10”)	538	1.2				

During the project, a key focus also was on longer-term stability testing of the 10” CMS membrane tubes. Typically, long-term testing of the membranes took place to establish membrane stability prior to shipment to USC for MR testing. The long-term performance stability of membrane HMR-52 (10”) is shown in Fig. 2.2, first in an M&PT standard module and then following installation in the USC MR module. Figure 2.2 shows the He permeance and He/N_2 selectivity over a period of about 33 days of testing at 250°C, the final three days being in the USC MR module. The membrane performance appears to be reasonably stable, although a slight drift downward in the He/N_2 selectivity is observed. Further, on transfer to the USC MR module, no change in the performance was observed. Figure 2.3 shows the performance of a different membrane (HMR-41(10”)) under similar conditions. Similarly, this membrane is also stable throughout the testing period. Figure 2.4 shows the stability testing of two latter generation membranes, specifically, the HMR-67 and HMR-72. As can be seen in Fig. 2.4, the performance is very stable. Both these parts were removed from testing and sent to USC for membrane reactor experiments, with results being presented in Sect. 4. Data with long-term testing (as long as 250 days) of several other parts can be found in the RPPR. These results are consistent with previous experience of our team prior to this project, in which, we have shown the CMS membranes being stable at 250°C in the presence of both reactive and inert gases for 1,000’s of hours of operation (e.g., see [1-5]).

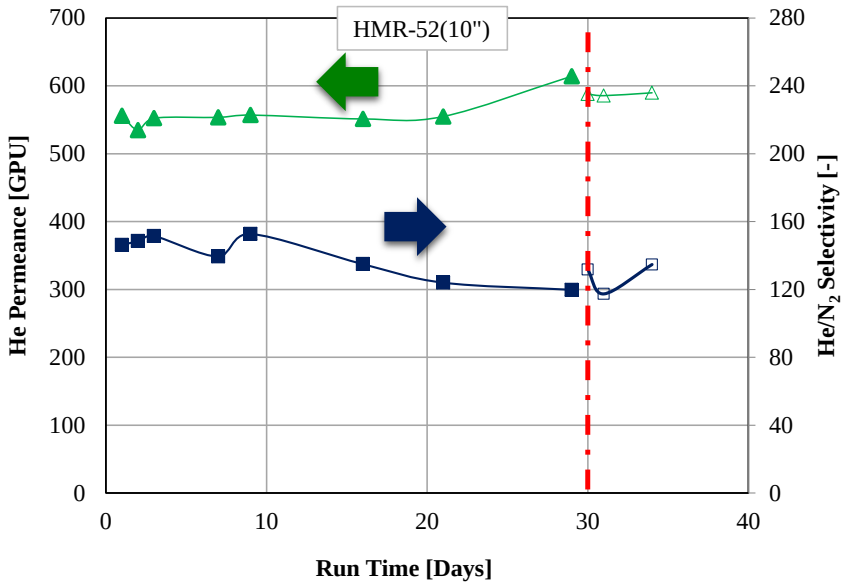

Figure 2.2. Thermal stability at 250°C in the presence of He and N_2 of the CMS membrane HMR-52 (10") before and after installation (dotted vertical line) in the USC MR module

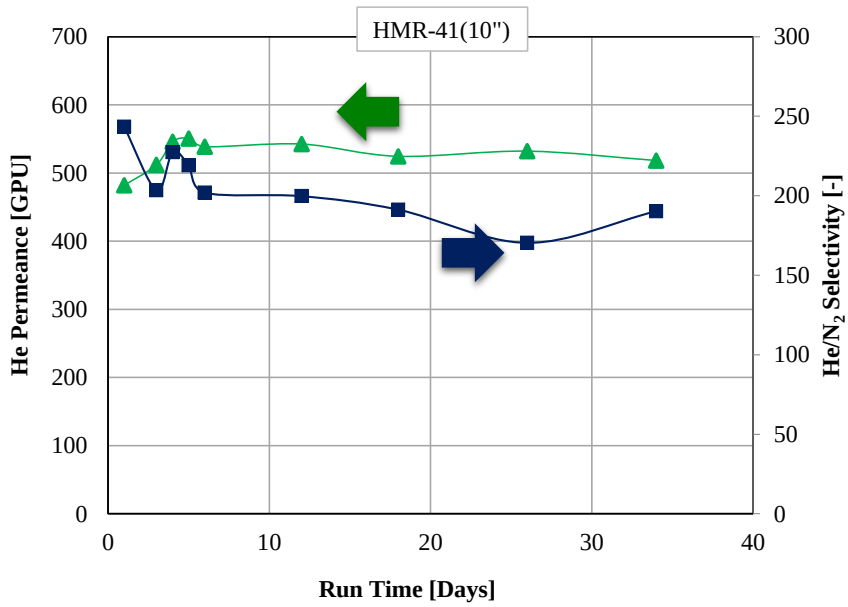

Figure 2.3. Thermal stability at 250°C in the presence of He and N_2 of the CMS membrane HMR-41 (10")

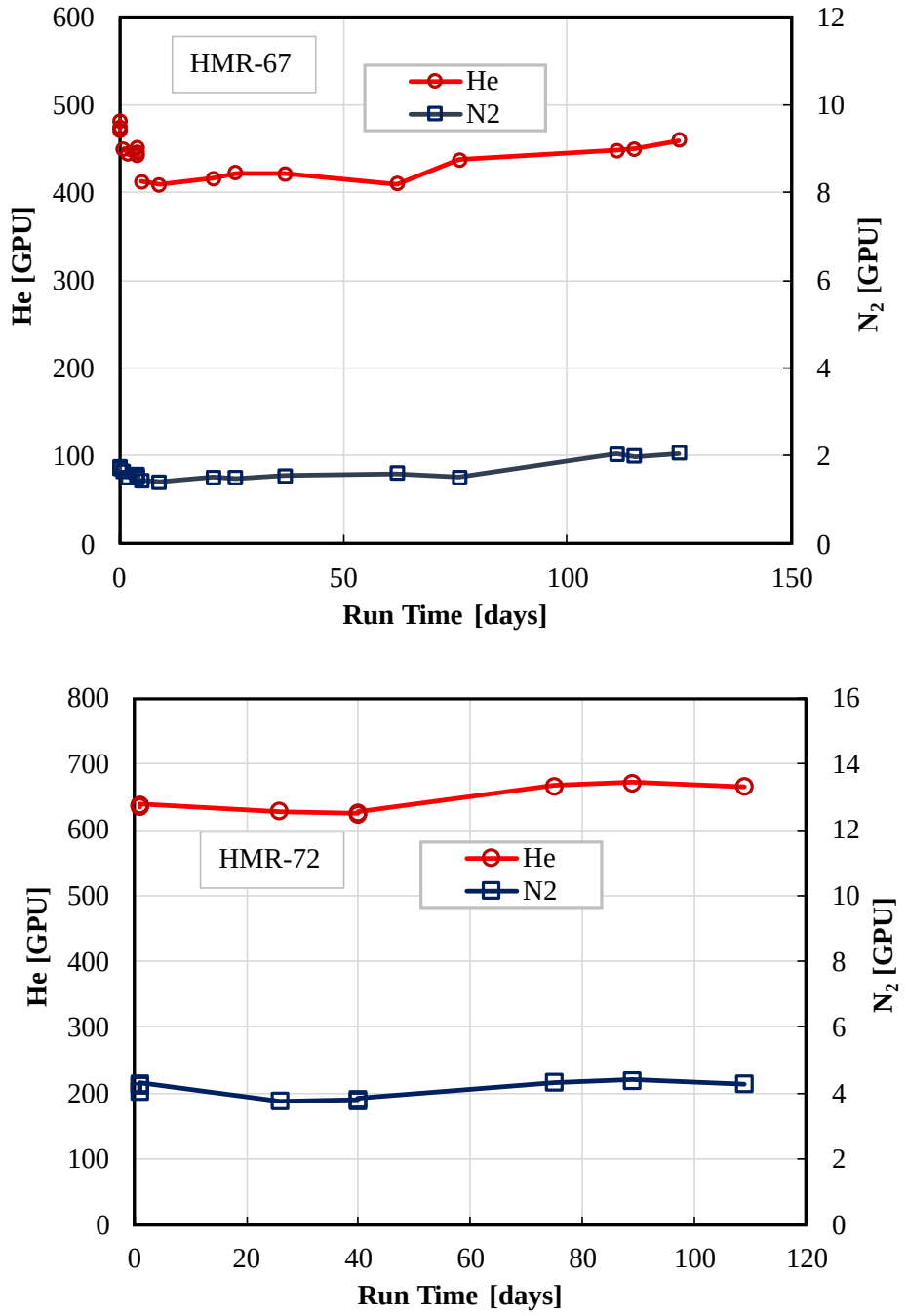

Figure 2.4. Thermal stability at 250°C in the presence of He and N_2 of HMR-67 (top) and HMR-72 (bottom) in M&PT standard testing module. Both membranes were transferred to the USC reactor modules for membrane reactor testing

2.2 - Preparation and Characterization of Adsorbents

The key focus of the activities described here is the preparation and characterization of the adsorbent materials for use in the AR. Hydrotalcite (HTC) materials (also known as layer double hydroxides or LDH) were selected for use in our project. The preparation and characterization of these HTC adsorbents is of importance to the overall performance of the proposed process, as the efficiency of the AR component is highly dependent on the working capacity of the HTC (mmol of CO_2 per gr of adsorbent) and its associated regeneration conditions. An ideal candidate HTC material for this project is one that has the maximum working capacity under the coal gasification environment with the mildest regeneration conditions possible. Moving towards this goal begins with a deeper understanding of the HTC structure, particularly as it relates to the CO_2 uptake mechanism. Once the structure/CO_2 uptake functional relationship is better defined/understood, one can then tailor the HTC composition to maximize the working capacity under the mildest realistic regeneration conditions.

In previous studies by our team [6-8], a comprehensive analysis of the structure vs. temperature behavior was performed for the Mg-Al-HTC, which is also the initial material of interest in this study. The thermo-gravimetric analysis (TGA) curve for an HTC material (with a chemical formula of $Mg_{0.73}Al_{0.29}(OH)_2(CO_3)_{0.15}.0.46H_2O$, as determined by ICP-MS and TGA) studied, is presented in Figure 2.5, while the composition of the evolved gases with temperature is presented in Fig. 2.6 (the TGA system at USC, where these studies were performed, was equipped with a mass analyzer to record the evolution of the various species). There are three major weight loss peaks observed in these Figures: (i) a ~13.5 wt% loss ending at ~190°C, which is attributed to the interlayer water loss of the HTC; (ii) a ~22.17 wt% loss, between 200 and 400°C, representing the loss of the hydroxyl groups primarily associated with the HTC structure; and (iii) a ~7.33 wt% loss beginning at ~400°C (for this particular HTC) and completing before ~650°C, representing the loss of CO_2, which comes from the carbonate species that are part of the HTC structure [7,8].

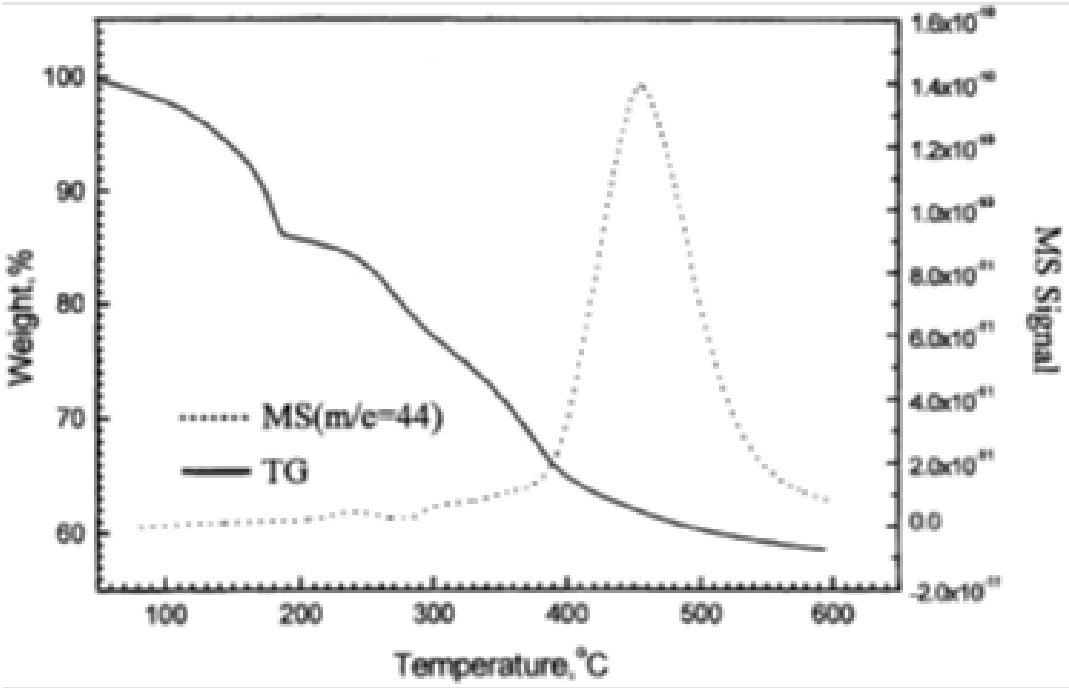

Figure 2.5. In-situ TGA-MS study of the Mg-Al-CO_3 HTC as a function of temperature

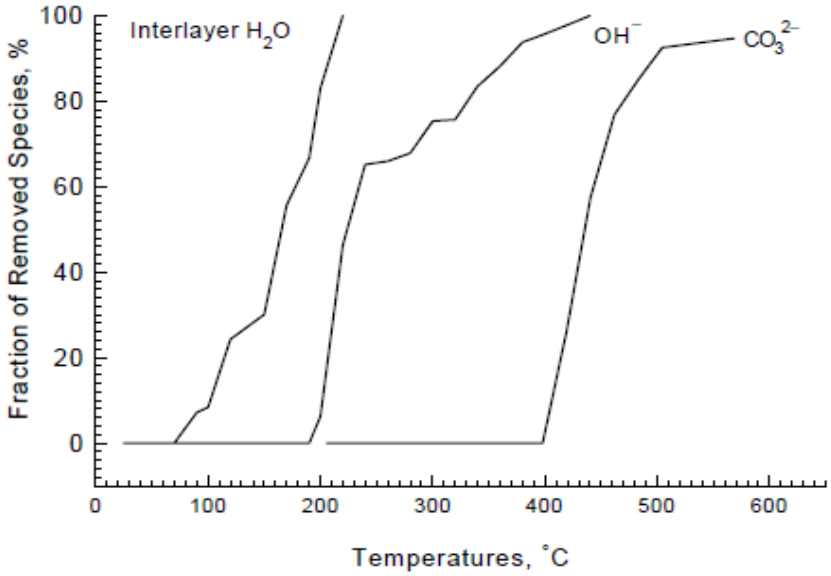

Figure 2.6. Fraction of the species removed from the Mg-Al-CO_3 HTC vs. temperature

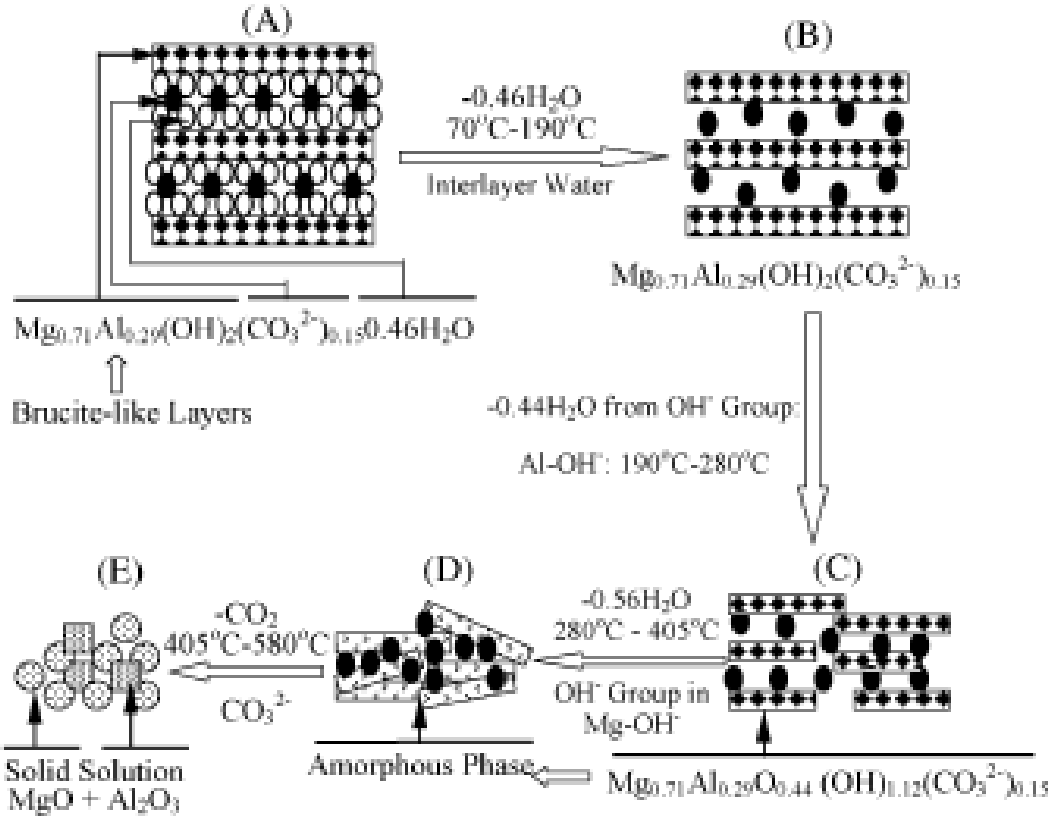

Figure 2.7. Thermal evolution of the structure of Mg-Al-CO_3 LDH

A schematic representing the thermal evolution of the HTC structure as a function of temperature is shown in Fig. 2.7 along with the proposed mechanism responsible for the weight loss and the observed structural changes (these structures are based, in addition to the TGA/mass analysis data, on in-situ XRD and DRIFTS analysis [7,8]).

To attain a very significant CO_2 uptake, the most direct route is to utilize the structural capacity, i.e., the ability of the calcined material (material D or E in Fig. 2.7) to exchange the CO_2 that is incorporated into the structure, specifically the CO_2 exchanged when one transitions from pattern D to E (see Fig. 2.7) to interconvert into material A, B, or C, depending on temperature and the regeneration atmosphere. Specifically, for a HTC with the structure $Mg_{1-X}Al_X(OH^-)_2(CO_3^{2-})_{X/2} \bullet yH_2O$, the reconstruction of the calcined structure E into the fully-hydrated HTC structure A is described by the following equation:

$$(1-X)\,\mathrm{MgO}+(X/2)\mathrm{Al_2O_3}+(X/2)\mathrm{CO_2}+(1+y)H_2O \rightarrow \mathrm{Mg}_{1-X}Al_X(OH^-)_2(CO_3^{2-})_{X/2}\bullet yH_2O \qquad \text{(R1)}$$

The estimated total wt% (per gr of the calcined material E) CO_2 uptakes for three common HTC materials with Mg:Al ratios of 2:1, 3:1, and 4:1 are 16.56 wt%, 12.80 wt%, and 10.37 wt%, respectively. These capacities are in line with what we (M&PT) have measured with these materials, as can be seen in Table 2.8 below (as well as with precise adsorption isotherm data measured at USC, see below). The mechanism via which CO_2 incorporates into the calcined HTC structure is very specific, and is expected to be independent of competition from other gas components, particularly water, which are present in the gasification environment. This has been shown to be true experimentally in this study (for further detailed discussions, see RPPR 4).

Though equation R1 above is, likely, to be the primary means via which CO_2 is "adsorbed/desorbed" by the HTC material under the prevailing AR conditions (250-450°C, up to 25 bar of pressure) one cannot preclude additional CO_2 uptake via a secondary route, especially at relatively low temperatures, through physical adsorption and/or chemisorption, which are processes dependent on the HTC surface area available. For calcined HTC, the surface area is typically high ~300 m^2/g (although relatively low compared to other common adsorbents, such as zeolites), but physisorption/chemisorption of CO_2 in the WGS environment is, likely, to be inhibited by other gases, such as water vapor and H_2S. The fact that route (R1) is, likely, the primary means via which the HTC "adsorbs" CO_2 under WGS relevant conditions implies that employing higher pressures is likely to accelerate the uptake rates, something which has been validated experimentally in this study (see RPPR 5, and further discussions to follow below).

In general, the synthesis of the HTC materials is relatively simple and straightforward, and a large variety of LDH materials (as HTC materials are also known) can be synthesized. During this study, we have prepared Mg-Al HTC materials targeting a theoretical Mg-to-Al ratio of 2–3. These materials have been bench-marked with a commercial product (obtained from ALCOA) as a reference material. The Mg-Al-CO_3 LDHs were prepared via the co-precipitation technique. They were prepared by first dissolving Mg and Al nitrates with different molar concentrations, [Mg]:[Al]=2-3 in water. These solutions were then added drop-

wise into a second precipitation solution containing Na_2CO_3 and NaOH at a pH controlled between 9-10. The resulting mixture was stirred for 1 hr, then aged at 65°C for 18 to 24 hr. The aged mixtures were vacuum-filtered and rinsed with distilled water. The precipitate was dried at 100°C for 24 hr in an oven. All chemicals were purchased from Sigma-Aldrich (USA).

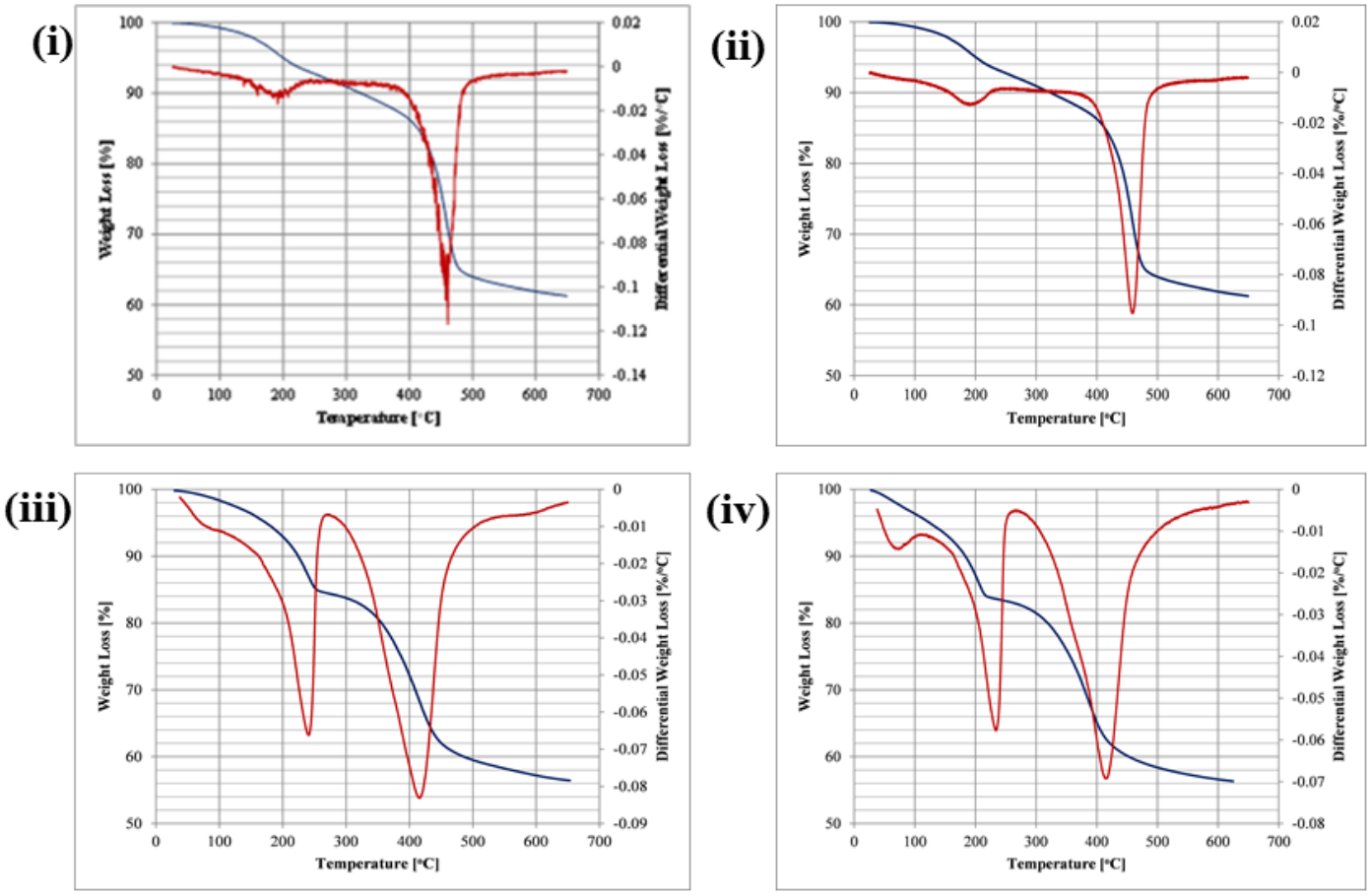

Figure 2.8. TGA of M&PT hydrotalcite samples: Starting from Top Left: (i) Alcoa TSO-1091-2. (ii) HT-3MgAl-121415-A1, the original M&PT prepared material. And two of the recently prepared samples as part of the large-batch preparation: (iii) HT-3MgAl-20g#1 and (iv) HT-3MgAl-G-20g-#4

The TGA and Derivative Thermogravimetric Analysis (DTG) curves of three of the HTC materials prepared together with the commercial material (Alcoa TSO-1091-2) are presented in Fig. 2.8. The characteristic weight loss regions identified from our previous study [7,8] (surface adsorbed water, hydroxyl group, and carbonate group losses) are present in these three materials as well, thus indicating the formation of a HTC material. The subtle differences

among the various TGA/DTG curves below ~250°C can be attributed to differences in the adsorbed moisture content of the as-prepared material.

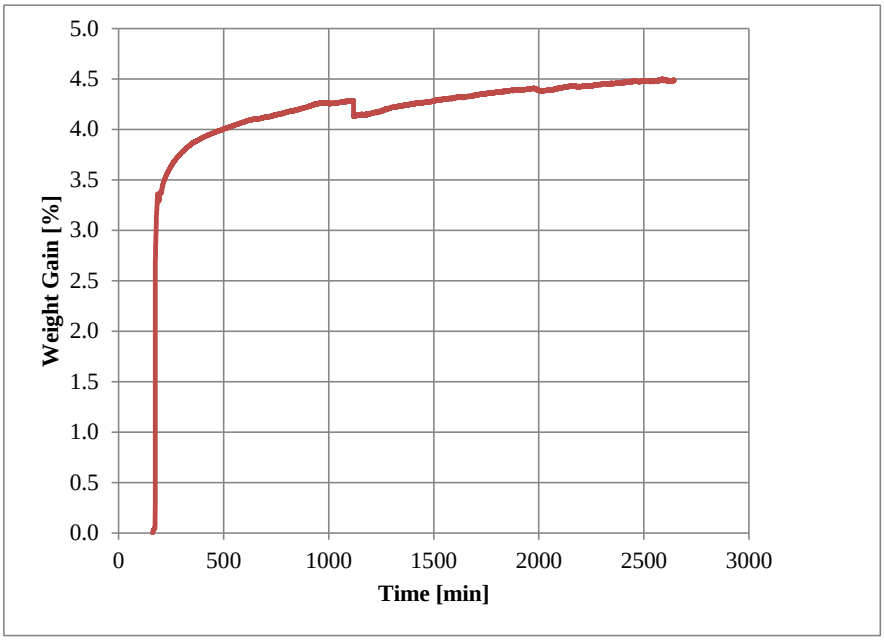

Figure 2.9. Long-term CO_2 adsorption profile at 400°C for HT-3MgAl-20g-#1 pre-calcined at 650°C in N_2

Table 2.8 is a summary of the CO_2 adsorption results obtained via TGA at 30°C in pure CO_2 with a number of the early HTC materials prepared after calcination at the noted temperatures and atmosphere (column 2). As can be seen, the CO_2 capacity for the HTC materials with a Mg-Al ratio of 3:1 is in the range of 9–10 wt%, which is in line with values calculated by Equation R1. Figure 2.9 shows the CO_2 adsorption uptake versus time at a higher temperature (400°C) for the hydrotalcite sample HT-3MgAl-20g-#1 after it had been subjected to a calcination at 650°C. The results in Fig. 2.9 are typical of what M&PT has observed in adsorption/desorption studies with these materials in their TGA system at atmospheric pressures, namely a very fast uptake of CO_2 followed by a gradual sorption period. We believe that this is consistent with the nature of these HTC materials, whereby CO_2 uptake is more akin to a gas-solid reaction rather than physisorption, as is typically the case for the more conventional adsorbents (e.g., zeolites).

Table 2.8. Summary of TGA results for CO_2 adsorption on variously prepared and calcined samples of HTC prepared by M&PT, and one commercial sample obtained from Alcoa

Sample ID	TGA Program	CO_2 Adsorption (%)	CO_2 Capacity (mmol/g)
HT-Alcoa-TSO-1091	400°C/4hr/N_2 30°C/4hr/CO_2	10.3	2.3
HT-3MgAl-121415-A	400°C/4hr/N_2 30°C/4hr/CO_2	9.3	2.1
HT-3MgAl-121415-A	600°C/1hr/N_2 30°C/4hr/CO_2	9.5	2.2
HT-3MgAl-121415-B	400°C/1hr/N_2 30°C/4hr/CO_2	9.3	2.1
HT-2MgAl-121515-D	400°C/1hr/N_2 30°C/4hr/CO_2	5.0	1.1
HT-3MgAl-02082016-G	400°C/1hr/N_2 30°C/4hr/CO_2	8.4	1.9
HT-3MgAl-G-20g-#1	400°C/1hr/N_2 30°C/4hr/CO_2	9.6	2.2
HT-3MgAl-G-20g-#4	400°C/1hr/N_2 30°C/4hr/CO_2	9.1	2.1
HT-3MgAl-G-20g-#6	400°C/1hr/N_2 30°C/4hr/CO_2	9.4	2.1

During this project, a large number of additional samples of hydrotalcite material were prepared by M&PT for use in the combined AR/MR long-term performance stability testing in batches of material, ranging in weight from 20 to 60 g per batch. Data from the QC spot-checking of the CO_2 adsorption capacity of several of these hydrotalcite batches are shown in Table 2.9, and they confirm that the prepared material have consistent properties among the various batches.

Table 2.9. Summary of TGA results for CO_2 adsorption on variously prepared and pre-treated (calcined) samples of hydrotalcite prepared by M&PT

Batches	Sample ID	Pretreatment condition	CO2 adsorption condition	CO2 Capacity (%)	CO2 Capacity(mmol/g)
	HT-Alcoa-TSO-1091	400°C/4hr/N2	30°C/4hr/CO2	10.3	2.3
	HT-3MgAl-121415-A	400°C/4hr/N2	30°C/4hr/CO2	9.3	2.1
8 g	HT-3MgAl-121415-A	600°C/1hr/N2	30°C/4hr/CO2	9.5	2.2
Batches	HT-3MgAl-121415-B	400°C/1hr/N2	30°C/4hr/CO2	9.3	2.1
	HT-2MgAl-121515-D	400°C/1hr/N2	30°C/4hr/CO2	5.0	1.1
	HT-3MgAl-02082016-G	400°C/1hr/N2	30°C/4hr/CO2	8.4	1.9
	Batch-20g-#1	650°C/N2	30°C/ovenight	9.6	2.2
3MgAl-G	Batch-20g-#2	650°C/N2			0.0
	Batch-20g-#3	650°C/N2			0.0
20 g	Batch-20g-#4	400°C/1hr/N2	30°C/4hr/CO2	9.1	2.1
	Batch-20g-#5	650°C/N2			0.0
Batches	Batch-20g-#6	400°C/1hr/N2	30°C/4hr/CO2	9.4	2.1
	Batch-20g-#7	650°C/N2			
	Batch-20g-#8	650°C/N2	30 °C/5676.5 min/CO2	14.7	
		650°C/N2	30 °C/6 hr/CO2	9.8	2.2
	Batch-50g-#1	650°C/N2	32°C/6820.5hr/CO2	11.2	2.6
	Batch-50g-#2	650°C/N2	32°C/4337.5hr/CO2	10.0	2.3
		650°C/N2	32°C/68 hr/CO2	9.7	2.2
	Batch-50g-#12	650°C/N2	30 °C/4032.5 min/CO2	10.1	2.30
	Batch-50g-#15	650°C/N2	32°C/5355hr/CO2	5.8	1.31
		650°C/N2	32°C/70hr/CO2	9.7	2.20
	Batch-50g-#16	650°C/N2	32°C/3842hr/CO2	13.2	3.01
		650°C/N2	32°C/68hr/CO2	10.7	2.43
3MgAl-G	Batch-50g-#17	650°C/N2	37°C/4338hr/CO2	14.3	3.25
		650°C/N2	32°C/5433hr/CO2	10.0	2.28
50 g	Batch-50g-#18	650°C/N2	30 °C/4412 min/CO2	5.2	1.19
		650°C/N2	30 °C/75hr/CO2	10.9	2.48
	Batch-50g-#19				0.00
Batches	Batch-50g-#20				0.00
	Batch-50g-#21	650°C/N2	32 °C/4398.5 min/CO2	10.5	2.38
	Batch-50g-#22	650°C/N2	32 °C/4398.5 min/CO2	9.7	2.20
	Batch-50g-#23	650°C/N2	32 °C/4398.5 min/CO2	9.4	2.14
	Batch-50g-#24	650°C/N2	32 °C/4398.5 min/CO2	10.1	2.30
	Batch-20g-#25	650°C/N2	32 °C/3,200 min/CO2	8.6	1.95
	Batch-20g-#26	650°C/N2	32 °C/3,200 min/CO2	9.1	2.07
3MgAl-G	Batch-20g-#27	650°C/N2	32 °C/3,200 min/CO2	8.5	1.93
20g	Batch-20g-#28	650°C/N2	32 °C/3,200 min/CO2	N/A	
Batches	Batch-20g-#29	650°C/N2	32 °C/3,200 min/CO2	N/A	
	Batch-20g-#30	650°C/N2	32 °C/3,200 min/CO2	N/A	
	HT-Alcoa-TSO-1091	400°C/4hr/N2	30°C/4hr/CO2	8.8	2.0
	2Q2018				
	Batch-20g-#31	650°C/N2	32 °C/3,200 min/CO2	9.1	2.07
	Batch-20g-#32 to #37	No QC			
	Batch-20g-#38	650°C/N2	32 °C/3,200 min/CO2	8.8	2.00
	Batch-20g-#39 to #41	No QC			
	Batch-20g-#42	650°C/N2	32 °C/3,200 min/CO2	9.4	2.14
	Batch-20g-#52	No QC			
	2Q2018				
3MgAl-G	Batch-60g-#1	650°C/N2	32 °C/3,200 min/CO2	9.1	2.07
60g	Batch-60g-#2	650°C/N2	32 °C/3,200 min/CO2	9.3	2.11
Batches	Batch-60g-#3	650°C/N2	32 °C/3,200 min/CO2	9.4	2.14

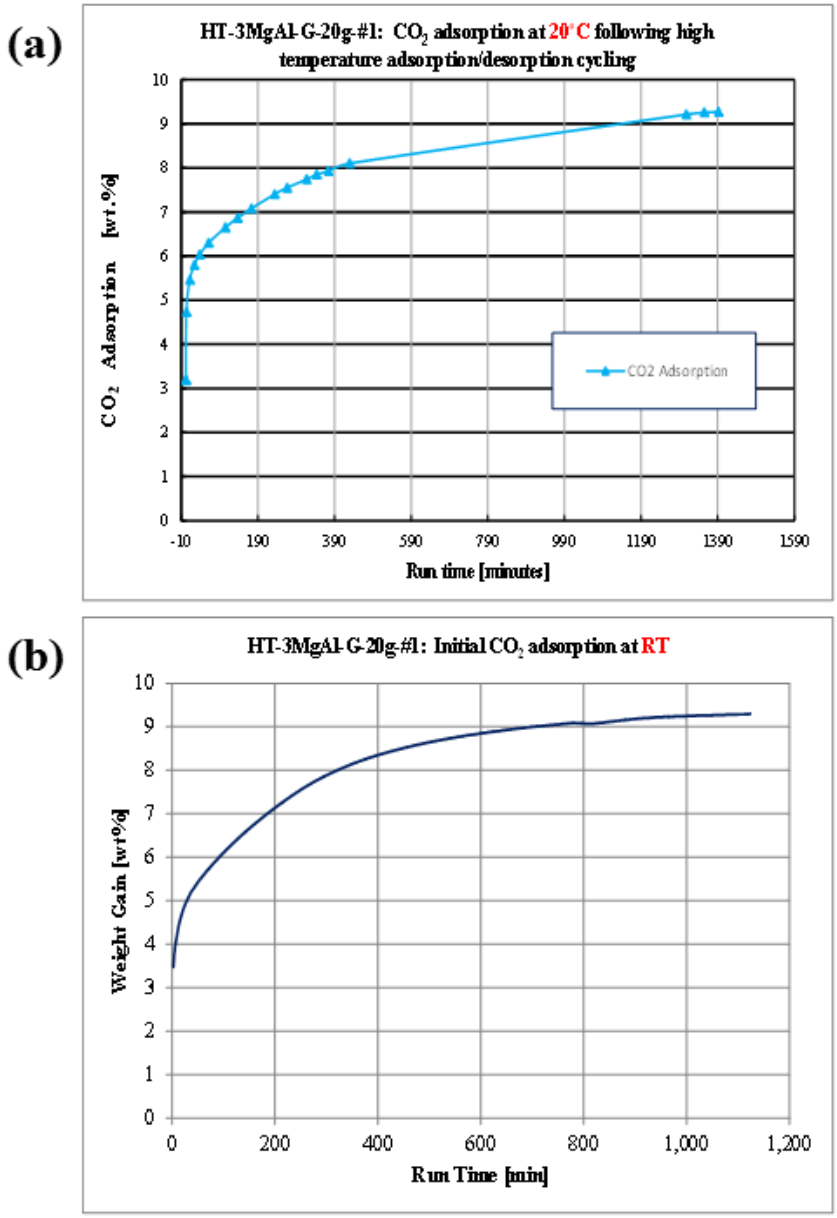

Figure 2.10. (a) CO_2 adsorption of M&PT hydrotalcite sample HT-3MgAl-20g-#1 at room temperature and atmospheric pressure. (b) The test was conducted after the final adsorption cycle at 200°C to confirm the original CO_2 adsorption capacity at RT (see also Table 2.8)

Multiple adsorption/desorption cycles (from 4 to >10, e.g., see RPPR 2, with adsorption temperatures ranging from room temperature to 450°C, and desorption temperatures ranging from 250-650°C) were conducted at various CO_2-containing atmospheres in the atmospheric pressure TGA system at M&PT, and have been previously reported in the various RPPRs. What is typically observed, is that the HTC's CO_2 capacity appears to decay very slightly from the first-to-second cycle, but then stabilizes so that the weight gain appears to be constant with

time beyond the first cycle. The materials have proven quite stable. For example, Fig. 2.10b shows the adsorption data at room temperature for the HT-3MgAl-20g-#1 HTC after it had undergone long-term cycling at various temperatures and CO_2 atmospheres. The adsorption behavior is almost identical to that measured at room temperature conditions the first time after the preparation of the material (Fig. 2.10a) and reported in Table 2.8.

The off-gas from a coal gasifier may contain significant levels of tar-like species that represent potential poisons for the hydrotalcite adsorbent. In the proposed process, the hydrotalcite material may be potentially exposed to raw off-gas with little, if any, pre-treatment. Hence, it is important that it is stable in terms of its CO_2 capacity over a large number of regeneration cycles. As part of this project, we have conducted a series of CO_2 adsorption and desorption/regeneration cycles in the presence of naphthalene as a surrogate for tar-like species present in untreated gasifier off gas. The purpose here was to assess the impact of naphthalene (model tars) on adsorption capacity. In this testing, a sample of hydrotalcite (HT-20g-#31) was exposed to naphthalene-laden CO_2 (ca. 350 to 880 ppm) for 6 to 8 hr at 200°C and 30 to 40 psig. Following this, the adsorbent was regenerated at 400°C in flowing N_2 for 5 to 6 hr. This adsorption/regeneration cycle was repeated 17 times. Following this testing, the hydrotalcite sample was removed for CO_2 capacity determination. In-situ capacity determination during the cyclic exposure testing was not possible with the test equipment available. Figure 2.11 shows pictures of the hydrotalcite adsorbent before and then after the full run of naphthalene exposures. Visually, it is clear that there is deposition of carbon on the hydrotalcite. Ex-situ determination of the CO_2 capacity was conducted using the TGA. Figure 2.12 shows the CO_2 adsorption at ambient pressure and 200°C following an 8-hr regeneration in CO_2 at 450°C. The CO_2 capacity of this hydrotalcite sample (HT-20g-#31) before naphthalene exposure as well as from the virgin HT-20g-#1 sample conducted in 2017 are shown for comparison. For all samples, the CO_2 capacity is very similar at 2.25 to 2.5 wt%, suggesting that naphthalene, and by extension other tar-like species likely do not impact the overall CO_2 removal capability.

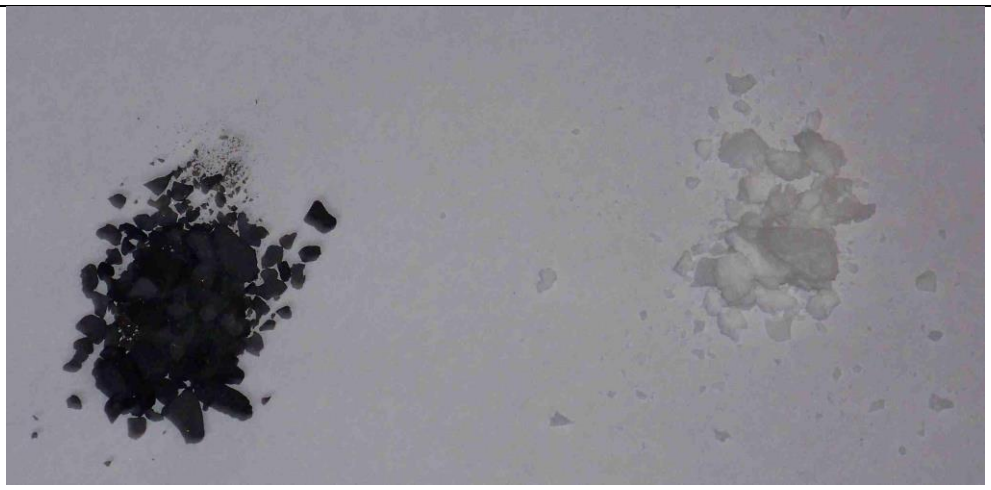

Figure 2.11. Photograph of the hydrotalcite sample after (left) and before (right) exposure to naphthalene in a cyclic CO_2 adsorption/regeneration study (17 cycles)

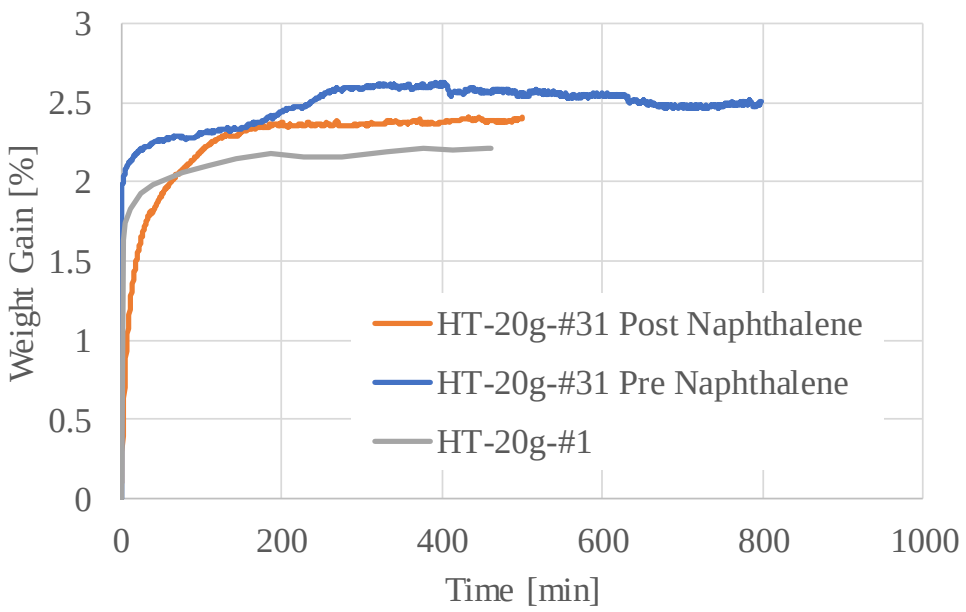

Figure 2.12. CO_2 capacity determination of the naphthalene exposed hydrotalcite sample (HT-20g-#31 Post-Naphthalene) compared with the unexposed virgin material (HT-20g-#31 Pre-Naphthalene) and a previously prepared hydrotalcite (HT-20g-#1). All samples were pre-calcined at 450°C in CO_2 prior to capacity measurement at 200°C. Testing was conducted at ambient pressure

2.3. Catalyst Activity Testing

In this project, a commercial Co/Mo-based sour-shift catalyst was employed in the MR and AR investigations. Our team has previously published [1-5] global rate expressions for this catalyst for a range of lower pressures. In this project we extended the range of applicability at

the anticipated process conditions (up to 300ºC and 25 bar). Sulfur-resistant $Co/Mo/Al_2O_3$ catalysts have been available commercially since the early 1970's and have been used in the WGS reaction with feed streams containing significant quantities of sulfur contaminants (e.g., coal-derived and heavy petroleum-derived syngas streams). The alumina support is thought to provide hydrothermal stability, making this class of catalysts desirable for both low- and intermediate-temperature WGS (200–450°C) applications.

In our studies, the WGS reaction is investigated using a commercial $Co/Mo/Al_2O_3$ sour-shift catalyst (see Table 2.10 for its chemical composition and other physical properties) in a lab-scale packed-bed reactor (for further description of the lab-scale experimental set-up see Sect. 3). Typically, kinetic experiments were run as part of the membrane reactor experiments, whereby after a particular MR experiment is completed, the permeate side of the membrane was closed and the MR effectively ran as a PBR.

Catalyst form	Extrudates
Catalyst size	0.003 m
Chemical Composition	CoO: 3-4 wt% MoO_3: 13-15 wt% Al_2O_3: 80-85 wt%
Bulk Density	$592.68*10^3$ g/m^3
Surface Area	160-220 m^2/g
Pore Volume	$0.55\text{-}0.65*10^{-6}$ m^3/g

Table 2.10. Physical and chemical properties of the $Co\text{-}Mo/Al_2O_3$ sour-shift catalyst

For the PBR (and MR) experiments, typically ~10 g of catalyst particles are crushed into smaller particles, and their sizes are sorted with the aid of mesh-screens in the range of 600-800 μm. Prior to loading them into the reactor, the catalyst particles are mixed and diluted

with quartz particles of the same size in order to completely fill the reactor space and to be able to conveniently operate the reactor bed under isothermal conditions. Since the Co and Mo metal components of the fresh catalyst, as received, are in their oxidized form, they must be sulfided prior to the initiation of the reaction. The activation procedure involves the in-situ reduction of the metals using a gas mixture containing H_2 and H_2S (up to 5 mol% of H_2S) using a temperature and pressure protocol as specified by the catalyst manufacturer. (In fact, a minimum ratio of H_2S/H_2O is required during the PBR/MR experiments in order to preserve the active sulfide form). Experiments are carried-out using simulated coal-derived syngas compositions and various W_C/F_{CO} values in the range of 50-200, where W_C is the weight of undiluted catalyst, and F_{CO} is the molar flow rate of CO (mol/hr) in syngas. For each experimental point, the reactor was allowed to run for 1 hr at steady-state conditions before WGS reactor conversion was measured.

The lab-scale PBR and MR experiments are run under isothermal conditions. For kinetic data analysis, we have utilized both the isothermal 1-D PBR model as well as the multi-scale PBR model described in Sect. 5 below. Results of these models were shown to be virtually identical since the effectiveness factors in the lab-scale PBR are close to 1 (~0.98 -1.0), so for the kinetic parameter fitting exercise we have exclusively utilized to date the 1-D PBR model.

In our group's previous work at lower pressures, we have employed an empirical power-law rate expression [1-5]:

$$-R_{CO} = A\exp(\frac{E}{RT})P_{CO}^{a}P_{H_2O}^{b}P_{CO_2}^{c}P_{H_2}^{d}(1-\beta) \quad (1)$$

$$\beta = \frac{1}{K_{eq}}\frac{P_{CO_2}P_{H_2}}{P_{CO}P_{H_2O}} \quad (2)$$

where P_i is the partial pressure for component i (atm), E the activation energy (J/mol), T the temperature (K), R the gas constant (J/mol K), and K_{eq} is the overall reaction equilibrium constant in terms of partial pressures. The equilibrium constant for the WGS can be computed by Equation 3 below:

$$K_{eq} = \exp(\frac{4577.8}{T} - 4.33) \quad (3)$$

We fit the above empirical model to the experimental conversion data, in order to derive the rate parameters (A, E, a, b, c and d). For the parameter fitting, we have utilized three built-in MATLAB functions (further details are presented in RPPR 6, and also [9]). Table 2.11 shows the fitted parameters calculated using the described method for the power law model for all the experimental data generated to date, and Fig. 2.13 shows the iso-conversion graph (experimental data vs. the calculated fit).

A[mol/(atm$^{(a+b+c+d)}$ · h · g)]	18957
E [J/mol]	58074
a	4
b	-1.46
c	0.13
d	-1.44

Table 2.11. Fitted kinetic parameters for the power-law rate model

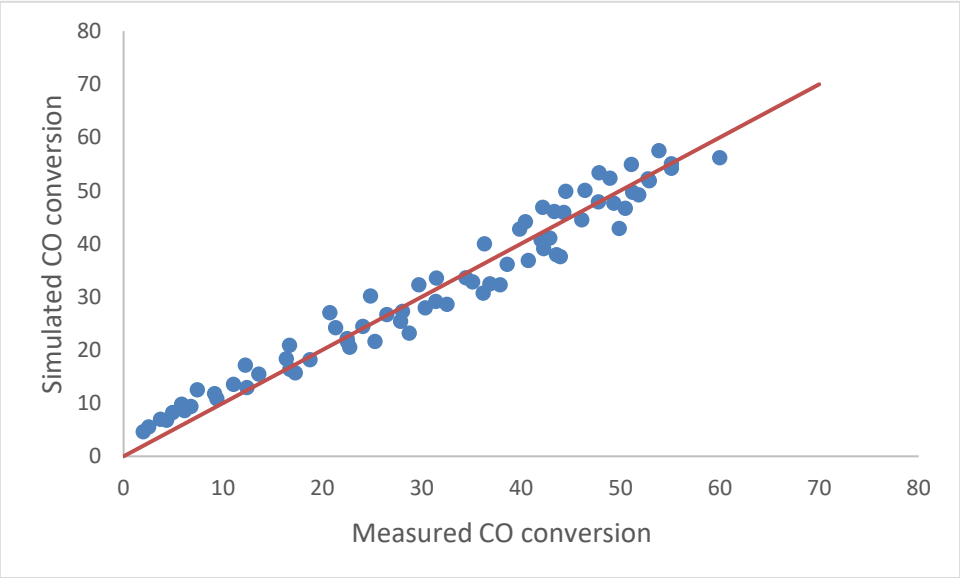

Figure 2.13. The iso-conversion graph

We also fit, in parallel, the WGS reaction rate data to three microkinetic models recently presented in [10] referred to as: (i) the formate intermediate model, (ii) the associative mechanism, and (iii) the direct oxidation mechanism. We discriminate among these rival models by calculating the root-mean-square deviation (RMSD) according to Equation 4.

$$RMSD = \sqrt{\frac{1}{n}\sum_{1}^{n}(X_e - X_s)^2} \quad (4)$$

where X_e is the measured experimental WGS conversion, and X_s is the calculated WGS reactor conversion defined by Equation 5.

$$X_{CO} = \frac{n_{COo}^{F} - n_{CO,exit}^{F}}{n_{COo}^{F}} \quad (5)$$

The results of these tests for the different models are shown in Table 2.12. Based on the data generated to date, the empirical model performs the best, and has as a result been utilized in the models to describe the MR and AR systems (see discussion in Sect. 5 below). Since the RMSD values for the empirical and the direct oxidation models are close, for all modeling efforts in Sect. 5 and 6 we employ the empirical kinetic model.

	RMSD
Direct oxidation	3.38
Associative	5.12
Formate intermediate	8.04
Empirical model	3.32

Table 2.12. Results for RMSD for each kinetic model

2.4 Summary and Conclusions

We have prepared throughout this project high-performance CMS membranes for use in the MR activities. These membranes display very high performance (meeting all the PMP performance targets) and have been shown to be stable in intermediate-term thermal stability

testing (consistent with our past experience). Further, we had success in developing very highly H_2/CO_2 selective membranes using our higher quality tubular substrates in conjunction with modification of the pyrolysis conditions.

HTC materials have also been prepared and characterized under atmospheric pressure conditions at M&PT and at higher pressures at USC (see Sect. 4 below). These materials have shown large uptake capacities towards CO_2 (>3wt%, the targeted value in the project). They have also been stable during CO_2 cycling in various atmospheres. During testing of the same materials at USC (as part of the AR preliminary testing protocol – see further discussions in Sect. 4 below), they have been studied under much higher pressures (>25 bar). Under these conditions these materials show excess sorption capacities >10 wt%, close to the capacities calculated based on equation R1. The current optimal HTC material is a Mg-Al-CO_3 LDH with a Mg:Al molar ratio of 3:1 prepared by M&PT following the procedure described above. During the project, M&PT prepared >2 kg of this material and shipped to USC for their testing.

A commercial sour-shift catalyst has been utilized in the experiments. The experimental data generated have been used to fit a kinetic model and its parameters for this reaction. This model is then used in the simulation of the MR-AR system as well as in the development of the preliminary TEA (see Sect. 6).

3.0. CONSTRUCTION OF THE LAB-SCALE SYSTEM AND INITIAL TESTING AND VALIDATION

The work presented in this Section was performed at USC as part of Tasks 3.0, 4.1. UCLA assisted with the analysis of the experimental data, and as described in Sect. 2, M&PT provided the CMS membranes and the adsorbent used in the experiments.

3.1. Design and Construction of the Lab-Scale Experimental System

In the initial phase of this project, we (USC) focused on the design of the AR lab-scale system and the modification of the existing (prior to the initiation of this project) MR lab-scale test unit to permit operation at higher pressures (up to 25 bar). A P&ID of the resulting experimental MR-AR lab-scale system can be seen in Fig. 3.1.

Many of the items needed for constructing the AR system and for modifying the existing MR unit were purchased from external vendors. Others were designed and fabricated at USC, like the AR itself (a schematic of one of the the two AR's employed is shown in Fig. 3.2 and a photograph in Fig. 3.3). It is made by using a 1.5" ID seamless stainless steel (SS) tube with a wall thickness of 0.12". The length of the reactor is 5.5". The catalysts/adsorbents are loaded inside the reactor through one of the reactor feed/outlet ports. Two SS porous filters (they consist of two small SS rings and one SS mesh) are installed in the inlet and outlet of the reactor to avoid tube blockage by catalyst/adsorbent fine particles. Three two-point thermocouples (fabricated by the Thermometric Corporation) are installed in the side of the reactor to monitor the bed temperature at two radial positions and at three equi-distanced axial positions of the bed. Each AR is installed inside the column oven of a HP Agilent 5890 Series II Gas Chromatograph that is used to control the temperature of the AR. The column oven size is 11" (height) x 12" (width) x 6" (depth), and comfortably fits the AR unit and associated plumbing (see Fig. 3.4 of the AR installed in the GC oven). The operating temperature range is 4℃ above room temperature to 450°C. The valid set-point range of the heating rate is 0 to 70°C/min. After a run, the cool-down rate of the oven is also very fast using the fan inside the

oven. Hence, it is not necessary to open the oven door when cooling down the oven temperature.

High-pressure water syringe pumps coupled with water evaporators were used to generate steam flows for the MR feed-side and sweep-side as well as for supplementing steam flows for the AR's. The construction of the water evaporator was completed by wrapping them up with heating tapes and the appropriate insulation, and all the interconnecting piping was also wrapped with heating tape and insulation for preheating the gas flow. Mass flow controllers were used for the delivery of the various gases including the simulated syngas calibrated for the appropriate range of flows (50 – 1000 sccm). The MR and the AR's are maintained at the required pressures (up to 25 bar) with the aid of the back-pressure regulators, whose performance was validated, and tested for leaking prior to the initiation of each series of experiments. During this initial project phase, we also modified several components of the existing MR lab-scale system, e.g., the existing pressure gauges were replaced with gauges that can operate up to 500 psig. Further details about the lab-scale experimental set-up can be found in RPPR 1 and 2, and also in Sect. 4. During the same period, the experimental protocols for operation of the set-up were formulated, and detailed descriptions, including the CO_2 breakthrough experiments and operation of the AR and MR sub-systems, were included in the RPPR 1 that was provided to the DOE PM.

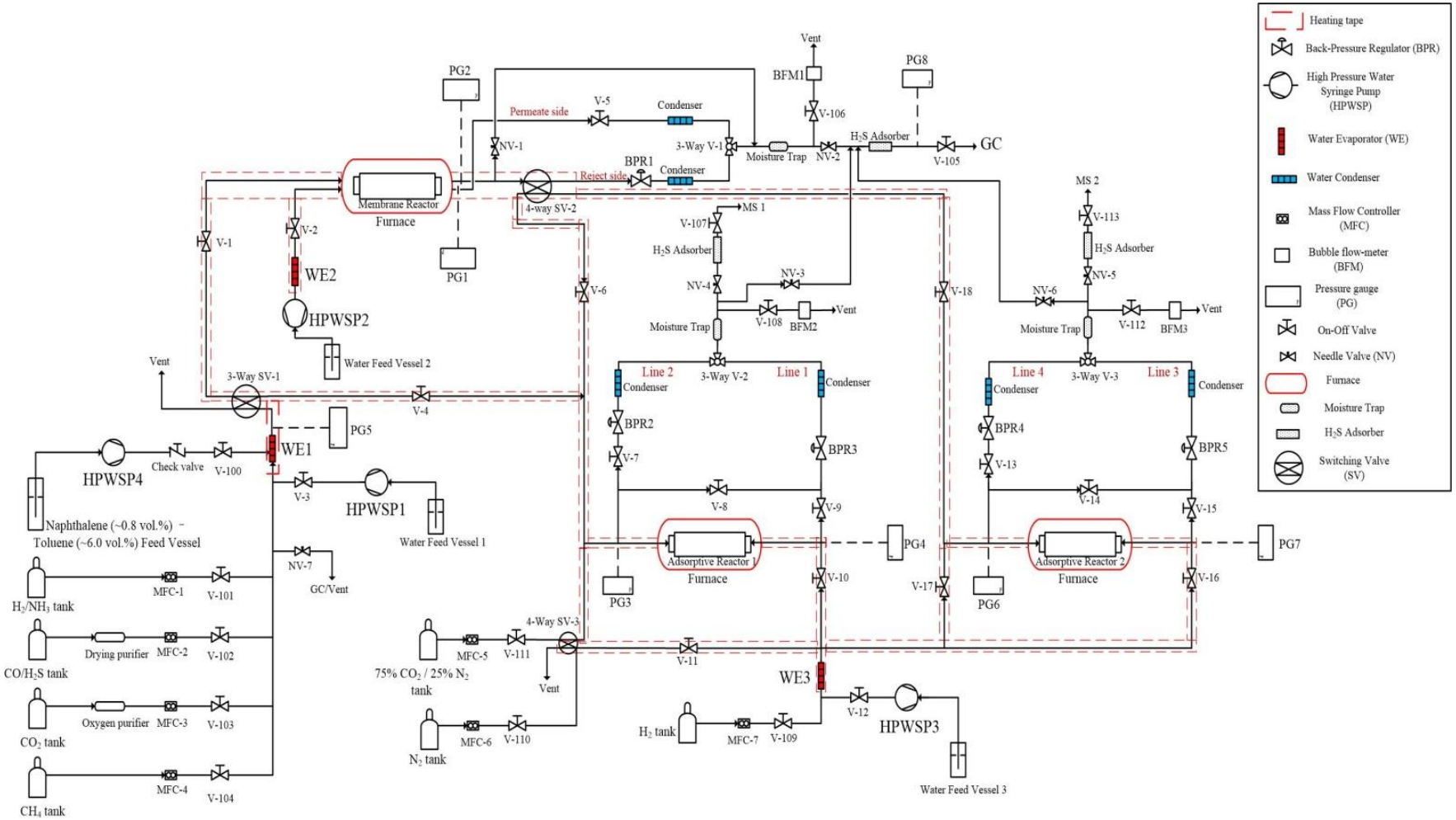

Figure 3.1. Experimental MR-AR lab-scale system

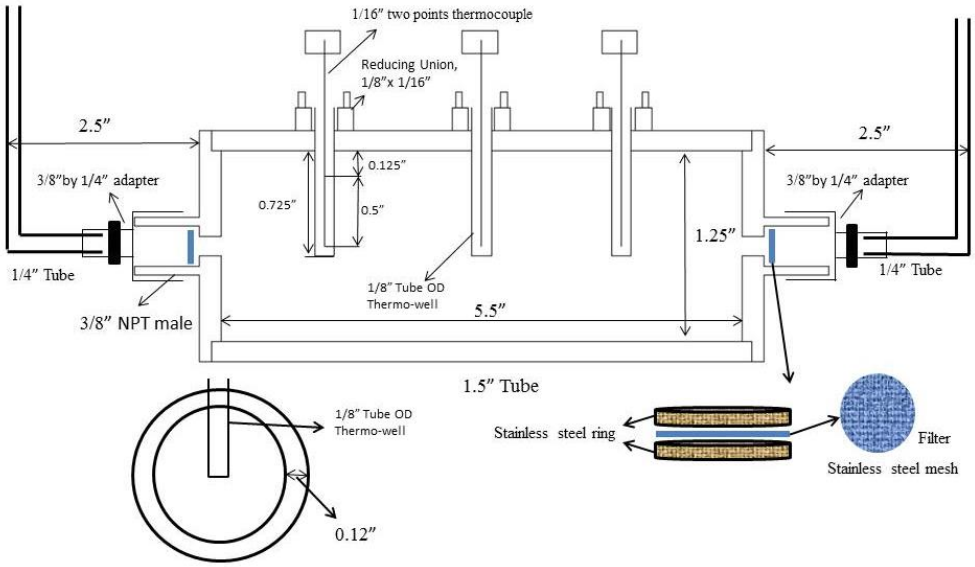

Figure 3.2. The schematic of the AR

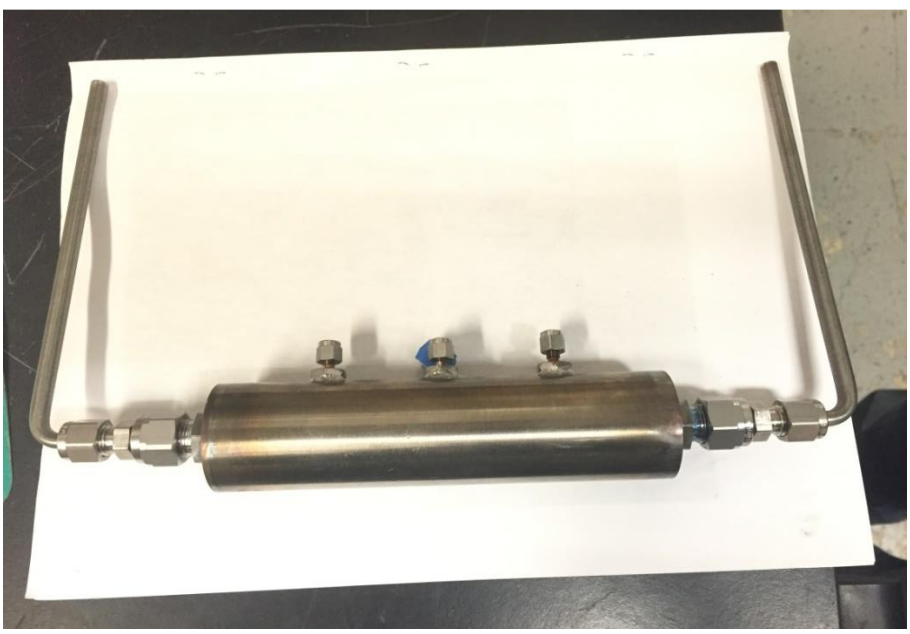

Figure 3.3. The photograph of the AR

Figure 3.4. The photograph of the AR with coiled tubing installed in the GC oven

3.2. Initial Testing of the Individual MR and AR Subsystems

After the completion of the lab-scale experimental system and prior to the initiation of the combined MR-AR system, the USC team focused its activities on the operation and testing of the individual AR and MR sub-systems of the lab-scale set-up. Key experimental parameters to be investigated included: (i) the membrane permeation characteristics (via the testing of CMS membranes with different permeation characteristics, as provided by M&PT, see Sect. 2); (ii) catalyst weight to CO molar flow rate (W/F_{CO}); and (iii) reactor temperature, feed and permeate pressures, and the permeate side (steam) purge rate. For the AR subsystem, key parameters to be studied included: (i) the catalyst and adsorbent weights; (ii) the operating envelope (i.e., temperature and pressure) of the adsorption/reaction cycle; and (iii) the desorption mode. The dependent variables that are monitored included exit stream compositions (determined by GC for the MR and GC/mass analyzer for the AR) and flow rates. Based upon the data collected, the CO conversion, H_2 recovery and purity, CO_2 recovery, and degree of adsorbent regeneration are calculated. A key focus of this task, in addition to validating the functional performance of the two subsystems, was to generate sufficient experimental data to validate the mathematical models, see Sect. 5 and prior RPPR, via comparison of the experimental results with the predictions from the mathematical model.

As a key first step of the AR studies, attention was first focused on the measurements of CO_2 breakthrough experiments (absent of catalyst) using the HTC adsorbent provided by M&PT. The CO_2 breakthrough experiments were performed using the AR test-rig (see Fig. 3.5 and further details in RPPR 3) portion of the MR-AR lab-scale set-up.

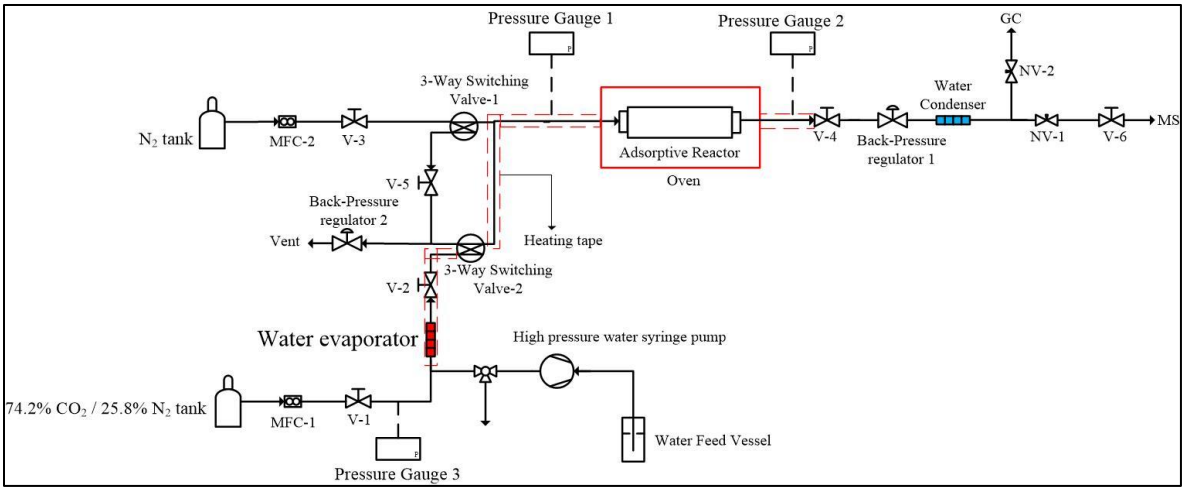

Figure 3.5. The experimental set-up used for the CO_2 breakthrough experiments

The AR was tested first empty to ensure that the reactor itself has no influence on the adsorption/desorption phenomena observed during the AR experiments (further details about the blank-test experimental procedure and data are found in RPPR 3). The empty reactor dynamics experiments show that the reactor itself has no influence on the adsorption/desorption phenomena observed (for further discussion, see RPPR 3).

Since in the AR lab-scale experiments, in order to maintain isothermality, the adsorbent and catalyst are diluted with equal size (600~850 μm) quartz particles, we also conducted experiments using only the quartz particles to verify that the quartz material does not interfere with the adsorption/desorption measurements, and to also determine the residence time characteristics of the AR system. For these experiments, the reactor was filled with 600~850 μm quartz particles only (no adsorbent or catalyst added). The blank experiments were carried out under 5, 10, 15, 20 and 25 bar of pressure, respectively. The detailed experimental procedure for the quartz experiments are as follows (refer to Figure 3.5 for the various devices): (1) Open the N_2 gas cylinder and V-3, set the flow rate at 500 ml/min (STP), in the meantime, heat the reactor oven to 400°C; (2) Adjust BPR1 and N_2 gas cylinder pressure regulator to pressurize the reactor up to 5,

10, 15, 20 and 25 bar, respectively; (3) Open the CO_2/N_2 gas cylinder and V-1, set the flow rate at 500 ml/min (STP) and direct the flow to the vent, in the meantime, adjust the BPR2 and gas cylinder pressure regulator to also pressurize the reactor up to 5, 10, 15, 20 and 25 bar, respectively; (4) Once both pressures are simultaneously stable, switch the CO_2/N_2 gas to the reactor feed-side using the 3-way switching valve, in the meantime, switch the N_2 gas to the vent; (5) Once the CO_2 partial pressure detected by the RGA is stable, switch the CO_2/N_2 gas to the vent, in the meantime, switch the N_2 gas to the feed-side (the bed pressure drop is very small ~0.1 psi under different pressures). The RGA measurements are also verified using GC. The experimental results again indicate that the quartz material does not interfere with the adsorption/desorption measurements (the detailed experimental results can be found in RPPR 3).

After completing the empty reactor and quartz only dynamic reactor experiments, CO_2 breakthrough experiments were carried out using the adsorbent (Mg-Al-CO_3 LDH with a Mg:Al molar ratio of 3:1) provided by M&PT. For these experiments, the reactor was filled with 14 g of HTC adsorbent (600~850 μm -- to generate this particular particle size fraction, the adsorbent particles as-received by M&PT were further screened and the particular size fraction was separated). Adsorbent particles were diluted with 104 g of equal size (600~850 μm) quartz particles. The experimental procedure for the CO_2 breakthrough experiments is the same with the quartz-only reactor experiments described above. CO_2 breakthrough curves were obtained at a constant oven temperature and different reactor pressures (up to 25 bar), as well as under a constant pressure of 25 bar for different oven temperatures (300-450°C). The exit compositions were measured by the RGA, with the measurements also verified using a GC. Figure 3.6 shows the breakthrough profile for the experiment performed at 10 bar. The temperature profiles of different bed points detected by the three two-point thermocouples are also shown (note that Inlet-0'', Middle-0'' and Outlet-0'' signify three different equidistant axial positions in the reactor, specifically 1.375 in, 2.75 in, and 4.125 in from the entrance of the bed, while Inlet-0.5'', Middle-0.5'' and Outlet-0.5'' signify three radial positions 0.5" away from the bed axis). All temperature profiles measured show a maximum in temperature, which is typical of exothermic packed-bed adsorption columns. However, the maximum temperature is less than 2°C higher than the feed temperature. There is also a small radial temperature gradient (less than 1°C), as expected for such columns. The bed pressure drop is very small (~0.1 psi) under different pressures during the CO_2

breakthrough experiments. Similar observations also apply to all experiments at various other pressures, see RPPR 3.

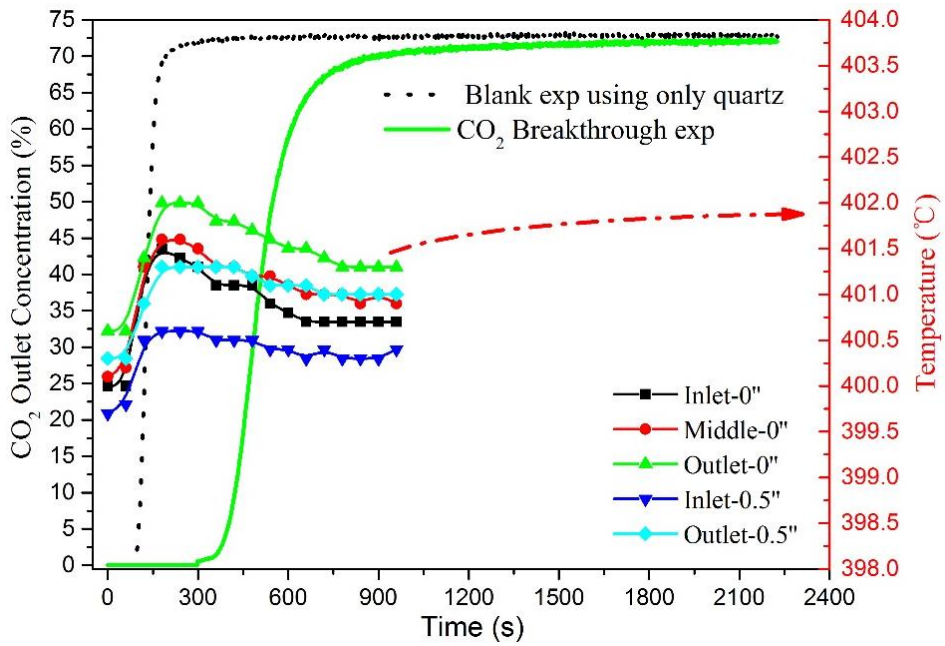

Figure 3.6. Experimental CO_2 breakthrough curves obtained with the HTC adsorbent provided by M&PT using a feed of 74.2 vol% of CO_2 in N_2 (Reactor pressure = 10 bar, Oven temperature = 400°C, Flow rate = 500 sccm); blank experiment using only the quartz particles also carried out under the same experimental conditions

The CO_2 breakthrough experimental results obtained for the HTC adsorbent at 400°C for different total pressures (5, 10, 15, 20 and 25 bar) are shown in Fig. 3.7. As can be seen in this figure (see also RPPR 3), the CO_2 breakthrough times (defined as the time when the exit CO_2 concentration became equal to 5% of the inlet CO_2 concentration), are in a range of 207-614 s

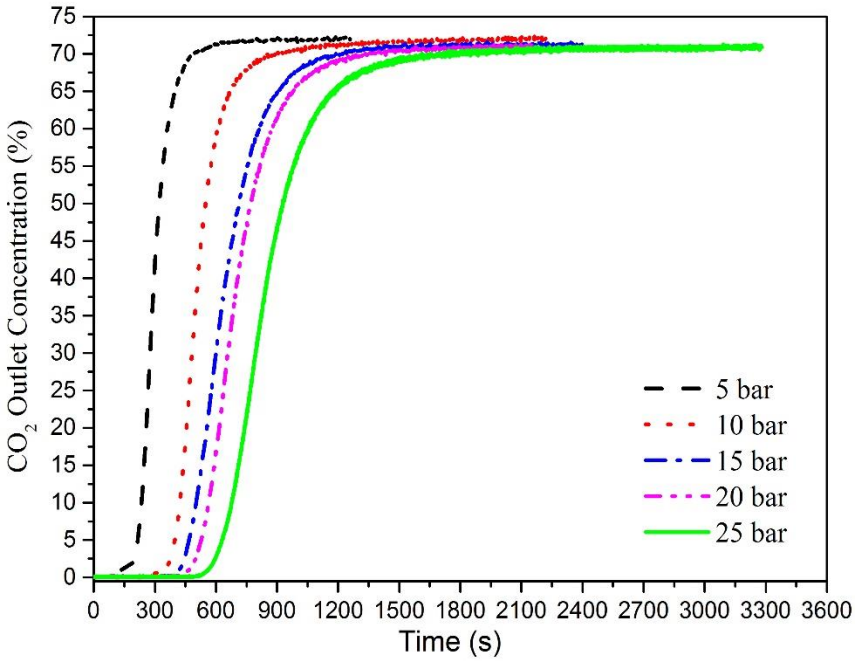

Figure 3.7. A summary of the experimental CO_2 breakthrough curves obtained with the HTC adsorbent provided by M&PT using a feed of 74.2 vol% CO_2 in N_2 at various reactor pressures (5, 10, 15, 20, 25 bar), (Oven temperature = 400°C, Flow rate = 500 sccm)

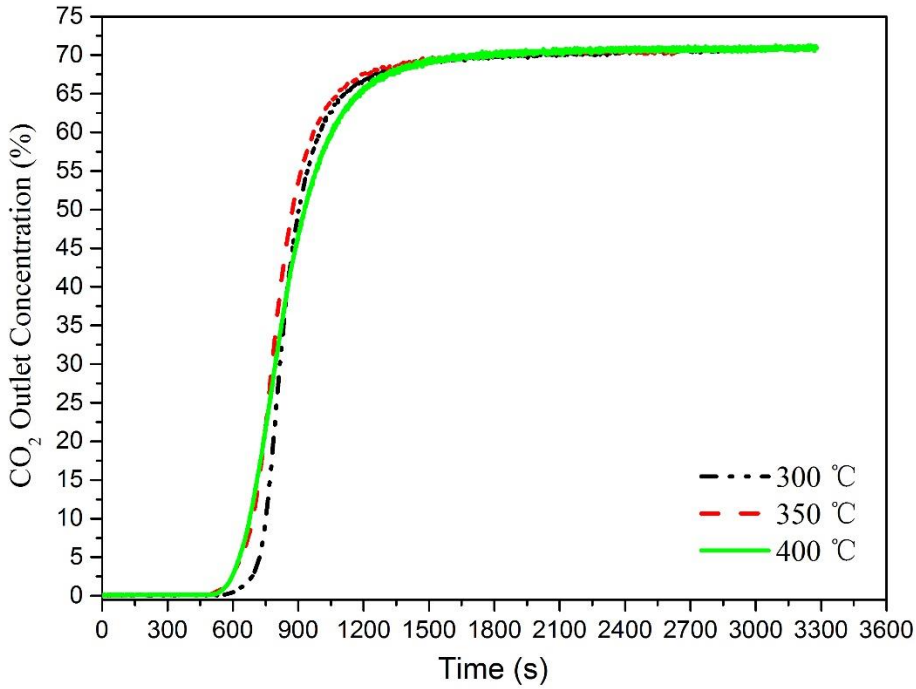

Figure 3.8. A summary of the experimental CO_2 breakthrough curves obtained with the HTC adsorbent provided by M&PT using a feed of 74.2 vol% CO_2 in N_2 and various oven temperatures (300, 350, 400°C), (Reactor pressure = 25 bar, Flow rate = 500 sccm)

depending on the total reactor pressure studied, with the times increasing with pressure, as expected. The CO_2 breakthrough curves under 25 bar and at different oven temperatures are presented in Fig. 3.8. The breakthrough time decreased as the reactor temperature increased, as expected, but with the effect saturating at higher temperatures.

Breakthrough experiments with CO_2 mixed with various steam concentrations (10-40 vol%) were also performed to investigate any interference that water may have on adsorption and breakthrough times. The presence of humidity appears to have little or no impact on the CO_2 adsorption characteristics of the HTC adsorbents, something which was also verified in the TGA studies at M&PT, and also in prior flow studies (for further experimental details and data, see RPPR 3).

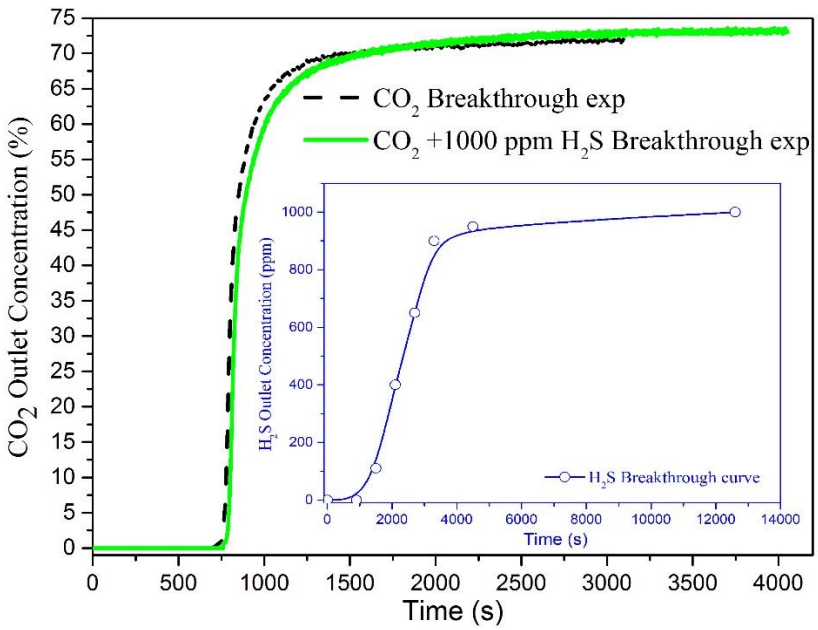

Figure 3.9. A summary of the experimental CO_2 breakthrough curves obtained with the HTC adsorbent provided by M&PT using a feed of 74.2 vol% CO_2 in N_2 and a feed of 74.2 vol% of CO_2 in N_2 with 1000 ppm H_2S (Reactor pressure = 25 bar, Oven temperature= 300°C, Total flow rate = 500 sccm). (Insert: H_2S breakthrough curve)

Breakthrough experiments were also performed with CO_2 mixed with various concentrations of H_2S. Typical results are shown in Fig. 3.9, which were performed under an AR pressure of 25 bar, a temperature of 300°C, with the CO_2 feed mixture containing 1000 ppm of H_2S. The CO_2 outlet concentration from the AR was measured using the RGA (the stream from

the outlet of the reactor was passed through a fixed-bed containing H_2S adsorbents in order to completely remove the H_2S before feeding it into the RGA to protect the instrument). We also directed a small slip-stream to the hood for measuring the H_2S outlet concentration using Drager tubes. In this series of experiments, first, a CO_2 (without H_2S) breakthrough experiment under a pressure of 25 bar and oven temperatures of 300^oC was performed. Subsequently, the CO_2 (with 1000 ppm H_2S) breakthrough experiment under a pressure of 25 bar and an oven temperature of 300^oC was also carried-out. As can be seen in Fig. 3.9, compared to the CO_2 breakthrough experiment without H_2S, the CO_2 breakthrough times increased slightly (~3% or ~25 s) in the presence of H_2S. The H_2S breakthrough curve is also presented in Fig. 3.9. The results indicate that the HTC is also an effective adsorbent for H_2S, whose outlet concentration rises slowly to 1000 ppm (equal to the inlet concentration 1000 ppm) when we run the experiment for longer times, ~3.5 hr, but despite this fact it does not interfere with CO_2 adsorption; this then manifests the fact that these two gases are adsorbed on the HTC via two completely different routes (e.g., route R1 for CO_2 and a physisorption/chemisorption route for H_2S).

In addition to the aforementioned experiments focusing on the adsorption characteristics of the HTC adsorbent (Mg-Al-CO_3 LDH with a Mg:Al molar ratio of 3:1, provided by M&PT) under WGS-relevant conditions, we have also carried-out a series of experiments with this adsorbent, whose main focus was to establish the desorption characteristics. For these experiments, the reactor was filled with 51.4 g of HTC adsorbent (600~850 μm particle size fraction) diluted with 60.8 g of equal size (600~850 μm) quartz particles. The detailed experimental procedures for these CO_2 breakthrough tests are as follows:

a) Heat the AR in 500 sccm N_2 at 450ºC, 5 bar for 1 hr, then cool to 250ºC. Once the reactor temperature is stable, switch to 500 sccm of 75% CO_2-25% N_2 mixture at 5 bar. Allow complete breakthrough, reheat in N_2 at 450ºC, and at 5 bar (20ºC/min heating rate to reach 450ºC) until no CO_2 is coming out from the reactor (within the accuracy of the RGA analyzer).
b) Increase the reactor pressure to 15 bar at 450ºC in flowing (500 sccm) N_2. Cool down to 250ºC, and once the reactor temperature is stable, switch to 500 sccm of 75% CO_2-25% N_2 mixture at 15 bar. Allow complete breakthrough, then reheat in N_2 at 450ºC and 15 bar (20ºC/min heating rate to reach 450ºC) until no CO_2 is coming out from the reactor.

c) Increase the reactor pressure to 25 bar, keep flowing (500 sccm) N_2 at 450ºC. Cool down to 250ºC, once the reactor temperature is stable, switch to 500 sccm of 75% CO_2-25% N_2 mixture at 25 bar. Allow complete breakthrough to occur, then reheat in N_2 at 450ºC under 25 bar (20ºC/min heating rate to reach 450ºC) until no CO_2 is coming out from the reactor.

The experimental CO_2 adsorption and desorption behavior of the top-performing HTC adsorbent (Mg-Al-CO_3 LDH with a Mg:Al molar ratio of 3:1) under different pressures at 250ºC can be seen in Fig. 3.10. The CO_2 balance calculation for each CO_2 adsorption/desorption cycle is also listed in Table 3.1. The regeneration procedure appears quite effective with more than 90% of the CO_2 being released within 2-4 min from the moment one switches from the CO_2/N_2 to the pure N_2 stream (for further details, see RPPR 4). (Please note that for the MR-AR experiments themselves, see Sect. 4, steam is used during the regeneration step.

Table 3.1. CO_2 mass balance for different adsorption pressures at 250ºC (flow rate = 500 sccm)

Experiments	Inlet (mol)	Outlet (mol)	Error (%)*
5 bar	0.3132	0.3087	1.4241
15 bar	0.4855	0.4662	3.9702
25 bar	0.46981	0.4501	4.2049

$^{*}\frac{\text{inlet}-\text{outlet}}{\text{inlet}}$ x 100%.

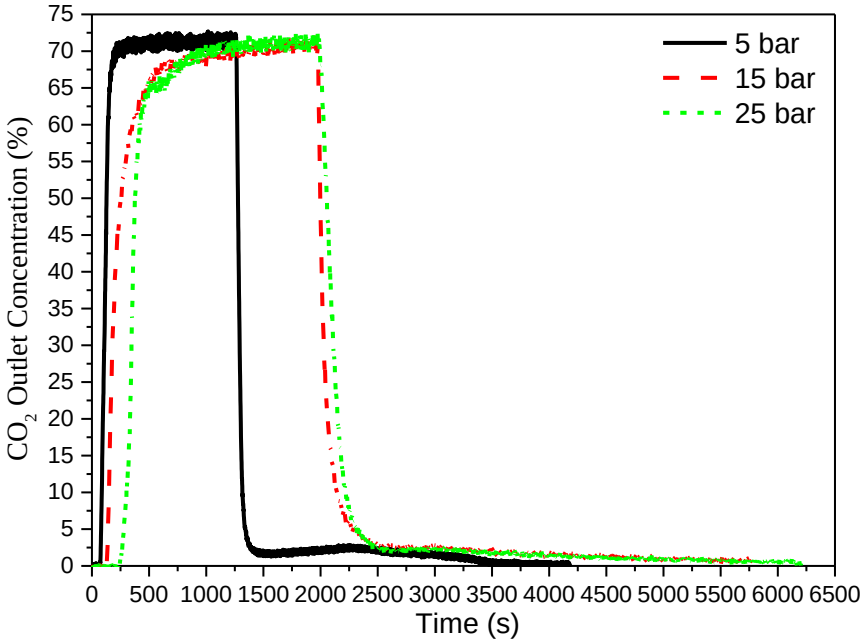

Figure 3.10. A summary of experimental CO_2 adsorption and desorption profiles of M&PT HTC adsorbent using a feed of 74.2 vol% of CO_2 in N_2 at various reactor pressures (e.g. 5, 15, 25 bar), (oven temperature = 250°C, flow rate = 500 sccm)

One of the key reasons for carrying out the above breakthrough experiments was to generate the required experimental data for validating the AR model, see previous RPPR and Sect. 5 below. The sorption characteristics for the HTC were generated in separate static adsorption experiments, a brief description of which is provided below (with additional details provided in RPPRs 4 and 5 and in an upcoming publication).

A schematic of the static experimental system for measuring CO_2 sorption isotherms on HTC adsorbents at high temperatures (up to 450°C) and high pressures (up to 28 bar) is shown in Fig. 3.11. It consists of two cells (Swagelok stainless steel miniature cylinders), which are identified as the sample-cell and the reference-cell, respectively. The nominal volumes of both cells are 10 cm^3 (these volumes are accurately determined via He expansion experiments, see RPPRs 4 and 5). Both the sample-cell and the reference-cell are installed in a GC oven to allow for strict temperature control (temperature fluctuation of less than 0.1 K around the set-point). Two ultra-precision digital pressure gauges, PG_s and PG_r (3D Instruments accu-cal plus digital test gauges with accuracy of 0.04% of reading plus 0.01% of full scale) are utilized to monitor the pressures inside the sample-cell and the reference-cell, respectively. A vacuum pump (Alcatel 2012A) is connected to the system for sample evacuation.

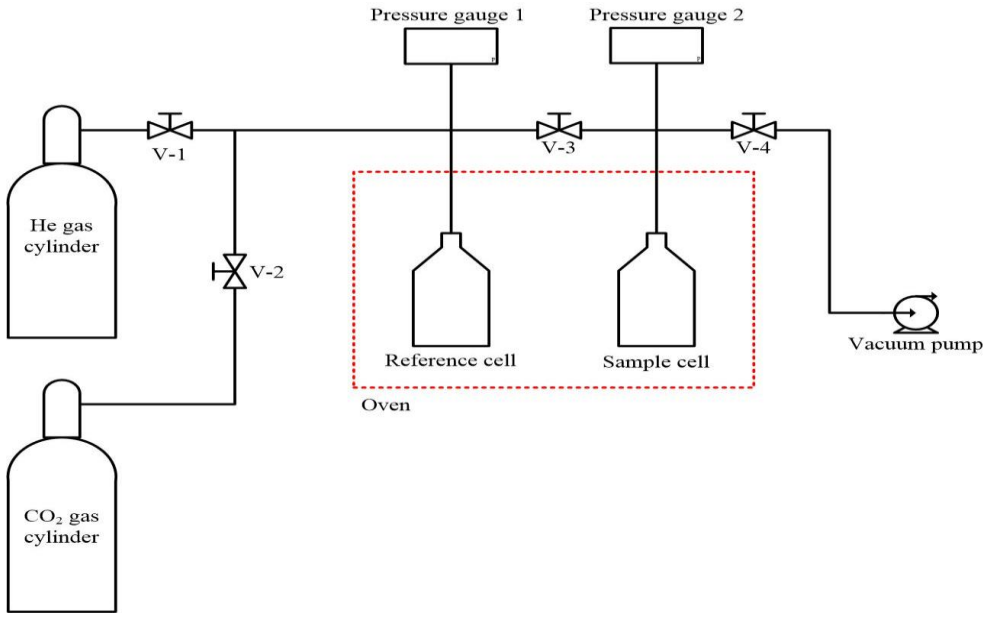

Figure 3.11. Schematic diagram of the static experimental set-up

The system is leak-tested using He prior to the sorption measurements at the relevant temperature and pressure conditions (e.g., 250ºC and pressures up to 33 bar, see RPPRs 4 and 5 for further details). As noted above, as the first step prior to the initiation of the sorption experiments, one needs to measure the volumes of the reference and sample cells. For that, we employ the He expansion technique with the aid of a known volume of quartz (the experimental protocol for the reference/sample cell volume measurement can be found in RPPR 5). The procedure for measuring CO_2 sorption on HTC adsorbents is as follows (refer to Fig. 3.11 for the various devices):

- Load the HTC sample (600~850 μm particle size) into the sample cell. Preheat the sample to the desired regeneration temperature (for the experiments presented here 450ºC) for 1 hr while vacuuming the sample at the same time. Then cool down the oven to 25ºC, close valves V-3 and V-4.
- Measure the skeletal (true solid) volume of HTC sample (see RPPR 5 for the exact procedure).
- Open valve V-2 to let CO_2 in to charge the reference cell to 15 bar (total pressure). Wait until the pressure and temperature stabilize in the reference cell.

- Open valve V-3 to allow the CO_2 gas to enter the sample cell. Wait until the adsorption reaches equilibrium.
- Close valve V-3. Repeat 3 - 4 while increasing the total pressure in the reference cell from 15 to 34 bar.

The static adsorption system model employs the following definitions and conservation equations:

$$n_{CO_2}^{g}(t) = \frac{P_{CO_2}(t)V^{g}(t)}{Z\left(T, P_{CO_2}(t)\right)RT} \qquad (3.1)$$

$$n_{CO_2}^{s}(t) = q_{CO_2}(t)W_{ad,f} = \frac{V_{CO_2}^{s}(t)}{v_{\alpha}(t)} \qquad (3.2)$$

$$n_{CO_2}^{ex}(t) \square n_{CO_2}^{s}(t) - \frac{P_{CO_2}(t)V_{CO_2}^{s}(t)}{Z\left(T, P_{CO_2}(t)\right)RT} = q_{CO_2}(t)W_{ad,f}\left[1 - \frac{P_{CO_2}(t)v_{\alpha}(t)}{Z\left(T, P_{CO_2}(t)\right)RT}\right] \qquad (3.3)$$

$$V^{s}(t) = V^{s}(0) + V_{CO_2}^{s}(t); \;\; V^{T} = V^{s}(t) + V^{g}(t) = V^{s}(0) + V_{CO_2}^{s}(t) + V^{g}(t) \qquad (3.4)$$

Mass Balances:

The solid and gas phase component balances are:

Solid Phase: $\left(\frac{mol}{kg \cdot s}\right)$

$$\frac{dq_{CO_2}(t)}{dt} = k_a\left[q_{CO_2}^{eq}\left(T, P_{CO_2}(t)\right) - q_{CO_2}(t)\right] \qquad (3.5)$$

Gas Phase: $\left(\frac{mol}{s}\right)$

$$\frac{d}{dt}\left(n_{CO_2}^{g}(t)\right) = -\dot{n}_l\left(P_{CO_2}(t)\right) - k_a\left[q_{CO_2}^{eq}\left(T, P_{CO_2}(t)\right) - q_{CO_2}(t)\right]W_{ad,f} \qquad (3.6)$$

Thus, the static adsorption system model is:

$$\left\{\begin{array}{l} \dfrac{dq_{CO_2}(t)}{dt} = k_a\left[q_{CO_2}^{eq}\left(T, P_{CO_2}(t)\right) - q_{CO_2}(t)\right] \\ \dfrac{d}{dt}\left(\dfrac{P_{CO_2}(t)\left[V^T - V^s(0) - q_{CO_2}(t)W_{ad,f}v_\alpha(t)\right]}{Z\left(T, P_{CO_2}(t)\right)RT}\right) = \\ -\left(\begin{array}{l} \dot{n}_l\left(P_{CO_2}(t)\right) + \\ +k_a\left[q_{CO_2}^{eq}\left(T, P_{CO_2}(t)\right) - q_{CO_2}(t)\right]W_{ad,f} \end{array}\right) \end{array}\right\} \quad (3.7)$$

The above model possesses a time invariant quantity, which allows the model to be written as:

$$\left\{\begin{array}{l} \dfrac{d}{dt}\left(\dfrac{P_{CO_2}(t)\left[V^T - V^s(0) - q_{CO_2}(t)W_{ad,f}v_\alpha(t)\right]}{Z\left(T, P_{CO_2}(t)\right)RT}\right) = -\left(\begin{array}{l} \dot{n}_l\left(P_{CO_2}(t)\right) + \\ +k_a\left[\begin{array}{l} q_{CO_2}^{eq}\left(T, P_{CO_2}(t)\right) - \\ -q_{CO_2}(t) \end{array}\right]W_{ad,f} \end{array}\right) \\ q_{CO_2}(t) = \dfrac{\left[\begin{array}{l} \left(\dfrac{P_{CO_2}(0)}{Z\left(T, P_{CO_2}(0)\right)} - \dfrac{P_{CO_2}(t)}{Z\left(T, P_{CO_2}(t)\right)}\right)\left[V^T - V^s(0)\right] + \\ +q_{CO_2}(0)W_{ad,f}\left(RT - \dfrac{P_{CO_2}(0)v_\alpha(0)}{Z\left(T, P_{CO_2}(0)\right)}\right) - RT\int_0^t \dot{n}_l\left(P_{CO_2}(t')\right)dt' \end{array}\right]}{W_{ad,f}\left(RT - \dfrac{P_{CO_2}(t)v_\alpha(t)}{Z\left(T, P_{CO_2}(t)\right)}\right)} \end{array}\right\} \quad (3.8$$

Using the definition of excess adsorbed moles then yields:

$$n_{CO_2}^{ex}(t) = \left[\begin{array}{l} \left(\dfrac{P_{CO_2}(0)}{Z\left(T, P_{CO_2}(0)\right)RT} - \dfrac{P_{CO_2}(t)}{Z\left(T, P_{CO_2}(t)\right)RT}\right)\left[V^T - V^s(0)\right] + \\ +q_{CO_2}(0)W_{ad,f}\left(1 - \dfrac{P_{CO_2}(0)v_\alpha(0)}{Z\left(T, P_{CO_2}(0)\right)RT}\right) - \int_0^t \dot{n}_l\left(P_{CO_2}(t')\right)dt' \end{array}\right] \quad (3.9)$$

$$n_{CO_2}^{ex}(t) - n_{CO_2}^{ex}(0) = \left[\begin{array}{l} \left(\dfrac{P_{CO_2}(0)}{Z\left(T, P_{CO_2}(0)\right)RT} - \dfrac{P_{CO_2}(t)}{Z\left(T, P_{CO_2}(t)\right)RT} \right) \left[V^T - V^s(0) \right] - \\ -\int_0^t \dot{n}_l \left(P_{CO_2}(t') \right) dt' \end{array} \right] \quad (3.10$$

The model derived above is used to identify the equilibrium isotherm relation by first calculating the excess adsorption using equation (3.10) at $P_{CO_2}\left(t = t_{final}\right)$ considering that equilibrium has been reached at $P_{CO_2}\left(t = t_{final}\right)$. Absolute adsorption can then be calculated using Equation 3.3, with both excess and absolute adsorption for CO_2 at 250°C being shown in Fig. 3.12. At higher pressures, excess adsorption shows non-monotonic behavior, but the calculated absolute adsorption isotherm shows an asymptotic behavior, as expected. The parameters of a Langmuir Isotherm (shown in Equation 3.11 below) that correlates well with the aforementioned absolute adsorption data calculations, are shown in Table 3.2. The resulting Langmuir calculated isotherm points are also shown in Figure 3.12. Further details about the analysis of the static system experimental data (including accounting for the experimental leak rate (LR) via the Dusty Gas Model) to generate the excess adsorption isotherms for CO_2 on HTC can be found in RPPR 5. as well as in an upcoming paper by our Group.

$$q^{eq} = \frac{m_{CO_2} b_{CO_2} P_{CO2}}{1 + b_{CO_2} P_{CO2}} \quad (3.11)$$

Table 3.2. Values of the Langmuir Isotherm parameters

m_{CO2} (mol/kg)	b (1/bar)
2.952592	3.690865

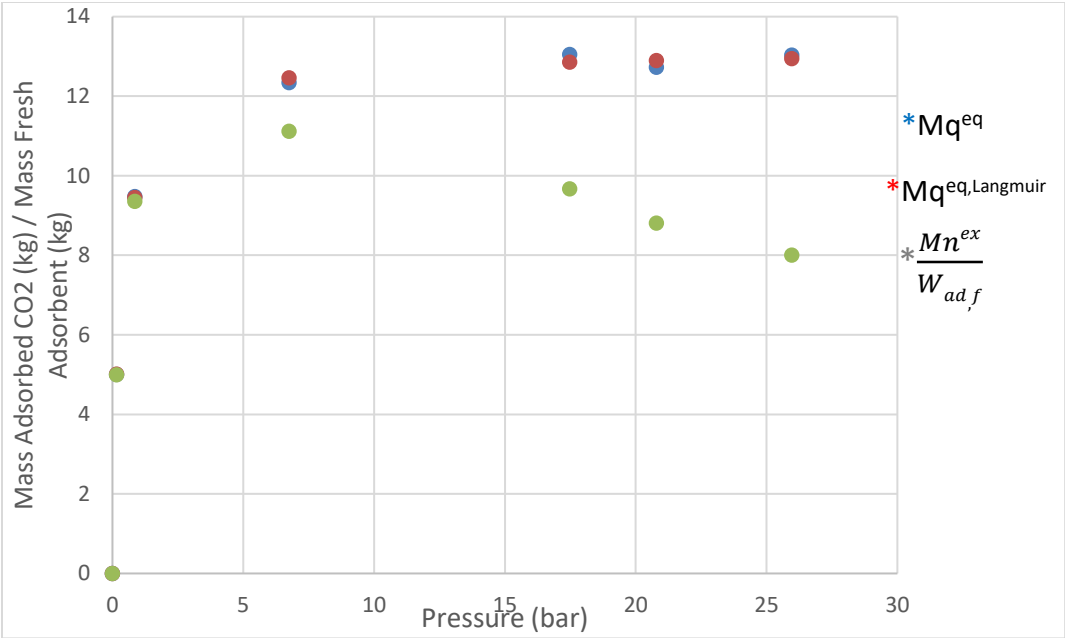

Figure 3.12. Excess and Absolute Adsorption Isotherm data and Langmuir Isotherm fit

During this initial project phase, we also initiated the sorption-enhanced water gas shift reaction (SEWGSR) experiments in the lab-scale AR with the key goal, once more, to generate sufficient experimental data to validate the mathematical models that are developed. Typical results are presented in Sect. 5 below. In the experiments we used a simulated syngas with composition (H_2:CO:CO_2:N_2:CH_4:NH_3:H_2S=0.51:1.00:0.36:2.28:0.1:0.0072:0.0031), typical of the composition of an air-blown gasifier off-gas (because of the inability of RGA to distinguish between N_2 and CO in most of the dynamic experiments, to be able to properly close mass balances, N_2 was replaced with Ar). The following experimental protocol was followed (refer to Fig. 3.13 for the definition of the various devices as well as RPPRs 3 and 4 for further details):

The Adsorptive Reactor (AR) System Operation. In this series of experiments, the AR is loaded with a HTC (Mg-Al-CO_3 LDH with a Mg:Al molar ratio of 3:1) adsorbent - Co/Mo-based sour WGS catalyst admixture (69 g of 600~850 μm HTC adsorbent particles, 10 g of Co/Mo-based sour-shift catalyst with equal particle size, and the adsorbent-catalyst admixture was diluted by 22 g of crushed quartz with equal particle size).

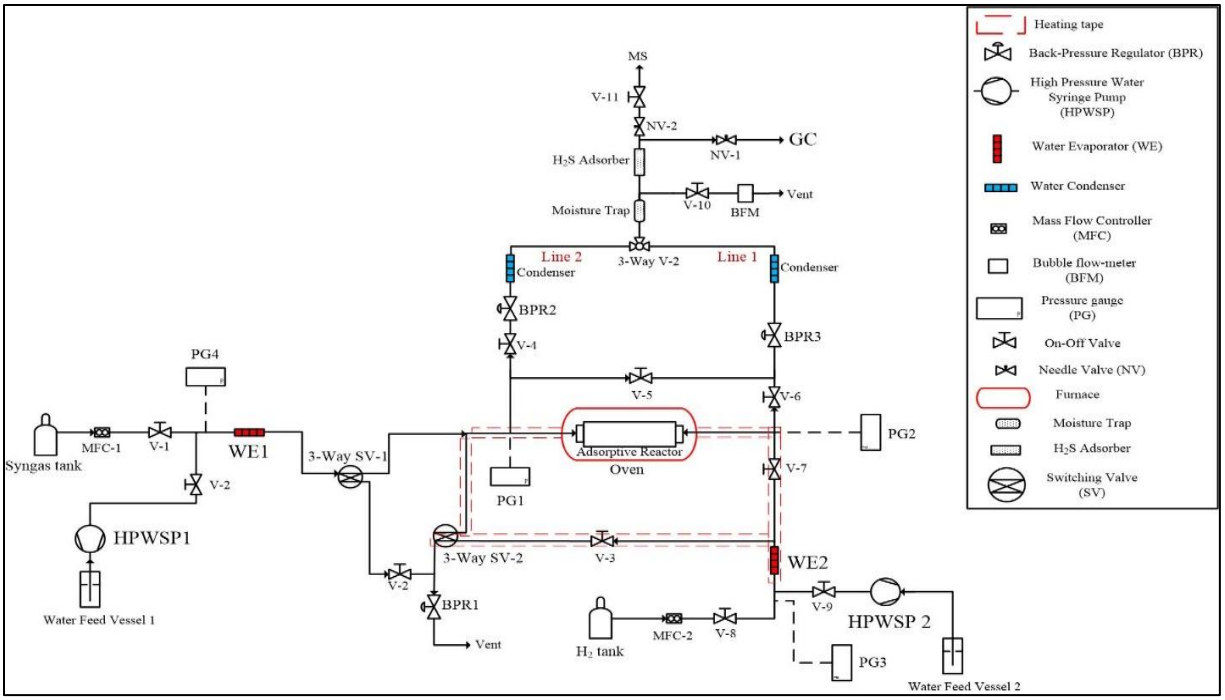

Figure 3.13. Experimental set-up of the SEWGSR experiments

<u>a. Pressurization-Step.</u> Pre-set the BPR1 to the approximate desired pressure setting (e.g., 25 bar) and prepare a mixture of steam and syngas at the prescribed ratio while directing the flow to the vent via the 3-way SV-1. Pre-set the BPR3 to the approximate desired pressure setting (e.g., 25 bar), open V-5 and V-7 (make sure V-3 -4 and V-6) are completely closed), open V-8 and the H_2 tank and set the MFC connected to the H_2 tank at the desired flow rate, open V-9 and HPWSP2 (control the steam flow rate via adjustment of the HPWSP2). The reactor is brought to the desired operating temperature (e.g., 300°C) in a flow of H_2 (or Ar) and steam gas-mixture of the desired composition (Exit to Feed). When the reactor temperature reaches 300°C, slightly adjust BPR3 until the pressure of AR reaches the set-point (e.g., PG2=25 bar, while monitoring/recording PG1 for potential pressure drops).

<u>b. Adsorption-Reaction Step.</u> When the AR pressure under H_2 and steam flow stabilizes to the desired pressure (e.g., 25 bar), open V-6, close V-5, and direct the prepared mixture of steam and syngas to the feed side (Feed to Exit) of the AR via the 3-Way SV-1, and close V-7 and V-8 and the H_2 tank. The effluent gas flow rate and composition will be continuously monitored via BFM and the MS and the GC (Completely close NV-1 and -2, open V-10, connect Line 1 to BFM via 3-Way V-2; open V-11, slightly adjust NV-2, direct a small slip-stream effluent gas flow to MS;

slightly adjust NV-1, direct a small slip-stream effluent gas flow to the GC for validating the MS measurements). Eventually, the adsorbents will become saturated, and the CO_2 will appear in the effluent gas (breakthrough).

c. Rinse-Step (Feed to Exit). Open V-3 (Make sure V-7 is completely closed), adjust the flow rate of steam to the desired level via HPWSP2, direct the steam to the vent via 3-Way SV-2, and adjust the BPR1 to 25 bar. When the H_2 purity and recovery decrease below the preset levels, switch the 3-Way SV-1 to the vent and direct the flow of the prepared high-pressure steam to the feed side of AR via the 3-Way SV-2. A rinse of the AR with high-pressure steam (equivalent to one reactor void volume) can push out the gas that is present in the voids, maximizing the H_2 recovery and minimizing the quantity of H_2 in the CO_2 product. The effluent gas flow rate and composition are continuously monitored via BFM and the MS (Completely close NV-1 and NV-2, open V-10, connect Line 1 to BFM via 3-Way V-2; open V-11, slightly adjust NV-2, direct a small slip-stream effluent gas flow to MS; slightly adjust NV-1, direct a small slip effluent gas flow to the GC for validating the MS measurements). During this step, the reactor temperature and pressure remain the same with the temperature and pressure of step 2b (e.g., 300°C and 25 bar, respectively).

d. Depressurization and Regeneration Step (Exit to Feed). Direct any high-pressure steam flow remaining in the line to the vent via 3-Way SV-2. Pre-set the BPR2 to the approximately desired pressure setting (25 bar). Open V-4, close V-6, open V-7, close V-3, direct the high-pressure steam flow to the AR (Exit to Feed). Adjust BPR2 to the desired desorption pressure (e.g., PG1=atmospheric); the CO_2 is desorbed by flowing steam through the reactor at a constant flow rate. During this step, the temperature of the reactor remains the same as that of steps 2b, 2c (e.g., 300°C). The effluent gas flow rate and composition are continuously monitored via the BFM and the MS (Completely close NV-1 and NV-2, open V-10, connect Line 1 to BFM via 3-Way V-2; open V-11, slightly adjust NV-2, direct a small effluent gas slip-stream flow to MS; slightly adjust NV-1, direct a small effluent gas slip-stream flow to the GC for validating the MS measurements). If desired to carry out the step at a higher temperature, after the desired regeneration pressure is reached, heat the reactor to the desired temperature (*e.g.* 400 or 450°C) while the reactor is continuously purged with low-pressure steam to further desorb the CO_2. The effluent gas flow rate and composition are continuously monitored via BFM2 and the MS. Continue this step until the CO_2 is completely desorbed and no CO_2 is detected in the effluent.

e. Pressurization-Step (Exit to Feed). If step 2d took place at a temperature higher than the reaction step, cool down the reactor to the desired reaction temperature for step 2b (e.g., 300°C). Set BPR3 to the desired pressure for step 2b. Open V-8, the H_2 tank, and set the flow rate of H_2 (via setting the MFC connected to the H_2 tank) and the steam flow rate (via adjustment of HPWSP2) to create the desired H_2 and steam gas-mixture. Close V-4, Open V-5 and V-7, close V-6. The reactor is then pressurized to the reaction pressure with H_2 and steam gas-mixture ($y_{H2} = y_{H2O} = 50\%$) again. At this point, regeneration of the reactor is completed. The cycle then restarts from step 2b.

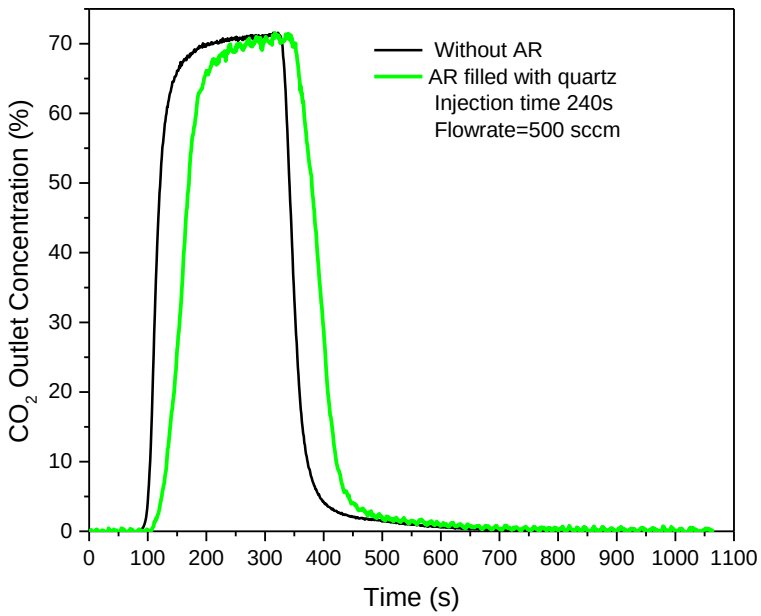

Figure 3.14. Dynamic experiments at 15 bar and 400°C with 240 s injection time and 500 sccm flow rate

For the validation of the AR models via the experimental data (see further discussion in Sect. 5 and also in RPPR 4), the dispersion characteristics of the AR and the dead times associated with the other lab-scale system components must be accurately analyzed and determined. For that, dynamic experiments with a pulse input of 74.2% CO_2-25% N_2 and of varying duration (e.g., 80, 140 s and 240 s) without the AR installed in the oven (the reactor part was replaced with a short quarter-inch tube) were carried out under different pressures (e.g., 5, 15, 25 bar) and temperatures

(e.g., 250ºC, 400ºC and 450ºC). The experiments were then repeated under the same conditions, but with the AR installed in the system while containing only quartz particles.

A set of such experimental data are shown in Fig. 3.14. For the analysis of the experimental data we utilize two approaches. In the first approach, we utilize the experimental dynamic response of the balance of the system in order to extract the AR dynamics via the convolution integral

$$y_{output} = \int_0^{\infty} E(t - t') y_{exp}(t')\, dt' \tag{3.12}$$

where $y_{output}(t)$ is the output result of the system in %, E(t) the residence time distribution, $y_{exp}(t)$ the experimental results without AR in %, t' the dummy variable for the integration in sec.

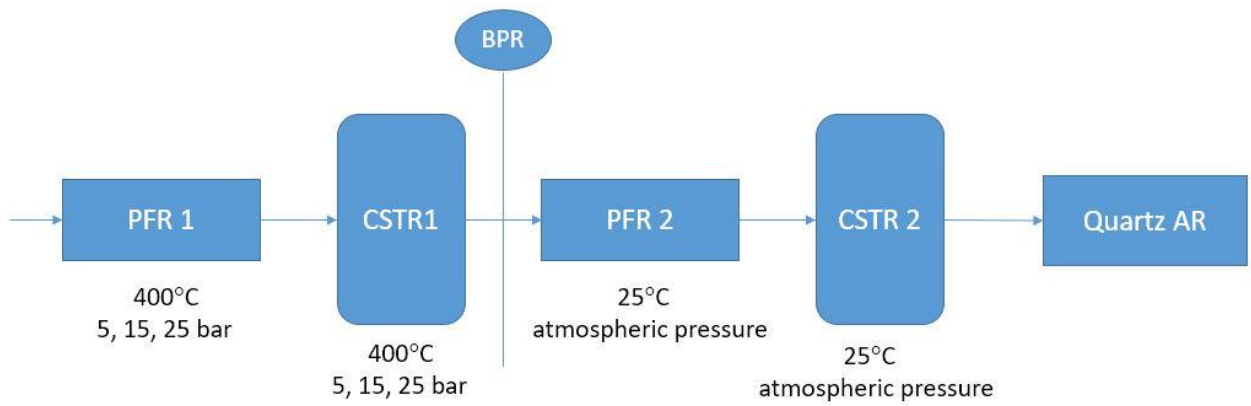

Figure 3.15. The dynamic diagram of the AR system

In the 2nd approach, we first approximate the dynamics of the balance of the system with an array of reactors (e.g., see Fig. 3.15 for a schematic – in the figure, CSTR means a continuously-stirred tank reactor while PFR stands for plug-flow reactor), which is then used to extract the AR dynamics. The dead times and AR dispersion dynamics are then taken into account when analyzing the AR experimental data, as discussed in Sect. 5.

During this reporting period, another key focus was the operation and testing of the individual membrane reactor MR sub-system utilizing the M&PT CMS membranes and the $Co/Mo/Al_2O_3$ sour-shift catalyst discussed in Sect. 2. A key focus of this task was to generate sufficient experimental data to validate the mathematical models developed, see Sect. 5. Figure

3.16 below shows the MR conversion vs. catalyst weight-to-CO molar flow rate (W/F_{CO}). (For these experiments we utilized CMS membrane HMR-52 (10”) whose properties are reported in Table 2.6). For the MR, conversion is defined as:

$$X_{CO} = \frac{n^F_{COo} - (n^F_{CO,exit} + n^P_{CO,exit})}{n^F_{COo}} \tag{3.13}$$

where n^F_{COo} is the CO molar flow rate at the inlet (mol/hr), $n^F_{CO,exit}$ is the CO molar flow rate at the exit of the reactor’s feed side (mol/hr), and $n^P_{CO,exit}$ is the CO molar flow rates at the exit of the reactor’s permeate side (mol/hr).

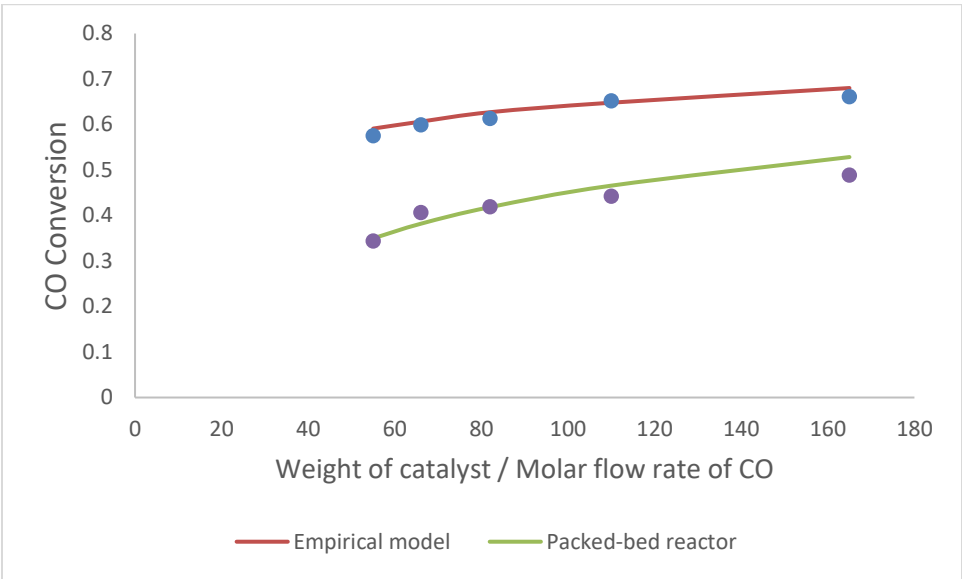

Figure 3.16. Conversion vs. W/F_{CO} for MR (feed pressure 14.5 bar, reactor temperature 250ºC, no sweep)

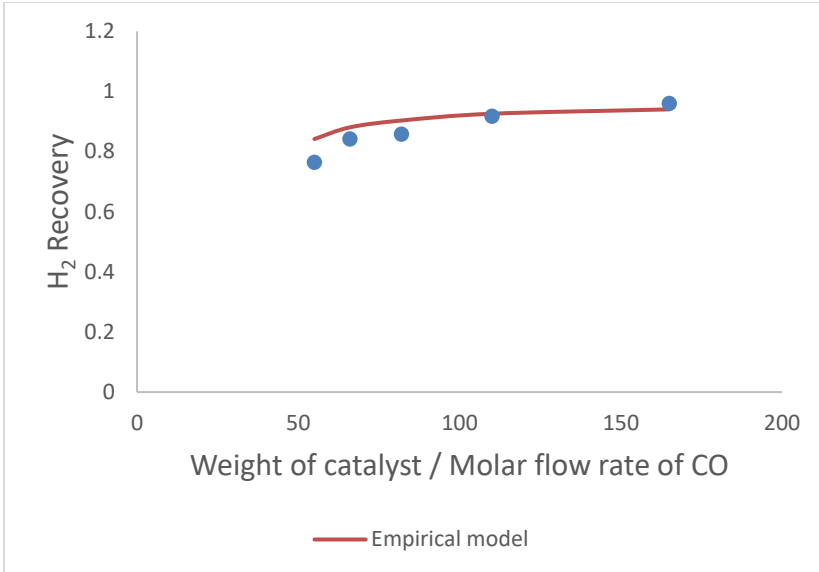

Figure 3.17. H_2 Recovery vs. W/F_{CO} for MR (feed pressure 14.5 bar, reactor temperature 250°C, no sweep)

Figure 3.17 shows the experimental H_2 recovery rate (shown also are the modeling simulations using the 1-D MR model) defined as:

$$Re_{H_2} = \frac{n^P_{H_{2,exit}}}{(n^F_{H_{2,exit}} + n^P_{H_{2,exit}})} \tag{3.14}$$

where $n^F_{H_{2,exit}}$ is the hydrogen molar flow rate at the exit of the reactor's feed side (mol/h) and $n^P_{H_{2,exit}}$ is the hydrogen molar flow rate at the exit of the reactor's permeate side (mol/h). Due to the high permeation rates through this high-throughput CMS membrane, high recovery rates are attained. Shown on the same figures are the predictions of the 1-D MR model. The model does a respectable job in predicting the experimental conversion data. In Sect. 5 below we describe the development of a Multi-scale MR model and its application to a MR experimental data employing a different CMS membrane.

3.3. Summary and Conclusions

In this Section of the report we report on the modification of an existing lab-scale test unit at USC to permit operation at higher pressures (up to 25 bar) and to incorporate a dedicated AR subsystem. The lab-scale system consists of: (i) the gas delivery system; (ii) the MR system containing the CMS membrane packed with WGS catalyst in its annulus; (iii) the AR subsystem, consisting of two adsorbent beds for continuous cycling between adsorption and desorption, and containing the adsorbent and catalyst with its appropriate valves and control hardware; (iv) overall system control hardware; and (v) the analysis section equipped with the appropriate analytical equipment. Graphite O-rings are employed as seals between the membrane and housing. GC-TCD and GC-FID are be used in concert with MFM to study the performance of the MR subsystem by measuring the total molar flow rates and analyzing the permeate and feed/reject side gas compositions. Since the AR subsystem operates under transient conditions, mass analyzers are used to track its performance, together with GC analysis at preset intervals (for validation of the mass analyzer's readings).

Initial testing focused on the individual components (i.e., MR and AR) of the MR-AR lab-scale system. Key experimental parameters investigated for the MR subsystem included: (i) the membrane permeation characteristics; (ii) reactor temperature, feed and permeate pressures, contact time, catalyst weight to CO molar flow rate (W/F_{CO}), and the permeate side (steam) purge rate. For the AR subsystem, key parameters studied included: (i) the catalyst and adsorbent weights; (ii) the operating envelope (i.e., temperature and pressure) of the adsorption/reaction cycle; and (iii) desorption mode. The dependent variables monitored included exit stream compositions and flow rates, and based on such data we quantify the CO conversion, H_2 recovery and purity, CO_2 recovery and purity, and degree of adsorbent regeneration. The experimental data have been used to validate a mathematical model developed as part of this project and described in further detail in Sect. 5.

4.0 LAB-SCALE TESTING AND VALIDATION OF THE ULTRA-COMPACT MR-AR PROCESS

4.1 Overview

As noted previously, the overarching objective of this lab-scale study is to prove the technical feasibility of the membrane- and adsorption-enhanced WGS process that employs a CMS membrane-based MR followed by two AR in parallel, operating alternately, utilized for the production of high-purity H_2 with simultaneous CO_2 capture during WGS reaction treating a coal gasifier off-gas. The results of this part of the study are presented in this section of the report. First, we describe a series of preliminary experiments, in which we investigated the integrated MR-AR system without employing steam sweep in the MR's permeate side. The experimental results show that membrane, catalyst, and adsorbent all operated stably under the integrated gasification combined cycle (IGCC)-relevant conditions. The stand-alone MR system displayed superior performance in CO conversion and hydrogen purity compared with the conventional PBR, and the MR-AR reactor sequence demonstrated high performance superior to that of a PBR with near 100 % conversions attained while the ARs are functional (with an ultrapure hydrogen stream exiting the AR and permeate-side hydrogen purities from the MR of ~75-80 %) under the IGCC-relevant operating condition with pressure up to 25 bar and temperature of 250°C. These results have experimentally validated the ability of the hybrid MR-AR process configuration to operate stably and properly under the desired conditions and to intensify the efficiency of the WGS reaction.

Subsequently, we investigated the integrated MR-AR system employing steam sweep in the MR's permeate side. The CMS membrane utilized for that part of the study has displayed very robust and stable performance during a long-term run (>500 hr run of H_2S exposure under IGCC relevant environments), and has maintained high He/N_2 (~126) and H_2/CO (~100) selectivities over a total of 742 hr of operation during the MR-AR experiments. We have experimentally tested the combined MR-AR in multiple-cycle runs (10-16 cycles), and the system has demonstrated superior performance to that of a conventional PBR with high purities for the hydrogen product which can be directly usable in a hydrogen turbine for power generation. In addition, we have carried-out parametric studies for optimization of the operation of the integrated MR-AR system by investigating various operating conditions for both the MR and the AR. We have found that under the experimental conditions of the multi-cycle experiments, the AR performance (with respect to catalyst and adsorbent performance) takes a few cycles to settle down to its eventual

“steady-state” value. We have shown, in addition, that membrane, catalyst and adsorbent have proven very robust and stable under the IGCC power generation conditions (large concentration H_2S, high-temperature and high-pressure) environment during the long-period MR-AR multiple-cycle runs.

4.2 Preliminary Experiments with no Steam Sweep

In what follows, we first briefly describe the lab-scale hybrid MR-AR system used in these experiments and its operation and evaluation under realistic pressure and temperature conditions akin to the IGCC environment. We then describe a preliminary set of experimental runs for simultaneous H_2 production and CO_2 capture for a range of pressures up to 25 bar while employing a simulated coal-derived air-blown gasifier off-gas. Specifically, the performance characteristics of the MR-AR system for a range of W/F_{CO} (weight of catalyst/molar flow rate of CO) conditions are presented.

4.2.1 Experimental Section

4.2.1.1 Materials

We have utilized in the MR a tubular CMS membrane with an inner diameter of 3.6 mm, outer diameter of 5.6 mm, and a length of 254 mm, prepared by M&PT. The membrane consists of a thin nanoporous CMS separation layer formed on the outside surface of a M&PT commercial asymmetric mesoporous alumina ceramic tube. The specific CMS membrane utilized (termed as the candle-filter membrane configuration) has only one end open to flow, for convenient installation and sealing into the reactor . A commercial $Co/Mo/Al_2O_3$ sour-shift catalyst provided by Clariant (USA) (whose physical and chemical properties are also reported in Sect. 2) was used for both the MR and the AR units. A Mg-Al-CO_3 layered double hydroxide (with a Mg/Al molar ratio of 3:1) CO_2 adsorbent was used in the AR; as described in Sect. 2, and it was prepared by our team (M&PT) using conventional approaches.

4.2.1.2 Experimental Set-up

For easy reference, a schematic of the lab-scale hybrid MR-AR system employed in the experiments in this Section is shown in Fig. 4.1. It consists of three parts (for further details about the lab-scale system, see Sect. 3 and the RPPR's):

(i) The MR section, which consists of the tubular stainless steel (SS) reactor (seated inside a furnace with six separate heating zones) with a length of 25.4 cm and inside diameter of 3.2 cm. To ensure isothermal reactor operation, the temperatures of the reactor is controlled with a six-point thermocouple connected to PID controllers. Temperature isothermality is confirmed via a thermocouple sliding inside a thermo-well imbedded in the reactor module. The tubular CMS membrane is sealed inside the reactor using graphite O's rings and compression fittings. 10 g of commercial $Co/Mo/Al_2O_3$ WGS catalyst mixed with ~90 g of crushed quartz particles (with the same size in the range of 600-850 μm) are loaded into the annular space in between the CMS membrane and the reactor body. The reason that we dilute the catalyst (and adsorbent, see below) with inert quartz particles is so that we completely fill the MR (and AR) volumes to avoid gas by-passing; this has the added benefit of making it more feasible to operate under isothermal conditions by diluting the catalyst and/or adsorbent and adding more heat capacity.

(ii) The AR section, which consists of two different tubular stainless steel reactors with a length of 14 cm and inside diameter of 3.8 cm, each AR being located inside its separate GC oven for temperature control (see Fig. 3.4 in Sect. 3). Three two-point thermocouples (fabricated by the Thermometric Corporation) are installed inside each AR to monitor the temperature at two radial and at three equidistant axial positions of the reactor. Both AR's are loaded with an admixture containing the hydrotalcite adsorbent (69 g), the $Co/Mo/Al_2O_3$ sour-shift WGS catalyst (10 g) and quartz (22 g), all with the same particle size in the range of 600-850 μm. Additionally, the AR section is equipped with an Argon gas cylinder, and its associated MFC, a high-pressure water syringe pump, and a steam-generating unit (evaporator), specifically designed for generating an Ar/steam mixture at the desired pressure (e.g., 25 bar) for regenerating the adsorbent in the AR. A separate steam-generating unit (high-pressure water syringe pump + evaporator) is installed in between the MR and AR units for supplying additional water to the AR feed stream (i.e., the MR reject-side stream) to adjust its H_2O/CO ratio, if so desired.

(iii) The analysis section, which consists of a Gas Chromatograph (GC) for measuring the concentrations of the MR exit gas streams, two separate Mass Spectrometers (residual gas analyzers or RGA) capable of instantaneously analyzing the gas composition of the AR exit gas streams, bubble flow-meters (BFM) for measuring the total MR exit dry-gas flow rates, condensers to remove the water from the exit streams of the MR and AR, and traps to remove the H_2S from the same streams to protect the GC and RGA instruments.

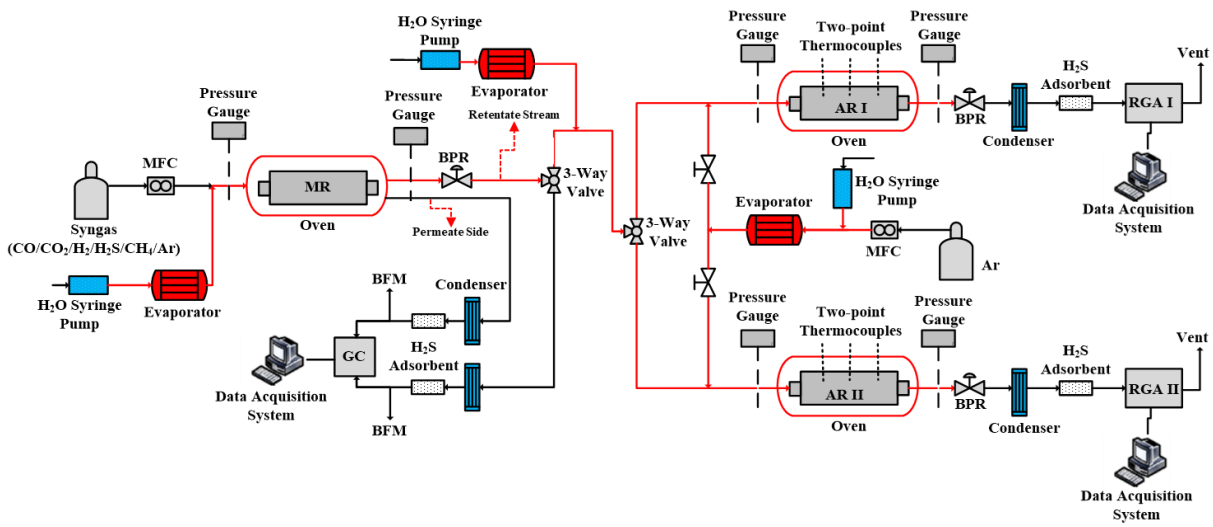

Figure 4.1. Experimental set-up used in the MR-AR experiments (red lines are heat-traced to prevent water from condensing; **MR:** Membrane Reactor; **AR:** Adsorptive Reactor; **MFC:** Mass Flow Controller; **BFM:** Bubble Flow-meter; **RGA:** Residue Gas Analyzer; **GC:** Gas Chromatography; **BPR:** Back Pressure Regulator)

4.2.1.3 Experimental Procedure

To monitor the state of the CMS membrane before and after the MR-AR experiments, we measured the single-gas permeances of the major syngas components (i.e., H_2, CO, CO_2, CH_4, N_2) and of He, an inert test gas, at pre-determined temperatures and pressures. Specifically, to carry-out these single-gas permeation tests the feed-side pressure of the MR was set to its appropriate value with the aid of a BPR while the permeate-side pressure was, typically, maintained at atmospheric conditions, and the permeate-side and reject-side flow rates were then measured with a bubble flow-meter. In order to convert the flows to STP conditions (m^3/h), the laboratory temperature and

pressure were also measured with a digital thermometer and an analog barometer, respectively. The ideal gas selectivity of the CMS membrane, α_{ij}, is defined as the ratio of the permeances of two pure gases, measured separately under the same pressure/temperature conditions:

$$\alpha_{ij} = \frac{Perm_i}{Perm_j} \tag{4.1}$$

where $Perm_i$ and $Perm_j$ are the permeance of the two pure gases, respectively, with i being the most permeable gas.

For the MR-AR experiments, since the Co and Mo metal components of the fresh (as received) catalyst, are in their oxidized form, they need to be sulfided prior to the initiation of the reaction. The activation procedure involves the in-situ reduction of the metals using a gas mixture containing H_2, N_2 and H_2S (up to 5 mol% of H_2S in H_2/N_2) using a temperature and pressure protocol, as specified by the catalyst manufacturer. In this series of experiments, we used a simulated coal-derived syngas (purchased as a certified, pre-mixed gas mixture from Praxair, Specialty Gases & Equipment), with composition: H_2:CO:CO_2:Ar:CH_4:H_2S= 0.51:1.00:0.36:2.28:0.1:0.0031, typical of air-blown gasifier off-gas (we substitute N_2 with Ar as to facilitate the analysis via the RGA, since N_2 interferes with the analysis of CO, but our studies have shown that both N_2 and Ar act as diluents and do not participate in the WGS reaction - Ar also serves in the dual capacity as an internal standard gas).

For each experiment, the conversion of the MR and the AR sub-systems and the overall combined MR-AR conversion were measured for different W/F_{CO} values (where W is the weight of the catalyst, and F_{CO} is the feed molar flow rate (mol/h) in the MR), while employing a constant H_2O/CO ratio (equal to 2.8 in the experiments reported here). The MR-AR experiments are performed at IGCC-relevant high-temperature and high-pressure (up to 25 bar) conditions. Before initiating the combined MR-AR experiment, the MR conversion was first allowed to reach steady state for at least 1 hr. To “bench-mark” the MR performance, in the experiments we also measure the corresponding conversion of the PBR under the same operating conditions. This is accomplished by closing the exit on the permeation side of the MR, and again allowing the system (now operating as a PBR) to reach steady state.

As shown in Figure 4.1 (see also Fig. 1.1), the reject-side (retentate) stream (a CO_2-rich stream, that also includes some H_2, unreacted CO, CH_4, N_2 and impurities like H_2S) of the MR serves as the feed for the AR. Though it is possible to operate the AR at different temperatures and pressures than those in the MR, in the experiments reported here the operating temperature and pressure for both reactors were kept the same. As noted above, one has the option to add additional steam to the feed stream into the AR (to potentially compensate for H_2O losses to the permeate side of the MR) to maintain the desired H_2O/CO ratio (for the experiments reported here, this ratio for the AR is also maintained at 2.8). To initiate the operation of the combined MR-AR system, once the MR operation reaches steady state, the MR's reject-side stream is directed to the feed of the AR via a 3-way valve to allow it to be first mixed with a sufficient flow of steam to maintain the desired H_2O/CO ratio. Prior to doing so, both AR's are pressurized simultaneously to the desired pressure and heated to the desired temperature with the aid of a 50 vol.% steam-50 vol.% inert gas (Argon) stream. While the MR reject-side (intermixed with any additional steam, if so desired) is directed into the first AR (AR I), the 50 vol.% steam/50 vol.% Argon stream continues to be directed to the second AR (AR II).

During the experiment, the AR I outlet gas is measured instantaneously using the RGA I. Once the AR I system reaches the desired level of performance (e.g., a pre-determined hydrogen product purity - in the experiments reported here we allow for complete adsorbent saturation in order to validate catalyst and adsorbent stability), the MR reject-side stream (plus any added steam) is then switched into the second AR (AR II), while the 50 vol.% steam/50 vol.% Argon stream is directed into AR I to regenerate the adsorbent in the reactor at the desired temperature (a temperature 400ºC is employed here) and duration (for 30 min in the experiments reported here). After completing the evaluation of the performance of the AR I and AR II sub-systems, the MR's reject-side stream is switched back away from the feed of the AR, and the MR performance, including the gas composition and flow rate of both the reject and the permeate sides, is studied again to verify if the MR performance has remained stable. The operating cycle is then again repeated to gauge system performance.

The total CO conversion of MR-AR overall system is defined as follows:

$$\mathrm{CO}\ (\%) = \frac{F^{\mathrm{M}}_{\mathrm{CO},feed} - (F^{\mathrm{A}}_{\mathrm{CO},exit} + F^{\mathrm{P}}_{\mathrm{CO},exit})}{F^{\mathrm{M}}_{\mathrm{CO},feed}} \times 100\% \qquad (4.2)$$

where $F^{\mathrm{M}}_{\mathrm{CO},feed}$ represents the molar flow rate of CO in the feed of the MR (mol/h), and $F^{\mathrm{A}}_{\mathrm{CO},exit}$ and $F^{\mathrm{P}}_{\mathrm{CO},exit}$ represent the molar flow rates of CO in the exit of the AR and the MR permeate-side, respectively.

The CO conversion of the MR subsystem is calculated by Equation 4.3

$$\mathrm{CO}\ (\%) = \frac{F^{\mathrm{M}}_{\mathrm{CO},feed} - (F^{\mathrm{R}}_{\mathrm{CO},exit} + F^{\mathrm{P}}_{\mathrm{CO},exit})}{F^{\mathrm{M}}_{\mathrm{CO},feed}} \times 100\% \qquad (4.3)$$

where $F^{\mathrm{R}}_{\mathrm{CO},exit}$ is the CO molar flow rate at the exit of the MR reject-side (mol/h).

The CO conversion of the PBR (when closing the MR permeate-side) is defined as follows

$$\mathrm{CO}\ (\%) = \frac{F^{\mathrm{M}}_{\mathrm{CO},feed} - F^{\mathrm{R}}_{\mathrm{CO},exit}}{F^{\mathrm{M}}_{\mathrm{CO},feed}} \times 100\% \qquad (4.4)$$

The CO conversion of the AR subsystem is defined as follows

$$\mathrm{CO}\ (\%) = \frac{F^{\mathrm{R}}_{\mathrm{CO},exit} - F^{\mathrm{A}}_{\mathrm{CO},exit}}{F^{\mathrm{R}}_{\mathrm{CO},exit}} \times 100\% \qquad (4.5)$$

where the CO molar flow (mol/h) at the exit of the MR reject-side functions as the feed of the AR.

The hydrogen purity (dry-basis) is calculated by Equation 4.6

$$Pu_{\mathrm{H_2}} = \frac{F^{\mathrm{P}}_{\mathrm{H_2},exit}}{F^{\mathrm{P}}_{\mathrm{H_2},exit} + F^{\mathrm{P}}_{\mathrm{CO},exit} + F^{\mathrm{P}}_{\mathrm{CO_2},exit} + F^{\mathrm{P}}_{\mathrm{CH_4},exit} + F^{\mathrm{P}}_{\mathrm{Argon},exit}} \times 100\% \qquad (4.6)$$

where $F^{\mathrm{P}}_{\mathrm{H_2},exit}$, $F^{\mathrm{P}}_{\mathrm{CO_2},exit}$, $F^{\mathrm{P}}_{\mathrm{CH_4},exit}$ and $F^{\mathrm{P}}_{\mathrm{Argon},exit}$ are the molar flow rates of hydrogen, CO_2, CH_4 and Argon at the exit of the MR permeate-side (mol/h), respectively.

The hydrogen recovery is calculated by Equation 4.7

$$Re_{\mathrm{H_2}} = \frac{F^{\mathrm{P}}_{\mathrm{H_2},exit}}{F^{\mathrm{R}}_{\mathrm{H_2},exit} + F^{\mathrm{P}}_{\mathrm{H_2},exit}} \times 100\% \qquad (4.7)$$

where $F^{\mathrm{R}}_{\mathrm{H_2},exit}$ is the hydrogen molar flow rate at the exit of the MR reject-side (mol/h).

4.2.2 Results and Discussion

4.2.2.1 Membrane Reactor Experiments

We employed in this study a CMS membrane prepared at M&PT. The membrane was loaded into the MR module at the M&PT laboratories, and its permeation characteristics were tested using two model inert gases (He and N_2) prior to the module being shipped to USC. Upon receiving the MR module from M&PT, the pure-gas permeances of N_2 and He were again measured at the same temperature and pressure conditions, and substantial differences were observed in the permeance values measured at USC, when compared to those measured at M&PT. A closer inspection of the MR module indicated that the end-fittings appeared loose and were, then, re-tightened. Subsequent measurement of the permeation properties indicated them to be more in line with those measured at M&PT (see Table 4.1), with the He/N_2 ideal selectivity (IS) measured at USC being, in fact, quite higher (173 vs. 122, see Table 4.1) than the one measured at M&PT, mostly, due to a lower N_2 permeance, indicative potentially of a leaking graphite sealing during the M&PT permeation test (It should be noted that single-gas and mixed-gas permeances with these CMS membranes are close to each other, and so are the ideal selectivity and separation factor. Single-gas permeances are significantly easier, and also more reliable to measure than mixed-gas permeances, and are thus utilized routinely here to monitor the state of the membrane during the MR-AR experiments. Further details about the permeation properties and the mechanism of transport of these membranes can be found elsewhere [11]). After the initial measurement of the membrane properties, 10 g of WGS catalyst were intermixed with ~90 g of crushed quartz, and the mixture was then carefully loaded into the MR module and activated according to the activation procedure recommended by the catalyst manufacturer.

Table 4.1. Pure-gas permeances of He and N_2 and corresponding ideal selectivity at various temperatures and pressures measured in the empty module

Lab	T (ºC)	P (bar)	Gas permeance (m^3(STP)/m^2 h bar)		Ideal selectivity (IS)
			He	N_2	He/N_2
MP&T	250	2.38	1.1110	0.0091	122
USC	250	2.38	1.0454	0.0061	173
USC	250	25	0.9641	0.0068	142

In this Section, we report experiments with the hybrid MR-AR system with the MR and AR subsystems operating at the same temperature (250°C) and pressure (15 and 25 bar), while varying the W/F_{CO} for the MR. Prior to initiating these experiments with the combined MR-AR system (i.e., switching the reject-side stream from the MR as feed into the AR) the MR was allowed to reach steady state and its conversion, H_2 purity (dry-basis) in the permeate stream and recovery were all measured, and are presented in Figs. 4.2, 4.3 and 4.4. We also measured the conversion and hydrogen purity of the reactor functioning as a PBR under the same experimental conditions, and those are also reported on the same Figures. (The gas compositions in these experiments were measured using a GC. For each experimental point, we withdrew and analyzed several samples until at least three consecutive measurements were in the range of ~5% error).

As can be seen in Fig. 4.2, the CO conversions for the MR are significantly higher than those of the PBR under all conditions studied (i.e., different W/F_{CO} and pressures). The most important advantage, however, of using the MR is shown in Figure 4.3, which compares the hydrogen purities of the processed syngas for the MR and PBR. Because the air-blown coal gasifier off-gas contains a large fraction of N_2, despite the relatively large conversions attained in the PBR, the hydrogen purity of the resulting product is so poor that it is hardly appropriate for use in power generation. On the other hand, the use of the MR that combines reaction and separation in one unit, in addition to improving the CO conversion, also provides a hydrogen product stream with sufficient purity to be directly usable in a hydrogen turbine for electricity generation (the calculated equilibrium conversion under these conditions is quite high ~ 98%, and for the W/F_{CO} and the membrane area employed in this lab-scale study neither the PBR nor the MR approach this value).

The important role that the AR plays as an add-on 2nd stage to the MR can be seen by studying the MR behavior in Figures 4.2 – 4.4. The need to capture a large fraction of the carbon in the gasifier off-gas for storage and sequestration (project target >90%), dictates that the CO conversion in a single-stage MR is quite high (for the off-gas composition used in these experiments, a CO conversion larger than 85% is needed, but most likely significantly higher than that, given the unavoidable losses during the CO_2 separation and capture steps). Such high conversions are, definitely, attainable in a MR, e.g., by increasing the amount of catalyst utilized (i.e., increasing the W/F_{CO}, see Fig. 4.2) or the membrane area, but doing so implies substantial additional capital cost. In addition, as Figs 4.2 – 4.4 make amply clear, increasing CO conversion

comes at a cost of diminished hydrogen product purity, which also implies additional carbon losses. Another key challenge for the stand-alone MR (as with the PBR), is meeting the purity requirements for the CO_2 stream (project target >95%) for storage and sequestration. For meeting this requirement, the reject stream from the MR (processing the air-blown gasifier syngas employed in this study) will have to undergo significant additional processing (e.g., a two-stage Selexol process). The combined MR-AR system readily meets the target without needing additional processing. It is superior, furthermore, to a stand-alone AR which produces a low-purity hydrogen stream, not much unlike the PBR, which requires substantial added treatment before it can be used for power generation (though the stand-alone AR has an advantage over the PBR, in that it produces a substantially pure CO_2 stream).

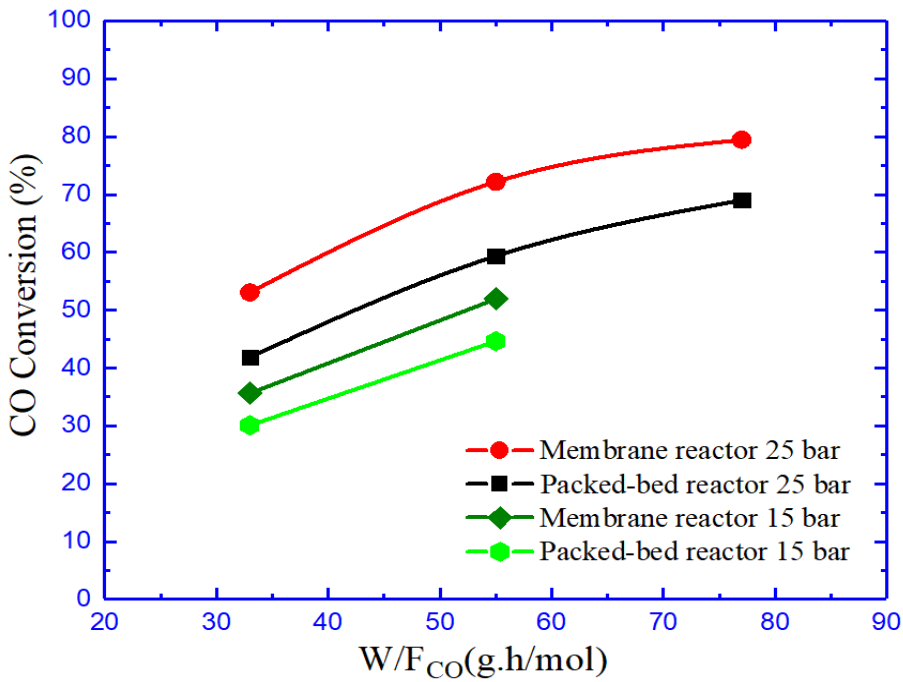

Figure 4.2. Conversion vs. W/F_{CO} for the membrane reactor and packed-bed reactor at 250°C

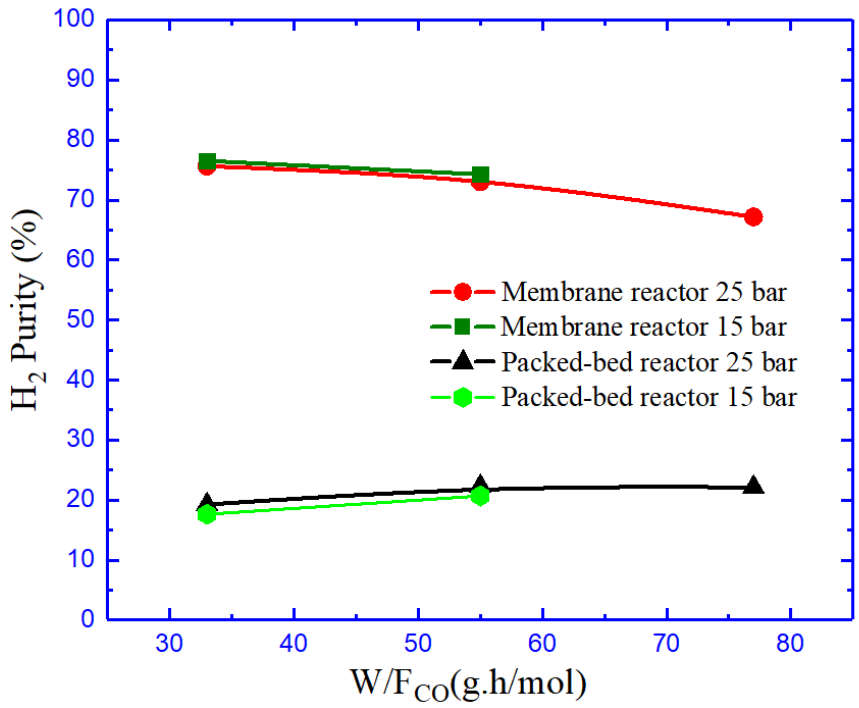

Figure 4.3. Hydrogen purity vs. W/F_{CO} for the MR and PBR at 250°C

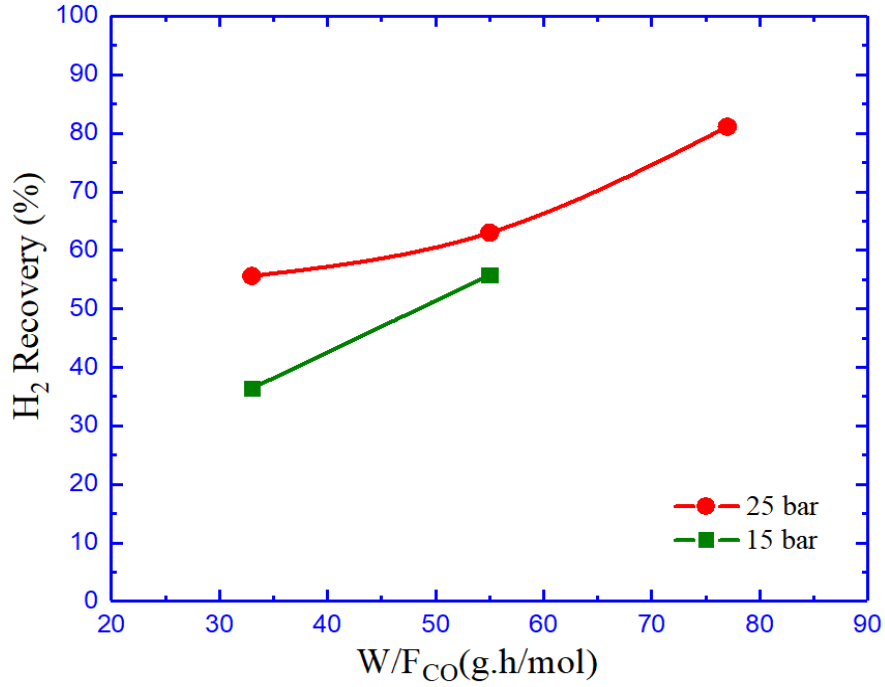

Figure 4.4. Hydrogen recovery vs. W/F_{CO} for the membrane reactor at 250°C

Another important objective of this preliminary lab-scale investigation is to validate the ability of the materials utilized (catalysts, membranes and adsorbents) to function stably under these harsh experimental conditions involving the processing of a simulated coal-gasifier off-gas containing a large concentration of H_2S with high-temperature and high-pressure steam. For that, the catalytic activity of the catalyst was monitored continuously (by measuring the steady state conversion in the MR, as well as the steady state conversion in the AR, after the adsorbent was saturated - see discussion to follow) and was shown to remain virtually identical for the duration of the experimental cycle lasting ~ two weeks. We monitored, in addition, the state of the CMS membrane by measuring the pure-gas permeances of all syngas components (H_2, N_2, CO, CO_2, CH_4), in addition to He and Argon, both before the MR-AR experiments were started, and also after the MR-AR experiments were completed. The measured permeance along with the corresponding IS values are shown in Table 4.2. Within the experimental accuracy of some of these measurements, the membrane properties remain quite invariant (particularly of the slow non-adsorbing gases like Ar and N_2, which are a much more sensitive indicator of the membrane developing cracks and pinholes).

Table 4.2. Single-gas permeances and ideal selectivities before and after the MR-AR experiments

	T (ºC)	P (bar)	Gas permeance (m^3(STP)/m^2 h bar)							Ideal selectivity (IS)			
			He	H_2	Ar	N_2	CO	CO_2	CH_4	H_2/Ar	H_2/CO	H_2/CO_2	H_2/CH_4
Before	250	25	1.0090	1.2112	0.0130	0.0099	0.0143	0.0346	0.0088	93	85	35	138
After	250	25	1.0397	1.2925	0.0130	0.0107	0.0153	0.0369	0.0095	99	79	35	136

4.2.2.2 Combined MR-AR Experiments

The performance of the two AR's (AR I and AR II) during the combined MR-AR experiments, in terms of the various exit gas molar flow rates in the AR (i.e., H_2, CO, CO_2), the CO conversion in the AR (Equation 4.5) as well as the total conversion in the MR-AR combined

system (Equation 4.2) as a function of time, is presented in Figs. 4.5 – 4.9 (the gas compositions and conversions in these Figures are measured via the RGA instrument, which samples and measures the exit composition at a frequency of 1 sample-point per second, so what is shown in Figs. 4.5 – 4.9 are the lines passing through this multitude of points). In Fig. 4.5, we show the behavior for both AR's for an operating pressure (for both the MR and AR) of 25 bar, and a feed W/F_{CO} (into the MR) of 33 g·h/mol during the first cycle of operation. Both reactors show typical AR behavior [12], whereby the initial AR conversion begins at a high value (~100% in this case) and starts to decline as the adsorbent gets saturated with CO_2 leveling-off finally at the conversion that would be attained if the reactor was operating as PBR (~64.26% for AR I and ~60.1% for AR II).

Figure 4.6 shows the behavior for both AR's for a larger value of W/F_{CO} (into the MR) of 77 g·h/mol. The experimental behavior is similar to that in Fig. 4.5 (for the smaller value of W/F_{CO}), other than the fact that the two reactors show ~ 100% conversion for a more extended time period, and the steady-state conversions in both ARs levels-off at a higher value of ~85%. Figures 4.7 and 4.8 show the behavior for the MR-AR experiments with the reactors operated at 250°C and at 15 bar of pressure. Though the qualitative behavior is similar to that at higher pressures, the reactor appears to be less efficient at lower pressures never reaching 100% conversion. This is, likely, the outcome of decreased residence times and adsorption rates at the lower pressures.

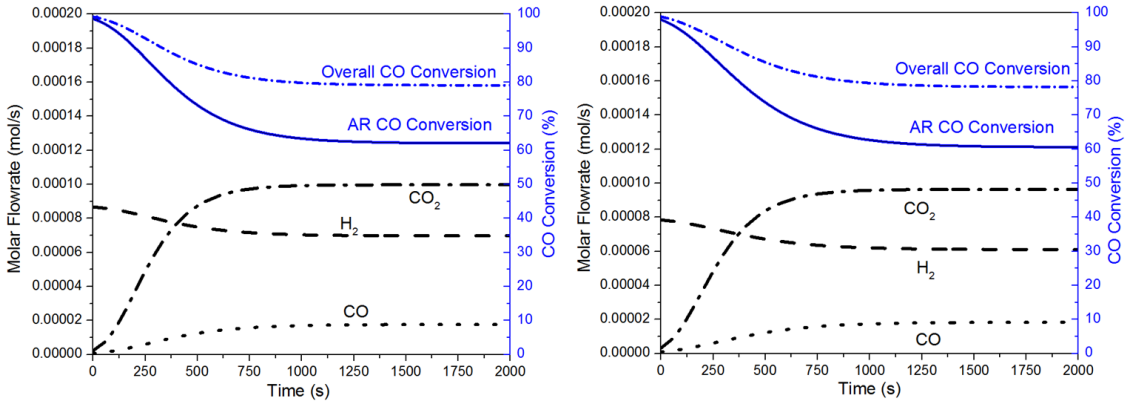

Figure 4.5. CO conversion in the AR and total MR-AR conversion, and molar flow rates of CO_2, H_2, CO in the two AR's. (Left) AR I, and (Right) AR II. Temperature of 250°C, pressure of 25 bar, H_2O/CO ratio of 2.8, with the MR operated with a W/F_{CO} of 33 g·h/mol

In the present study, during each MR-AR experiment, the ARs were allowed to run for ~1 hr to approach steady-state, so as to monitor the state of the catalyst and adsorbent. In field operations, of course, the AR will be taken off-line, once the carbon loss (and/or hydrogen purity) would exceed (or fall below) a certain threshold value dictated by the corresponding process design calculations.

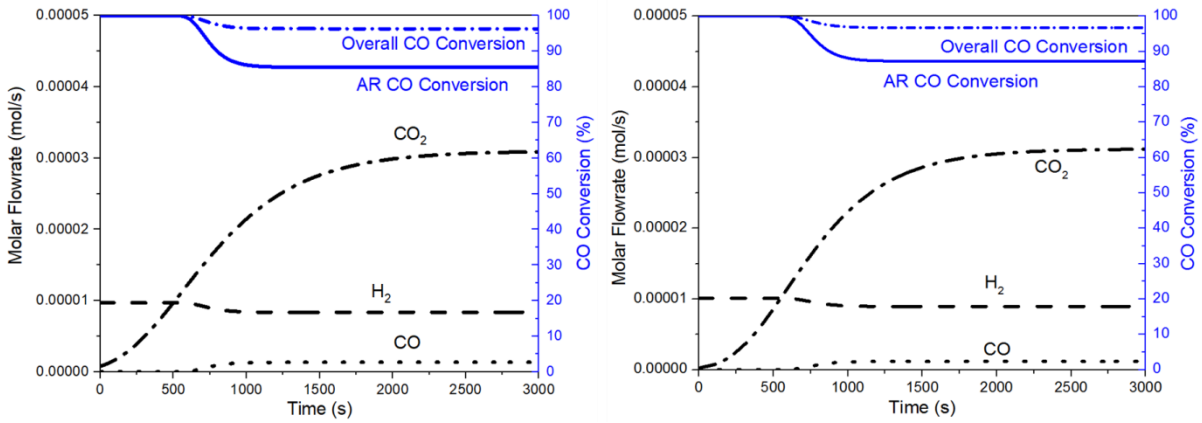

Figure 4.6. CO conversion in the AR and total MR-AR conversion, and molar flow rates of CO_2, H_2, CO in the two AR's. (Left) AR I, and (Right) AR II. Temperature of 250°C, pressure of 25 bar, H_2O/CO ratio of 2.8, with the MR operated with a W/F_{CO} of 77 g·h/mol

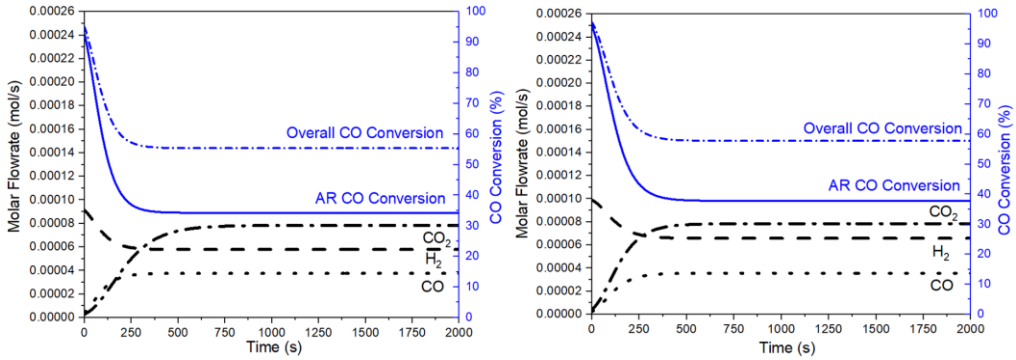

Figure 4.7. CO conversion in the AR and total MR-AR conversion, and molar flow rates of CO_2, H_2, CO in the two AR's. (Left) AR I, and (Right) AR II. Temperature of 250°C, pressure of 15 bar, H_2O/CO ratio of 2.8, with the MR operated with a W/F_{CO} of 33 g·h/mol

After the adsorption/reaction part of the experimental cycle in a given AR was completed, the temperature in this AR was raised to 400°C under a gas mixture (i.e., 50 vol.% steam - 50 vol.% Argon) flow and kept there for an additional 30 min for the adsorbent to be regenerated. (In the meantime, the reject side from the MR was switched to the other AR for the adsorption/reaction part of the cycle for this reactor to commence). Upon completion of the regeneration the temperature of the AR was lowered under the same gas mixture flow to 250°C for the second adsorption/reaction cycle to begin. Figure 4.9 shows the behavior of the MR-AR system, operated at 250°C and a pressure of 25 bar (with a MR feed W/F_{CO} equal to 55 g·h/mol) after two cycles of operation.

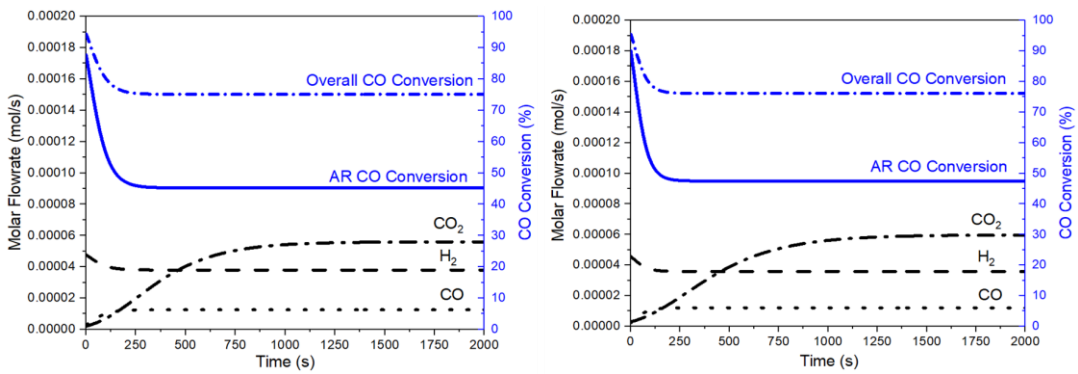

Figure 4.8. CO conversion in the AR and total MR-AR conversion, and molar flow rates of CO_2, H_2, CO in the two AR's. (Left) AR I, and (Right) AR II. Temperature of 250°C, pressure of 15 bar, H_2O/CO ratio of 2.8, with the MR operated with a W/F_{CO} of 55 g·h/mol

The data in Fig. 4.9 indicate quite a reproducible behavior, which is indicative of the fact that the hydrotalcite adsorbent and WGS catalyst used in this study show good reversibility during the sorption-desorption cycles and remarkable stability in the coal-gasifier off-gas atmosphere. That these hydrotalcite materials are capable of functioning so well under these harsh conditions is in line with cyclic adsorption/desorption studies by our Group under non-reactive conditions, and prior AR studies under more moderate conditions by other investigators [13]. And it points out the promise that all materials (membranes, catalysts, and adsorbents) tested here show for the practical application of the proposed technology.

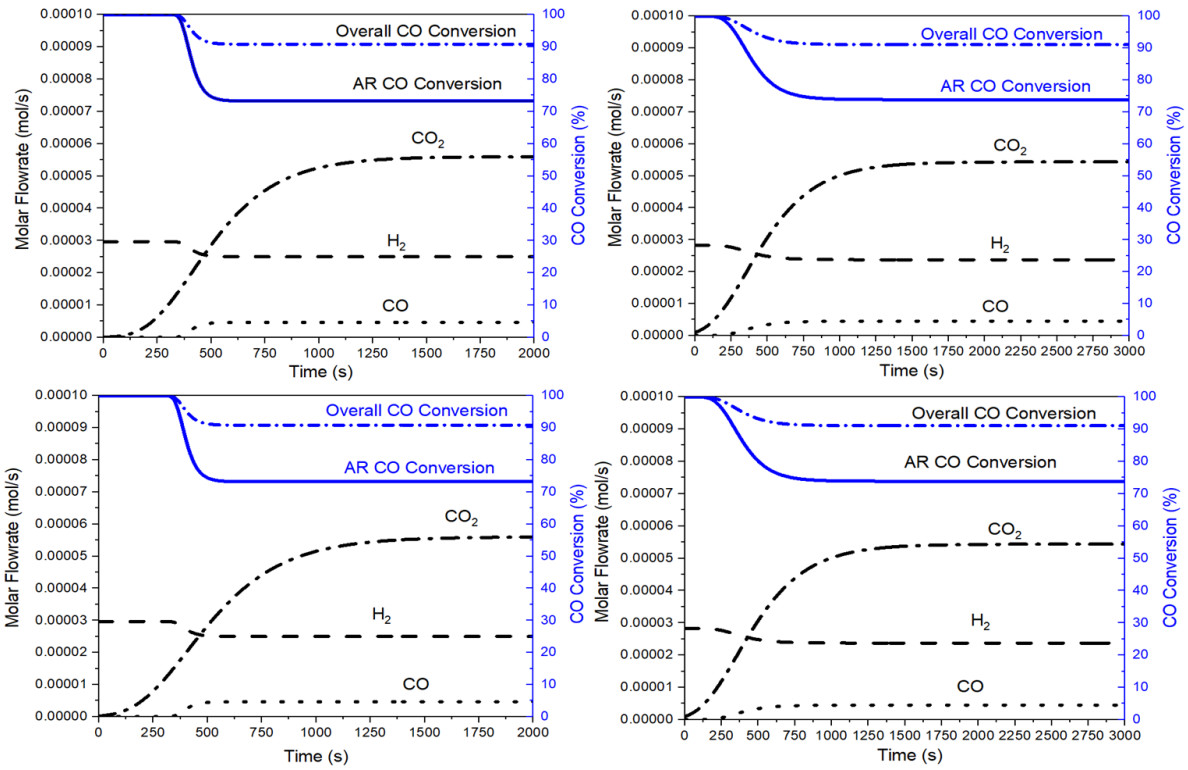

Figure 4.9. CO conversion in the AR and total MR-AR conversion, and molar flow rates of CO_2, H_2, CO in the two AR's. (Left Top) AR I, first cycle, (Right Top) AR II, first cycle, (Left Bottom) AR I, second cycle, (Right Bottom) AR II, second cycle. Temperature of 250°C, pressure of 25 bar, H_2O/CO ratio of 2.8, with the MR operated with a W/F_{CO} of 55 g·h/mol

4.3 Long-Term MR-AR Experiments

In Sect. 4.2, we presented a preliminary experimental study of a novel reactor configuration, consisting of a MR followed by two ARs in parallel, operating alternately, utilized for the production of high-purity hydrogen with simultaneous CO_2 capture during the water−gas shift reaction treating a coal gasifier off-gas. In the study, we used a commercial sour-shift WGS catalyst ($Co/Mo/Al_2O_3$) in both the MR and the AR. A CMS membrane was used in the MR, and a hydrotalcite adsorbent was used in the AR. The experimental results show that membrane, catalyst, and adsorbent all operated stably under IGCC-relevant conditions. The MR−AR reactor sequence displayed performance superior to that of a conventional PBR with near 100% conversions attained while the ARs are functional (with an ultrapure hydrogen stream exiting the AR and permeate-side hydrogen purities from the MR of ∼75−80%). Thus, these findings manifest

the ability of the hybrid MR−AR process configuration to operate properly under the desired conditions and to intensify the efficiency of the WGS reaction, as well as to validate its potential to function as a high-efficiency, ultra-compact process for incorporation into IGCC power plants for environmentally-benign power generation with pre-combustion CO_2 capture.

In that study, we operated the integrated MR-AR without steam sweep by employing a specific CMS membrane with only one end open to flow (termed as the candle-filter membrane configuration). To compensate for the water losses into the permeate-side of the MR, a separate steam-generating unit was employed to supply additional steam to the AR feed stream; this however, increases the capital cost for the process due to the fact that high temperature (250°C) and high pressure (up to 25 bar) steam is costly. In order to improve the process design for this integrated MR-AR system, before initiating the study in this Section we upgraded the integrated MR-AR lab-scale system so that we can provide a steam sweep in the MR's permeate side, and also to be able to increase the permeate-side pressure above atmospheric.

The potential advantages of operating the MR-AR system with steam sweep include the following: (i) Adding steam sweep during MR operation is able to reduce the water losses to the permeate-side from the reject-side of the MR, thus enhancing the CO conversion and H_2 recovery by eliminating the loss of reactant H_2O from the reject-side of the MR where the WGS reaction takes place; (ii) the use of steam sweep on the permeate-side of the MR as well the increase in the MR's permeate-side pressure helps to maintain the H_2O:CO ratio in the exit of the MR reject-side to a sufficiently high level so that there is no need to supply any additional high-pressure and-temperature steam to the AR feed stream. The latter requires installing a separate steam-generating unit in between the MR and the AR system, as we did in the experiments reported in Sect. 4.2.

A key objective of this series of experiments, furthermore, was to investigate the feasibility of running the integrated MR-AR system for long time periods (500 hr long, much longer than the run times reported in Sect. 4.2). This is in preparation for a similar length, future bench-scale run under field conditions employing real syngas. An important goal for the experiments was to investigate catalyst/adsorbent stability and, in particular, the CMS membrane performance stability during exposure to H_2S and other syngas components for a period of >500 hr. Furthermore, during the over the >500 hr long run, the plan was to carry-out additional parametric studies of the hybrid MR-AR system to determine the optimal operating conditions in order to

improve the process performance. The optimization parameters we investigated included the operating conditions for the MR (e.g., W/F_{CO}, H_2O/CO ratio, steam sweep ratio, steam sweep pressure in the MR's permeate side, etc.) and for the AR (e.g., sorption-enhanced WGS reaction time, adsorbent regeneration time, regeneration pressure, etc.). The experimental findings of this >500-hr experimental run are described below.

4.3.1 Experimental Section

4.3.1.1 Materials

For the experiments reported in this Section performed with the hybrid MR-2AR system while utilizing steam as a sweep, a tubular CMS membrane with an inner diameter of 3.6 mm, outer diameter of 5.6 mm, and a length of 254 mm was utilized in the MR. The CMS membrane was prepared by M&PT. and consists of a thin nanoporous CMS separation layer formed on the outside surface of a M&PT commercial asymmetric mesoporous alumina ceramic tube. Unlike the CMS membrane utilized in the experiments in Sect. 4.2, which had only one end open to flow and was employed in the MR in the candle-filter membrane configuration, the particular CMS membrane utilized in the experiments reported here has both ends open to flow. During the MR experiments, the membrane is sealed on both ends to the tubular SS reactor using graphite O' rings and Swagelok compression fittings. Steam, when employed as a sweep, flows from the one open end of the tube and exits from the other end. The steam sweep is generated by employing a high-pressure water syringe pump and a steam-generating unit (evaporator). A commercial $Co/Mo/Al_2O_3$ sour-shift catalyst provided by Clariant (USA) was utilized for both the MR and the AR units. We have also used in the AR unit a $Mg\text{-}Al\text{-}CO_3$ double- layered hydroxide (with a Mg/Al molar ratio of 3:1) CO_2 adsorbent prepared by M&PT using conventional approaches.

4.3.1.2 Experimental Set-up and Procedure

The schematic of the lab-scale MR-AR set-up employed for the experiments presented in this Section is shown, for quick reference, in Fig. 4.10. The system was modified from the MR-AR system used in the experiments in Sect. 4.2, by adding a high-pressure water syringe pump and evaporator on the MR permeate side, in order to generate the steam that can then be used as sweep

stream in the MR permeate side. In addition, a BPR was installed at the line connected to the exit of the MR permeate side in front of the water condenser, in order to be able to control the steam sweep pressure on the MR's permeate side (in the experiments in this Section, the pressure was varied in the range from 1-3 bar). 10 g of commercial $Co/Mo/Al_2O_3$ sour-shift catalyst intermixed with glass balls of similar particle size (600~850 μm in diameter) were loaded into the annular space in the MR in between the reactor body and the CMS membrane. The remaining parts of the experimental set-up are detailed in Sect. 4.2.

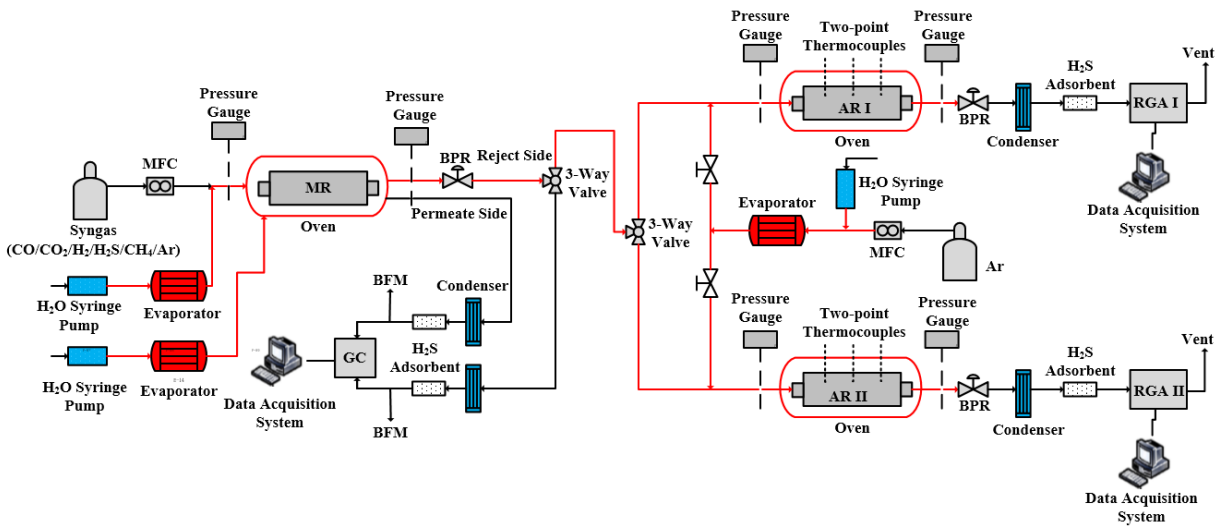

Figure 4.10. Experimental set-up used in the MR-AR experiments (red lines are heat-traced to prevent water from condensing; **MR:** Membrane Reactor; **AR:** Adsorptive Reactor; **MFC:** Mass Flow Controller; **BFM:** Bubble Flow-meter; **RGA:** Residue Gas Analyzer; **GC:** Gas Chromatography; **BPR:** Back Pressure Regulator)

To study whether the state of the CMS membrane is stable during the MR-AR experiments with steam sweep, the single-gas permeances of the major syngas components (i.e., CO, CO_2, CH_4, H_2, N_2) and of He (an inert fast gas which serves as a safe surrogate to monitor the H_2 permeance of the CMS membrane) were frequently measured at predetermined temperatures and pressures. Specifically, to initiate these single-gas permeation tests, we adjusted the BPR to pressurize the feed-side of MR up to its appropriate value, while the MR permeate-side pressure was, typically, maintained at atmospheric conditions. A bubble flow-meter was employed to measure the MR's reject-side and permeate-side flow rates. The laboratory temperature and pressure were measured

with a digital thermometer and an analog barometer respectively in order to be able to convert the volumetric flows to STP conditions (m^3/h).

For the MR-AR experiments with steam sweep presented here, we have used fresh catalyst, in which the Co and Mo metal components are in their oxidized form and, therefore, need to be activated (sulfided) prior to the initiation of the reactor runs. The activation procedure, which is described in detail in the RPPRs (and in some of the recent publications by our Group [11,12]) follows a temperature and pressure protocol recommended by the catalyst manufacturer. The MR-AR experiments presented here are carried-out using a simulated coal-derived syngas feed mixture (H_2: CO: CO_2: Ar: CH_4: H_2S=0.51:1:0.36:2.28:0.1:0.0031, typical of an air-blown gasifier off-gas).

The long-term (>500 hr) experimental run began by testing the MR-AR system components individually prior to initiating the feasibility testing of the combined MR-AR system. Experiments have been run at various W/F_{CO} values for the MR feed (where W is the weight of undiluted catalyst (g), and F_{CO} is the molar flow rate of CO (mol/hr) in the syngas), as well as different H_2O/CO ratios and steam sweep ratios (defined as the ratio of the sweep stream molar flow rate to the feed molar flow rate) in the MR's permeate side. For all the experiments reported here, we employed a steam sweep at two different permeate-side pressures of 1 and 3 bar (experiments with no sweep have also been carried-out). All the MR-AR experiments reported here were performed at 250°C and a MR reject-side and AR pressure of 25 bar (experiments employing a MR-AR pressure of 15 bar have also been carried-out). As part of the testing of the stability of the catalyst, adsorbent and membrane in the integrated MR-AR system, we have performed multiple-cycle (typically 10 - 16 cycles) MR-AR experiments. During these experiments, we have tested different MR feed pressures, W/F_{CO} values, H_2O/CO ratios, steam sweep ratios and different steam sweep pressures in the MR permeate side and evaluated their impact on the performance of the AR in the cyclic operation, the goal here being to study the optimum conditions for the MR-AR system as a whole. Furthermore, during the multi-cycle run, we have tested the system performance under different AR reaction times (25-58 min), different regeneration pressure (15-25 bar), and different regeneration times at 400°C (10-70 min). Prior to initiating the combined MR-AR experiments, the MR conversion was first allowed to reach steady state for at least 2 hr. During this time period, the RGA was utilized to measure the gas composition

for both the MR's reject side and permeate side. To "benchmark" the MR performance for these experiments, we also measured the corresponding conversion of the PBR under the same operating condition by closing the exit on the permeate side of the MR and allowing the system to operate as a PBR under steady-state conditions.

As illustrated in Fig. 4.10, the reject-side (retentate) stream (a CO_2-rich stream, that also includes some H_2, unreacted CO, CH_4, Ar, and impurities like H_2S) from MR serves as the feed for the AR. Similar with the MR-AR experiments without steam sweep detailed in Sect. 4.2, although we have the capability of operating the AR at different temperatures and pressures than those in the MR, in the experiments presented here we have kept the operating temperature and pressure for both reactors the same. As noted above, instead of adding additional steam to the feed stream into the AR to potentially compensate for steam losses into the permeate side of the MR (in an effort to maintain the desired H_2O/CO ratio in the AR feed stream), the installation of a separate steam-generating unit (high-pressure water syringe pump + evaporator) on the MR permeate side allowed for steam to be generated and used as a sweep stream in the MR permeate side. The use of steam sweep, and also increasing the permeate-side pressure (up to 3 bar in the experiments reported in this Section) with the aid of the BPR installed at the end of the MR's permeate stream line, has allowed us to maintain the desired H_2O/CO ratio in the AR feed stream without needing to supply additional steam in between the MR and the AR units, as we did in the experiments presented in Sect. 4.2.

To initiate the operation of the combined MR-AR system, the MR subsystem performance (in terms of CO conversion, hydrogen recovery and purity, which are monitored via a GC that is used to measure the composition of the reject side and that of the permeate side) is, typically, allowed to stabilize before switching the MR reject stream as a feed into the AR(s). Meanwhile, both ARs are simultaneously pressurized to the desired pressure (up to 25 bar) and heated to the desired temperature using a 50 vol %/50 vol % steam/Argon gas mixture. Once the MR reject side flow rate, gas composition and steam concentration are stable, we switch the MR reject-side stream to the AR feed-side via a 3-way valve and begin the MR-AR multi-cycle experiments. While the MR reject-side is directed into the first AR (AR I), the 50 vol %/50 vol % steam/Argon stream continues to be directed into the second AR (AR II). During the experiment, the AR I outlet gas is measured instantaneously via the RGA I; in most of the experiments reported here, we have

allowed for the sorption-enhanced water gas shift reaction time in the AR to be long enough (25-58 min depending on the operating conditions selected) so that the adsorbent became saturated with CO_2, and we obtained the so-called "pseudo-steady state" for CO conversion in the AR prior to being switched into the regeneration mode. Once the AR I system reached the "pseudo-steady state", the MR reject-side stream was then switched into the second AR (AR II), while the 50 vol %/50 vol % steam/Argon stream was directed into AR I to regenerate the adsorbent in the reactor at the desired temperature (a temperature of 400°C was employed here) and duration (10-70 min in these experiments for investigation of the optimization parameter). After completing the evaluation of the performance for both the AR I and AR II subsystems, the MR's reject-side stream was switched back away from the feed of the AR, and the MR performance (including the gas composition and flow rate of both reject and permeate sides) was studied again to verify if the MR performance has remained stable. It should be noted that during the multiple-cycle (10-16 cycles) run with the integrated MR-AR system, the MR subsystem's performance and its robustness to the simulated coal-derived syngas conditions was monitored before the multiple-cycle run, in the middle of the multiple-cycle run and after the multiple-cycle run had been completed by employing a GC to measure the MR reject-side and permeate-side stream gas composition and a bubble flow meter (BFM) to measure the dry-gas flow rate.

4.3.2 Results and Discussion

4.3.2.1 Membrane Studies

The CMS membrane employed in this study was installed inside the MR empty module at the M&PT laboratories, and prior to the module being shipped to USC, its permeation characteristics were tested using helium and nitrogen (both of which serve as model inert gases, where He is indicative of fast gases like H_2 and the N_2 is indicative of slow gases like CO). Upon receiving the MR module with the CMS membrane at USC, the single-gas permeances of He and N_2 were again measured at the same temperature and pressure conditions. The properties of the as received membrane (in the empty module) measured at M&PT as well as at USC are shown in Table 4.3. There is a difference observed in the measurement of He permeances among the two laboratories, with the He permeance measured at USC being 9.1 % larger than the M&PT measurement; however, there is only a slight difference observed in the measurement of N_2, which

is below the 5% experimental error, which is typical with such measurements. Consequently, the He/N_2 separation factor measured at USC is about 5% (189 vs. 179) larger than its value measured at M&PT. As detailed throughout this report, we have routinely observed and reported such differences (5-10%) in the He measurements among the two laboratories.

Table 4.3. Single- gas permeances of N_2 and He at various temperatures and pressures measured in the empty module

Lab	T (°C)	Pressure (bar)	He*	N_2*	SF§ (He/N_2)
M&PT	20	3.07	0.1477	0.00827	18
M&PT	250	3.07	1.2060	0.00675	179
USC	250	3.07	1.3265	0.00702	189
USC	250	25	1.2740	0.00824	155

*Gas permeance [m^3/m^2 h bar];
§ Separation factor

Subsequently, 10 g of catalyst intermixed with glass balls of similar particle size (600~850 μm in diameter) were loaded into the reactor, and the membrane permeation characteristics were measured again, and the values are shown in Table 4.4. There is a statistically significant decrease in the He permeance, and a smaller (and, likely, statistically insignificant) decrease in the N_2 permeance. That both permeances decrease, is indicative of the fact that the loading of the catalyst caused no damage to the membrane, because when the membrane's CMS layer is damaged the N_2 permeance increases greatly. We ascribe the decrease in the He permeance to the catalyst/glass balls potentially blocking/hindering access to parts of the surface of the CMS membrane.

Table 4.4. Single- gas permeances of N_2 and He at 250°C and 25 bar measured in the module after loading the catalyst

T (°C)	Pressure (bar)	He*	N_2*	SF§ (He/N_2)
250	25	1.0382	0.00807	129

*Gas permeance [m^3/m^2.h.bar];
§ Separation factor.

The catalyst was then activated. The activation procedure has been described in detail elsewhere in this report, and involves exposing the catalyst to 5% H_2S in a N_2/H_2 mixture at high temperatures for ~ 36 hr. After the catalyst activation, the membrane properties were measured once more, and are shown in Table 4.5 below.

Table 4.5. Single- gas permeances of He, N_2, H_2, N_2, A_r, CO, CO_2 and methane at 250°C and 25 bar after the catalyst activation

Test date	T (°C)	Pressure (bar)	He*	N_2*	H_2*	CO*	CO_2*	A_r*	CH_4*	SF§ (He/N_2)	SF§ (H_2/CO)
After catalyst activation	250	25	1.0206	0.00857	0.9507	0.00981	-	-	-	119	97
After 2 days	250	25	-	-	-	-	0.01375	0.00768	0.01038	-	-
After 3 days	250	25	1.0192	0.00866	0.9679	0.00981	-	-	-	118	99

*Gas permeance [m^3/m^2.h.bar];
§ Separation factor.

From Tables 4.4 and 4.5 above, one notices a slight ~1.7% (statistically insignificant) decrease in the He permeance, and a small ~6.1% increase in the N_2 permeance after activating the catalyst. The H_2/CO separation factor of around 98 - 99 is well above the project target value of 80.

One of the key objectives of the MR-AR experiments is to evaluate the membrane stability under these harsh experimental conditions involving exposing the membrane to simulated syngas with large concentration of H_2S and high-temperature and high-pressure steam during a long-

period run (over 500 hr). During four months of testing of the MR-AR system, the membrane properties were shown to be very stable, as shown in Tables 4.6 and 4.7 and in Figs. 4.11 and 4.12. The only notable exception is the CO_2 permeance for which the initial measured value is ~11.7% less than its final value measured. We ascribe this difference to experimental error in the measurement of the original value (since the value at the end of the 500 hr was measured repeatedly), because there are only slight, if any, differences measured with the other slow gases (e.g., the initial and final permeance values for CO and N_2 are virtually identical), and there is no valid scientific explanation why only the CO_2 permeance would change significantly during the long-period run (in fact, measurement of the permeance of condensable gases like CO_2 in microporous membranes, at high pressure, is notoriously difficult because of the long transients observed).

Table 4.6. Single- gas permeances of He, N_2, H_2, N_2, CO, at 250°C and 25 bar during the 500-hr run

Exposure to Syngas/H_2S Hr	He*	N_2*	H_2*	CO*	SF§ (He/N_2)	SF§ (H_2/CO)	Comments
0	1.0382	0.00807	-	-	129	-	After loading the catalyst
36	1.0206	0.00857	0.9507	0.00981	119	97	After catalyst activation
36	-	-	-	-	-	-	
36	1.0192	0.00866	0.9679	0.00981	118	99	
50	0.97741	0.00810	-	-	121	-	
66	1.0003	0.00804	-	-	124	-	
84	0.99471	0.00817	-	-	122	-	
108	0.995	0.008277	-	-	120	-	
122	1.023	0.00857	-	-	119	-	
186	1.004945	0.008252			122		
244	1.005	0.008247			122		
265	1.01894	0.00833	-	-	122	-	
402	0.9943	0.008288			120		
542	1.0061	0.00854	-	-	118	-	
542	1.0087	-	0.9558	0.00980	-	98	

*Gas permeance [m^3/m^2 h bar];
§ Separation factor.

Table 4.7. Single- gas permeances of A_r, CO_2 and methane before and after the 500 hr run

Test date	T (°C)	Pressure (bar)	CO_2*	A_r*	CH_4*
Before 500 hr run	250	25	0.01375	0.00768	0.01038
After 500 hr run	250	25	0.01558	0.00828	0.01027

*Gas permeance [m^3/m^2.h.bar];
§ Separation factor.

Table 4.8. Single- gas permeances of He, N_2 at 250°C and 15 bar after a total of 742 hr exposure to H_2S

Exposure to Syngas/H_2S Hr	He*	N_2*	SF§ (He/N_2)	SF§ (H_2/CO)	Comments
742	1.0203	0.008071	126	-	After the MR-AR experiment

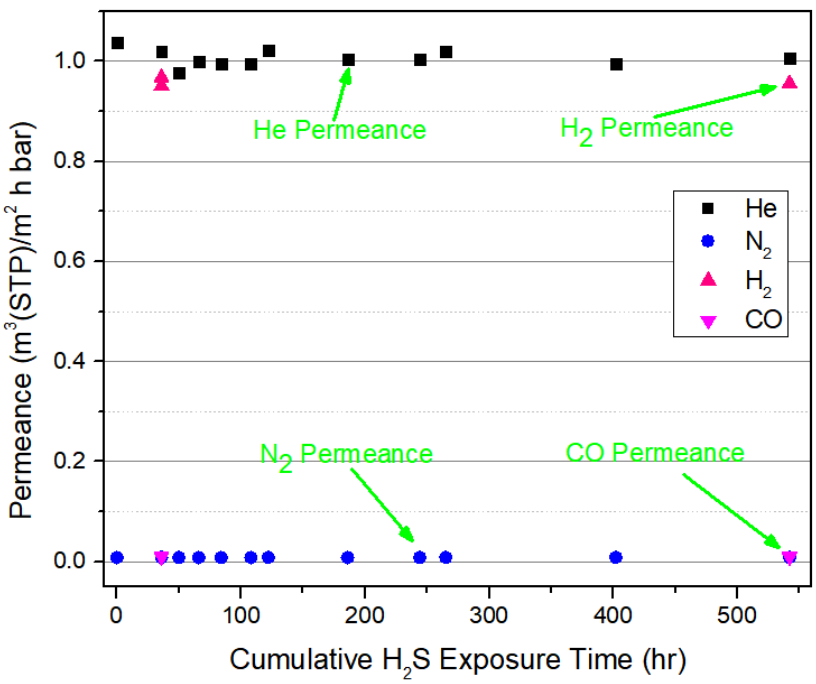

Figure 4.11. Single-gas permeances vs. H_2S exposure time during the >500-hour run

Table 4.6 (and Figs. 4.11 and 4.12) report the He, N_2, H_2 and CO permeances and the He/N_2, H_2/CO selectivities as a function of the cumulative H_2S/syngas exposure time. As the data presented in the Table (and in the Figures) show, after 542 hr of exposure time to H_2S/syngas, the permeances for He, H_2, N_2 and CO were experimentally indistinguishable from those measured before the run, and the H_2/CO separation factor stayed constant at 98, which is significantly higher than the project target value of 80. Thus, one may conclude that for this CMS membrane, the membrane properties are very robust and stable under the cumulative 542 hours run of H_2S exposure and under the 250°C temperature and 25 bar pressure environments. After completing

all the experiments at a pressure of 25 bar pressure, we continued the experiments at a different pressure of 15 bar. At the conclusion of this series of MR-AR experiments (a total exposure time to H_2S of 742 hr), the membrane still shows a high He/N_2 selectivity (~126), as shown in Table 4.8.

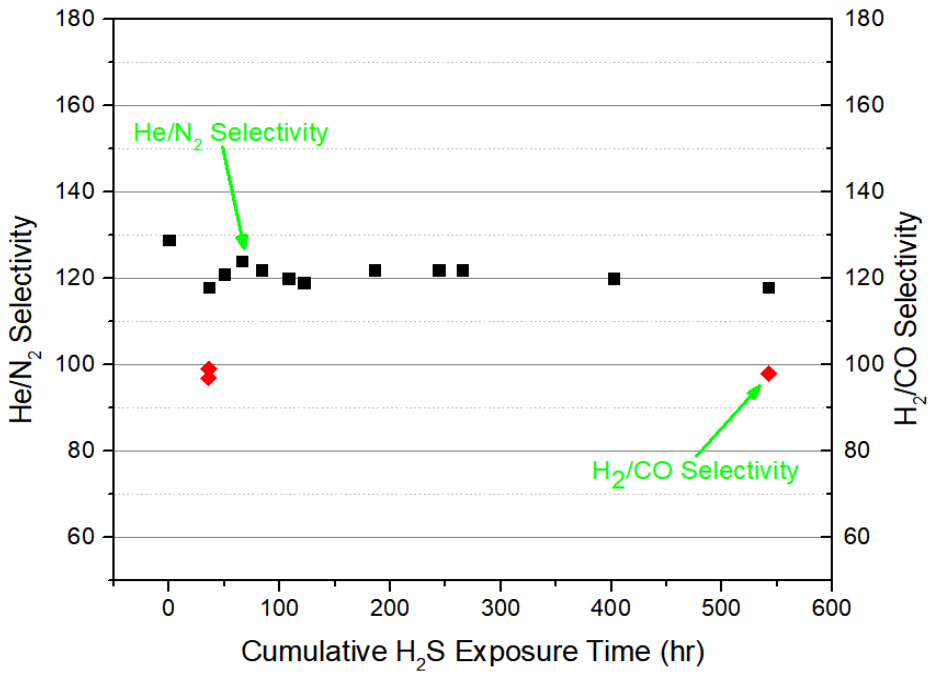

Figure 4.12. He/N_2 and H_2/CO selectivities vs. H_2S exposure time during the >500-hour run

4.3.2.2 MR-AR Multiple-Cycle Run

To assure that upstream of the AR (i.e., the MR reject side which serves as the feed stream for the AR), the state of the membrane and catalyst in the MR is stable, during each multi-cycle experiment, we continue to monitor the MR subsystem performance with respect to MR CO conversion, H_2 purity and recovery in order to verify both membrane and catalyst stability. Fig. 4.13 shows these MR properties during a multi-cycle MR-2AR run as a function of time of stream (expressed in this Figure as syngas/H_2S total exposure time). At the beginning of this run, the catalyst and membrane had been exposed to syngas/H_2S for a total of 405 hr and by the time the final MR performance measurement, shown on this Figure, was made the catalyst and membrane

had undergone an additional ~70 hr of exposure. It is clear from the Figure, that both the membrane and catalyst employed in the MR show quite stable performance.

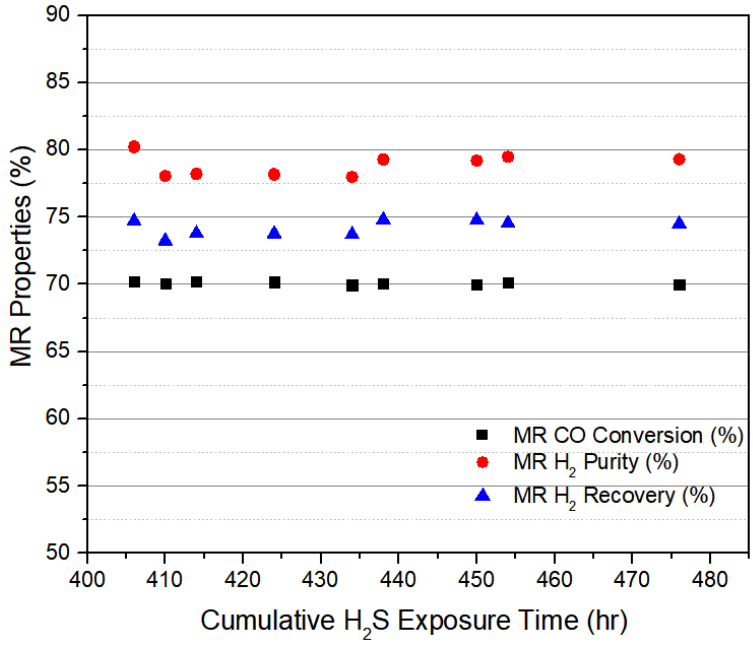

Figure 4.13. The MR properties during a multi-cycle run. Experimental conditions: T=250°C, feed pressure=25 bar, permeate-side pressure 3 bar, with steam sweep ratio=0.49, H_2O/CO ratio of 4.3, W/F_{CO}= 66 g·h/mol, air-blown gasifier model syngas (CMS#23)

In the MR-AR multiple-cycle run experiments, to properly characterize the AR behavior, we have defined the "AR effect time" into two different ways: (i) the difference between the H_2 emergence time (to account for any system dead times) and the time when the CO_2 exit composition reaches 5 %; (ii) the difference between the H_2 emergence time (to account for any system dead times) and the time when the AR's CO conversion decreases below 95 %. During the aforementioned time period, the AR works in the sorption-enhanced water gas shift reaction mode, whereby the adsorbent is still effective, and only a small amount of CO_2, specifically below 5%, exits the reactor, and the conversion in the AR is >95%, which also means that the conversion for the combined MR-AR system is >>95% as well (as the exit stream from the MR is the feed-stream into the AR). Figures 4.14 – 4.15 show the "AR effect time" during a multi-cycle MR-AR run (for the first 10 cycles we employed the MR-2AR configuration, with the remaining 6 cycles being run in the MR-AR configuration). From this Figure, one notices that the "AR effect time" takes a few cycles to settle to the eventual "steady-state" value of ~400 sec.

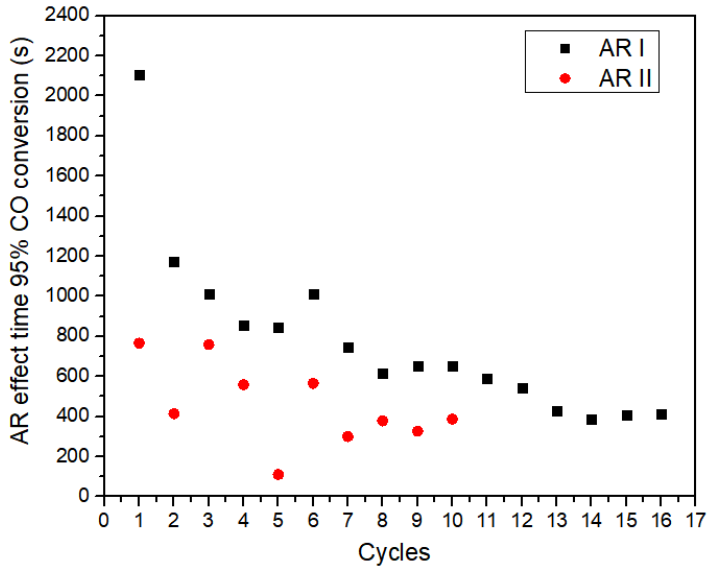

Figure 4.14. The AR effect time w.r.t 95 % CO conversion during multi-cycle run. Experimental conditions: T=250°C, feed pressure=25 bar, permeate-side pressure 3 bar, with steam sweep, W/F_{CO}= 66 g·h/mol, air-blown gasifier model syngas (CMS#23)

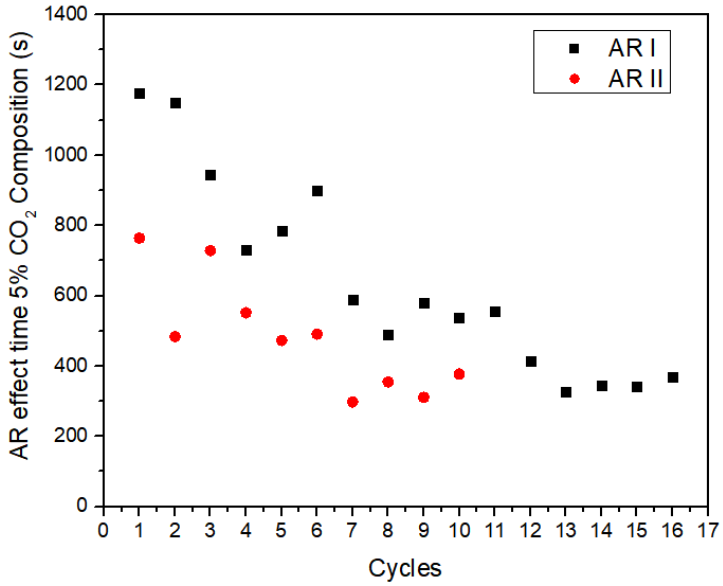

Figure 4.15. The AR effect time w.r.t 5 % CO_2 composition during multi-cycle run. Experimental conditions: T=250°C, feed pressure=25 bar, permeate-side pressure 3 bar, with steam sweep, W/F_{CO}= 66 g·h/mol, air-blown gasifier model syngas (CMS#23)

In addition, for the experiments shown in Figs. 4.14 – 4.16, we allowed for the sorption-enhanced water gas shift reaction time to be long enough (58 min in this case) so that the adsorbent becomes saturated with CO_2. Figure 4.16 reports the "pseudo-steady state" CO conversion in the

AR prior to being switched into the regeneration mode. It takes again a few cycles before the conversion settles down to its eventual steady state value and the catalyst activity and adsorbent performance become stable.

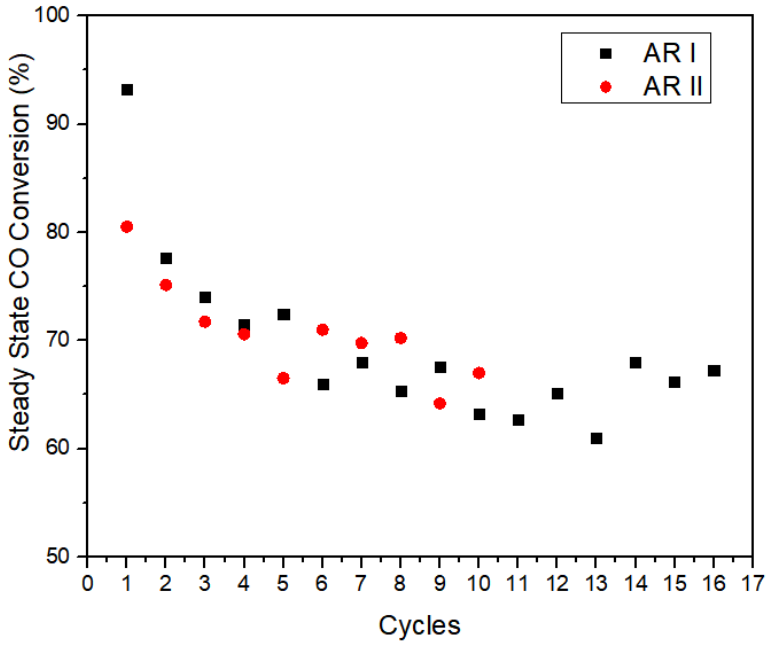

Figure 4.16. The AR steady-state CO conversion during a multi-cycle run. Experimental conditions: T=250°C, feed-side pressure=25 bar, permeate-side pressure 3 bar, with steam sweep, W/F_{CO}= 66 g·h/mol, air-blown gasifier model syngas (CMS#23)

Furthermore, we have also previously investigated catalyst robustness in the AR during adsorbent regeneration. We have performed a continuous 18-cycle experiment during which we employed various regeneration temperatures (i.e., 350, 400, 450°C) and varied the regeneration times (i.e., 10, 30, 60 min) for each selected temperature, with the results shown in Fig. 4.17. (For these experiments the AR sorption-enhanced water gas shift reaction run-time is selected long enough so that the AR reaches its pseudo-steady state CO conversion). As can be seen in Fig. 4.17, the CO steady state conversion remained quite stable, which validated the fact that the catalyst is very robust during the various regeneration treatments.

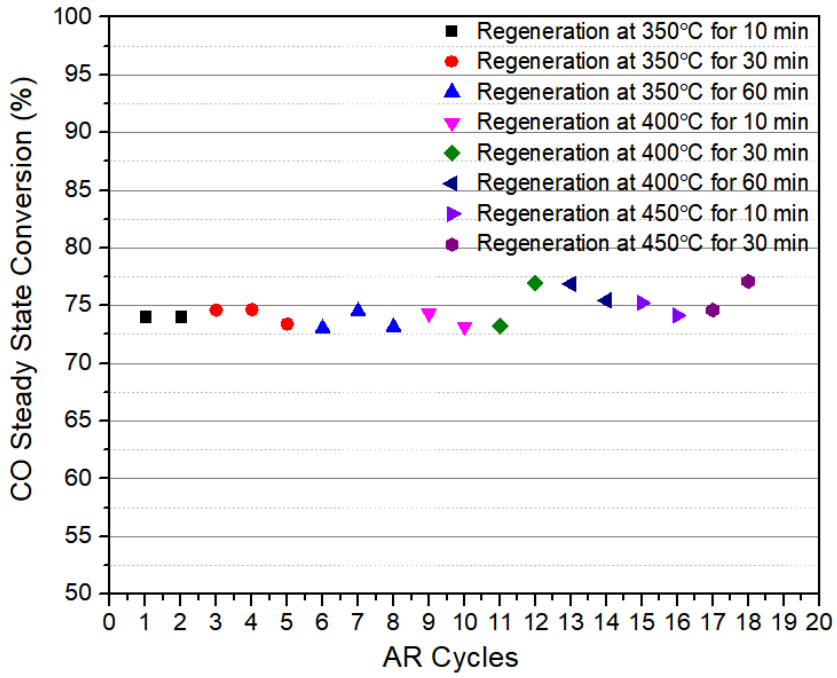

Figure 4.17. AR pseudo-steady conversion after adsorbent saturation for various regeneration protocols, as shown on the Figure. Temp=250°C, pressure=5 bar, Wc/F_{CO}=121 g·h/mol, W_{Ad}/W_c= 6.9:1

Because temperature is also a key operating parameter, in the experiments, the temperatures profiles during the sorption-enhanced water gas shift reaction mode and the adsorbent regeneration mode at different bed points of the AR were also recorded via three two-point thermocouples installed in the AR. A typical temperature profile is shown in Fig. 4.18 (note that Inlet-0'', Middle-0'' and Outlet-0'' signify three different equidistant axial positions in the reactor, specifically 1.375 in, 2.75 in, and 4.125 in from the entrance of the bed, while Inlet-0.5'', Middle-0.5'' and Outlet-0.5'' signify three radial positions 0.5" away from the bed axis). As Fig. 4.18 indicates, the reactor is fairly isothermal with radial and axial profiles being, typically, less than 2-5°C. The bed pressure drop is also very small (~0.1 psi) under all conditions studied during the MR-AR experiments. The lack of significant pressure drops and temperature gradients make it a more straightforward task to model the experimental data, and thus to validate the reactor models used in process design and optimization and in the TEA studies, Sect. 6 below.

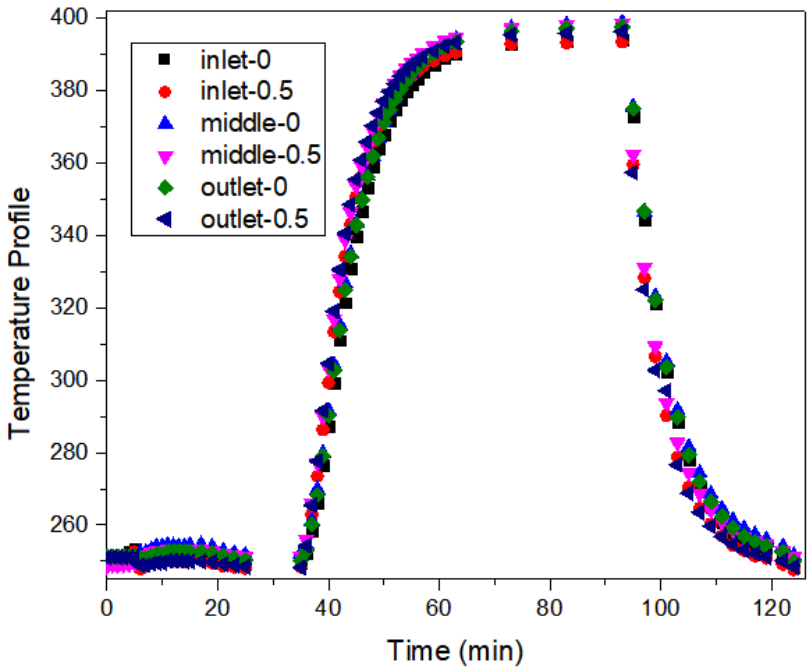

Figure 4.18. Temperature profiles of AR operated at 250°C and 25 bar using W/F_{CO} = 66 and H_2O/CO =3.22, steam sweep ratio=0.5, permeate side pressure=3 bar

4.4. Summary and Conclusions

In this Section of the report, an integrated MR-AR system, which consists of a MR followed by two ARs, was investigated. This integrated MR-AR system was experimentally evaluated for the WGS reaction in the context of the IGCC power generation application. The CMS membrane employed exhibited very robust and stable performance during the long-term run (over a >500 hr run of H_2S exposure at 25 bar of pressure) and maintained high He/N_2 selectivity (~126) over a total of 742 hr of H_2S exposure during the MR-AR run.

The combined MR-AR lab-scale system was tested during numerous multiple-cycle runs and displayed superior performance to that of a conventional PBR with high purities for the hydrogen product which can be directly usable in a hydrogen turbine for power generation. During the MR-AR multiple-cycle run, we continued to monitor MR subsystem performance with respect to MR CO conversion, H_2 purity and recovery in order to verify both membrane and catalyst stability. The membrane and catalyst in the MR both displayed stable performance during

the long-period run. To properly characterize and monitor the AR behavior, we have defined the "AR effect time" in two different ways, and during the MR-AR multiple-cycle run, we have found that the "AR effect time" takes a few cycles to settle to its eventual "steady-state" value. We have also monitored the "pseudo-steady state" CO conversion in the AR prior to being switched into the regeneration mode by allowing for the sorption-enhanced water gas shift reaction time to be long enough so that the adsorbent becomes saturated with CO_2. We also found that it takes again a few cycles before the conversion settles down to its eventual steady state value. Further, the catalyst in the AR demonstrated very robust and stable performance during a continuous 18-cycle experiment under various regeneration treatment. Thus, one may conclude that the membrane, catalyst and adsorbent are very robust and stable under the large concentration H_2S, high-temperature and high-pressure IGCC-like environment during the long-period MR-AR multiple-cycle run.

5.0 MODEL SIMULATIONS AND DATA ANALYSIS

The work presented in this Section was carried-out by UCLA as part of Tasks 4.2 and 5.3. Simulations of the combined (MR-AR) system were performed, using our (UCLA) multi-scale, steady-state model for the MR, and dynamic AR model. The modeling equations can be found in the Appendix in this report, and also in two recent publications [13, 14] by our Group..

5.1 Model Simulation

Simulated coal-derived syngas with composition (H_2:CO:CO_2:N_2:CH_4:H_2S:H_2O= 0.51:1.00:0.36:2.28:0.1:0.0031:2.8) was fed to the feed (retentate) side of the MR. W_{cat}/F_{CO} values in the MR were varied within a range of 22-221 g_{cat}*h/mol-CO by changing the MR inlet flow rate, while the AR was considered to operate at a temperature of 250ºC and a pressure of 25 bar. In this series of simulations, 10 g of catalyst was utilized in both the MR and the AR, while 69 g of hydrotalcite adsorbent was used for the AR simulations. In the simulations, the membrane permeances were taken to be ($m^3/(m^2.h.bar)$), consistent with the membrane properties discussed in Sect. 2:

H_2=1.54; CO=0.0028; CO_2=0.044; CH_4=0.014, H_2O=0.5133.

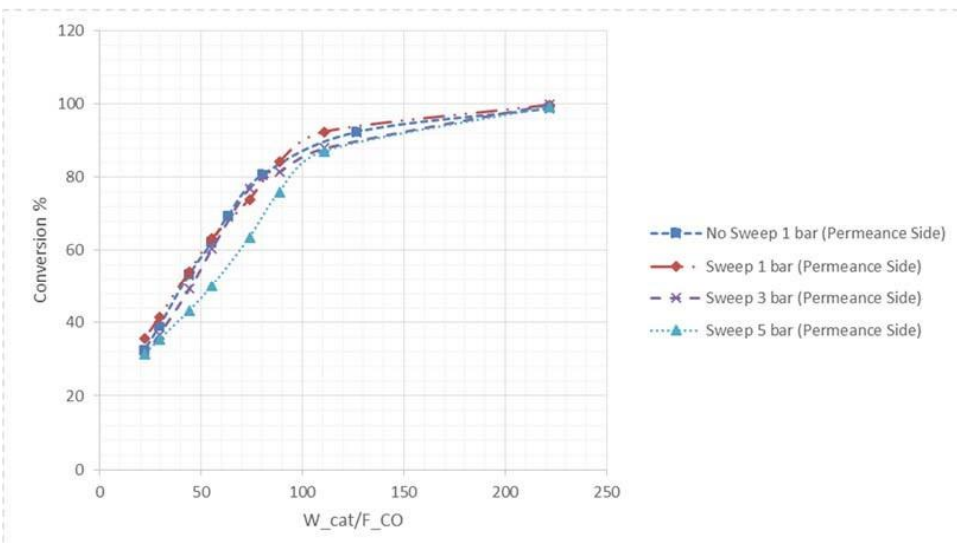

Figure 5.1. CO Conversion vs. W_{cat}/F_{CO}

Figures 5.1-5.3 illustrate the MR outlet CO conversion, H_2 recovery, and H_2O/CO outlet molar ratio as a function of W_{cat}/F_{CO}. Simulations were performed for no-sweep (permeation zone pressure 1 bar) and steam sweep (permeation zone pressure at 1 bar, 3 bar and 5 bar) conditions in the permeation zone. The sweep pressure conditions seem to have little influence on CO conversion, while H_2 recovery is shown to decrease with increasing permeation zone pressure.

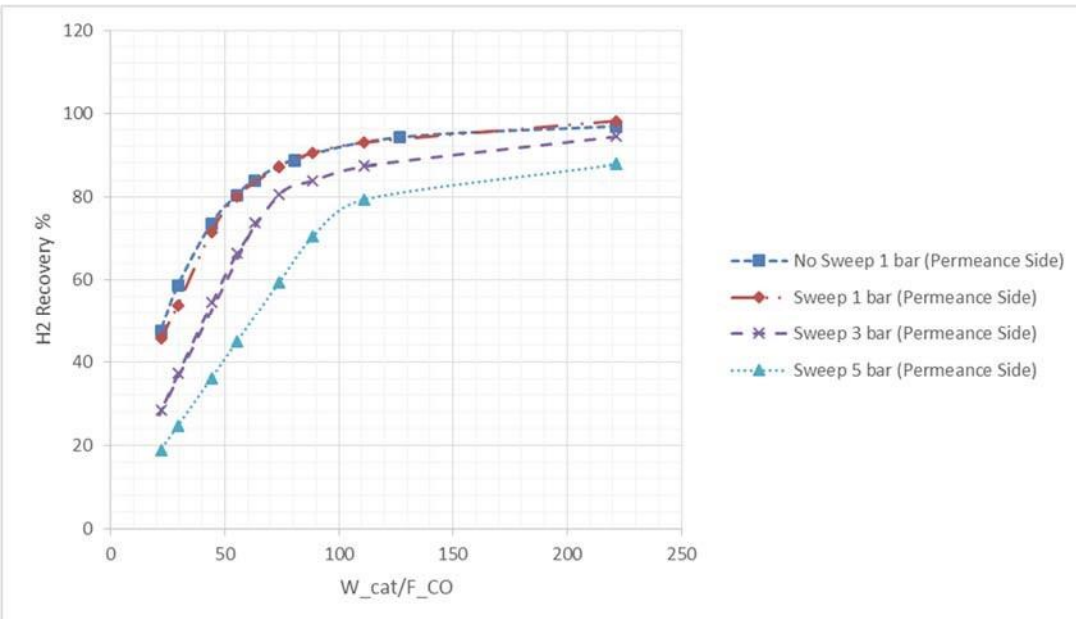

Figure 5.2. H_2 recovery vs. W_{cat}/F_{CO}

As shown in Fig. 5.3, the H_2O/CO outlet molar ratios are less than 1 for conditions of no-sweep (permeation zone pressure 1 bar), and H_2O sweep (1 bar), while they stay above 1 and 3 at 3 bar and 5 bar, respectively. This phenomenon occurs because of the H_2O permeation through the membrane. Molar flow rates (total, retentate and permeate) are shown in Fig. 5.4 as a function of W_{cat}/F_{CO}. The MR inlet and outlet total molar flow rates are practically identical, thus confirming the accuracy of the simulation. Figure 5.5 illustrates the retentate and permeate outlet species mole fractions as a function of W_{cat}/F_{CO}.

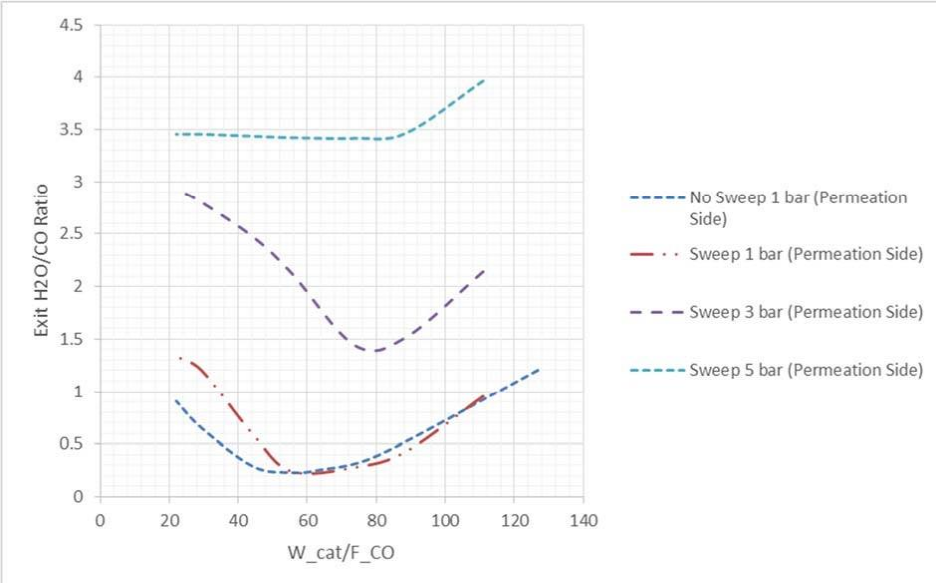

Figure 5.3. MR exit H_2O/CO ratio vs. W_{cat}/F_{CO}

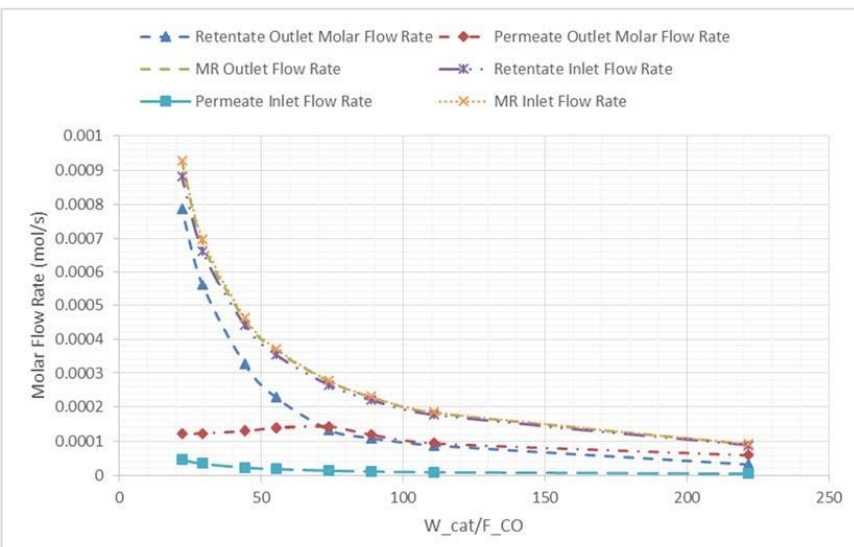

Figure 5.4. MR total molar flow rates vs. W_{cat}/F_{CO}

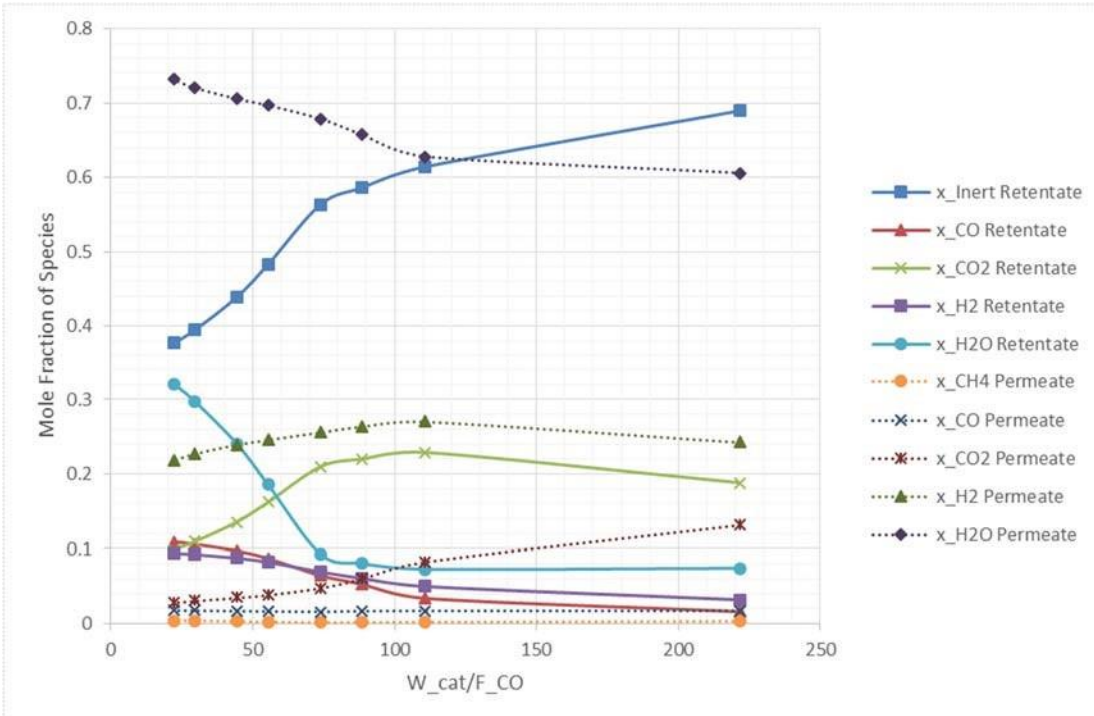

Figure 5.5. MR outlet species mole fractions vs. W_{cat}/F_{CO}

Having identified above an MR permeation zone pressure of 3 bar as a promising operating condition, we next carried-out AR simulation studies using the corresponding MR retentate outlet as an AR inlet during the adsorption part of the AR operation. Defining as switch time, the longest time of AR adsorptive operation for which the CO outlet mole fraction is practically zero, allows illustration of the switch time in Fig. 5.6, for various inlet W_{cat}/F_{CO} ratios (with H_2O sweep agent and 3 bar permeation zone pressure). The range for the switch time is between 140-495 s for the range (22-221) of W_{cat}/F_{CO}. Figure 5.7 illustrates the CO_2 loading (q_{CO2}) axial profiles along the AR for four different adsorption/desorption switch times (100 s, 150 s, 190 s and 200 s), and for the MR conditions of W_{cat}/F_{CO} =55, H_2O sweep agent and permeation zone pressure=3 bar. In Fig. 5.7, the [0, 1] and [1, 2] x-axis intervals illustrate AR CO_2 loading axial profiles during the adsorption/desorption parts of the AR's 1st operating cycle for the four aforementioned switch times (100 s, 150 s, 190 s, 200 s). Correspondingly, [2, 3] and [3, 4] represent the 2nd cycle; [4, 5] and [5, 6] the 3rd cycle; [6, 7] and [7, 8] the 4th cycle and [8, 9] and [9, 10] the 5th cycle. As can be seen in Fig 5.7, the AR attains its long-term behavior by the fourth cycle, for switch times of

100 s, 150 s, 190 s, and 200 s. In other words, the AR axial profiles of adsorbed CO_2 at the end of the adsorption and desorption parts of each cycle are no longer changing after the fourth cycle, irrespective of whether the cycle lasts 100 s or 200 s. The differences of the adsorbed CO_2 profile integrals, at the end of the adsorption and desorption parts of each cycle, represent the net amount of CO_2 released by the AR during that adsorption/desorption cycle.

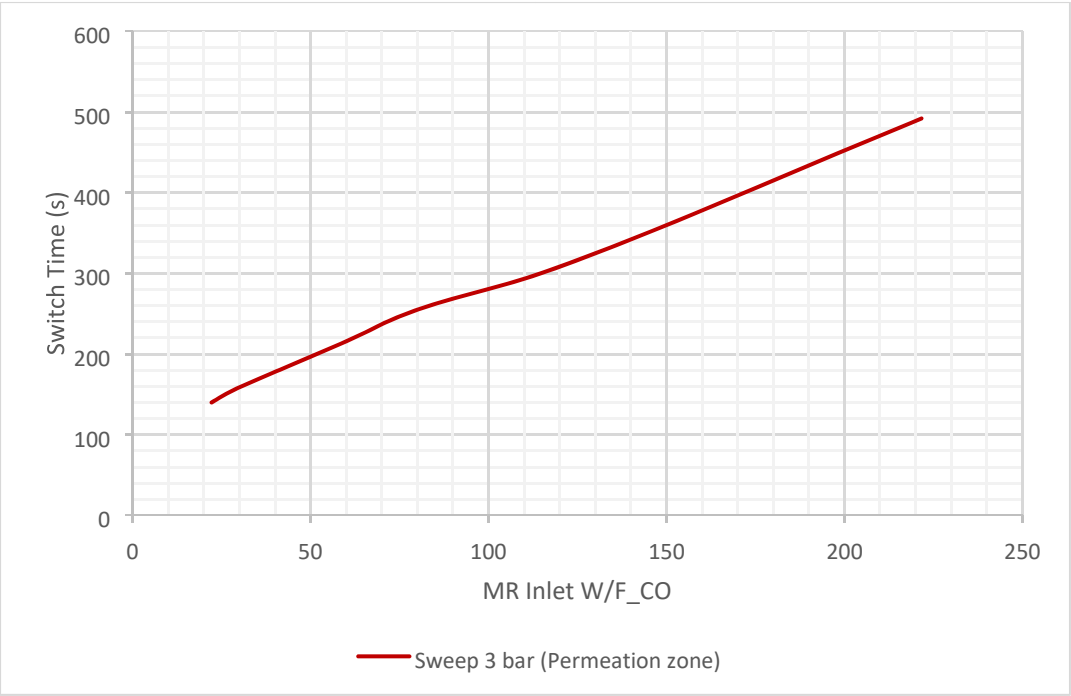

Figure 5.6. Switch time vs. W_{cat}/F_{CO}

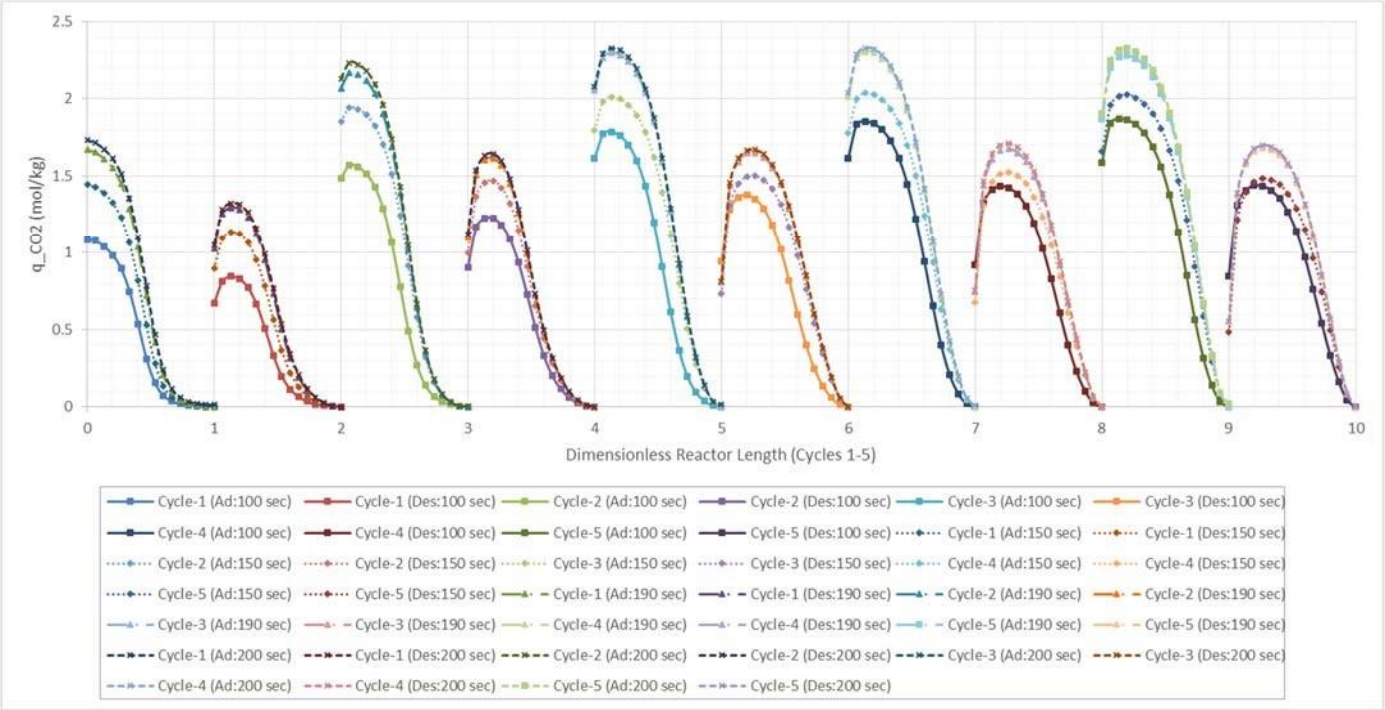

Figure 5.7. AR CO_2 loading axial profiles for 4 switch times and 5 operating cycles

Further, the model's power and flexibility were demonstrated by carrying-out numerical simulations for both the packed-bed and membrane reactors for various inlet operating conditions (pressure/temperature/composition/flow rate) and design parameters (catalyst amount, membrane area, permeability and catalyst pellet size). It was shown that significant variation of the catalyst pellets' effectiveness factor occurs along the MR axial direction, and that catalyst pellets of the same diameter exhibit different effectiveness factors within the PBR and MR. Most studies in the membrane reactor literature, on the simulation of water-gas shift reaction applications in MR's, assume a constant effectiveness factor along the reactor. Our multi-scale model is not restricted by this limiting assumption, and can thus be used to assess the behavior of PBR and MR with catalyst pellet sizes ranging from the lab scale to the industrial scale.

The species i effectiveness factor is given by the ratio of the net mass flow of i at the pellet's surface, over the mass generation rate of the same species, if all catalyst material was completely exposed to the conditions at the pellet's surface. Figure 5.8 represents the axial profile for the species' effectiveness factor for the PBR and MR, respectively. All the species' effectiveness

factors are equal to each other throughout the reactor, for both the PBR and the MR. All the species' effectiveness factors show some axial variability for all pellet sizes along the PBR, while the effectiveness factor exhibits a significant drop (min 0.9974 / max 0.9988 → min 0.655 / max 0.77) in transition from lab-scale to the industrial-scale pellet sizes (pellet diameter 0.06 cm →1 cm). However, switching from PBR to MR conditions leads to a different effectiveness factor behavior, both in terms of axial profile variation, and variation over different pellet sizes. In contrast to the behavior in a PBR, all the species' effectiveness factors show significant decline along the MR axial direction, for all pellet sizes. Another interesting feature is that the species' effectiveness factor shows some increase for the lab-scale pellet sizes (diameter 0.06 cm →0.3 cm, effectiveness factor 0.7 → 0.775), while the species' effectiveness factor exhibits a significant drop for the industrial-scale pellet sizes (diameter 0.3 cm →1 cm, effectiveness factor 0.775 → 0.53).

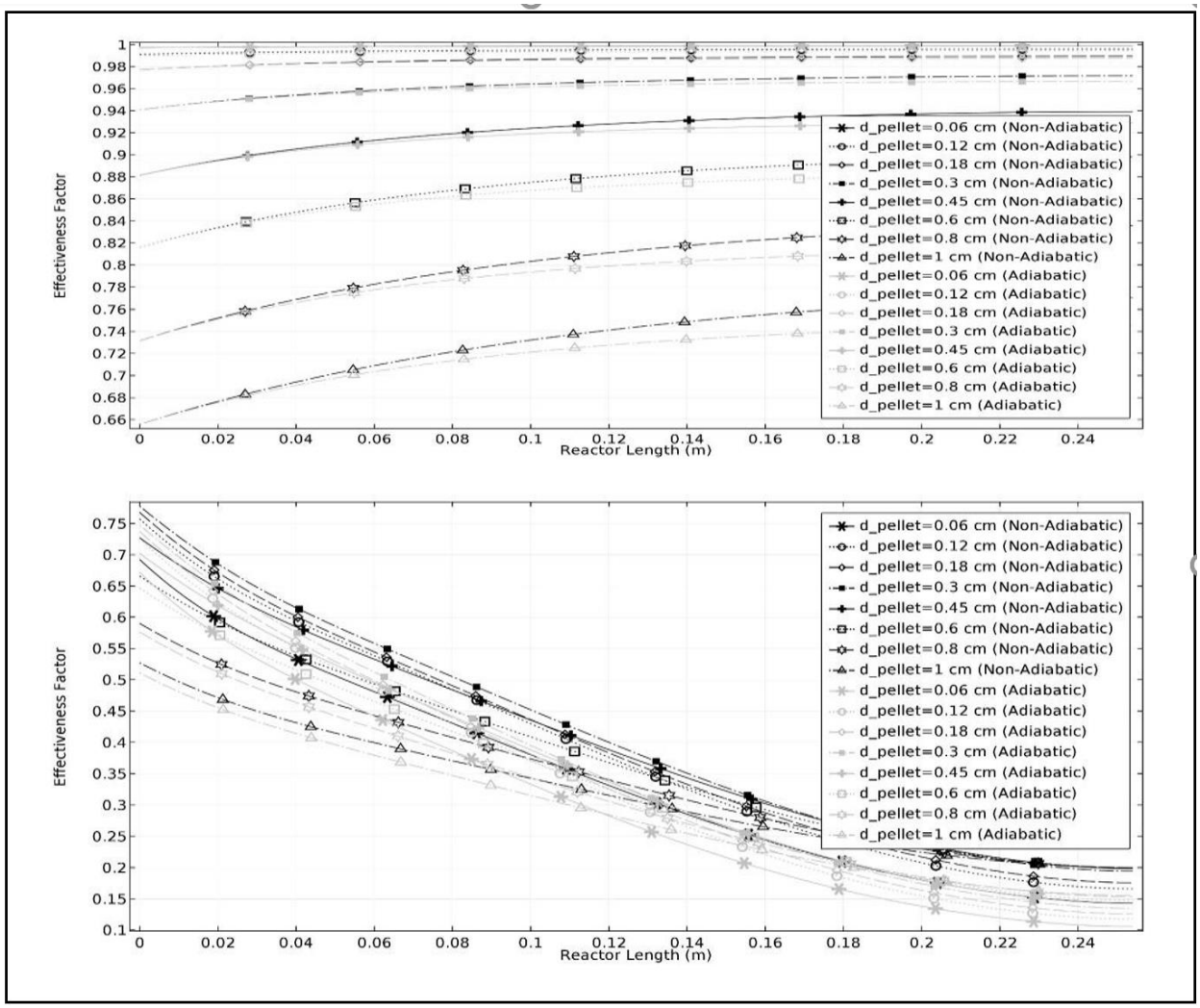

Figure 5.8. Effectiveness factor axial profiles for various pellet sizes (Conventional PBR-Up and MR-Down)

Subsequently, simulations of the combined membrane reactor (MR)-adsorptive reactor (AR) system were performed, using our multi-scale, steady-state model for the MR, and our dynamic AR model. Simulated coal-derived syngas with composition (H_2:CO:CO_2:N_2:CH_4:H_2S:H_2O=0.51:1.00:0.36:2.28:0.1:0.0031:2.8) was fed to the feed (retentate) side of the MR. W_{cat}/F_{CO} values in the MR were varied within a range of 22-221 g_{cat}*h/mol-CO by changing the MR inlet flow rate, while the AR was considered to operate at a temperature of 250ºC and a pressure of 25 bar. In this series of simulations, 10 g of catalyst was utilized in both the MR and the AR, while 69 g of hydrotalcite adsorbent was used for the AR simulations. In the simulations, the membrane permeances were as follows ($m^3/(m^2.h.bar)$): H_2=1.54; CO=0.0028;

CO_2=0.044; CH_4=0.014, H_2O=0.5133. For pellet diameters used at the industrial scale, appreciable temporal and axial variations of the catalyst/adsorbent pellet effectiveness factors in the AR are demonstrated, as shown in the Figures below.

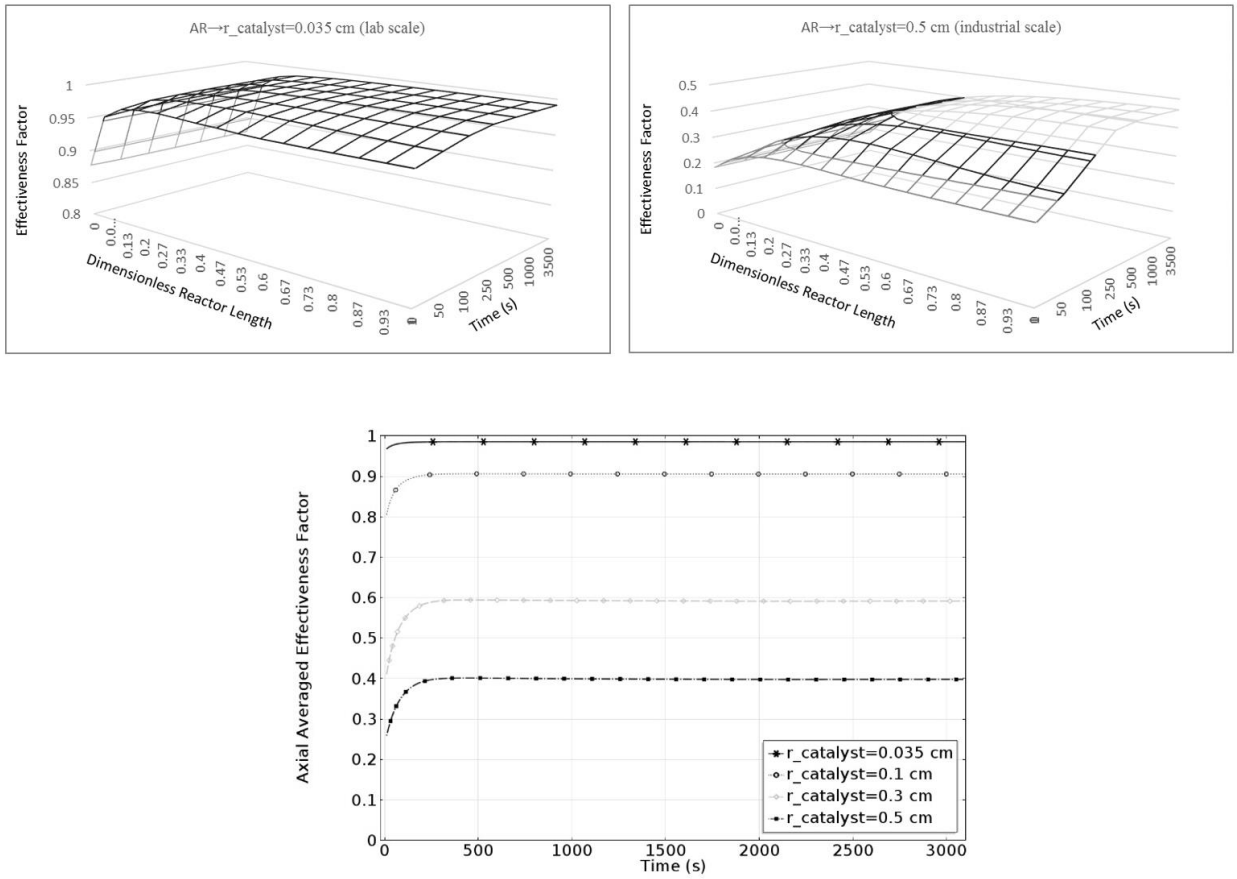

Figure 5.9. Catalyst-pellet effectiveness factor AR axial profiles for various pellet sizes (523 K, 25 bar and W_{cat}/F_{CO}=88 g*h/mol)

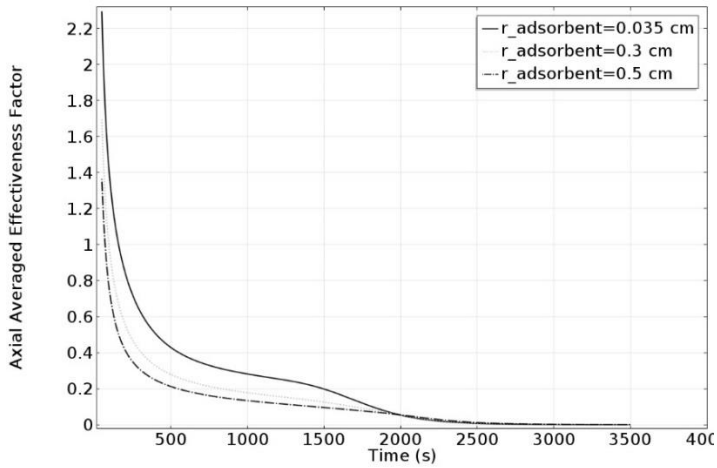

Figure 5.10. Adsorbent-pellet effectiveness factor AR axial profiles for various pellet sizes (523 K, 25 bar and W_{cat}/F_{CO}=88 g*h/mol)

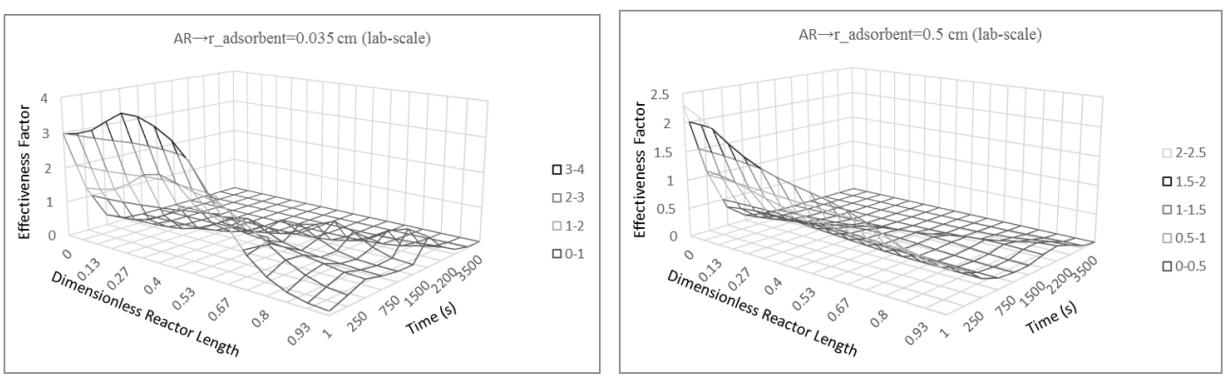

Figure 5.11. Adsorbent-pellet local effectiveness factor AR axial-temporal profiles for various pellet sizes (523 K, 25 bar and W_{cat}/F_{CO}=88 g*h/mol)

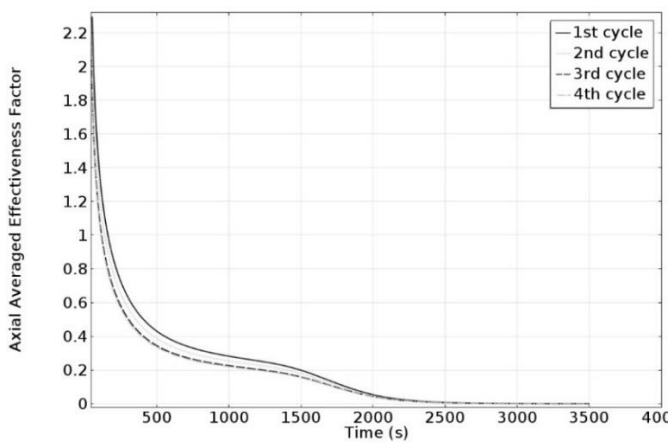

Figure 5.12. Adsorbent-pellet effectiveness factor AR axial profiles for various cycles (523 K, 25 bar and W_{cat}/F_{CO}=88 g*h/mol)

One of this study's key aspects focuses on the evaluation of catalyst/adsorbent pellet effectiveness factors in the AR, using the developed multi-scale model, thus assessing the behavioral and quantitative changes brought about while transitioning from lab-scale to industrial-scale pellet sizes. The effectiveness factor for species i is given by the ratio of the net mass flow of species i at the pellet's surface, over the mass generation (destruction) rate of the same species, if all catalyst material was completely exposed to the conditions at the pellet's surface. Since there is only one reaction taking place in the reactor (the water gas shift reaction) with equal stoichiometric coefficients for all species, the effectiveness factor is the same for all species. In addition, the dynamic nature of the AR process suggests that the net i_{th} species mass flow at the pellet's surface accommodates not only the reaction occurring in the catalyst pellet or the adsorption occurring in the adsorbent pellet, but also helps meet the i_{th} species' accumulation needs within the pellet's pores. This suggests that early in the AR's operation, when the accumulation needs are the largest, the values of the effectiveness factor can be greater than one. Figure 5.9 illustrates the catalyst pellet's effectiveness factor axial profile for the AR, which exhibits an appreciable decline as the pellet size increases (for pellet diameter 0.07 cm the effectiveness factor varies from a min of 0.87 to a max of 0.995; for pellet diameter 1.00 cm the effectiveness factor varies from a min of 0.18 to a max of 0.48 respectively). Figure 5.10 illustrates the adsorbent pellet's axially-averaged effectiveness factor temporal profile for the AR. For times up to ~2000

s, the adsorbent axial-averaged effectiveness factor decreases while the adsorbent pellet size increases. After 2000 s, the effectiveness factors for the various pellet sizes become equal and approach zero, indicating that the adsorbent pellets are nearing their full capacity. Changing adsorbent pellet size from lab-scale to industrial-scale leads to average effectiveness factor declines of approximately 30%. Figure 5.11 shows the local effectiveness factor behavior of the adsorbent pellet along the AR at various operating times. At small operating times, and in the first 30% of the reactor's length, an effectiveness factor above 3 and 1.5 for the pellet sizes 0.035 and 0.5 cm, respectively, is observed, indicating that a significant part of the incoming flux is for accumulation purposes. The effectiveness factor values trend downwards at larger operating times, as the adsorbent pellets in the AR begin to saturate. The effectiveness factor values are also small at longer reactor lengths, even at small operating times, as CO_2 is scarce at these lengths and times, due to its adsorption at short AR lengths. In application, the AR operates in a cyclical nature; therefore, Figure 5.12 demonstrates the adsorbent pellet's axially-averaged effectiveness factor for various operating cycles. It can be seen that for a given cycling time, the adsorbent pellet's effectiveness factor reaches its long-term behavior within about four cycles.

5.2 Experimental Data Validation

To experimentally validate our models, we carried out the combined MR-AR simulations using simulated coal-derived syngas with composition (H_2:CO:CO_2:Ar:CH_4:H_2S= 0.51:1.00:0.36:2.28:0.1:0.0031), W_{cat}/F_{CO} values of 55 and 66 g_{cat}*h/mol-CO for the MR feed, as well as a H_2O/CO ratio of 1.1. The combined MR-AR simulations were performed at a temperature of 250ºC and a pressure of 15 bar. In the simulations, the membrane permeances are taken as ($m^3/(m^2.h.bar)$): H_2=1.39; CO=0.0032; CO_2=0.051; CH_4=0.033, H_2O=1.1. AR performance (H_2/Ar, and CO/Ar, and CO_2/Ar molar ratios) for the combined MR-AR system are illustrated in Figs. 5.13-5.15, and are shown to be consistent with experimental results. Additional examples of the model fits of the experimental behavior of the individual MR and AR subsystems can be found in Sect. 4, in the BP1 Continuation Application document, and in the various RPPR's.

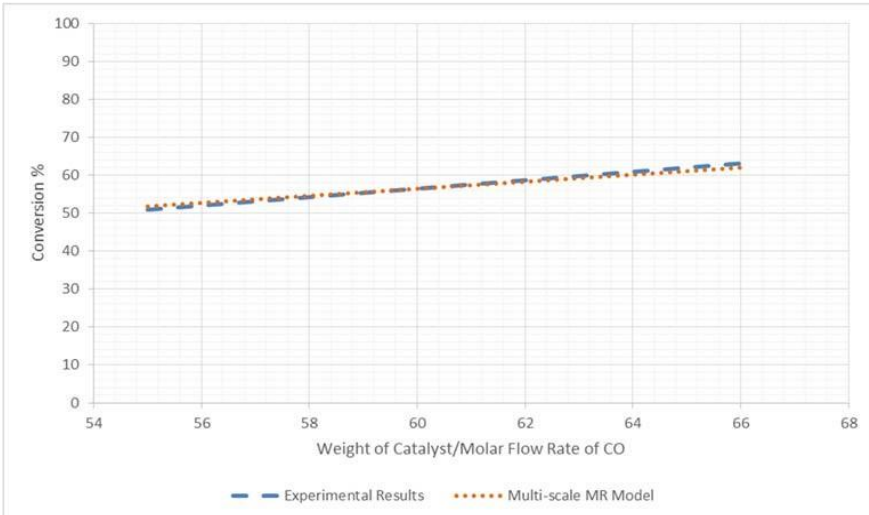

Figure 5.13. MR experimental vs. model results for various W_{cat}/F_{CO}

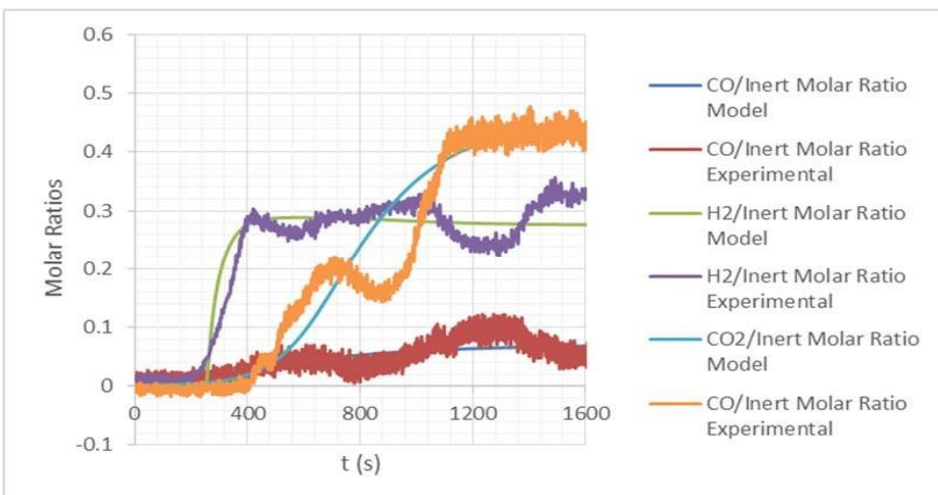

Figure 5.14. AR profiles corresponding to the MR operating with W_{cat}/F_{CO} = 55 and H_2O/CO = 1.1

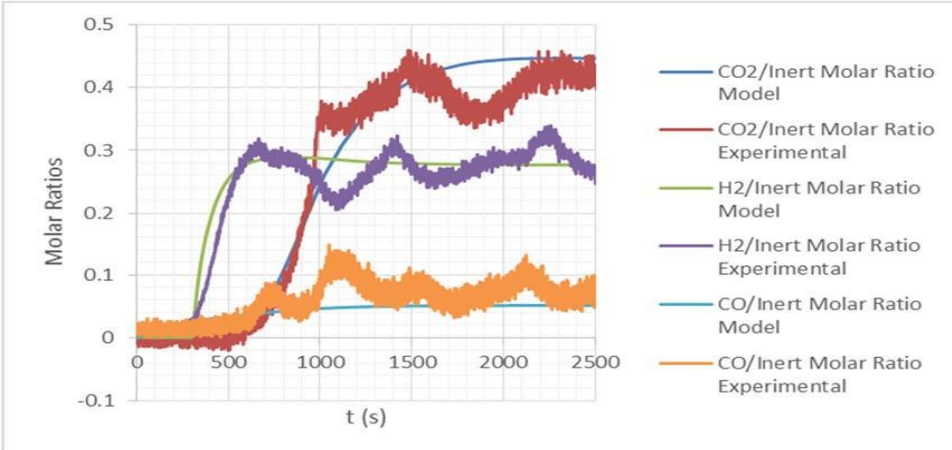

Figure 5.15.. AR profiles corresponding to the MR operating with W_{cat}/F_{CO} = 66 and H_2O/CO = 1.1

5.3 Summary and Conclusions

In this section of the report, the performance of the combined (MR-AR) system was studied using a multi-scale, steady-state model for the MR, and a multi-scale dynamic AR model. The modeling and simulations were carried out using simulated syngas with varying ranges of W_{cat}/F_{CO}. In the sequence, the MR's outlet is fed to the AR inlet. The accuracy of the simulation is ascertained by ensuring that the MR inlet and outlet total molar flow rates are identical.

The multi-scale model's power and flexibility were demonstrated by carrying-out numerical simulations for packed-bed, membrane, and adsorptive reactors for various inlet operating conditions (pressure/temperature/composition/flow rate) and design parameters (catalyst amount, membrane area, permeability and catalyst pellet size). All model results have been experimentally validated as they agree with experiments.

The model simulations establish that for the MR the sweep pressure has little influence on CO conversion, while H_2 recovery decreases with increasing sweep pressure. It is also shown that a MR permeation zone sweep pressure of 3 - 5 bar keeps the H_2O/CO outlet molar ratios above 1 and 3 respectively. The AR model simulations, using the corresponding MR retentate outlet as an AR inlet during the adsorption part of the AR operation, are employed to identify the AR process switch times. For various inlet W_{cat}/F_{CO} ratios (with H_2O sweep agent and 3 bar permeation zone

pressure) the switch times were shown to range between 140-495 s for the range of 22-221 W_{cat}/F_{CO}.

The multiscale model's simulations also establish that effectiveness factors for catalyst pellets (in PBR, MR, AR environments) and for adsorbent pellets (in AR environments) can exhibit significant variations along the reactor's length. Furthermore, pellets of the same diameter exhibit different effectiveness factors at different reactor axial locations.

6.0 PRELIMINARY PROCESS DESIGN/OPTIMIZATION AND ECONOMIC EVALUATION

6.1 – Process Design/Optimization

Here we present the results of simulation-based optimization studies that have been carried-out to characterize acceptable ranges for both the operating and the design parameters, so as to meet and optimize the pre-defined process performance specifications. A simulated coal-derived syngas with composition (H_2:CO:CO_2:N_2:CH_4:H_2S:H_2O = 0.51:1.00:0.36:2.28:0.1:0.0031:1.1) was fed to the retentate side of the MR. The $W_{cat}/F_{CO,0}$ values in the MR were varied within a range of 20-95 g_{cat}*h/mol-CO by changing the MR inlet flow rate, while the MR was operated at a temperature of 250ºC and a pressure of 25 bar. In the simulations, the membrane permeances utilized were (m^3/m^2.h.bar): H_2=1; CO=0.0027; CO_2=0.0018; CH_4=0.0027, H_2O=0.333. The simulation conditions for the MR included a sweep ratio of 0.1 and permeate-side pressure of 4 bar. The MR retentate outlet (for various MR- $W_{cat}/F_{CO,0}$ values) was then fed into the AR inlet for adsorption operation. Similarly, the $W_{cat}/F_{CO,0}$ values were varied within a range of 50-200 g_{cat}*h/mol-CO by changing the AR inlet flow rate. The AR operating conditions are a temperature of 250ºC and a pressure of 25 bar, and simulations are repeated for the various AR-W_{ad} (amount of adsorbent)/W_{cat} (amount of catalyst) values by changing the amount of adsorbent.

The AR requires dynamic operation, since the adsorbent's capacity is not limitless, and adsorbent regeneration is eventually required. Thus, two times are defined in regard to the AR's reaction/adsorption operation: (1) the minimum time of operation, which is defined as the time that CO_2 is first detected at the reactor exit, and (2) the maximum time of operation , which is the time for which the corresponding time-averaged mass flow rate of carbon exiting the AR during the entire reaction/adsorption phase (plus carbon lost through membrane) up to that point reaches 10% (a target carbon capture rate for this project) of the constant mass flow rate of carbon entering the AR during the same period. Essentially, defining the minimum and maximum operating times creates the AR operating flexibility of sifting between 100-90 % CO_2 capture rate.

The cyclical nature of an AR's operation, suggests that the time for which the AR operates in the reaction/adsorption mode is of great significance for the AR process economics, flexibility and safety. It is, therefore, important to know the AR's minimum and maximum operating times.

Figure 6.1 illustrates that the minimum and maximum AR operating times are increasing functions of AR $W_{cat}/F_{CO,0}$, for various AR inlets, each of which is obtained for a different MR W_{cat}/F_{CO} ratio. The minimum (maximum) time increases from about 200 s (300 s) for MR W_{cat}/F_{CO} = 80 and AR W_{cat}/F_{CO} = 50, to about 1500 s (2000 s) for MR W_{cat}/F_{CO} = 20 and AR W_{cat}/F_{CO} = 200. Figure 6.1 also illustrates that the minimum and maximum AR operating times are decreasing functions of MR $W_{cat}/F_{CO,0}$, for a fixed AR W_{cat}/F_{CO} ratio. Indeed, as MR- $W_{cat}/F_{CO,0}$ increases, CO conversion at the MR exit increases, resulting in a higher CO_2 AR inlet flowrate, which then requires lower AR- $W_{cat}/F_{CO,0}$, and thus lower minimum and maximum AR operating times.

6.1.1 MR-$W_{cat}/F_{CO,0}$ and AR-$W_{cat}/F_{CO,0}$ Effect on Minimum/Maximum AR Operating Times and Corresponding Average Total Conversions:

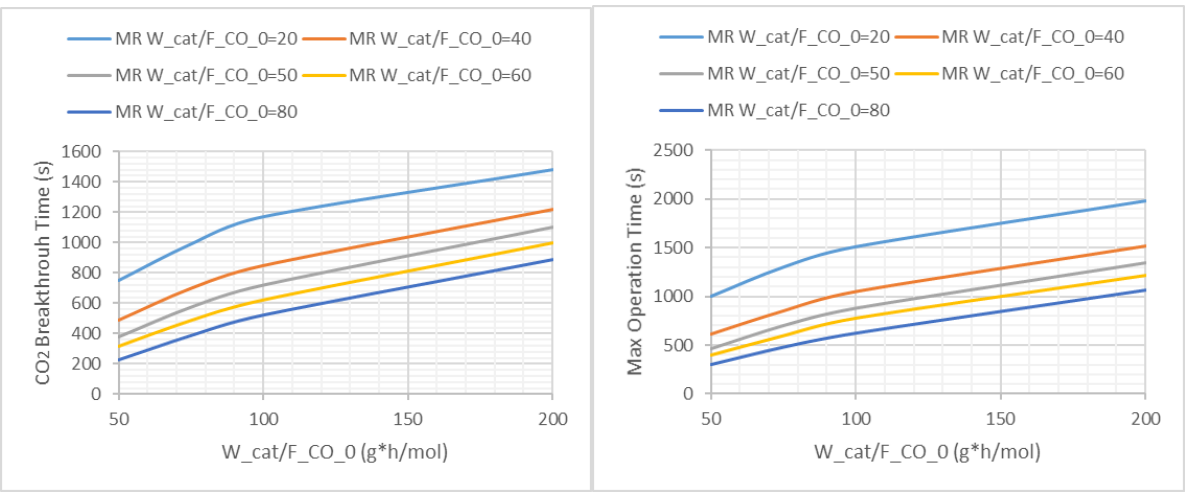

Figure 6.1. AR CO_2 breakthrough time (Left) and AR maximum operation time (Right) vs. AR-$W_{cat}/F_{CO,0}$ values for various MR exit compositions. W_{ad}/Wcat=6

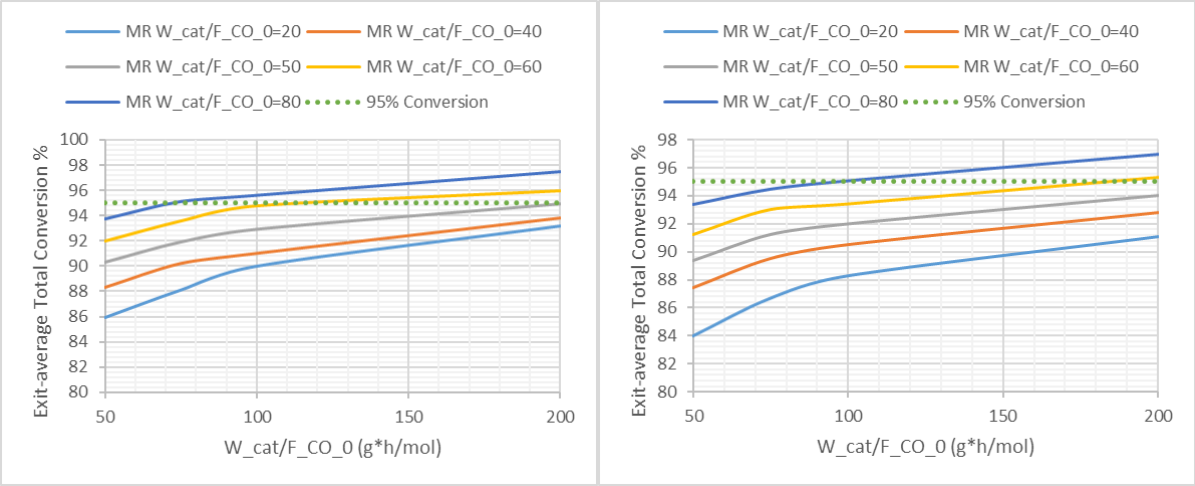

Figure 6.2. Exit-average total (MR+AR) CO conversion vs. AR- $W_{cat}/F_{CO,0}$ values for MR exit compositions. (Left- The minimum time of operation and Right- The maximum time of operation). W_{ad}/W_{cat}=6

Figure 6.2 illustrates that the total (both MR and AR) time-averaged CO conversions, over both the minimum and maximum AR operating times, are increasing functions of AR $W_{cat}/F_{CO,0}$, for various AR inlets, each of which is obtained for a different MR W_{cat}/F_{CO} ratio. One of the most important success criteria for the proposed process is obtaining at least 95% total CO conversion through the combined MR/AR system. However, as can be seen in Figure 6.2, the total min-95% CO conversion is not acquired for all cases and AR- $W_{cat}/F_{CO,0}$ values. The total conversion decreases, while the value of MR- $W_{cat}/F_{CO,0}$ decreases. The CO conversion averaged over the minimum (maximum) operating times shown in Fig. 6.2- Left (Fig. 6.2 -Right), values of 75, 110, 200 (100, 190, >200) AR- $W_{cat}/F_{CO,0}$ are needed to attain 95 % total conversion for MR- $W_{cat}/F_{CO,0}$ values of 80, 60, 50, respectively. These results suggest that 95% conversion can be attained by either running the MR at higher MR- $W_{cat}/F_{CO,0}$ values (around 70-80) with mid-range values of AR- $W_{cat}/F_{CO,0}$ (around 90-100) or running the MR at mid-range MR- $W_{cat}/F_{CO,0}$values (around 50-60) with higher values of AR- $W_{cat}/F_{CO,0}$ (above 200). Increasing the inlet H_2O/CO molar ratio would be another alternative to achieve higher total conversions. Starting the MR at higher inlet H_2O/CO molar ratios may have the following effects: (1) increasing MR conversion for lower MR- $W_{cat}/F_{CO,0}$ values, (2) decreasing permeate-side pressure (increasing H_2 recovery and CO_2 lost through membrane), (3) having higher MR outlet H_2O/CO values leads to higher average AR CO conversions, (4) and to increasing excess use of steam and decreasing production rate.

6.1.2 W_{ad}/W_{cat} Effect on Minimum/Maximum AR Operating Times and Corresponding Average Total Conversions

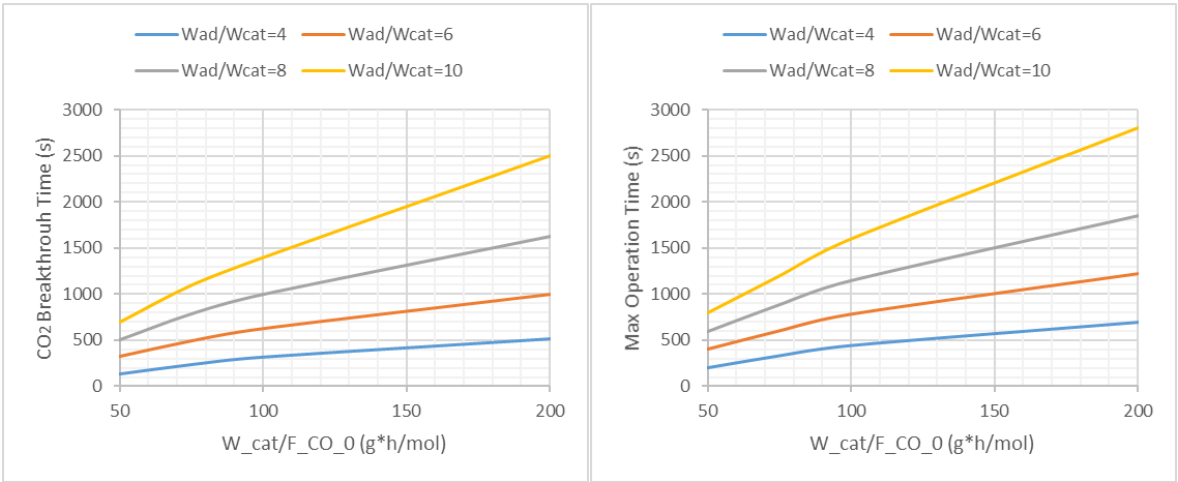

Figure 6.3. AR CO_2 breakthrough time (Left) and AR maximum operation time (Right) vs. AR-$W_{cat}/F_{CO,0}$ values for various W_{ad}/W_{cat} values. MR $W_{cat}/F_{CO,0}$ =60

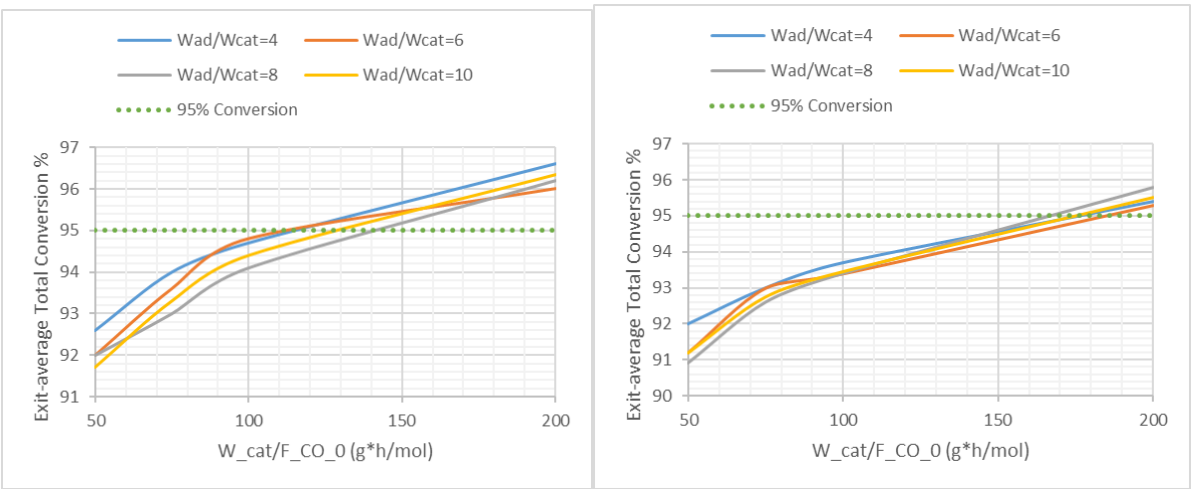

Figure 6.4. Exit-average total (MR+AR) CO conversion vs. AR- $W_{cat}/F_{CO,0}$ values for various W_{ad}/W_{cat} values. MR $W_{cat}/F_{CO,0}$ =60

The effect of W_{ad}/W_{cat} on the AR's minimum and maximum operating times and average total conversions is shown in Figs. 6.3-6.4. As expected, CO_2 breakthrough time and maximum

operating times are favored by higher W_{ad}/W_{cat} ratios. Increasing the W_{ad}/W_{cat} ratios from 4 to 10 increases the CO_2 breakthrough time from 500 s to 2500 s and the maximum operating time from 700 s to 2800 s. All these results suggest that the MR-AR system easily meets the >95% H_2, CO_2 purity, >90% CO_2 capture, and >95% CO conversions criteria, demanded for IGCC power plants. These detailed simulation results suggest that the novel MR-AR process sequence readily fulfills carbon capture system (CCS) targets on CO conversion, H_2 purity, and CO_2 capture, and therefore represents a promising pre-combustion capture alternative for IGCC power plants.

Subsequently, optimization was performed on the MR-AR combined system through a series of simulations with varying parameters, as detailed in Table 6.1 below.

	T (ºC)	**P (bar)**	**W/F (g-cat*h/mol-CO**	**H_2O/ CO Ratio**	**Sweep-Case**	**Permeance Pressure (bar)**	**Sweep Ratio**	**SF H_2O**
1	250	25	25-110	1.1	No-sweep	1	-	3
2	250	25	25-110	1.1	Sweep	1	0.1	3
3	250	25	25-110	1.1	Sweep	3	0.1	3
4	250	25	25-110	1.1	Sweep	5	0.1	3
5	250	25	25-110	1.1	Sweep	7	0.1	3
6	250	25	25-110	1.1	Sweep	1	0.5	3
7	250	25	25-110	2	Sweep	1	0.1	3
8	250	25	25-110	2	Sweep	3	0.1	3
9	250	25	25-110	2	Sweep	14	0.1	3
10	250	25	25-110	3	Sweep	1	0.1	3
11	250	25	25-110	3	Sweep	3	0.1	3
12	250	25	25-110	3	Sweep	14	0.1	3
13	250	15	25-110	3	Sweep	1	0.1	3
14	250	15	25-110	3	Sweep	8	0.1	3
15	300	25	25-110	3	Sweep	1	0.1	3
16	300	25	25-110	1.1	Sweep	1	0.1	3
17	300	15	25-110	1.1	Sweep	1	0.1	3
18	300	15	25-110	3	Sweep	1	0.1	3
19	300	15	25-110	3	No-Sweep	1	-	3
20	250	25	25-110	1.1	Sweep	1	0.2	3
21	250	25	25-110	1.1	Sweep	1	0.3	3
22	250	25	25-110	1.1	Sweep	1	0.1	2
23	250	25	25-110	1.1	Sweep	3	0.1	2
24	250	25	25-110	1.1	Sweep	8	0.1	2
25	250	25	25-110	2	Sweep	1	0.1	2
26	250	25	25-110	2	Sweep	3	0.1	2
27	250	25	25-110	2	Sweep	8	0.1	2
28	250	25	25-110	3	Sweep	1	0.1	2
29	250	25	25-110	3	Sweep	3	0.1	2

30	250	25	25-110	3	Sweep	8	0.1	2
31	250	25	25-110	1.1	Sweep	1	0.1	1
32	250	25	25-110	1.1	Sweep	3	0.1	1
33	250	25	25-110	1.1	Sweep	8	0.1	1
34	250	25	25-110	2	Sweep	1	0.1	1
35	250	25	25-110	2	Sweep	3	0.1	1
36	250	25	25-110	2	Sweep	8	0.1	1
37	250	25	25-110	3	Sweep	1	0.1	1
38	250	25	25-110	3	Sweep	3	0.1	1
39	250	25	25-110	3	Sweep	8	0.1	1

Table 6.1. MR simulation cases vs. design parameters

The results from the above simulations can be found in Figs. 6.5 – 6.8, which illustrate the MR outlet's CO conversion, H_2 recovery, H_2O/CO outlet molar ratio and CO_2 recovery as a function of W_{cat}/F_{CO}. The MR is then optimized through case elimination as follows:

<u>Case elimination steps</u>:

1) Based on the simulation results (cases 2-16, 10-15 and 13-18), the temperature (250 - 300ºC) does not appear to have a significant effect, so we can choose either 250ºC or 300ºC as the MR operating temperature.

2) Operating the reactor at higher pressures has a positive effect (cases 10-13, 16-17 and 15-18) on reactor performance. Thus, it is reasonable to select the operating pressure as high as possible (25 bar).

3) We determine the minimum (CO conversion) as 50 %. The thick green line in Fig. 6.5 shows this condition. In Fig. 6.5, the cases above this line are acceptable in terms of the minimum CO conversion criterion. When we consider all cases, it is possible to obtain min-50% and max-97% between the range of 58-110 W_{cat}/F_{CO} values, see Fig. 6.5.

4) Similar to CO conversion, we determine the minimum (H_2 recovery) as 50 %. Therefore, the range of values above the thick green line in Fig. 6.6 indicates the valid cases' zone. Approximately 30% of the cases partly/totally fail to fulfill this criterion because of high permeance pressure (7-14 bar). This effect can be seen in Fig. 6.6.

5) In our proposed system, we employ the MR's exit stream as the AR's inlet stream. Therefore, a value of 1.1 is considered as the minimum H_2O/CO molar ratio of the MR's exit stream in terms

of being able to maintain catalyst activity in the AR. In Fig. 6.7, above the green line is again the acceptable cases'zone. The MR's exit H_2O/CO molar ratio is the most decisive operating condition, since almost 50% of the cases are eliminated in this step. Low MR inlet H_2O/CO molar ratio (1.1) and permeate side pressure (1 bar) are the main reasons for this outcome. In this step, the ranges of 1.1-1.7 (MR's inlet H_2O/CO molar ratio) and no sweep-1-2 bar (permeate side pressure) are not considered an optimum range for the MR.

6) As mentioned before, the goal for the proposed process is to capture min. 90% of CO_2. Thus, a 5% CO_2 loss through the membrane is defined as the maximum in Fig. 6.8. Below the thick green line is the acceptable cases' zone for this criterion, which causes a loss of many cases.

The above suggest that cases 8, 11, and 29 are optimal when all criteria are considered, namely minimum acceptable CO conversion, minimum acceptable H_2 recovery, minimum acceptable MR exit H_2O/CO ratio, and maximum acceptable CO_2 loss through the membrane. Also, it was found that the range of (40/45-65) W_{cat}/F_{CO} values is the most suitable range for cases 8, 11, and 29 since W_{cat}/F_{CO} values below 40 and above 65 do not satisfy the determined maximum and minimum criteria of the MR unit.

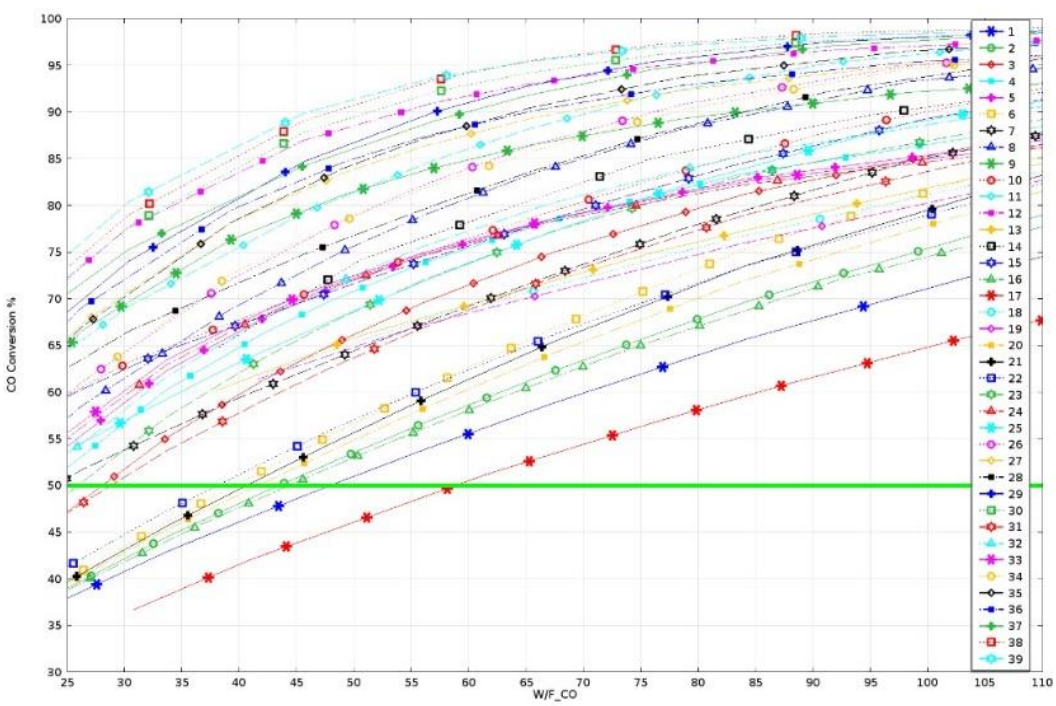

Figure 6.5. CO conversion vs. W_{cat}/F_{CO}

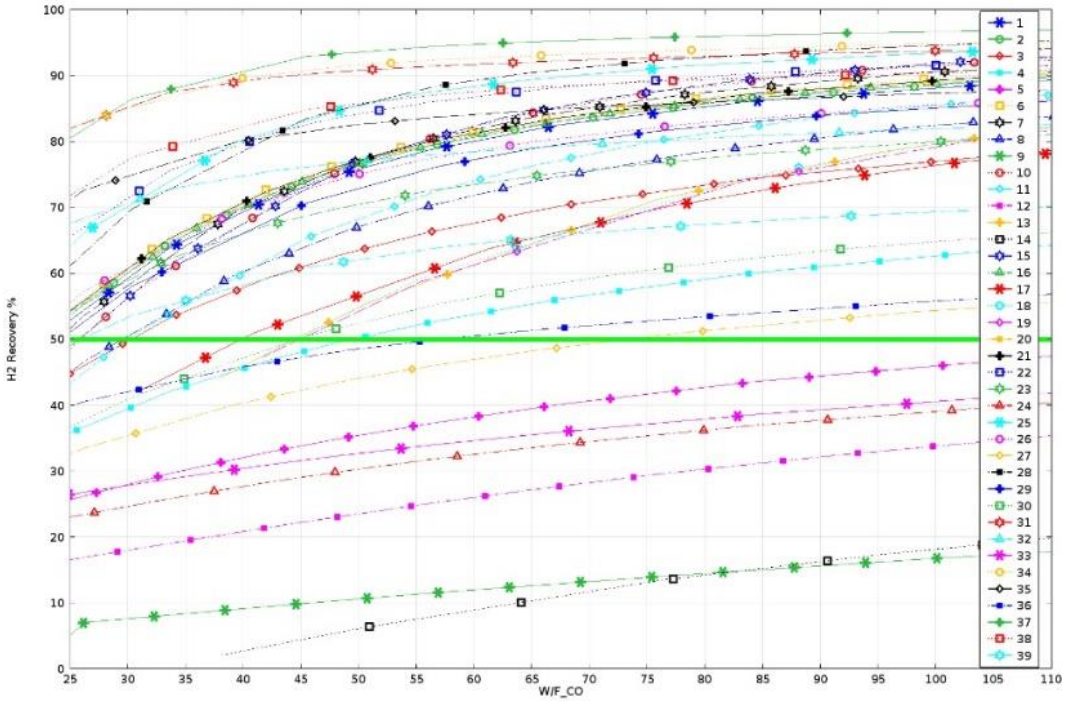

Figure 6.6. H_2 Recovery vs. W_{cat}/F_{CO}

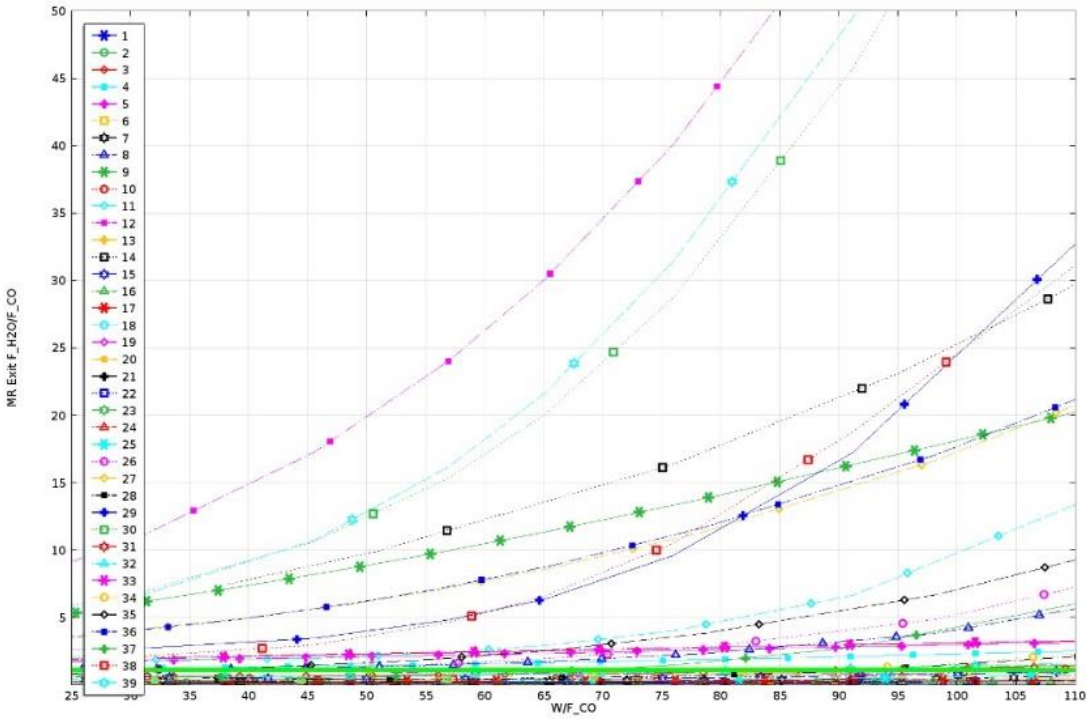

Figure 6.7. Exit H_2O/CO ratio vs. W_{cat}/F_{CO} (all cases)

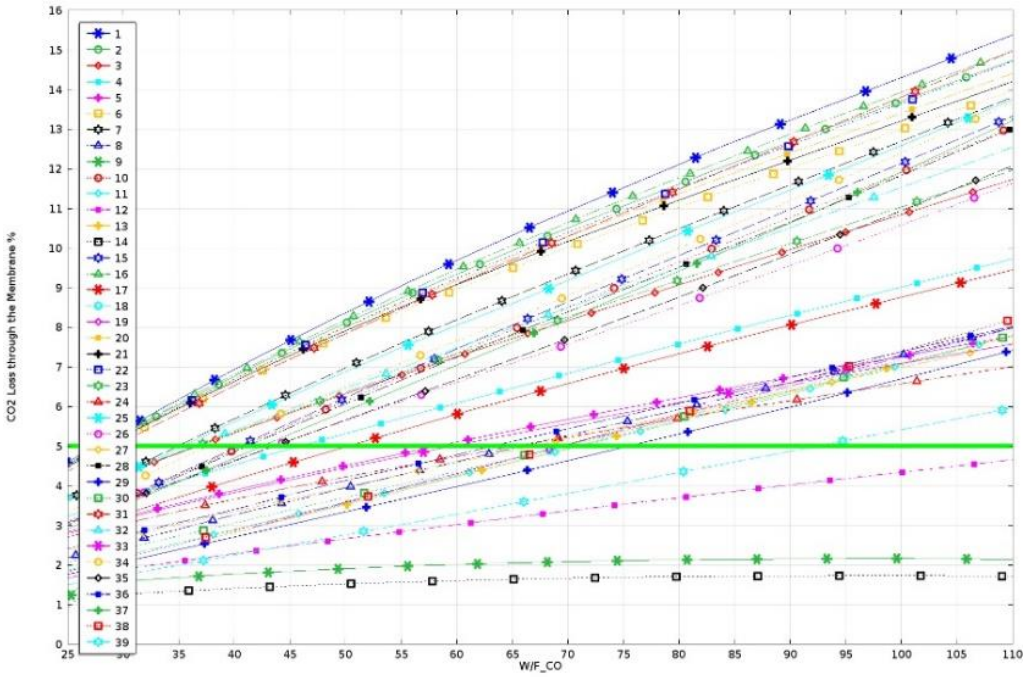

Figure 6.8. CO_2 recovery vs. W_{cat}/F_{CO}

A second set of simulations (Cases 40-55) were performed to investigate the optimal range for permeate-side pressure and sweep ratios on MR performance. Based on the simulation results, illustrated in Figs. 6.9 – 6.12, the optimal range for the permeate-side pressure was determined to be between 3-8 bar, while the optimal sweep ratios are between 0.1-0.3. Selecting MR permeation-side pressure above 8 bar causes significant reduction of H_2 recovery.

Additionally, the following other key conclusions were obtained:

1) The H_2 recovery increases 20-40 % when permeate-side pressure decreases from 8 bar to 3 bar for optimal cases 8 and 29.

2) The CO_2 lost increases 6-10 % when the permeate-side pressure decreases from 8 bar to 3 bar for optimal cases 8 and 29.

3) The H_2 recovery increases 6-9 % when the sweep ratio increases from 0.1 to 0.3 bar for the optimum cases 8 and 29.

4) The CO_2 loss increases 2-6% when the sweep ratio increases from 0.1 to 0.3 bar for the optimum cases 8 and 29.

	T (ºC)	P (bar)	W/F (g-cat*h/mol-CO	H_2O/CO Ratio	Sweep-Case	Permeance Pressure (bar)	Sweep Ratio	SF H_2O
8	250	25	25-110	2	Sweep	3	0.1	3
40	250	25	25-110	2	Sweep	4	0.1	3
41	250	25	25-110	2	Sweep	5	0.1	3
42	250	25	25-110	2	Sweep	6	0.1	3
43	250	25	25-110	2	Sweep	8	0.1	3
44	250	25	25-110	2	Sweep	10	0.1	3
45	250	25	25-110	2	Sweep	3	0.3	3
46	250	25	25-110	2	Sweep	3	0.5	3
47	250	25	25-110	2	Sweep	3	0.7	3
29	250	25	25-110	3	Sweep	3	0.1	2
48	250	25	25-110	3	Sweep	4	0.1	2
49	250	25	25-110	3	Sweep	5	0.1	2
50	250	25	25-110	3	Sweep	6	0.1	2
51	250	25	25-110	3	Sweep	8	0.1	2
52	250	25	25-110	3	Sweep	10	0.1	2
53	250	25	25-110	3	Sweep	3	0.3	2
54	250	25	25-110	3	Sweep	3	0.5	2
55	250	25	25-110	3	Sweep	3	0.7	2

Table 6.2: MR simulation cases vs. design parameters

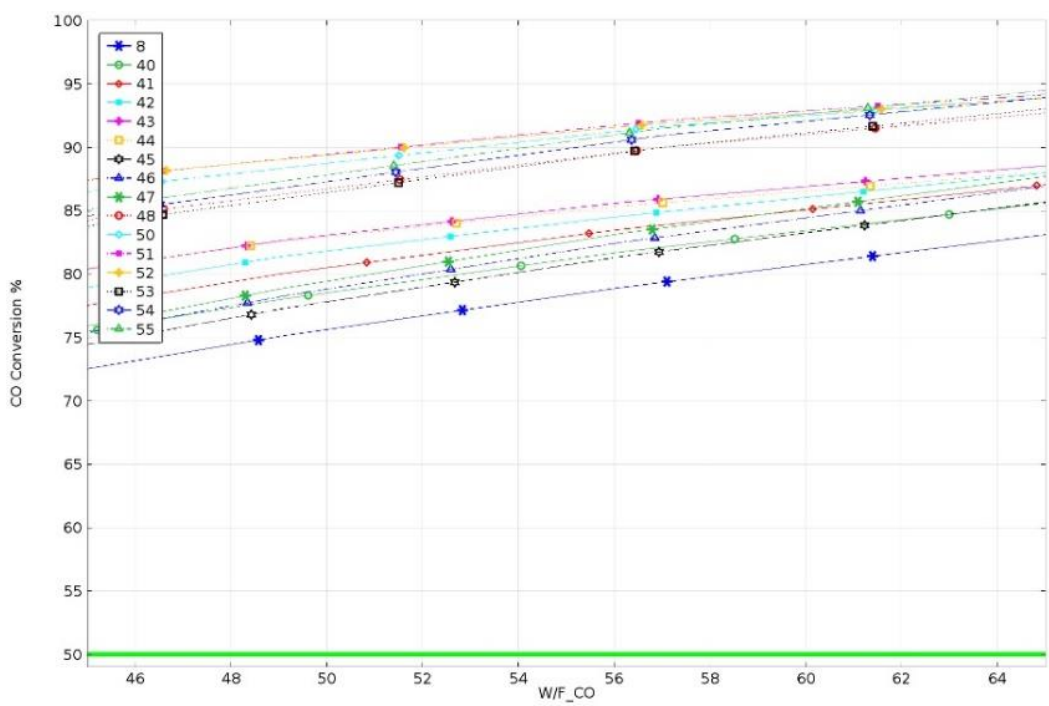

Figure 6.9. CO conversion vs. W_{cat}/F_{CO}

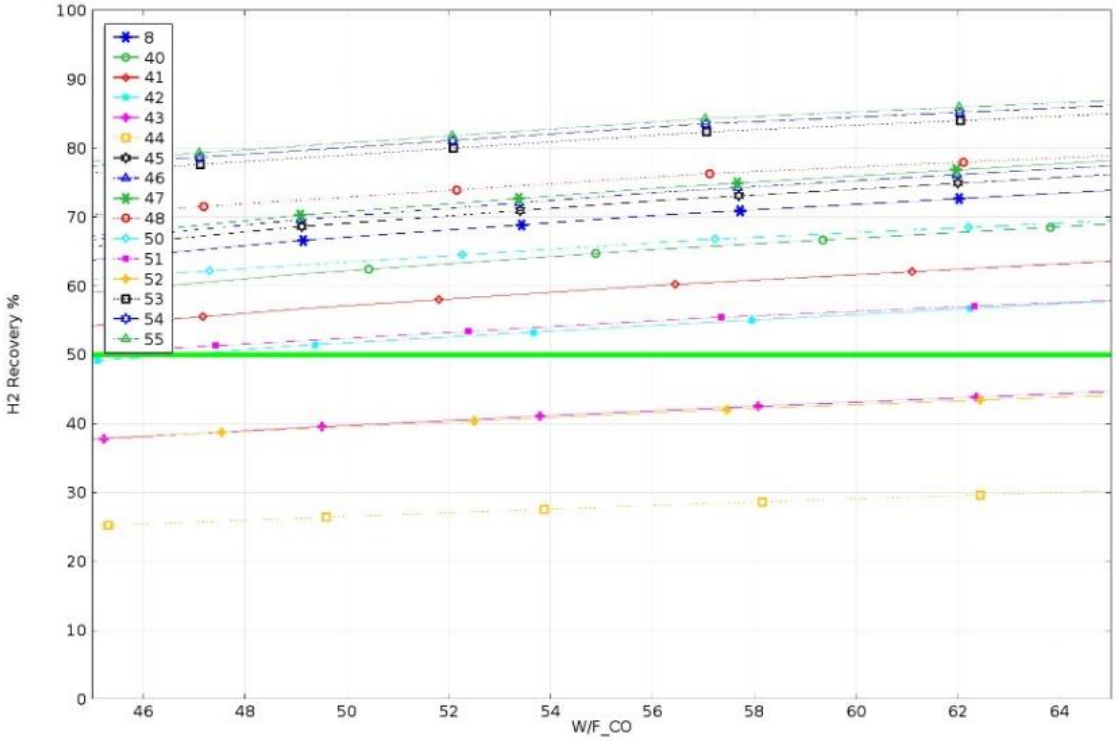

Figure 6.10. H_2 Recovery vs. W_{cat}/F_{CO}

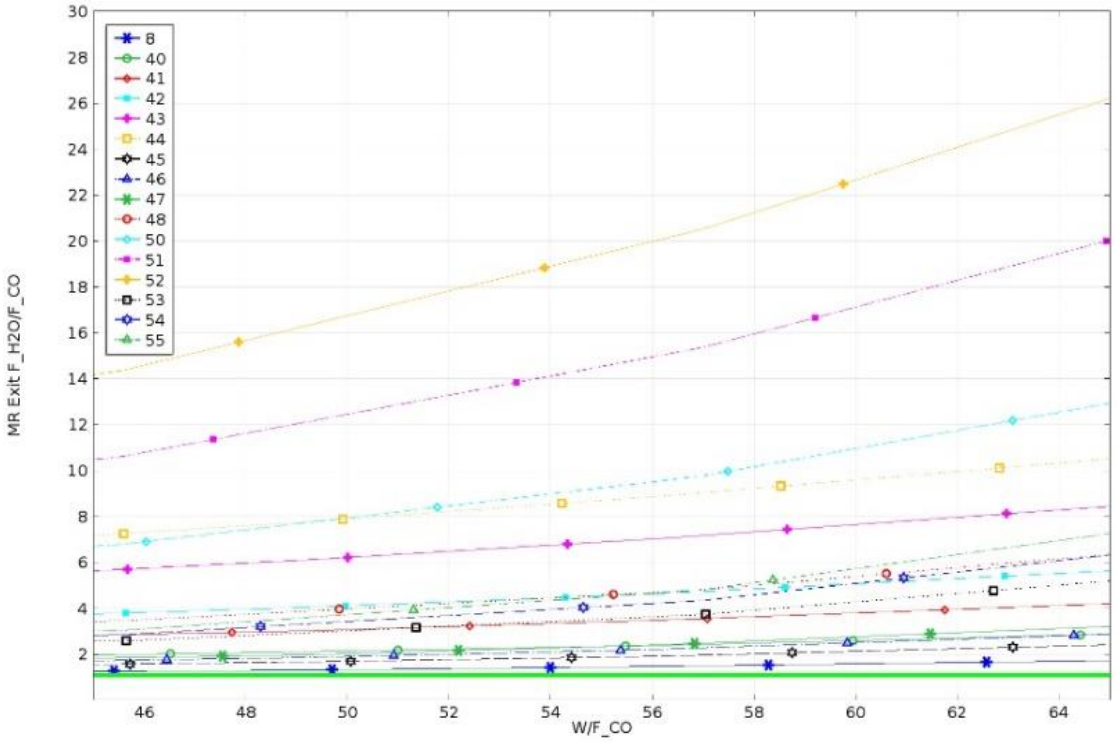

Figure 6.11 26. Exit H_2O/CO ratio vs. W_{cat}/F_{CO} (all cases)

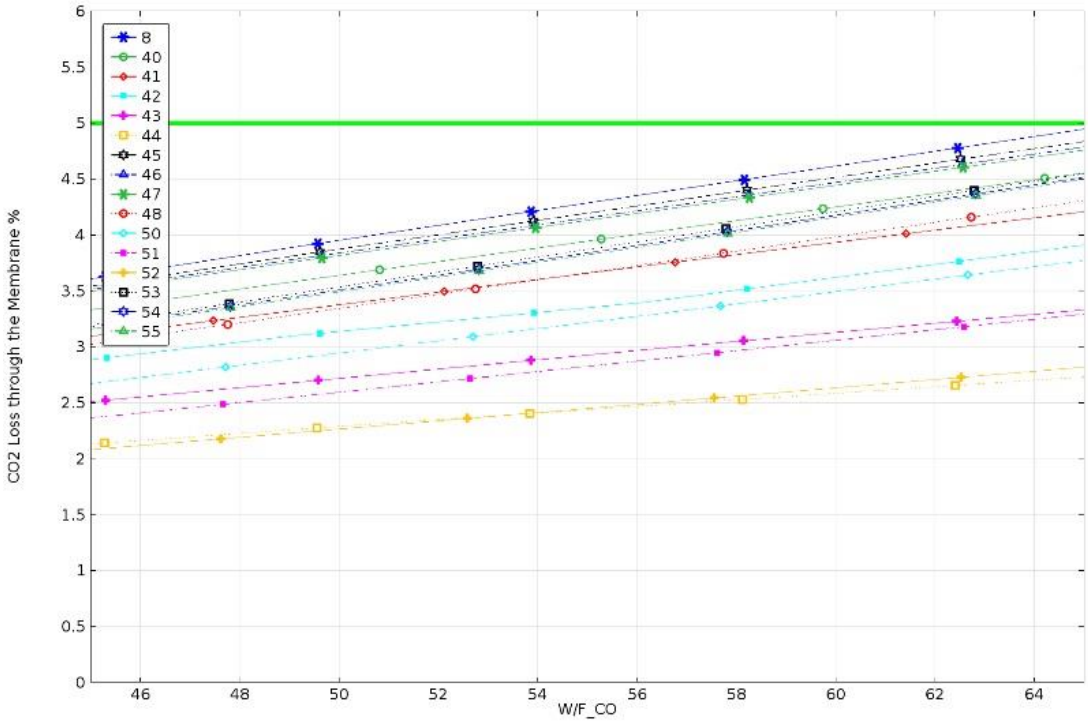

Figure 6.12. CO_2 recovery vs. W_{cat}/F_{CO}

Having identified above the most promising MR cases (8, 11 and 29), we next carried-out AR simulation studies using the corresponding MR retentate outlet as AR inlet during the adsorption part of AR operation. The switch time (time before the AR operation is changed from adsorption to desorption) is limited by the CO_2 outlet molar flow rate, which cannot exceed more than 5% of the combined system's total CO_2. Figure 6.13 illustrates the switch time for various inlet MR W_{cat}/F_{CO} ratios corresponding to case 8. The range for the switch time is between 13.5-17 min for the W_{cat}/F_{CO} range of 40-65. Due to the cyclical nature of an adsorptive reactor's operation (as discussed previously), obtaining the highest possible switch time during operation increases the process flexibility and safety. For the combined system the optimal switch time lies within a range of min-13.5 min and max-17 min for the considered range of W_{cat}/F_{CO}.

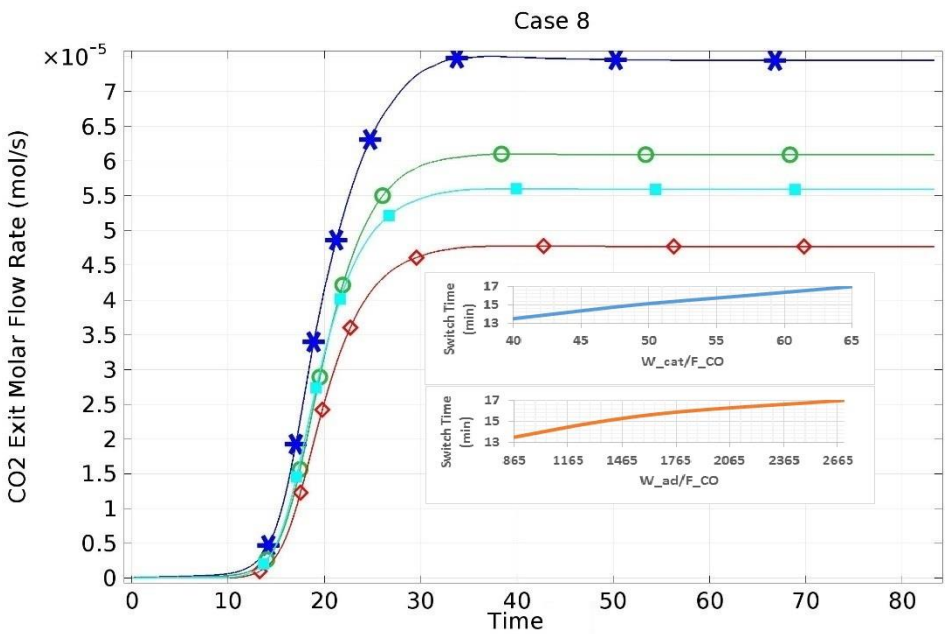

Figure 6.13. AR CO_2 switch times vs. time for various W_{cat}-W_{ad}/F_{CO}

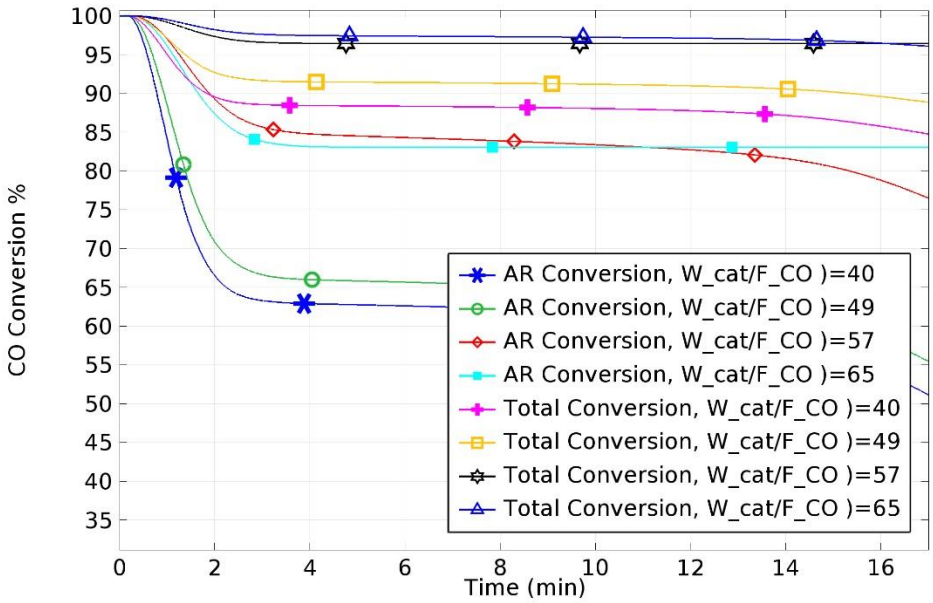

Figure 6.14. CO conversion vs. time for various W_{cat}-W_{ad}/F_{CO}

Figure 6.14 illustrates the total (MR followed by AR) and AR CO conversions for various inlet MR W_{cat}/F_{CO} ratios for case 8. When changing the value W_{cat}/F_{CO}, the catalyst amount is kept constant, while the inlet syngas velocity is modified. The velocity is a key operational parameter in the AR process. Reducing the inlet syngas velocity results in a decrease in CO conversion, and

AR switch time. As was previously mentioned, one of the most important success criteria for the proposed process is obtaining total min-95% CO conversion through the combined MR/AR system. Looking back to the MR studies, we have defined that the range of W_{cat}/F_{CO} values (40/45-65) as the most suitable range. However, as can be seen in Fig. 6.14, the total min-95% CO conversion is not acquired for this entire range. The total conversion decreases from 97% to 88%, while the value of W_{cat}/F_{CO} decreases from 65 to 40. Thus, it is necessary to narrow this W_{cat}/F_{CO} range to 55-65 to meet min-95% CO conversion.

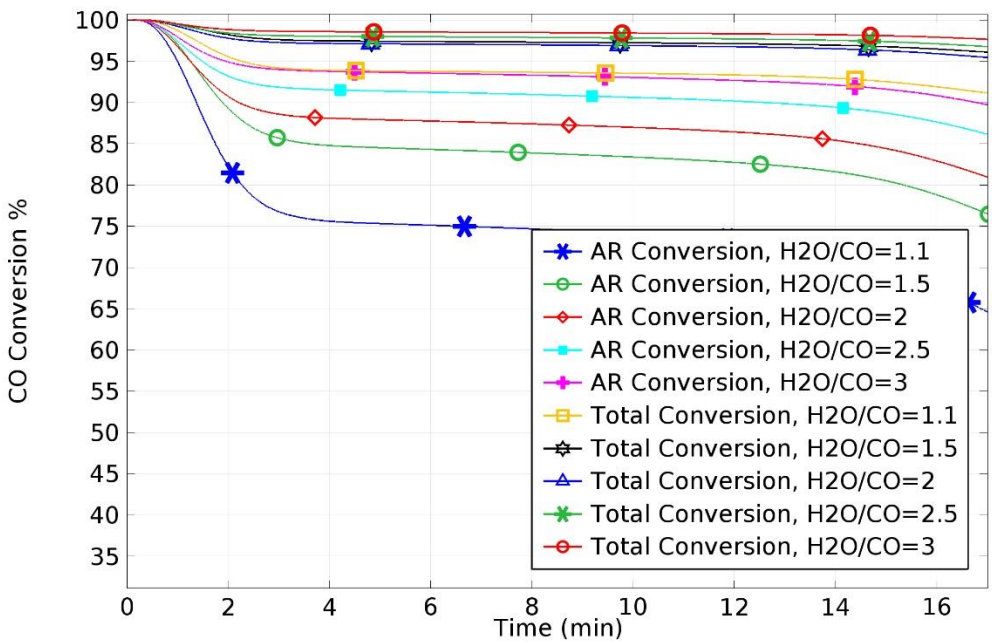

Figure 6.15. CO Conversion vs. time for various H_2O/CO ratios

The effect of the inlet AR H_2O/CO molar flow ratios on CO conversion is shown in Fig. 6.15. CO conversion and CO_2 breakthrough time are favored with higher H_2O/CO ratios. Increasing the H_2O/CO ratios from 1.1 to 3 improves the total CO conversion from 92 to 98%. The study of various H_2O/CO ratios suggests that the value of 1.4 as a minimum H_2O/CO ratio is required to reach the operating goal of min-95% CO conversion. However, when we consider all success criteria, analyzing the MR and AR simultaneously demonstrates that the range of 1.8-3 (inlet MR H_2O/CO molar flow ratios) fulfills all success criteria. In summary, feeding the MR with 1.8-3 H_2O/CO molar flow ratios and ensuring min-1.4 H_2O/CO molar flow ratios at the AR inlet

are suggested. Although cases 8, 11 and 29 fulfill these conditions, intermediate (after MR exit or before AR inlet) water can be added to the system in case a min-1.4 H_2O/CO molar flow ratios at the AR inlet is not reached.

6.2 TEA Analysis

A preliminary TEA was carried out, of the combined MR-AR system implemented into an IGCC plant, as depicted in Fig. 6.16 below. The inlet to the combined MR-AR system was 29,284 kmol/hr, with mole fractions of 0.2823, 0.1089, 0.3190, 0.2689 of CO, CO_2, H_2O, H_2 respectively, while the remaining 0.0209 mole fraction corresponded to a mixture of inert species (including CH_4).

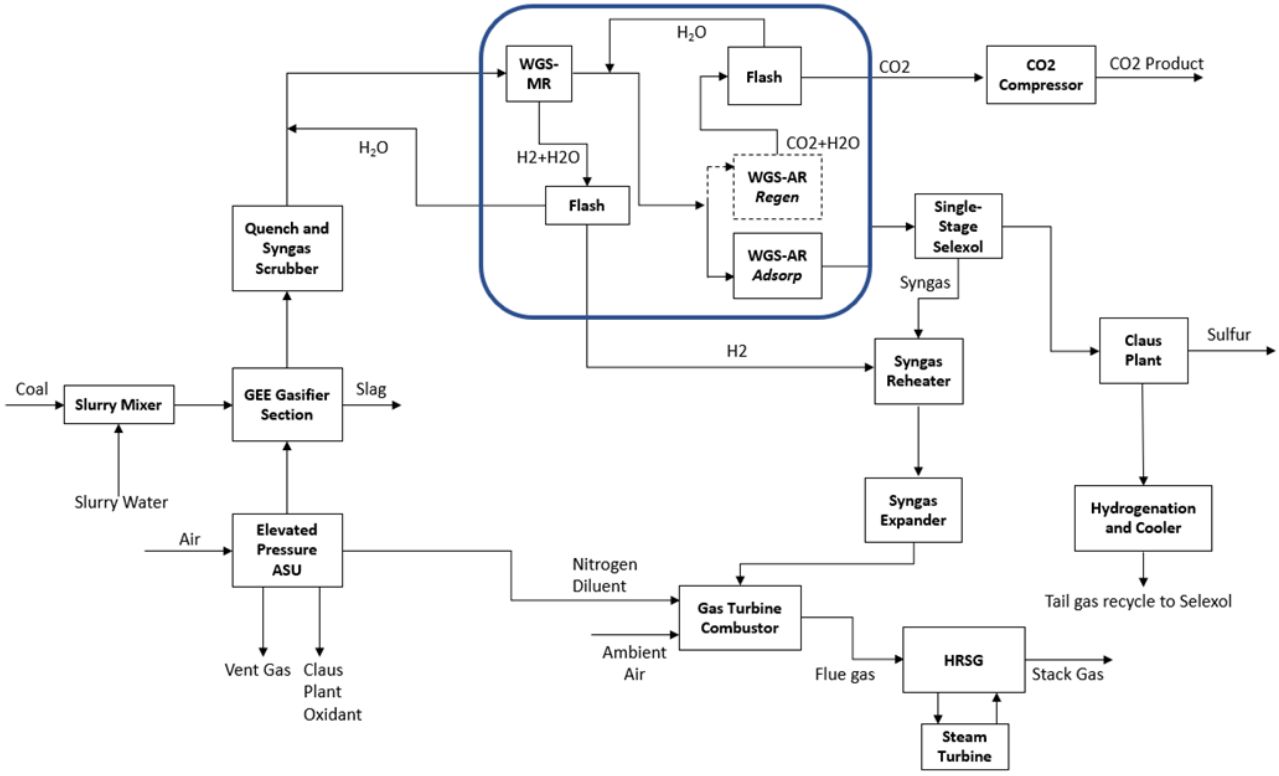

Figure 6.16: MR-AR process within IGCC plant

The MR-AR inlet flow is identical to the inlet of the traditional IGCC pre-combustion CCS plant, and a counter-current sweep MR followed by four ARs (two adsorbing and two desorbing) are implemented that include inter-stage cooling to accommodate the WGS reaction's exothermicity. The retentate outlet of the MR-AR sequence is consequently cooled once more before undergoing a series of separations, the first of which is a flash separator that removes the excess water from the system. Following the flash separator, a Single-Stage Selexol unit is implemented, that removes the sulfur (which is sent to a Claus Plant for post-processing). The MR permeate stream is mixed with the purified gas before entering the Gas Combustion Turbine. Table 6.3 below details the performance of the proposed MR-AR plant, as compared to a typical IGCC plant with CCS.

	CO Conversion	**Catalyst Amount (ft^3)**	**Adsorbent (kg)**
MR-AR Combined System	99%	4,064* (2,553**)	606,912
IGCC WGS Reactor	97%	6,246	0

Table 6.3: Metric comparison of baseline pre-combustion CCS IGCC with IGCC MR-AR

The MR-AR design vs. the baseline design features higher CO conversion (99% vs. 97%), and higher adsorbent amount (606,912 kg of adsorbent vs. no adsorbent). The MR-AR design also requires lower amount of catalyst vs. the baseline design. The amount of catalyst needed to initially load all MR-AR reactors (which contributes to the catalyst capital cost) is 4,064 ft^3 vs. 6,246 ft^3 for the baseline design. However, since the AR is operated periodically, its catalyst is not exposed continuously to a reactive environment, and thus this catalyst's lifetime is longer compared to that of catalyst used continuously, as in the baseline design. Thus, the amount of catalyst needed for continuous replacement (which contributes to the catalyst operating cost) is 2,553 ft^3 vs. 6,246 ft^3 for the baseline design.

	% CO Conversion	% H_2 Recovery	% CO_2 Purity	% CO_2 Recovery
Target	>95	>90	>95	>90
MR-AR Design	99	99	99	92

Table 6.4. Metric comparison of IGCC MR-AR with performance targets

As shown in Table 6.4 above, the MR-AR design meets all performance targets, as it features 99% > 95% CO conversion, 99% > 90% H_2 recovery, 99% > 95% CO_2 purity, and 92% > 90% CO_2 recovery.

	Capital Cost ($/1000)	Variable Operating Cost ($)	Net Power (MWe)	N_2 Product (ton/h)	COE (No N_2 sale/ N_2 Sale) ($/MWh)	CO_2 Captured Cost (No N_2 sale/ N_2 Sale) ($/tonne)
IGCC CCS	**$1,840,115**	**$46,580,032**	**543**	**0**	**135.4**	**63.2**
MR-AR Design	**$1,539,820**	**$47,672,487**	**593**	**619**	**113.1/ 86.3**	**39.3/5.1**

Table 6.5: Cost comparison of baseline pre-combustion CCS IGCC with IGCC MR-AR

As shown in Table 6.5, the MR-AR design's cost characteristics compared to the IGCC w/CCS baseline design are as follows: The MR-AR has a lower capital cost ($1,539,820,000 vs. $1,840,115,000), a higher operating cost ($47,672,487 vs. $46,580,032), generates higher net power (593 MWe vs. 543 MWe), generates pure N_2 product (619 ton/h vs. 0 ton/h), has lower cost of electricity (COE) (113.1 $/MWh with no N_2 sales or 86.3 $/MWh with N_2 sales at $30/ton, vs. 135.4 $/MWh) and lower CO_2 capture cost (39.3 $/ton for MR-AR IGCC with no N_2 sales or 5.1 $/ton for MR-AR IGCC with $30/ton N_2 sales, vs. 63.2 $/ton for the IGCC w/CCS baseline). Thus, the MR-AR IGCC design not only meets, but surpasses all targets when compared to the baseline IGCC w/CCS plant. In addition, the MR-AR IGCC design can produce a higher net power (9.2% more) than the baseline IGCC w/CCS. Finally, from an economic standpoint, the MR-AR IGCC design features a cost of electricity (COE) of 113.1 $/MWh with no N_2 sales (86.3 $/MWh with N_2 sales at $30/ton), which is 16.4% (36.3%) lower than the IGGC w/CCS baseline design's COE

of 135.4$/MWh. Further, the MR-AR IGCC design features a CO_2 capture cost of 39.3 $/ton with no N_2 sales (5.1 $/ton with N_2 sales at $30/ton), which is 37.8% (91.9%) lower than the IGGC w/CCS baseline design's CO_2 capture cost of $63.2/ton. A significant contributor to this lower COE originates from the use of water as diluent in the Gas Combustion Turbine, which enables the sale of the N_2 produced in the Air Separation Unit (ASU) at a price of $30/ton, [16]. The full performance summary, capital cost, and operating cost breakdown can be found in Tables 6.6 – 6.8.

Performance Summary	Baseline IGCC with CCS (Case B5B)	MR-AR IGCC
Combustion Turbine Power, MWe	464	464
Sweet Gas Expander Power, MWe	7	11
Steam Turbine Power, MWe	264	264
Total Gross Power, MWe	**734**	**739**
Air Separation Unit Main Air Compressor, kWe	67,330	67,330
Oxygen Compressor, kWe	10,640	10,640
Nitrogen Compressors, kWe	35,640	35,640
CO_2 Compression, kWe	31,160	2,997
Acid Gas Removal, kWe	19,230	2,590
Balance of Plant, kWe	26,870	26,870
Total Auxiliaries, MWe	**191**	**146**
Net Power, MWe	**543**	**593**

Table 6.6: Performance summary of pre-combustion IGCC with CCS and IGCC MR-AR

	Case:	B5B – GEE Radiant IGCC w/ CO_2					Estimate Type:			Conceptual	
	Plant Size (MW,net):	543					Cost Base:			Jun 2011	
Item No.	Description	Equipment Cost	Material Cost	Labor Direct	Labor Indirect	Bare Erected Cost	Eng'g CM H.O.& Fee	Contingencies Process	Contingencies Project	Total Plant Cost $/1,000	Total Plant Cost $/kW
	1	Coal & Sorbent Handling									
	Subtotal	$17,335	$3,040	$13,259	$0	$33,633	$3,363	$0	$7,399	$44,396	$75
	2	Coal & Sorbent Prep & Feed									
	Subtotal	$29,564	$5,170	$17,541	$0	$52,275	$5,227	$1,906	$11,882	$71,290	$120
	3	Feedwater & Miscellaneous BOP Systems									
	Subtotal	$29,677	$9,494	$12,243	$0	$51,415	$5,142	$0	$12,479	$69,035	$116
	4	Gasifier & Accessories									
	Subtotal	$384,551	$14,421	$91,949	$0	$490,920	$49,092	$30,249	$76,387	$646,648	$1,090
	5A	Gas Cleanup & Piping									
5A.1	Single Stage Selexol	$3,970	$0	$3,346	0	$7,316	$732	$0	$1,610	$9,658	$16
5A.2	Elemental Sulfur Plant	$12,451	$2,427	$15,954	$0	$30,833	$3,083	$0	$6,783	$40,699	$69
5A.3	Mercury Removal	$1,973	$0	$1,491	$0	$3,464	$346	$173	$797	$4,780	$8
5A.4	Reactor Vessels (MR+AR)	$2,415	$0	$966	$0	$3,381	$338	$0	$744	$4,463	$8
5A.5	Membrane Pack	$9,892	$0	w/equip	$0	$9,892	$989	$0	$2,176	$13,057	$22
5A.6	Flash Separators	$690	$0	$276	$0	$966	$97	$0	$212	$1,275	$2
5A.7	Fuel Gas Piping	$0	$812	$531	$0	$1,343	$134	$0	$296	$1,774	$3
5A.9	HGCU Foundations	$0	$735	$495	$0	$1,230	$123	$0	$406	$1,760	$3
5A.10	Heat Exchange Network	$12,987	$0	w/equip	$0	$12,987	$1,299	$0	$2,857	$17,143	$29
Subtotal		$44,378	$3,974	$23,059	$0	$71,411	$7,141	$173	$15,881	$94,609	$160
	5B	CO_2 Compression									
5B.2	CO_2 Compression & Drying	$5,126	$769	$2220	0	$8,115	$811	0	$1,785	$10,711	$18
Subtotal		$5,126	$769	$2220	0	$8,115	$811	0	$1,785	$10,711	$18
	6	Combustion Turbine & Accessories									
Subtotal		$117,901	$1,016	$9,975	$0	$128,892	$12,889	$11,909	$16,270	$169,960	$286
	7	HRSG, Ducting, & Stack									
Subtotal		$33,630	$2,884	$9,498	$0	$46,012	$4,601	$0	$5,797	$56,411	$95
	8	Steam Turbine Generator									
Subtotal		$55,693	$1,108	$16,654	$0	$73,456	$7,346	$0	$12,319	$93,121	$157
	9	Cooling Water System									
Subtotal		$8,296	$12,271	$9,900	$0	$30,467	$3,047	$0	$7,077	$40,591	$68
	10	Ash & Spent Sorbent Handling Systems									
Subtotal		$17,787	$9,928	$17,885	$0	$45,600	$4,560	$0	$5,403	$55,563	$94

11	Accessory Electric Plant									
Subtotal	$36,715	$16,126	$29,455	$0	$82,297	$8,230	$0	$17,319	$107,845	$182
12	Instrumentation & Control									
Subtotal	$13,381	$2,713	$8,797	$0	$24,891	$2,489	$1,245	$4,807	$33,431	$56
13	Instrumentation & Control									
Subtotal	$3,923	$2,312	$10,297	$0	$16,532	$1,653	$0	$5,456	$23,641	$40
14	Instrumentation & Control									
Subtotal	$0	$8,248	$9,382	$0	$17,630	$1,763	$0	$3,175	$22,568	$38
Total	$819,238	$93,474	$302,270	$0	$1,214,986	$121,497	$45,482	$212,551	$1,539,820	$2,597

Table 6.7: Capital cost summary of IGCC MR-AR

Case:	B5B – GEE Radiant IGCC w/ CO_2				Cost Base:	Jun 2011
Plant Size (MW,net):	579	Heat Rate-net (Btu/kWh):		10,459	Capacity Factor (%):	80
Operating & Maintenance Labor						
Operating Labor				**Operating Labor Requirements per Shift**		
Operating Labor Rate (base):	39.70	**$/hour**		Skilled Operator:	2.0	
Operating Labor Burden:	30.00	**% of base**		Operator:	10.0	
Labor O-H Charge Rate:	25.00	**% of labor**		Foreman:	1.0	
				Lab Tech's, etc.:	3.0	
				Total:	**16.0**	
Fixed Operating Costs						
					Annual Cost	
					($)	
Annual Operating Labor:					$7,233,658	
Maintenance Labor:					$18,843,231	
Administrative & Support Labor:					$6,519,222	
Property Taxes and Insurance:					$36,802,296	
Total:					**$69,398,406**	
Variable Operating Costs						
					($)	
Maintenance Material:					$35,348,580	
Consumables						
	Consumption				**Cost ($)**	
	Initial Fill	**Per Day**	**Per Unit**	**Initial Fill**		
Water (/1000 gallons):	0	6,108	$1.67	$0	$2,985,305	
Makeup and Waste Water Treatment Chemicals (lbs)	0	25,026	$0.27	$0	$2,845,681	
Carbon (Mercury Removal) (lb):	135,182	231	$5.50	$743,501	$371,751	
Shift Catalyst (ft^3):	2,553	3.39	$700	$2,844,744	$568,949	
Adsorbent (lb)	303,456	0.81	$1	$606,912	$121,382	
Membrane Packs (m^2)	w/equip	n/a	$650	$0	$535,780	
Selexol Solution (gal):	19,038	3	$36.79	$700,421	$30,340	
Claus Catalyst (ft^3):	w/equip	2.01	$203.15	$0	$119,487	
Subtotal:				**$4,895,578**	**$7,578,675**	
Waste Disposal						
Spent Mercury Catalyst (lb.):	0	231	$0.65	$0	$43,941	
Flyash (ton):	0	0	$0.00	$0	$0	
Slag (ton):	0	641	$25.11	$0	$4,701,292	
Subtotal:				**$0**	**$4,745,232**	
By-Products						
Sulfur (tons):	0	146	$0.00	$0	$0	
Subtotal:				**$0**	**$0**	
Variable Operating Costs Total:				**$16,547,652**	**$47,672,487**	
Fuel Cost						
Illinois Number 6 (ton):	0	5,844	$68.54	$0	$116,961,258	
Total:				**$0**	**$116,961,258**	

Table 6.8: Operating cost summary for IGCC MR-AR

6.3 Sensitivity Analysis

A sensitivity analysis was also carried-out on the most critical technology parameters affecting the COE in the TEA. These parameters include the membranes lifespan along with the sale price of the Nitrogen produced via the ASU. The membrane lifespan assumed for the TEA presented in Sect. 6.2 above is 10 years, per MP&T. As can be seen from Table 6.9, the sensitivity analysis details the cost of membranes replacement for a lifespan ranging from 2-10 years. A 5-year lifespan would increase the COE of the plant by 0.2%, while a 2-year lifespan would increase the COE by 0.6%.

Sensitivity Analysis – Membrane Reactor Lifespan					
	Consumption				Cost ($)
	Initial Fill	Per Day	Per Unit	Initial Fill	Annual Cost
10 Year MR Lifespan					
Membrane Packs (m^2)	w/equip	n/a	$650	$0	$535,780
Total Variable Cost:				$16,547,652	$47,672,487
Total COE:					86.3
5 Year MR Lifespan					
Membrane Packs (m^2)	w/equip	n/a	$650	$0	$1,071,560
Total Variable Cost:				$10,074,435	$48,208,277
Total COE:					86.5
2 Year MR Lifespan					
Membrane Packs (m^2)	w/equip	n/a	$650	$0	$2,678,900
Total Variable Cost:				$10,074,435	$49,815,607
Total COE:					86.8

Table 6.9: Sensitivity Analysis for Membrane Reactor Lifespan

The ASU produces 619 ton/h of pure Nitrogen, which can be sold for approximately $30/ton [16]. The cost of semi-pure (99%) bulk Ntrogen has been quoted at approximately $414/ton by different Nitrogen providers, such as Praxair and West Air Gas. This cost metric includes transportation, storage, and delivery costs. Therefore, to account for these costs, $30/ton was the cost implemented in the TEA as the onsite Nitrogen sale price. Table 6.10 details the sensitivity analysis carried-out for nitrogen sale prices varying from $1/ton to $414/ton. If Nitrogen

was to be sold at $1/ton, this would make the MR-AR design's COE to be 17.1% lower than the COE of the baseline IGCC w/CCS, while a Nitrogen sale price of $414/ton would pay for all plant expenditures. From Tables 6.5 and 6.10, it can be seen that the baseline IGCC w/CCS COE decreases from 135.4 $/MWh to 113.1 $/MWh, 112.2 $/MWh, 86.3 $/MWh, and -255.8 $/MWh when no N_2 is sold, and N_2 is sold at $1/ton, $30/ton, and $414/ton, respectively. This represents a 16%, 17%, 36% and over 100% reduction in baseline IGCC w/CCS COE.

Sensitivity Analysis – Nitrogen Sale Price					
	Consumption				Cost ($)
	Initial Fill	Per Day	Per Unit	Initial Fill	Annual Profit
$30/ton Nitrogen Price					
Nitrogen (tons)	0	14,591	$30	$0	$111,228,000
Total COE ($/MWh)					86.3
$1/ton Nitrogen Price					
Nitrogen (tons)	w/equip	n/a	$1	$0	$3,707,600
Total COE ($/MWh)					112.2
$414/ton Nitrogen Price					
Nitrogen (tons)	w/equip	n/a	$414	$0	$1,534,946,400
Total COE ($/MWh)					-255.8

Table 6.10: Sensitivity Analysis for Nitrogen Sale Price

6.4. Summary and Conclusions

The results of the simulation-based optimization studies are presented in this section, which identifies acceptable ranges for design and operating parameters to meet predetermined process performance requirements of >95% CO conversion, >90% H_2 recovery, >95% CO_2 purity and >90% CO_2 recovery. The minimum (maximum) AR operating times are increasing functions of AR $W_{cat}/F_{CO,0}$, and decreasing functions of MR $W_{cat}/F_{CO,0}$, for a fixed AR W_{cat}/F_{CO} ratio. The minimum (maximum) operating times of 75, 110, 200 (100, 190, >200) AR- $W_{cat}/F_{CO,0}$ are needed to attain 95 % total CO conversion for MR- $W_{cat}/F_{CO,0}$ values of 80, 60, 50, respectively. Increasing the AR's W_{ad}/W_{cat} ratio also increases the AR's operating time, which in turn influences AR process economics, flexibility and safety.

Optimization was performed on the MR-AR combined system through a series of simulations with varying parameters. For the overall MR/AR system, a CO conversion of at least 95% is attainable within the W_{cat}/F_{CO} range of 55 – 65. A H_2O/CO molar ratio above 1.4 in the AR

feed (MR's exit stream) maintains catalyst activity in the AR and still meets the min-95% CO conversion requirement. The optimal range for permeate-side pressure is 3 – 8 bar, and the optimal sweep ratios are 0.1 – 0.3.

A TEA analysis is carried-out for an optimal MR/AR IGCC plant. When compared to a baseline IGCC plant, the MR/AR plant attains higher CO conversion (99% vs. 97%), lower continuous catalyst usage (2,533 ft^3 vs. 6,246 ft^3), higher net power production (593 MWe vs. 543 MWe), lower CO_2 capture cost (5.10 $/ton with $30/ton N_2 sales vs. 63.20 $/ton), and lower COE (86.3 $/MWh with $30/ton N_2 sales vs. 135.4 $/MWh). The MR/AR plant COE is 36.3% less than that of the baseline IGCC w/CCS COE.

NOMENCLATURE

Symbol	*Definition*	*Unit*
p	Superscript represent the pellet	-
r	Superscript represent the reactor	-
$perm$	Superscript represent the permeation zone	-
B_O	Friction factor	m^2
c_f^p	Bulk gas concentration in pellet	mol/m^3
c_f^r	Bulk gas concentration in reactor	mol/m^3
c_f^{perm}	Bulk gas concentration in permeation zone	mol/m^3
c_j^{perm}	Bulk gas concentration of the species j	mol/m^3
C_{cat}	Heat capacity of the catalyst	$J/kg \cdot K$
C_{ad}	Heat capacity of the adsorbent	$J/kg \cdot K$
C_{qua}	Heat capacity of the quartz	$J/kg \cdot K$
C_j^p	Heat capacity of jth species in the pellet	$J/kg \cdot K$
C_j^r	Heat capacity of jth species in the reactor	$J/kg \cdot K$
C_j^{perm}	Heat capacity of jth species in the permeation zone	$J/kg \cdot K$
D_{ij}^{eff}	Effective regular diffusivity of ith species	m^2/s
D_{iK}^{eff}	Effective Knudsen diffusivity of ith species	m^2/s
$D_{Z,\mathrm{j}}$	Dispersion coefficient of species j	m^2/s
d_{pore}	Pellet pore diameter	m
d_p	Diameter of the catalyst pellet	m
E	Activation energy	J/mol
h	Heat transfer coefficient	$W/m^2 \cdot K$
H_j	Enthalpy of the jth species	J/mol

K_{eq}	Overall reaction equilibrium constant	-
M_i	Molecular mass of ith species	$kg\,i/mol\,i$
$\overrightarrow{n_j^p}$	Molar diffusion flux of the jth species in the pellet	$mol/m^2 \cdot s$
$\overrightarrow{n_j^r}$	Molar diffusion flux of the jth species in the reactor	$mol/m^2 \cdot s$
Nu	Nusselt number	-
$n_{CO_2}^{ex}$	Number of CO_2 molecules adsorbed in excess	$mol\,CO_2$
$n_{CO_2}^{g}$	Number of CO_2 moles in gas at time t	$mol\,CO_2$
$n_{CO_2}^{s}$	Number of CO_2 moles adsorbed in the solid at time t	$mol\,CO_2$
$\dot{n}_l$	Leak molar flowrate at Pressure P	Pa
P^p	Pressure of the pellet	bar
P^r	Pressure of the reactor	bar
P_{CO}	Partial pressure of the CO in reactor	bar
P_{CO_2}	Partial pressure of the CO_2 in reactor	bar
P_{H_2}	Partial pressure of the H_2 in reactor	bar
P_{H_2O}	Partial pressure of the H_2O in reactor	bar
P_r	Prandtl number	-
q_{CO_2}	Number of CO2 moles adsorbed at time t, per mass of fresh adsorbent	$mol\,CO_2/kg$
R	Universal gas constant	$J/mol.K$
R_k	Reaction rate	$mol/g-cat \cdot s$
Re	Reynold Number	-
T^p	Temperature of the pellet	K
T^r	Temperature of the reactor	K
$(T^p)^s$	Temperature at the surface of the pellet	K
x_j	Mole fraction of the jth species	-

V^T	Total system volume	m^3
$V^s_{CO_2}$	Volume occupied by gas at time t	m^3
V^g	Volume occupied by gas at time t	m^3
V^s	Volume occupied by solid adsorbent (including adsorbed CO_2) at time t.	m^3
$W_{ad,f}$	Total mass of fresh adsorbent	kg
$\overrightarrow{v^p_f}$	Molar average velocity of gas mixture in pellet	m/s
$\overrightarrow{v^r_f}$	Molar average velocity of gas mixture in reactor	m/s
v_{jk}	Stoichiometric coefficient of component j in reaction k	-
v_α	Ratio of volume occupied by adsorbed CO_2 over number of moles of adsorbed CO_2	$m^3 / mol\, CO_2$
ρ^p_s	Density of the solid phase in the pellet	kg/m^3
ρ^r_s	Density of the solid phase in the reactor	kg/m^3
λ	Conductivity of gas mixture	$W / m \cdot K$
$\Delta H_{R,k}$	Heat of reaction	J / mol
η_j	Effectiveness factor	-
τ	Tortuosity	-
β_c	Fraction of the reactor volume occupied by catalysts	-
μ_g	Dynamic viscosity of the gas mixture	$Pa \cdot s$
μ_i	Dynamic viscosity of the ith species	$Pa \cdot s$
λ_z	Effective conductivity	$W / m \cdot K$

REFERENCES

1. Abdollahi, M., Yu, J., Liu, P.K.T., Ciora, R., Sahimi, M., and Tsotsis, T.T., "Hydrogen Production from Coal-Derived Syngas Using a Catalytic Membrane Reactor Based Process," *J. Membrane Sci.*, 363, 160, 2010.

2. Abdollahi, M., Yu, J., Liu, P.K.T., Ciora, R., Sahimi, M., and Tsotsis, T.T., "Process Intensification in Hydrogen Production from Syngas," *Ind. Eng. Chem. Res*., 49, 10986, 2010.

3. Liu, P.K.T., Sahimi, M., Tsotsis, T.T., "Process Intensification in Hydrogen Production *via* Membrane-Based Reactive Separations," *Current Opinion in Chemical Engineering*, 1, 342, 2012.

4. Parsley, D., Ciora, R.J., Flowers, D.L., Laukaitaus, J., Chen, A, Liu, P.K.T., Yu, J., Sahimi, M., Bonsu, A., and Tsotsis, T.T., "Field Evaluation of Carbon Molecular Sieve Membranes for Separation and Purification of Hydrogen from Coal- and Biomass-Derived Syngas," *J. Membrane Sci*., 450, 81, 2014.

5. Yu, J., Tan, M., Liu, P.K.T., Sahimi, M., and Tsotsis, T.T., "Hydrogen Production from Biomass-Derived Syngas Using a Catalytic Membrane Reactor Based Process," *Ind. Eng. Chem. Res*., 53, 819, 2014.

6. Dadwhal, M., Kim, T, Sahimi, M., and Tsotsis, T.T., "A Study of CO_2 Transport in Layered Double Hydroxides (LDH): The Effect of Particle Size," *Ind. Eng. Chem. Res*., 47, 6150, 2008.

7. Kim, Y., Yang, W., Liu, P.K.T., Sahimi, M., and Tsotsis, T.T., "The Thermal Evolution of the Structure of a Mg-Al-CO_3 Layered Double Hydroxide (LDH). Sorption Reversibility Aspects," *Ind. Eng. Chem. Res*., 43, 4559, 2004.

8. Yang, W., Kim, Y., Liu, P.K.T., Sahimi, M., and T. T. Tsotsis, "A Study by *In-Situ* Techniques of the Thermal Evolution of the Structure of a Mg-Al-CO_3 Layered Double Hydroxide (LDH)," *Chem. Eng. Sci*., 57, 2945, 2002.

9. Garshasbi, A., Process Intensification in Hydrogen Production via Membrane-Based Reactive Separations, PhD Thesis, University of Southern California, May 2017.

10. De La Osa, A. R., A. De Lucas, A. Romero, J. L. Valverde, and P. Sánchez. "Kinetic Models Discrimination for the High Pressure WGS Reaction over a Commercial Co/Mo Catalyst." *International Journal of Hydrogen Energy* 36, 9673, 2011.

11. Garshasbi, A., Chen, H., Cao, M., Karagöz, S., Ciora, R.J., Liu, P.K.T, Manousiouthakis, V.I. and Tsotsis, T.T., "Membrane-Based Reactive Separations for Process Intensification During Power Generation," Catalysis Today, 331, 18, 2019.

12. Chen, H., Cao, M., Manousiouthakis, V.I., and Tsotsis, T.T., "An Experimental Study of an Intensified Water-Gas Shift Reaction Process Using a Membrane Reactor/Adsorptive Reactor Sequence," *Ind. Eng. Chem. Res.*, 57, 13650, 2018.

13. H. Van Dijk, S. Walspurger, P. Cobden, R. Van den Brink, F. De Vos, Testing of hydrotalcite-based sorbents for CO2 and H2S capture for use in sorption enhanced water gas shift, International Journal of Greenhouse Gas Control 5, 505, 2011.

14. Karagöz, S., Da Cruz, F.E., Tsotsis, T.T., and Manousiouthakis, V.I., "Multi-Scale Membrane Reactor (MR) Modeling and Simulation for the Water Gas Shift Reaction," *Chemical Engineering & Processing: Process Intensification*, 133, 245, 2018.

15. Karagöz, S., Tsotsis, T.T., and Manousiouthakis, V.I., "Multi-scale Modeling and Simulation of a Novel Membrane Reactor (MR)/Adsorptive Reactor (AR) Process," In Press, *Chemical Engineering & Processing: Process Intensification*, 137, 146, 2019.

16. Schmidt S, Clayton R. Dynamic Design of a Cryogenic Air Separation Unit, (2013) 41.

STATE POINT DATA TABLE

Table 2. State-Point Data for Membrane Based Systems

	Units	Measured/ Estimated Performance	Projected Performance
Materials Properties			
Materials of Fabrication for Selective Layer		Carbon Molecular Sieve	
Materials of Fabrication for Support Layer (if applicable)		alumina	
Nominal Thickness of Selective Layer (μm)		2-3	2-3
Membrane Geometry		Tubular	Tubular
Max Trans-Membrane Pressure	bar	>82 bar	>82 bar
Hours tested without significant degradation		>16,000 in the lab; >1000 at NCCC	
Membrane Performance			
Temperature	°C	250 – 300	250 - 300
Pressure Normalized Flux for Permeate (CO_2 or H_2)	GPU or equivalent	500, H_2	900
H_2/H_2O Selectivity	-	2-4	>3
H_2/N_2 Selectivity	-	>100	>100
H_2/H_2S Selectivity	-	>100	>100
CO_2/H_2 Selectivity	-		
H_2/CO_2 Selectivity	-	>200	>200
Type of Measurement (Ideal or mixed gas)	-	Mixed gas	Mixed gas
Proposed Module Design			
Flow Arrangement	-	Co/countercurrent, cross-flow	
Packing Density	m^2/m^3	>450	
Shell-Side Fluid	-	Permeate	

***Definitions for Table 2*:**
Membrane Geometry – flat discs or sheets, hollow fibers, tubes, etc.
Pressure Normalized Flux – For materials that display a linear dependence of flux on partial pressure differential, this is equivalent to the membrane's permeance.
GPU – Gas Permeation Unit, which is equivalent to 10^{-6} $cm^3/(cm^2 \cdot s \cdot cmHg)$ at 1 atm and 0 °C. For non-linear materials, the dimensional units reported shall be based on flux measured in $cm^3/(cm^2 \cdot s)$ (at 1 atm and 0 °C) with pressures measured in cm Hg. Note: 1 GPU = 3.3464×10^{-6} $kgmol/(m^2 \cdot s \cdot kPa)$ [SI units]
Type of Measurement – Either mixed or pure gas measurements; projected permeance and selectivities shall be for mixture of gases found in de-sulfurized flue gas.
Flow Arrangement – Typical gas-separation module designs include spiral-wound sheets, hollow-fiber bundles, shell-and-tube, and plate-and-frame, which result in either co-current, counter-current, cross-flow arrangements, or some complex combination of these.
Packing Density – Ratio of the active surface area of the membrane to the volume of the module.
Shell-Side Fluid – Either the permeate or retentate stream.

Table 3. State-Point Data for Sorbent Based Systems

	Units	Measured/ Estimated Performance	Projected Performance
Sorbent			
True Density @ STP	kg/m^3	2849-3066	2849-3066
Bulk Density	kg/m^3	1322-1423	1322-1423
Average Particle Diameter	mm	0.6-0.8	2-3
Particle Void Fraction	m^3/m^3	0.536	0.536
Packing Density	m^2/m^3	0.406	0.406
Solid Heat Capacity @ STP	kJ/kg·K	0.5 - 0.65*	0.5 - 0.65
Crush Strength	kg_f	N/A**	10 - 15
Attrition Index	-	N/A**	0.1% – 0.2%
Adsorption			
Pressure	bar	25 bar	>25 bar
Temperature	°C	250-300	250-300
Equilibrium Loading	gmol CO_2/kg	~3	~3
Heat of Adsorption	kJ/gmol CO_2	~10	-
Desorption			
Pressure	bar	25 bar	>25 bar
Temperature	°C	400-450	<400
Equilibrium Loading	gmol CO_2/kg	0.1-0.2	<0.1
Heat of Desorption	kJ/gmol CO_2	~10	-

***Definitions for Table 3*:**
STP – Standard Temperature and Pressure (15 °C, 1 atm)
Sorbent – Adsorbate-free (*i.e.* CO_2-free) and dry material as used in adsorption/desorption cycle.
Adsorption – The conditions of interest for adsorption are those that prevail at maximum sorbent loading. Measured data are preferable to estimated data.
Desorption – The conditions of interest for desorption are those that prevail at minimum sorbent loading. Operating pressure and temperature for the desorber/stripper are process dependent. Measured data are preferable to estimated data.
Pressure – The pressure of CO_2 in equilibrium with the sorbent. If the vapor phase is pure CO_2, this is the total pressure, and if it is a mixture of gases, this is the partial pressure of CO_2.
Packing Density – Ratio of the active sorbent area to the bulk sorbent volume.
Loading – The basis for CO_2 loading is mass of dry sorbent.
*Heat capacity is estimated from literature information.
**Not available as yet. Present project employs powders

APPENDIX

Multiscale Mathematical Model of the MR Process (from {[13])

In this work, the generic indication of domain α can assume the following values: p , q , r and per ; representing the catalyst pellet, quartz pellet, reactor, and permeation domains respectively. For the catalyst pellet and the reactor multiphase systems, the generic phase γ can assumed the following values: f and s , representing fluid or solid phases respectively. Quartz pellet and permeation domains are assumed to be mono-phase, with γ equals to s and f respectively. In addition, quartz is considered a rigid solid body with constant mass. Assuming no structural changes during reaction inside of the pellet, stagnant solid phase, no phase changing in the reaction mixture, the total mass conservation equation for all domain-phase pairs in the MR system is shown in Eq. (A.1) to (A.5).

Pellet-Fluid:
$$0=\frac{\partial}{\partial t}\left(\varepsilon_{f,V}^{p}\sum_{i=1}^{\upsilon}\rho_{f,i}^{p}\right)+\vec{\nabla}\cdot\left[\varepsilon_{f,A}^{p}\sum_{i=1}^{\upsilon}\left(\rho_{f,i}^{p}\overrightarrow{v_{f,i}^{p}}\right)\right];\quad i=1,\upsilon \tag{A.1}$$

Pellet-Solid:
$$0=\frac{\partial}{\partial t}\left(\varepsilon_{s,V}^{p}\sum_{i=1}^{\upsilon}\rho_{s,i}^{p}\right);\quad i=1,\upsilon \tag{A.2}$$

Reactor-Fluid:
$$\sum_{i=1}^{v}\overrightarrow{S_{f-per,i}^{r}}=\frac{\partial}{\partial t}\left(\varepsilon_{f,V}^{r}\rho_{f}^{r}\right)+\vec{\nabla}\cdot\left(\varepsilon_{f,A}^{r}\rho_{f}^{r}\overrightarrow{v_{f}^{r}}\right) \tag{A.3}$$

Reactor-Solid:
$$0=\frac{\partial}{\partial t}\left(\varepsilon_{s,V}^{r}\rho_{s}^{r}\right) \tag{A.4}$$

Permeation-Fluid:
$$-\sum_{i=1}^{v}\overrightarrow{S_{f-per,i}^{r}}=\frac{\partial}{\partial t}\left(\rho_{f}^{per}\right)+\vec{\nabla}\cdot\left(\rho_{f}^{per}\overrightarrow{v_{f}^{per}}\right) \tag{A.5}$$

The species mass conservation equation for each domain-phase pair obtained from the RTT are shown in Eq. (A.6) to (A.10).

Pellet-Fluid:
$$M_{i}R_{f,i}^{p}=\frac{\partial}{\partial t}\left(\varepsilon_{f,V}^{p}w_{f,i}^{p}\rho_{f}^{p}\right)+\vec{\nabla}\cdot\left(\varepsilon_{f,A}^{p}\overrightarrow{N_{f,i}^{p}}\right)\quad;\quad i=1,\upsilon \tag{A.6}$$

Pellet-Solid:
$$0=\frac{\partial}{\partial t}\left(\varepsilon_{s,V}^{p}\rho_{s,i}^{p}\right)\quad;\quad i=1,\upsilon \tag{A.7}$$

Reactor-Fluid:
$$\overrightarrow{S_{f-per,i}^{r}}+M_{i}R_{f,i}^{r}=\frac{\partial}{\partial t}\left(\varepsilon_{f,V}^{r}w_{f,i}^{r}\rho_{f}^{r}\right)+\vec{\nabla}\cdot\left[\varepsilon_{f,A}^{r}\left(w_{f,i}^{r}\rho_{f}^{r}\overrightarrow{v_{f}^{r}}+\overrightarrow{n_{f,i}^{r}}\right)\right]\quad;\quad i=1,\upsilon \tag{A.8}$$

Reactor-Solid:
$$0=\frac{\partial}{\partial t}\left(\varepsilon_{p-s,V}^{r}\rho_{s,i}^{r}\right)\quad;\quad i=1,\upsilon \tag{A.9}$$

Permeation-Fluid: $$-\overrightarrow{S^{r}_{f-per,i}} = \frac{\partial}{\partial t}\left(w^{per}_{f,i}\rho^{per}_{f}\right) + \vec{\nabla}\cdot\left(w^{per}_{f,i}\rho^{per}_{f}\overrightarrow{v^{per}_{f}}\right) \quad ; \quad i = 1,\upsilon \tag{A.10}$$

The solution-diffusion model is used to describe the permeation through membrane. In this model, permeation is proportional to the difference between the species' partial pressure at the tube and shell sides, gas boundary layer resistance near the membrane surface is neglected, and infinitely selective membrane is assumed. The integration of Henry's law (solubility) and Fick's law (diffusion) results in Eq.(A.11) for the flux of the permeating species [1].

$$\overrightarrow{J^{per}_{f,i}} = \frac{D\cdot S\cdot \Delta p_j}{\delta} = \frac{Pe\cdot \Delta p_j}{\delta} \tag{A.11}$$

In Eq.(A.11), D is the diffusion coefficient of the species on the membrane side, S is the gas solubility, Δp_j is the difference between the jth species partial pressure at tube and shell side, δ is the membrane thickness, and Pe is the so-called permeability coefficient.

The species flux through membrane can be represented by using the Sieverts' Law [2];

$$\overrightarrow{J^{per}_{f,i}} = \frac{P_e}{\delta}\left[\left(p^{r}_{f,i}\right)^{n} - \left(p^{per}_{f,i}\right)^{n}\right] \in CS^{per} \tag{A.12}$$

The Arrhenius Law expresses the relation between the permeability and the temperature;

$$P_e = P_e^{0} exp\left(-\frac{E_a^m}{R\cdot T}\right) \tag{A.13}$$

According to the the Sieverts' Law and the Arrhenius Law, the flux increases by decreasing the membrane thickness and increasing the temperature. Many studies have verified the applicability of the Sieverts' law to CMS membranes**.**

The source term $\overrightarrow{S^{r}_{f-per,i}}$ in Eq. (A.3), (A.5), (A.8) and (A.10) represents the species mass lost in reaction zone through permeation zone at the control surface CS^{per} of the permeation domain.

$$\overrightarrow{S^{r}_{f-per,i}} = \begin{Bmatrix} \overrightarrow{J^{per}_{f,i}} & if\ \text{1D} \\ 0 & if\ \text{2D or 3D} \end{Bmatrix} \tag{A.14}$$

The momentum conservation equation for each domain-phase pair as a function of the mass average velocity $\overrightarrow{v^{\alpha}_{\gamma}}$ of phase γ within the domain α is shown in Eq.(A.15) to (A.19).

Pellet-Fluid:

$$\overrightarrow{S_f^p} = \left\{ \begin{array}{l} \dfrac{\partial}{\partial t}\left(\varepsilon_{f,V}^p \sum_{i=1}^{\upsilon} w_{f,i}^p \rho_f^p \overrightarrow{v_{f,i}^p} \right) + \\ \vec{\nabla} \cdot \left[\left(\varepsilon_{f,A}^p \sum_{i=1}^{\upsilon} w_{f,i}^p \rho_f^p \overrightarrow{v_{f,i}^p} \right) \left(\sum_{i=1}^{\upsilon} w_{f,i}^p \overrightarrow{v_{f,i}^p} \right) \right] \end{array} \right\} \quad ; \quad i = 1, \upsilon \tag{A.15}$$

Pellet-Solid:

$$\overrightarrow{S_s^p} = 0 \quad ; \quad i = 1, \upsilon \tag{A.16}$$

Reactor-Fluid:

$$\overrightarrow{S_f^r} = \frac{\partial}{\partial t}\left(\varepsilon_{f,V}^r \rho_f^r \overrightarrow{v_f^r} \right) + \vec{\nabla} \cdot \left(\varepsilon_{f,A}^r \rho_f^r \overrightarrow{v_f^r} \overrightarrow{v_f^r} \right) \tag{A.17}$$

Reactor-Solid:

$$\overrightarrow{S_s^r} = 0 \tag{A.18}$$

Permeation-Fluid:

$$\overrightarrow{S_f^{per}} = \frac{\partial}{\partial t}\left(\rho_f^{per} \overrightarrow{v_f^{per}} \right) + \vec{\nabla} \cdot \left(\rho_f^{per} \overrightarrow{v_f^{per}} \overrightarrow{v_f^{per}} \right) \tag{A.19}$$

The source term $\overrightarrow{S_\gamma^\alpha}$ in Eq.(A.15) and (A.19) typically consists of Reynold stresses, body forces, momentum exchange, mass exchange, equilibration and non-equilibrium pressure, and average stresses.

For the energy equation development in all MR domains presented, solid phase is considered stagnant, and the potential and kinetic energies, the work done by the fluid onto the solid, and the effect of interphase viscous friction are all considered negligible. Also, radiation-based energy transport is not considered to be essential for this application. Fourier's law is used to account for heat conduction, and the reacting mixture's enthalpy is calculated using an ideal gas mixture assumption. Then, the energy equations for each domain-phase pair in the system are presented in Eq.(A.20) to (A.23).

Pellet-Fluid:

$$\left\{ \begin{array}{l} -q_{f\to s}^p + \vec{\nabla} \cdot \left(\varepsilon_{f,A}^p \lambda_f^p \vec{\nabla} T_f^p \right) \\ -\sum_{i=1}^{\upsilon} \varepsilon_{f,A}^p \left(\dfrac{1}{M_i} C_{P,i}^p \right) \overrightarrow{n_{f,i}^p} \cdot \vec{\nabla} T_f^p \\ -\sum_{i=1}^{\upsilon} \tilde{h}_i^p R_{f,i}^p + \sum_{i=1}^{\upsilon} \tilde{h}_i^p \dfrac{\partial}{\partial t}\left(\varepsilon_{f,V}^p c_{f,i}^p \rho_f^p \right) \end{array} \right\} = \left\{ \begin{array}{l} \left[\sum_{i=1}^{\upsilon} \varepsilon_{f,V}^p \rho_f^p \left(c_{f,i}^p C_{P,i}^p \right) \dfrac{\partial T_f^p}{\partial t} \right] \\ \quad + \left[\sum_{i=1}^{\upsilon} \varepsilon_{f,A}^p \rho_f^p \left(c_{f,i}^p C_{P,i}^p \right) \right] \left(\overrightarrow{v_f^p} \cdot \vec{\nabla} T_f^p \right) \end{array} \right\} \tag{A.20}$$

Pellet-Solid:

$$q_{f\to s}^p + \vec{\nabla} \cdot \left[\varepsilon_{s,A}^p \lambda_s^p \vec{\nabla} T_s^p \right] = \varepsilon_{s,V}^p \rho_s^p C_V^p \frac{\partial T_s^p}{\partial t} \tag{A.21}$$

$$\textit{Reactor-Fluid}\left\{\begin{array}{l}-q^{r}_{f\to s}-q^{r}_{r-f\to per-f}+\vec{\nabla}\cdot\left(\varepsilon^{r}_{f,A}\lambda^{r}\vec{\nabla}T^{r}_{f}\right)\\ -\sum_{i=1}^{\upsilon}\left[\varepsilon^{r}_{f,A}\left(\frac{1}{M_i}C^{r}_{P,i}\right)\overrightarrow{n^{r}_{f,i}}\cdot\vec{\nabla}T^{r}_{f}\right]\\ -\sum_{i=1}^{\upsilon}\left[\frac{1}{M_i}\tilde{h}^{r}_{f,i}\vec{\nabla}\cdot\left(\varepsilon^{r}_{f,A}\overrightarrow{n^{r}_{f,i}}\right)\right]\end{array}\right\}=\left\{\begin{array}{l}\varepsilon^{r}_{f,V}\rho^{r}_{f}\left(\sum_{i=1}^{\upsilon}c^{r}_{f,i}C^{r}_{P,i}\right)\frac{\partial T^{r}_{f}}{\partial t}\\ +\varepsilon^{r}_{f,A}\rho^{r}_{f}\left(\sum_{i=1}^{\upsilon}c^{r}_{f,i}C^{r}_{P,i}\right)\overrightarrow{v^{r}_{f}}\cdot\vec{\nabla}T^{r}_{f}\end{array}\right\} \tag{A.22}$$

$$\textit{Permeation-Fluid:}\quad q^{r}_{r-f\to per-f}+\vec{\nabla}\cdot\left(\lambda^{per}_{f}\vec{\nabla}T^{per}_{f}\right)=\left\{\begin{array}{l}\rho^{per}_{f}\left(\sum_{i=1}^{\upsilon}c^{per}_{f,i}C^{per}_{V,i}\right)\frac{\partial T^{per}_{f}}{\partial t}-\frac{\partial p^{per}_{f}}{\partial t}\\ +\rho^{per}_{f}\left(\sum_{i=1}^{\upsilon}c^{per}_{f,i}C^{per}_{P,i}\right)\overrightarrow{v^{per}_{f}}\cdot\vec{\nabla}T^{per}_{f}\end{array}\right\} \tag{A.23}$$

The proximity of the solid and fluid phases in the pellet domain induces a high heat transfer coefficient between the two phases, which in turn leads to a common temperature T^{p} for the pellet's solid-fluid composite system. The resulting composite energy equation is given by Eq.(A.24).

$$\left\{\begin{array}{l}\vec{\nabla}\cdot\left[\left(\lambda^{p}\right)\vec{\nabla}T^{p}\right]\\ -\sum_{i=1}^{\upsilon}\varepsilon^{p}_{f,A}\left(\frac{1}{M_i}C^{p}_{P,i}\right)\overrightarrow{n^{p}_{f,i}}\cdot\vec{\nabla}T^{p}\\ -\sum_{i=1}^{\upsilon}\tilde{h}^{p}_{i}R^{p}_{f,i}+\sum_{i=1}^{\upsilon}\tilde{h}^{p}_{i}\frac{\partial}{\partial t}\left(\varepsilon^{p}_{f,V}c^{p}_{f,i}\rho^{p}_{f}\right)\end{array}\right\}=\left\{\begin{array}{l}\left[\varepsilon^{p}_{s,V}\rho^{p}_{s}C^{p}_{V,s}+\sum_{i=1}^{\upsilon}\varepsilon^{p}_{f,V}\rho^{p}_{f}\left(c^{p}_{f,i}C^{p}_{P,i}\right)\right]\frac{\partial T^{p}}{\partial t}\\ +\left[\sum_{i=1}^{\upsilon}\varepsilon_{A}\rho^{p}_{f}\left(c^{p}_{f,i}C^{p}_{P,i}\right)\overrightarrow{v^{p}_{f}}\right]\cdot\vec{\nabla}T^{p}\end{array}\right\} \tag{A.24}$$

In this work, the heat exchanged among the fluid, solid phases in reaction zone and permeation zone, $q^{r}_{f\to s}$, is composed of six terms: the enthalpy carried by the species' mass flux between the reactor and the pellet domains at the control surface CS^{p} of the pellet domain, Eq.(A.26); the enthalpy carried by the species' mass flux between the reactor and the permeation domains at the control surface CS^{per} of the permeation domain, Eq.(A.27); the convective heat flux exchanged between the fluid in the reactor and the pellet solid phase at the control surface CS^{p} of the pellet domain, Eq.(A.28); the convective heat flux exchanged between the fluid in the reactor and the quartz solid phase at the control surface CS^{q} of the quartz domain, Eq.(A.29); a source term q^{r}_{e} that accounts for any external heat flux crossing the considered reactor control surface

CS^r, Eq.(A.30); and a source term q_i^r that accounts for any internal heat flux crossing the considered permeation control surface CS^{per}, Eq.(A.31).

$$q_{f\to s}^r = q_{mp}^r + q_{mper}^r + q_p^r + q_q^r + q_e^r + q_i^r \tag{A.25}$$

$$q_{mp}^r = \varepsilon_{p-s,V}^r \left(\frac{A^p}{\varepsilon_{s,V}^p V^p} \right) \sum_{i=1}^{\nu} \left[\left(\frac{1}{M_i} \tilde{h}_{f,i}^r \varepsilon_{f,A}^p \overrightarrow{N_i^p} \right) \Bigg|^{CS^p} \cdot \vec{n} \right] \in CS^p \tag{A.26}$$

$$q_{mper}^r = \left(\frac{A^{per}}{V^r} \right) \sum_{i=1}^{\nu} \left[\left(\frac{1}{M_i} \overrightarrow{N_i^{per}} \left(\tilde{h}_{f,i}^r - \tilde{h}_{f,i}^{per} \right) \right) \Bigg|^{CS^{per}} \cdot \vec{n} \right] \in CS^{per} \tag{A.27}$$

$$q_p^r = \varepsilon_{p-s,V}^r \left(\frac{A^p}{\varepsilon_{s,V}^p V^p} \right) \left[\varepsilon_{s,A}^p h^p \left(T_f^r - T^p \right) \Big|^{CS^p} \right] \in CS^p \tag{A.28}$$

$$q_q^r = \varepsilon_{q-s,V}^r \left(\frac{A^q}{\varepsilon_{s,V}^q V^q} \right) \left[\varepsilon_{s,A}^q h^q \left(T_f^r - T^q \right) \Big|^{CS^q} \right] \in CS^q \tag{A.29}$$

$$q_e^r = \begin{Bmatrix} \left(\frac{4}{d^t} \right) U^{fr} \left(T_f^r - T^f \right) & if \ \text{1D} \\ 0 \quad if \quad \text{2D or 3D} \end{Bmatrix} \in CS^r \tag{A.30}$$

$$q_i^r = \begin{Bmatrix} \frac{A^{per} U^{per}}{V^r} \left(T_f^r - T_f^{per} \right) & if \ \text{1D} \\ 0 \quad if \quad \text{2D or 3D} \end{Bmatrix} \in CS^{per} \tag{A.31}$$

In the application of the adiabatic case on the MR, we consider globally adiabatic reactor (with respect to the environment, no external coolant or heater or $q_e^r = 0$). However, we utilize the Eq.(A.31) to express the heat flux between reaction zone and environment for the non-adiabatic reactor case.

In this study, we consider steady-state reactive transport in the pellet domains, a spherical pellet, homogeneous porous structure along the pellet, a mean pore diameter, a constant reaction kinetics and reaction orders over the entire range of conditions simulated, and no side reaction occurs. For the pellet-fluid subsystem, a source term for the momentum balance is obtained by adding the DGM for all species. The reactor configuration is given by a one-dimensional tubular reactor with no axial dispersion, thus radial concentration and temperature gradients are neglected.

Gradients explicitly inside of each phase and between phases are satisfied on one-dimensional reactor simulation (axial), even though the system has a higher dimensionality [3].

The cross-sectional average momentum equation can be written as [4 and 5]:

$$\frac{\partial}{\partial t}\left(\varepsilon_{f,V}^{r}\rho_{f}^{r}\overrightarrow{v_{f}^{r}}\right)+\vec{\nabla}\cdot\left(\rho_{f}^{r}\overrightarrow{v_{f}^{r}}\overrightarrow{v_{f}^{r}}\right)=\left\{\begin{array}{l}-\varepsilon_{f,V}^{r}\vec{\nabla}p_{f}^{r}+\varepsilon_{f,V}^{r}\rho_{f}^{r}\vec{g}+\\ \vec{\nabla}\cdot\overrightarrow{v_{f}^{r}}\left(\mu_{f}^{r}\left(\vec{\nabla}\overrightarrow{v_{f}^{r}}+\left(\vec{\nabla}\overrightarrow{v_{f}^{r}}\right)^{T}\right)\right)+\varepsilon_{f,V}^{r}\left(K_{D}\overrightarrow{v_{f}^{r}}+K_{v}\overrightarrow{v_{f}^{r}}^{2}\right)\end{array}\right\} \tag{A.32}$$

The process is steady-state and the gravity term is neglected in horizontal tube. The bed friction in porous reactor plays the main role in pressure drop of the bed. Also, the gas phase velocity is normally not very large [4 and 5]. Because of these factors the momentum equation can be reduced to the following form;

$$\vec{\nabla}p_{f}^{r}=-K_{D}\overrightarrow{v_{f}^{r}}-K_{v}\overrightarrow{v_{f}^{r}}^{2}=\vec{\nabla}p_{f}^{r}=-150\frac{\left(1-\varepsilon_{f,V}^{r}\right)^{2}}{\left(\varepsilon_{f,V}^{r}\right)^{3}d_{p}^{2}}-\mu_{f}^{r}1.75\frac{\left(1-\varepsilon_{f,V}^{r}\right)}{\left(\varepsilon_{f,V}^{r}\right)^{3}d_{p}}\rho_{f}^{r}\overrightarrow{v_{f}^{r}}\overrightarrow{v_{f}^{r}} \tag{A.33}$$

where K_D and K_V are constants for the viscous and kinetic pressure drop [4].

Table 1: Properties dependence

Property description	Dependence in the simulation	
	Pellet	Reactor
Fluid phase viscosity	$\mu_f^p=\mu_f^p\left(T^p,\left\{c_i^p\right\}\right)$	$\mu_f^r=\mu_f^r\left(T^r,\left\{c_i^r\right\}\right)$
Fluid phase conductivity	$\lambda_s^p=\lambda_s^p\left(T^r\right)$	$\lambda_f^r=\lambda_f^r\left(T^r,p^r,\left\{c_i^r\right\}\right)$
Binary diffusion coefficients	$D_{ij}^p=D_{ij}^p\left(T^p,p^p\right)$	$D_{ij}^r=D_{ij}^r\left(T^r,p^r\right)$
Knudsen diffusivities	$D_{iK}=D_{iK}\left(T^p\right)$	–
Species i heat capacity	$C_{P,i}^p=C_{P,i}^p\left(T^p\right)$	$C_{P,i}^r=C_{P,i}^r\left(T^r\right)$
Species i molar enthalpy	$\tilde{h}_{f,i}^p=\tilde{h}_{f,i}^p\left(T^p\right)$	$\tilde{h}_{f,i}^r=\tilde{h}_{f,i}^r\left(T^r\right)$

The regular diffusion, effective diffusion coefficients employed in the above equations, are estimated using the binary regular diffusion coefficients predicted by Chapman-Enskog theory [6-7], combined with a correction factor accounting for the length and tortuosity of the diffusion path. The equations to estimate the binary diffusion coefficient for polar and non-polar

gas mixtures are based on Poling, Prausnitz and O'Connell's work [8]. For ideal gas mixtures, Stefan-Maxwell diffusivities and the binary diffusivities are almost identical [4].

Table 2: Constitutive laws and other model equations

Dimensionless Groups:

$$Nu = \frac{hd_p}{\lambda_f^r},\ Re = \frac{\overrightarrow{v_f^r}\rho_f^r d_p}{\mu_f^r},\ Pr = \frac{C_{P,f}^r \mu_f^r}{\lambda_f^r} \qquad \text{(A.34)}$$

The viscosity of Gas Mixture:

$$\mu_f^\alpha = \sum_{i=1}^{v} \frac{x_{f,i}^\alpha \mu_{f,i}^\alpha(T)}{\sum_{i=1}^{v} x_{f,i}^\alpha \phi_{ij}}, \qquad \phi_{ij} = \frac{\left[1+\left(\mu_{f,i}^\alpha(T)/\mu_{f,j}^\alpha(T)\right)^{1/2}\left(M_j/M_i\right)^{1/4}\right]^2}{8\left(1+\left(M_i/M_j\right)\right)^{1/2}} \text{ [9] (A.35)}$$

Thermal Conductivity:

$$\lambda^p = \varepsilon_{s,V}^p \lambda_s^p + \varepsilon_{f,V}^p \lambda_f^p \qquad \text{(A.36)}$$

$$\lambda^r = \lambda^s + \varepsilon_{f,V}^r \lambda_{f,eff}^r,\ \lambda^s = \varepsilon_{p-s,V}^r \lambda_{p-s}^r + \varepsilon_{c-s,V}^r \lambda_{c-s}^r$$

(A.37)

Thermal Conductivity of Pure Gases:

$$\lambda_{f,i}^r = A_i + B_i T + C_i T^2 + D_i T^3 \quad \text{[10]} \qquad \text{(A.38)}$$

Thermal Conductivity of Gas Mixture:

$$\lambda_f^r = \sum_{i=1}^{v} \frac{x_{f,i}^r \lambda_{f,i}^r(T)}{\sum_{j=1}^{N_s} x_{f,i}^r \phi_{ij}}, \qquad \phi_{ij} = \frac{\left[1+\left(\mu_{f,i}^\alpha(T)/\mu_{f,j}^\alpha(T)\right)^{1/2}\left(M_j/M_i\right)^{1/4}\right]^2}{8\left(1+\left(M_i/M_j\right)\right)^{1/2}} \text{ [9] (A.39)}$$

The effective axial conductivity:

$$\frac{\lambda_{f,eff}^r}{\lambda_f^r} = \frac{\lambda_f^0}{\lambda_f^r} + 0.75(Pr)(Re),\ \frac{\lambda_z^0}{\lambda_f^r} = \varepsilon_{f,V}^r + \frac{1-\varepsilon_{f,V}^r}{0.139\varepsilon_{f,V}^r - 0.0339 + \frac{2}{3}\left(\frac{\lambda_f^r}{\lambda^s}\right)} \text{ [3]}$$

(A.40)

Specific Heat Capacity of Pure Gases:

$$C_{P,i}^\alpha = a_{0,i} + a_{1,i}t + a_{2,i}t^2 + a_{3,i}t^3 + a_{4,i}/t^2,\ \ t = \left(T/1000\right) \quad \text{[11]} \qquad \text{(A.41)}$$

Specific Heat Capacity of Gas Mixture:

$$C_{P,f}^{\alpha} = \sum_{i=1}^{v} \frac{x_{f,i}^{\alpha} M_i C_{P,i}^{\alpha}}{\sum_{j=1}^{v} x_{f,i}^{\alpha} M_i} \text{ [9]} \qquad \text{(A.42)}$$

Standard Enthalpy of Gases:

$$\tilde{h}_{f,i}^{\alpha} = \tilde{H}_i^0 + a_{0,i} t + a_{1,i} \frac{t^2}{2} + a_{2,i} \frac{t^3}{3} + a_{3,i} \frac{t^4}{4} - \frac{a_{4,i}}{t} + a_{5,i} - a_{6,i}, \quad t = \left(T / 1000 \right) \text{ [9]} \qquad \text{(A.43)}$$

Nomenclature (Mathematical Model of the MR Process)

English Symbols

$A^p \left(m^2 \; of \; domain \; p \right)$ Area of the control surface of domain p

$A_c^r \left(m^2 \right)$ Cross section area of the tubular reactor

$B_O \left(m^2 \right)$ Viscous flow parameter of domain p

$c_{\gamma,i}^{\alpha} \left(\frac{mol \; of \; species \; i \; in \; phase \; \gamma \; within \; domain \; \alpha}{m^3 \; of \; phase \; \gamma \; within \; domain \; \alpha} \right)$ Species' i molar density of phase γ within domain α

$c_{\gamma}^{\alpha} \left(\frac{mol \; of \; phase \; \gamma \; within \; domain \; \alpha}{m^3 \; of \; phase \; \gamma \; within \; domain \; \alpha} \right)$ Total molar density of phase γ within domain α

$C_{P,i}^{\alpha} \left(\frac{J \; of \; species \; i \; in \; phase \; \gamma \; within \; domain \; \alpha}{\left(mol \cdot K \right) of \; the \; i^{th} \; component \; of \; phase \; \gamma \; within \; domain \; \alpha} \right)$ Species' i molar specific heat at constant pressure of phase f within domain α

$C_V^{\alpha} \left(\frac{J \; phase \; s \; within \; domain \; \alpha}{\left(mol \cdot K \right) of \; phase \; s \; within \; domain \; \alpha} \right)$ Species' i molar specific heat at constant volume of phase s within domain α

$CS^{\alpha} \left(m^2 \; of \; domain \; \alpha \right)$ Control surface of domain α

$CV^{\alpha} \left(m^3 \; of \; domain \; \alpha \right)$ Control volume of domain α

$D \left(\frac{m^2}{s} \right)$ Diffusion coefficient of the species on the membrane side

$D_{ij}^{\alpha} \left(\frac{m^2 \; of \; phase \; f \; within \; of \; domain \; \alpha}{s} \right)$ Species' i and j binary diffusion coefficient of phase γ within domain α

$D_{ij}^{eff}\left(\frac{m^2\ of\ domain\ p}{s}\right)$ Species' i and j effective binary diffusion coefficient in domain p

$D_{iK}\left(\frac{total\ m^2\ of\ domain\ p}{s}\right)$ Species' i Knudsen diffusion coefficient in domain p

$\tilde{D}_i^r\left(\frac{m^2\ of\ phase\ f\ within\ domain\ r}{s}\right)$ Species' i thermal diffusion coefficient of phase f within domain r

$d^p(m)$ Diameter of the catalytic pellet

$d_{pore}^p(m)$ Mean pore diameter in domain p

$d^r(m)$ Diameter of the tubular reactor

$F_{CO}(mol/h)$ Inlet CO molar flow rate

$h^\alpha\left(\frac{J\ \ from\ phase\ f\ within\ domain\ \alpha}{\left(\left(m^2\cdot K\right)of\ \ phase\ s\ within\ domain\ \alpha\right)\cdot s}\right)$ Interfacial heat transfer coefficient between phase f within domain α and phase s within domain α.

$H_\gamma^\alpha\left(\frac{J\ of\ \ phase\ \gamma\ within\ domain\ \alpha}{kg\ of\ \ phase\ \gamma\ within\ domain\ \alpha}\right)$ Mass specific enthalpy of phase γ within domain α

$\tilde{H}_i^0\left(\frac{J\ \ of\ species\ i\ \ in\ phase\ f}{mol\ of\ species\ i\ \ in\ phase\ f}\right)$ Species' i standard molar enthalpy of formation

$\tilde{h}_{\gamma,i}^\alpha\left(\frac{J\ \ of\ \ phase\ \gamma\ within\ domain\ \alpha}{mol\ of\ \ phase\ \gamma\ within\ domain\ \alpha}\right)$ Species' i molar enthalpy of phase γ within domain α

$\lambda_\gamma^\alpha\left(\frac{J\ \ of\ \ phase\ \gamma\ within\ domain\ \alpha}{\left((m\cdot K)of\ \ phase\ \gamma\ within\ domain\ \alpha\right)\cdot s}\right)$ Thermal conductivity of phase γ within domain α

$\overrightarrow{j_{\gamma,i}^\alpha}\left(\frac{kg\ of\ species\ i\ \ in\ \ phase\ \gamma\ within\ domain\ \alpha}{\left(m^2\ of\ \ phase\ \gamma\ within\ domain\ \alpha\right)\cdot s}\right)$ i^{th} species diffusion molar flux in phase γ within domain α

$\overrightarrow{J_{\gamma,i}^\alpha}\left(\frac{kg\ of\ species\ i\ \ in\ \ phase\ \gamma\ within\ domain\ \alpha}{\left(m^2\ of\ \ phase\ \gamma\ within\ domain\ \alpha\right)\cdot s}\right)$ i^{th} species combined diffusion-convection molar flux in phase γ within domain

$k_m(m/s)$ Mass transfer coefficient

$L^r(m)$ Length of the tubular reactor

$M_i(kg\ of\ i/mol\ of\ i)$ i^{th} species molar mass

$\vec{n}(dimensionless)$ Unit vector direction of the differential area dA of the CS.

$\overrightarrow{n^{\alpha}_{\gamma,i}}\left(\frac{kg\ of\ species\ i\ in\ phase\ \gamma\ within\ domain\ \alpha}{\left(m^2\ of\ phase\ \gamma\ within\ domain\ \alpha\right)\cdot s}\right)$ i^{th} species diffusion mass flux in phase γ within domain α

$\overrightarrow{N^{\alpha}_{\gamma,i}}\left(\frac{kg\ of\ species\ i\ in\ phase\ \gamma\ within\ domain\ \alpha}{\left(m^2\ of\ phase\ \gamma\ within\ domain\ \alpha\right)\cdot s}\right)$ i^{th} species combined diffusion-convection mass flux in phase γ within domain α

Nu Nusselt number

$p^{\alpha}_{\gamma}\left(\frac{J\ of\ phase\ f\ within\ domain\ \alpha}{m^3\ of\ phase\ f\ within\ domain\ \alpha}\right)$ Pressure of phase γ within domain α

P_r Prandtl number

$P_e\left(\frac{mol}{m\cdot s\cdot Pa^{0.5}}\right)$ Permeability coefficient

$\overrightarrow{Q^{\alpha}_{\gamma}}\left(\frac{J\ of\ phase\ \gamma\ within\ domain\ \alpha}{\left(m^2\ of\ phase\ \gamma\ within\ domain\ \alpha\right)\cdot s}\right)$ Heat flux into phase γ within domain α

$\overrightarrow{q^{\alpha}_{f\to s}}\left(\frac{J\ from\ phase\ f\ to\ s\ within\ domain\ \alpha}{\left(m^3\ of\ domain\ \alpha\right)\cdot s}\right)$ Heat transferred from phase f to s within domain α

$\overrightarrow{q^{\alpha}_{f\to per}}\left(\frac{J\ from\ phase\ f\ to\ s\ within\ domain\ \alpha}{\left(m^3\ of\ domain\ \alpha\right)\cdot s}\right)$ Heat transferred from phase f to per within domain α

$\overrightarrow{q^{r}_{p}}\left(\frac{J\ from\ domain\ r\ to\ domain\ p}{\left(m^3\ of\ domain\ r\right)\cdot s}\right)$ Heat transferred from domain r to domain p due to convection.

$\overrightarrow{q^{r}_{q}}\left(\frac{J\ from\ domain\ r\ to\ domain\ p}{\left(m^3\ of\ domain\ r\right)\cdot s}\right)$ Heat transferred from domain r to domain q due to convection.

$\overrightarrow{q^{r}_{e}}\left(\frac{J\ from\ exterior\ to\ domain\ r}{\left(m^3\ of\ domain\ r\right)\cdot s}\right)$ Heat transferred from the exterior to domain r.

$\overrightarrow{q^{r}_{i}}\left(\frac{J\ from\ exterior\ to\ domain\ r}{\left(m^3\ of\ domain\ r\right)\cdot s}\right)$ Heat transferred from the interior to domain per.

$\overrightarrow{q^{r}_{mp}}\left(\frac{J\ from\ domain\ r\ to\ domain\ p}{\left(m^3\ of\ domain\ r\right)\cdot s}\right)$ Heat transferred from domain r to domain p due to mass flux

$\overrightarrow{q^{r}_{mper}}\left(\frac{J\ from\ domain\ r\ to\ domain\ p}{\left(m^3\ of\ domain\ r\right)\cdot s}\right)$ Heat transferred from domain r to domain per due to mass flux

$R_{\gamma,i}^{\alpha}\left(\frac{mols\ of\ species\ i\ in\ phase\ \gamma\ within\ domain\ \alpha}{\left(m^3\ of\ domain\ \alpha\right)\cdot s}\right)$ i^{th} species volumetric generation rate in phase γ within domain α

$\bar{R}_{f,i}^{p}\left(\frac{mols\ of\ species\ i\ in\ phase\ f\ within\ domain\ p}{\left(kg\ of\ phase\ s\ within\ domain\ p\right)\cdot s}\right)$ i^{th} species phase s specific generation rate in phase f within domain p

$\tilde{R}\left(J/mol.K\right)$ Universal gas constant

R_e Reynold Number

$r\left(m\ of\ domain\ p\right)$ spatial variable of domain p

$r^p\left(m\right)$ Radius of the pellet

$\overrightarrow{S_{\gamma}^{\alpha}}\left(\frac{kg\ of\ phase\ \gamma\ within\ domain\ \alpha}{\left(m^2\ of\ domain\ \alpha\right)\cdot s^2}\right)$ Momentum source term of phase γ within domain α

$\tilde{S}_{\gamma\to\gamma'}^{\alpha}\left(\frac{J\ of\ phase\ \gamma\ to\ \gamma'\ within\ domain\ \alpha}{\left(m^3\ of\ domain\ \alpha\right)\cdot s^2}\right)$ Interphase energy transfer source term in domain α

$\overrightarrow{S_{f-per,i}^{\alpha}}\left(\frac{kg\ of\ phase\ f\ within\ domain\ \alpha}{\left(m^2\ of\ domain\ \alpha\right)\cdot s^2}\right)$\ Interphase mass transfer source term in domain α

$S\left(\frac{mol}{m^3 Pa^{0.5}}\right)$ Gas solubility

$T_{\gamma}^{\alpha}\left(K\right)$ Temperature of phase γ within domain α

$T^{\alpha}\left(K\right)$ Temperature of the composite phase in domain α

$T^{fr}\left(K\right)$ Temperature of the furnace

$\overrightarrow{\overrightarrow{\mathrm{T}}}_{\gamma}^{\alpha}\left(\frac{kg\ of\ phase\ \gamma\ within\ domain\ \alpha}{\left(m\ of\ phase\ \gamma\ within\ domain\ \alpha\right)\cdot s^2}\right)$ Viscous momentum flux tensor of phase γ within domain α

$U^{fr}\left(\frac{J\ transferred\ from\ domain\ r\ to\ furnace}{\left(\left(m^2\cdot K\right)of\ interphase\ contact\right)\cdot s}\right)$ Global heat transfer coefficient between the furnace and domain r

$U^{per}\left(\frac{J\ transferred\ from\ domain\ r\ to\ domain\ per}{\left(\left(m^2\cdot K\right)of\ interphase\ contact\right)\cdot s}\right)$ Heat transfer coefficient between the domain per and domain r

$V^p\left(m^3\ of\ domain\ p\right)$ Total volume of domain p

$\overrightarrow{v_{\gamma}^{\alpha}}\left(m/s\right)$ Mass average velocity of the phase γ within domain α

$\overrightarrow{v_{\gamma,i}^{\alpha}}\left(m/s\right)$ i^{th} species velocity in phase γ within domain α

$w_{\gamma,i}^{\alpha}\left(\frac{kg\ of\ species\ i\ in\ phase\ \gamma\ within\ domain\ \alpha}{kg\ of\ phase\ \gamma\ within\ domain\ \alpha}\right)$ i^{th} species mass fraction in phase γ within domain α.

$W_{cat}\left(g\right)$ Amount of catalyst

$W_{quartz}\left(g\right)$ Amount of quartz

$x_{\gamma,i}^{\alpha}\left(\frac{mol\ of\ species\ i\ in\ phase\ \gamma\ within\ domain\ \alpha}{mol\ of\ phase\ \gamma\ within\ domain\ \alpha}\right)$ i^{th} species molar fraction in phase γ within domain α

Greek symbols:

$\varepsilon_{\gamma,V}^{\alpha}\left(\frac{m^3\ of\ phase\ \gamma\ within\ domain\ \alpha}{total\ m^3\ of\ domain\ \alpha}\right)$ Volumetric fraction of phase γ within domain α

$\varepsilon_{\gamma,A}^{\alpha}\left(\frac{m^2\ of\ phase\ \gamma\ within\ domain\ \alpha}{total\ m^2\ of\ domain\ \alpha}\right)$ Surface fraction of phase γ within domain α

$\rho_{\gamma}^{\alpha}\left(\frac{kg\ of\ phase\ \gamma\ within\ domain\ \alpha}{m^3\ of\ phase\ \gamma\ within\ domain\ \alpha}\right)$ Mass density of phase γ within domain α

$\rho_{\gamma,i}^{\alpha}\left(\frac{kg\ of\ species\ i\ in\ phase\ \gamma\ within\ domain\ \alpha}{m^3\ of\ phase\ \gamma\ within\ domain\ \alpha}\right)$ i^{th} species mass concentration in phase γ within domain α

$\tau\left(\frac{m\ of\ diffusion\ path\ length\ in\ phase\ f\ within\ domain\ p}{m\ of\ CV\ length\ in\ domain\ p}\right)$ Tortuosity of phase f within domain p.

$\mu_{f}^{\alpha}\left(\frac{kg\ of\ species\ i\ in\ phase\ \gamma\ within\ domain\ \alpha}{\left(m\ of\ phase\ \gamma\ within\ domain\ \alpha\right)\cdot s}\right)$ Viscosity of phase f within domain α

$\upsilon\left(dimensionless\right)$ Total number of species in the phase-domain

$\Phi_{\gamma}^{\alpha}\left(\frac{J\ of\ phase\ \gamma\ within\ domain\ \alpha}{kg\ of\ phase\ \gamma\ within\ domain\ \alpha}\right)$ Mass specific potential energy of phase γ within domain α

$\lambda^{\alpha}\left(J\ within\ domain\ \alpha/m^2\cdot K\cdot s\right)$ Conductivity within domain α

δ Membrane thickness

References (Mathematical Model of the MR Process)

[1] Nunes, S. P., & Peinemann, K. V. *Membrane technology* (p. 596). Wiley-vch, 2001.

[2] Vadrucci, M., Borgognoni, F., Moriani, A., Santucci, A., & Tosti, S. Hydrogen permeation through Pd–Ag membranes: surface effects and Sieverts' law. *International journal of hydrogen energy*. 2013; 38(10): 4144-4152.

[3] Rout, K. R., & Jakobsen, H. A. A numerical study of fixed bed reactor modelling for steam methane reforming process. *The Canadian Journal of Chemical Engineering*. 2015; 93(7): 1222–1238.

[4] Jakobsen, H. A. Chemical reactor modeling. Multiphase Reactive Flows, Berlin, Germany: Springer-Verlag, 2008.

[5] Kuzeljevic, Z. V., & Dudukovic, M. P. Computational modeling of trickle bed reactors. *Industrial & Engineering Chemistry Research*. 2012; 51(4): 1663-1671.

[6] da Cruz, F. E., Karagöz, S., & Manousiouthakis, V. I. Parametric studies of steam methane reforming using a multiscale reactor model. *Industrial & Engineering Chemistry Research*. 2017; 56(47):14123-14139.

[7] Chapman, S., & Cowling, T. G. The mathematical theory of non-uniform gases: an account of the kinetic theory of viscosity, thermal conduction and diffusion in gases. Cambridge university press, 1970.

[8] Poling, B. E., Prausnitz, J. M., & O'connell, J. P. The properties of gases and liquids (Vol. 5). New York: Mcgraw-hill, 2001.

[9] Kee, R. J., Coltrin, M. E., & Glarborg, P. Chemically reacting flow: theory and practice. John Wiley & Sons, 2005.

[10] Wesenberg, M. H., Ströhle, J., & Svendsen, H. F. A study of the heating section of a gas heated steam reformer. *International Journal of Chemical Reactor Engineering*. 2007; 5(1).

[11] NIST Chemistry WebBook. (n.d.). Retrieved October 10, 2016, from http://webbook.nist.gov/chemistry/ NIST

Multiscale Mathematical Model of the AR Process (from [14])

In this work, to be able to differentiate among the various AR domains, the catalyst pellet, adsorbent pellet, and reactor domains are identified by the superscripts c, a, and r, while fluid and solid phases in each mentioned domain, are identified by the subscripts f and s. The symbols γ (fluid or solid) and. α .(catalyst or adsorbent or reactor) represent phases and domains. In the AR, mass, momentum, and energy are continuously interchanged between the gas phase surrounding the catalyst/adsorbent pellets and the catalyst/adsorbent pellets' gas and solid interior. Consider the mass of phase γ in the domain α, and the assumptions: (1) no structural changes during reaction inside the catalyst pellet; stagnant solid phase; no phase change in the reaction mixture (2) no structural changes during adsorption inside the adsorbent pellet; stagnant solid phase; no phase change (CO_2 transformation from gas phase to an adsorbed phase) in the adsorbing mixture. Then, the total mass conservation equations for catalyst/adsorbent domain-phase pairs in the AR system are shown in equations (2) through (5) below:

Catalyst-Fluid:
$$0 = \varepsilon_{f,V}^{c} \frac{\partial}{\partial t}\left(\sum_{i=1}^{\upsilon} \rho_{f,i}^{c}\right) + \varepsilon_{f,A}^{c} \vec{\nabla} \cdot \left[\sum_{i=1}^{\upsilon}\left(\rho_{f,i}^{c} \overrightarrow{v_{f,i}^{c}}\right)\right]; \quad i = 1, \upsilon \tag{2}$$

Catalyst-Solid:
$$0 = \frac{\partial \rho_{s}^{c}}{\partial t} \tag{3}$$

Adsorbent-Fluid:
$$-\sum_{i=1}^{v} M_i R_{f,i}^{a} = \frac{\partial}{\partial t}\left(\varepsilon_{f,V}^{a} \sum_{i=1}^{\upsilon} \rho_{f,i}^{a}\right) + \vec{\nabla} \cdot \left[\varepsilon_{f,A}^{a} \sum_{i=1}^{\upsilon}\left(\rho_{f,i}^{a} \overrightarrow{v_{f,i}^{a}}\right)\right]; \quad i = 1, \upsilon \tag{4}$$

Adsorbent-Solid:
$$\sum_{i=1}^{v} M_i R_{f,i}^{a} = \frac{\partial}{\partial t}\left(\varepsilon_{s,V}^{a} \rho_{s}^{a}\right) \tag{5}$$

The species mass conservation equations for catalyst/adsorbent domain-phase pairs are shown in equations (6) through (9) below:

Catalyst-Fluid:
$$M_i R_{f,i}^{c} = \varepsilon_{f,V}^{c} \frac{\partial}{\partial t}\left(w_{f,i}^{c} \rho_{f}^{c}\right) + \varepsilon_{f,A}^{c} \vec{\nabla} \cdot \left(\overrightarrow{N_{f,i}^{c}}\right) \quad ; \quad i = 1, \upsilon \tag{6}$$

Catalyst-Solid:
$$0 = \frac{\partial \rho_{s,i}^{c}}{\partial t} \quad ; \quad i = 1, \upsilon \tag{7}$$

Adsorbent-Fluid: $$-M_i R^a_{f,i} = \frac{\partial}{\partial t}\left(\varepsilon^a_{f,V} w^a_{f,i} \rho^a_f\right) + \vec{\nabla}\cdot\left(\varepsilon^a_{f,A}\overrightarrow{N^a_{f,i}}\right) \quad ; \quad i = 1,\upsilon \tag{8}$$

Adsorbent-Solid: $$M_i R^a_{f,i} = \frac{\partial}{\partial t}\left(\varepsilon^a_{s,V}\rho^a_{s,i}\right) \quad ; \quad i = 1,\upsilon \tag{9}$$

In the catalyst/adsorbent pellet domains, species transport occurs through three mechanisms: molecular and Knudsen diffusion, and viscous flow. Surface diffusion, thermal diffusion, capillarity condensation, molecular sieving, and solubility mechanisms [1-5], are not considered in this application. Hydrotalcite adsorbents are polycrystalline materials, with a bimodal pore size distribution consisting of a macroporous region generated by the interstitial space in between the crystallites and a nanoporous region within the crystallites themselves. In this work, it is considered that at the crystallite level intrinsic reaction kinetic manifest themselves, resulting in a combined reaction transport species description in which diffusion fluxes account for the transport through hydrotalcite macroporous region for which the average pore size is 0.63 micrometers. In the model, the combined diffusion-convection mass flux. $\overrightarrow{N^\alpha_{\gamma,i}}$. of species i within the pellet domain is described using the Dusty-Gas Model (DGM) [6], as shown in Eq. (10)

$$\begin{aligned}&\sum_{j=1}^{\nu}\frac{1}{D^{eff}_{ij}}\left[\frac{x^\alpha_{f,j}}{M_i}\left(\varepsilon^\alpha_{f,A}\overrightarrow{N^\alpha_{f,i}}\right) - \frac{x^\alpha_{f,i}}{M_j}\left(\varepsilon^\alpha_{f,A}\overrightarrow{N^\alpha_{f,j}}\right)\right] + \left(\frac{1}{M_i D_{iK}}\right)\left(\varepsilon^\alpha_{f,A}\overrightarrow{N^\alpha_{f,i}}\right) = \\ &= -\vec{\nabla}c^\alpha_{f,i} + x^\alpha_{f,i}\vec{\nabla}c^\alpha_{f,tot} - \left(\frac{1}{p^\alpha} + \frac{1}{D_{iK}}\frac{B_O}{\mu^\alpha_f}\right)c^\alpha_{f,i}\vec{\nabla}p^\alpha \quad ; \; i = 1,\upsilon\end{aligned} \tag{10}$$

In general, most industrial multiphase reactors involve reactions with more than two species. Thus, advanced multicomponent flux models, such as the DGM, are required to model species transport [7]. The species i volumetric generation rate in the pellet-fluid subsystem is quantified by the underlying reaction, and adsorption rates. Eq. (11) reflects the relation between the volumetric and the specific generation rates for the pellet domains.

$$R^\alpha_{f,i} = \varepsilon^\alpha_{s,V}\rho^\alpha_s \overline{R}^\alpha_{f,i} \tag{11}$$

For the energy equation development in the pellet domain presented here, the solid phase is considered stagnant, and the potential and kinetic energies, the work done by the fluid onto the solid, and the energetic effect of interphase viscous friction are all considered negligible. Also, radiation-based energy transport is not considered to be essential for this application. Fourier's law is used to account for heat conduction, and the reacting mixture's enthalpy is calculated using an

ideal gas mixture assumption. The proximity of the solid and fluid phases in the pellets domains induce a high heat transfer coefficient between the two phases, which in turn leads to a common temperature T^{α} for the pellet's solid-fluid composite system. The resulting composite energy equation is given by Eq. (12).

$$\left\{\begin{array}{l}\vec{\nabla}\cdot\left[\left(\lambda^{\alpha}\right)\vec{\nabla}T^{\alpha}\right] \\ -\sum_{i=1}^{\upsilon}\varepsilon_{f,A}^{\alpha}\left(\frac{1}{M_i}C_{P,i}^{\alpha}\right)\overrightarrow{n_{f,i}^{\alpha}}\cdot\vec{\nabla}T^{\alpha} \\ -\sum_{i=1}^{\upsilon}\tilde{h}_i^{\alpha}R_{f,i}^{\alpha}+\sum_{i=1}^{\upsilon}\tilde{h}_i^{\alpha}\frac{\partial}{\partial t}\left(\varepsilon_{f,V}^{\alpha}c_{f,i}^{\alpha}\rho_f^{\alpha}\right)\end{array}\right\}=\left\{\begin{array}{l}\left[\varepsilon_{s,V}^{\alpha}\rho_s^{\alpha}C_{V,s}^{\alpha}+\sum_{i=1}^{\upsilon}\frac{1}{M_i}\varepsilon_{f,V}^{\alpha}\rho_{f,i}^{\alpha}C_{P,i}^{\alpha}\right]\frac{\partial T^{\alpha}}{\partial t} \\ +\left[\sum_{i=1}^{\upsilon}\varepsilon_{f,A}^{\alpha}\frac{1}{M_i}\rho_{f,i}^{\alpha}C_{P,i}^{\alpha}\overrightarrow{v_f^{\alpha}}\right]\cdot\vec{\nabla}T^{\alpha}\end{array}\right\} \quad (12)$$

The set of initial and boundary conditions for the solution of the pellet-scale model equations is presented in Table 1.

Table 1 Initial and boundary conditions for catalyst/adsorbent pellet-scale model equations

Initial Conditions:	***Boundary Conditions:***
$\left.\begin{array}{l}w_{f,i}^{\alpha}=\left(w_{f,i}^{\alpha}\right)_{in} \\ T^{\alpha}=T^{r}=T_{in} \\ p^{\alpha}=\left(p^{\alpha}\right)_{in} \\ Q_r=-\lambda^{\alpha}\vec{\nabla}T^{\alpha}=0 \\ \vec{\nabla}p^{\alpha}=0\end{array}\right\}$ *for* $t=0,\ \forall r$ (13)	$\left.\begin{array}{l}\overrightarrow{N_{f,i}^{\alpha}}=0 \\ Q_r=-\lambda^{\alpha}\vec{\nabla}T^{\alpha}=0 \\ \vec{\nabla}p^{\alpha}=0\end{array}\right\}$ *for* $r=0,$ $\left.\begin{array}{l}-k_{m,j}\left(w_{f,i}^{r}c_f^{r}-w_{f,i}^{\alpha}\rho_f^{\alpha}\right)=\overrightarrow{n_{f,i}^{p}}+w_{f,i}^{\alpha}\rho_f^{\alpha}\overrightarrow{v_f^{\alpha}} \\ -h^{\alpha}\left(T^{r}-T^{\alpha}\right)=Q_r+\left(\sum_{j=1}^{n_s}w_{f,i}^{\alpha}\rho_f^{\alpha}C_{f,i}^{\alpha}\right)\overrightarrow{v_f^{\alpha}}T^{\alpha} \\ w_{f,i}^{\alpha}=w_{f,i}^{r} \\ p^{\alpha}=p^{r}\end{array}\right\}$ *for* $r=r^{\alpha}$ (14)

Reactor-Scale (Bulk Gas) Modeling

Similar to the pellet-scale model development, the total mass conservation equation for the reactor domain-phase pair is shown below in Eqns. (15) to (16), where in equation 16 $\varepsilon_{s,V}^{r}$ represents the solid phase fraction inside the reactor, as opposed to $\varepsilon_{s,V}^{a}$ in equation 5 which represents the solid phase fraction inside a single adsorbent pellet.

Reactor-Fluid:

$$-\sum_{i=1}^{v}\overrightarrow{S_{f-ad,i}^{r}}=\frac{\partial}{\partial t}\left(\varepsilon_{f,V}^{r}\rho_f^{r}\right)+\vec{\nabla}\cdot\left(\varepsilon_{f,A}^{r}\rho_f^{r}\overrightarrow{v_f^{r}}\right) \quad (15)$$

Reactor-Solid:

$$\sum_{i=1}^{v} \overrightarrow{S^r_{f-ad,i}} = \frac{\partial}{\partial t}\left(\varepsilon^r_{s,V}\rho^r_s\right) \tag{16}$$

The species mass conservation equation for the reactor domain-phase pair is shown in equations (17) to (18).

Reactor-Fluid:

$$\begin{aligned} &-\overrightarrow{S^r_{f-ad,i}} + M_i R^r_{f,i} = \frac{\partial}{\partial t}\left(\varepsilon^r_{f,V} w^r_{f,i}\rho^r_f\right) + \vec{\nabla}\cdot\left[\varepsilon^r_{f,A}\left(w^r_{f,i}\rho^r_f\overrightarrow{v^r_f} + \overrightarrow{n^r_{f,i}}\right)\right], i = 1,\upsilon \\ &\overrightarrow{n^r_{f,i}} = -\varepsilon^r_{f,V} D_Z \vec{\nabla} w^r_{f,i}, i = 1,\upsilon \end{aligned} \tag{17}$$

where, in this work, the gradient terms are one-dimensional, and the term $\overrightarrow{n^r_{f,i}} = -\varepsilon^r_{f,V} D_Z \vec{\nabla} w^r_{f,i}$ accounts for axial dispersion.

Reactor-Solid:

$$\overrightarrow{S^r_{f-ad,i}} = \frac{\partial}{\partial t}\left(\varepsilon^r_{s,V} w^r_{s,i}\rho^r_s\right) \quad ; \quad i = 1,\upsilon \tag{18}$$

The source term $\overrightarrow{S^r_{f-ad,i}}$ represents the species mass lost from the bulk gas phase through adsorption. The species i volumetric generation rate in the reactor-fluid subsystem is quantified by Eqs. (19) and (20), which enforces its equality to the product of a surface to volume adjustment ratio times the overall i^{th} species combined diffusion-convection mass flux, at the control surface CS^{α} of the pellet domain.

$$R^r_{f,i} = \varepsilon^r_{c-s,V}\frac{A^c}{\varepsilon^c_{s,V}V^c}\left[\left(\varepsilon^c_{f,A}\overrightarrow{N^c_i}\right)\Big|^{CS^c}\right] \tag{19}$$

$$-\overrightarrow{S^r_{f-ad,i}} = \varepsilon^r_{a-s,V}\frac{A^a}{\varepsilon^a_{s,V}V^a}\left[\left(\varepsilon^a_{f,A}\overrightarrow{N^a_i}\right)\Big|^{CS^a}\right] \tag{20}$$

The momentum conservation equation for the reactor domain-phase pair as a function of the mass average velocity $\overrightarrow{v^{\alpha}_{\gamma}}$ of phase γ within the domain α is shown in equations (21) to (22).

Reactor-Fluid:

$$\overrightarrow{S^r_f} = \frac{\partial}{\partial t}\left(\varepsilon^r_{f,V}\rho^r_f\overrightarrow{v^r_f}\right) + \vec{\nabla}\cdot\left(\varepsilon^r_{f,A}\rho^r_f\overrightarrow{v^r_f}\overrightarrow{v^r_f}\right) \tag{21}$$

Reactor-Solid:

$$\overrightarrow{S^r_s} = \frac{\partial}{\partial t}\left(\varepsilon^r_{s,V}\rho^r_s\overrightarrow{v^r_s}\right) + \vec{\nabla}\cdot\left(\varepsilon^r_{s,A}\rho^r_s\overrightarrow{v^r_s}\overrightarrow{v^r_s}\right) \tag{22}$$

The cross-sectional average momentum equation can be written as [8]:

$$\frac{\partial}{\partial t}\left(\varepsilon_{f,V}^{r}\rho_{f}^{r}\overrightarrow{v_{f}^{r}}\right)+\vec{\nabla}\cdot\left(\rho_{f}^{r}\overrightarrow{v_{f}^{r}}\overrightarrow{v_{f}^{r}}\right)=\left\{\begin{array}{l}-\varepsilon_{f,V}^{r}\vec{\nabla}p_{f}^{r}+\varepsilon_{f,V}^{r}\rho_{f}^{r}\vec{g}+\\ \vec{\nabla}\cdot\overrightarrow{v_{f}^{r}}\left(\mu_{f}^{r}\left(\vec{\nabla}\overrightarrow{v_{f}^{r}}+\left(\vec{\nabla}\overrightarrow{v_{f}^{r}}\right)^{T}\right)\right)+\varepsilon_{f,V}^{r}\left(K_{D}\overrightarrow{v_{f}^{r}}+K_{v}\overrightarrow{v_{f}^{r}}^{2}\right)\end{array}\right\} \tag{23}$$

The gravity term is neglected (the reactor tube is horizontal), while the fluid-particle friction is the main pressure drop contributor in the reactor bed. Also, as the gas phase velocity is considered not very large, [9], the momentum equation can be reduced to the following form:

$$\frac{\partial}{\partial t}\left(\rho_{f}^{r}\overrightarrow{v_{f}^{r}}\right)+\vec{\nabla}p_{f}^{r}=-K_{D}\overrightarrow{v_{f}^{r}}-K_{v}\overrightarrow{v_{f}^{r}}^{2}=\vec{\nabla}p_{f}^{r}=-150\frac{\left(1-\varepsilon_{f,V}^{r}\right)^{2}}{\left(\varepsilon_{f,V}^{r}\right)^{3}d_{p}^{2}}-\mu_{f}^{r}1.75\frac{\left(1-\varepsilon_{f,V}^{r}\right)}{\left(\varepsilon_{f,V}^{r}\right)^{3}d_{p}}\rho_{f}^{r}\overrightarrow{v_{f}^{r}}\overrightarrow{v_{f}^{r}} \tag{24}$$

where K_D and K_V are constants for the viscous and kinetic pressure drop terms, [2].

The reactor energy balance quantifies the evolution of the reacting mixture's temperature, accounting for both solid-gas energy transport, and enthalpic convection. The reacting mixture's enthalpy is calculated using an ideal gas mixture assumption, which is well justified for the prevailing reactor temperature and pressure conditions. For energy equation development, the solid phase is considered stagnant, and the potential and kinetic energies, the work done by the fluid onto the solid, and the effect of interphase viscous friction are all considered negligible. Fourier's law is used to account for heat conduction, and the fluid is considered to be an ideal gas. Then, for the reactor domain's fluid phase, the RTT derived energy balance is shown in Eq. (25).

$$\textit{Reactor-Fluid}\left\{\begin{array}{l}-q_{f\to s}^{r}+\vec{\nabla}\cdot\left(\varepsilon_{f,A}^{r}\lambda^{r}\vec{\nabla}T_{f}^{r}\right)\\ -\sum_{i=1}^{\upsilon}\left[\varepsilon_{f,A}^{r}\left(\frac{1}{M_{i}}C_{P,i}^{r}\right)\overrightarrow{n_{f,i}^{r}}\cdot\vec{\nabla}T_{f}^{r}\right]\\ -\sum_{i=1}^{\upsilon}\left[\frac{1}{M_{i}}\tilde{h}_{f,i}^{r}\vec{\nabla}\cdot\left(\varepsilon_{f,A}^{r}\overrightarrow{n_{f,i}^{r}}\right)\right]\end{array}\right\}=\left\{\begin{array}{l}\varepsilon_{f,V}^{r}\left(\sum_{i=1}^{\upsilon}\frac{1}{M_{i}}\rho_{f,i}^{r}C_{V,i}^{r}\right)\frac{\partial T_{f}^{r}}{\partial t}\\ -\frac{\partial}{\partial t}\left(\varepsilon_{f,V}^{r}p_{f}^{r}\right)\\ +\varepsilon_{f,A}^{r}\left(\sum_{i=1}^{\upsilon}\frac{1}{M_{i}}\rho_{f,i}^{r}C_{P,i}^{r}\right)\overrightarrow{v_{f}^{r}}\cdot\vec{\nabla}T_{f}^{r}\end{array}\right\} \tag{25}$$

In this work, the energy exchanged between the fluid, and solid phases is composed of five "heat" terms, Eq. (26): the enthalpy carried by the species' mass flux between the reactor and the catalyst-pellet domains, Eq. (27); the convective heat flux exchanged between the fluid in the reactor and the catalyst-pellet solid phase, Eq. (28); the enthalpy carried by the species' mass flux between the reactor and the adsorbent-pellet domains, Eq. (29); the convective heat flux exchanged between the fluid in the reactor and the adsorbent-pellet solid phase, Eq. (30); a source term q_{ex}^{r}

that accounts for any external heat flux crossing the considered reactor control surface CS^r for one-dimensional models, Eq. (31);

$$q^r_{f\to s} = q^r_{c,1} + q^r_{c,2} + q^r_{\mathrm{a},1} + q^r_{\mathrm{a},2} + q^r_{ex} \tag{26}$$

$$q^r_{c,1} = \varepsilon^r_{c-s,V}\left(\frac{A^c}{\varepsilon^c_{s,V}V^c}\right)\sum_{i=1}^{\nu}\left[\left(\frac{1}{M_i}\tilde{h}^c_{f,i}\varepsilon^c_{f,A}\overrightarrow{N^c_i}\right)\Bigg|^{CS^c}\cdot\vec{n}\right] \tag{27}$$

$$q^r_{c,2} = \varepsilon^r_{c-s,V}\left(\frac{A^c}{\varepsilon^c_{s,V}V^c}\right)\left[\varepsilon^c_{s,A}h^c\left(T^r_f - T^c\right)\Big|^{CS^c}\right] \tag{28}$$

$$q^r_{\mathrm{a},1} = \varepsilon^r_{a-s,V}\left(\frac{A^a}{\varepsilon^a_{s,V}V^a}\right)\sum_{i=1}^{\nu}\left[\left(\frac{1}{M_i}\tilde{h}^a_{f,i}\varepsilon^a_{f,A}\overrightarrow{N^a_i}\right)\Bigg|^{CS^a}\cdot\vec{n}\right] \tag{29}$$

$$q^r_{\mathrm{a},2} = \varepsilon^r_{a-s,V}\left(\frac{A^a}{\varepsilon^a_{s,V}V^a}\right)\left[\varepsilon^a_{s,A}h^a\left(T^a_f - T^a\right)\Big|^{CS^a}\right] \tag{30}$$

$$q^r_{ex} = \begin{cases} \dfrac{A^rU^r}{V^r}\left(T^r_f - T^{fur}_f\right) & if\ \ \mathrm{1D} \\ 0 \quad if \quad \mathrm{2D\ \ or\ \ 3D} \end{cases} \tag{31}$$

Table 2 Initial and boundary conditions for reactor-scale model equations

Initial Conditions:	***Boundary Conditions:***
$\left.\begin{array}{l} w^r_{f,i} = \left(w^r_{f,i}\right)_{in} \\ w^r_{f,H_2O} = w^r_{f,N_2} = 0.5, \\ T^r_f = \left(T^r_f\right)_{in} \\ p^r_f = \left(p^r_f\right)_{in} \end{array}\right\} for\ t=0,\ \forall z \quad (32)$	$\left.\begin{array}{l} \overrightarrow{v^r_f} = \left(\overrightarrow{v^r_f}\right)_{in} \\ p^r_f = \left(p^r_f\right)_{in} \\ -\varepsilon^r_{f,V}D_Z\vec{\nabla}w^r_{f,i} = -\left(\overrightarrow{v^r_f}\right)_{in}\cdot\left(\left(w^r_{f,i}\right)_{in} - w^r_{f,i}\right) \\ -\lambda^r\vec{\nabla}T^r_f = -\varepsilon^r_{f,A}\rho^r_f\left(\sum_{i=1}^{\upsilon}c^r_{f,i}C^r_{P,i}\right)\left(\overrightarrow{v^r_f}\right)_{in}\cdot\left(\left(T^r_f\right)_{in} - T^r_f\right) \end{array}\right\} for\ z=0,\ \left.\begin{array}{l} \vec{\nabla}T^r_f = 0 \\ \overrightarrow{n^r_j} = 0 \\ \vec{\nabla}p^r_f = 0 \end{array}\right\} for\ z=L \quad (33)$

For the case study in this work, binary diffusion coefficients for polar and non-polar gas mixtures are estimated using the model presented by Poling, Praunitz and O'Connell's [10], which

was developed from the Chapman-Enskog theory. Constitutive laws and other model equations are shown in Table 2 of the MR model equations.

Catalyst/Adsorbent Effectiveness Factor Definitions and Quantification: In this study, we calculate, through the employed multiscale model temporal effectiveness factors both for the catalyst as well as the adsorbent pellet. The temporal effectiveness factor for the ith species is defined by Eq. (34), where the superscript ζ refers to either the catalyst or the adsorbent pellet.

$$\eta_i^{\zeta} \hat{=} \frac{\iint_{CS} \left(\varepsilon_{f,A}^{\zeta} \overline{N_i^{\zeta}} \right) \cdot \vec{n}\, dA^t}{\iiint_{CV} M_i \varepsilon_{s,V}^{\zeta} \rho_{c/a}\, \bar{R}_i^{\zeta} \big|_{CS}\, dV} = \frac{\textit{the net mass flow of ith species at pellet's surface}}{\textit{the volumetric mass generation rate of the same species}} \;;\; i = 1, \upsilon \tag{34}$$

Similarly, the length-averaged effectiveness factor is given by Eq. (35):

$$\eta_i^{ave-\zeta}(z) \hat{=} \frac{\int_0^{L^r} \left[\left(\frac{A_c^r \varepsilon_{s,V}^r}{V^{c/a} \varepsilon_{s,V}^{c/a}} \right) \iint_{CS} \left(\varepsilon_{f,A}^{\zeta} \overline{N_i^{\zeta}} \right) \cdot \vec{n}\, dA^t \right](z)\, dz}{\int_0^{L^r} \left[\left(\frac{A_c^r \varepsilon_{s,V}^r}{V^{\zeta} \varepsilon_{s,V}^{\zeta}} \right) \iiint_{CV} M_i \varepsilon_{s,V}^{\zeta} \rho_{cat}\, \bar{R}_i^{\zeta} \big|_{CS}\, dV \right](z)\, dz} \;;\; i = 1, \upsilon \tag{35}$$

This allows one to quantify the impact of the various transport and sorption/reaction processes, and also enables the assessment of behavioral and quantitative changes during the transition from lab-scale to industrial-scale pellet sizes. The catalyst or adsorbent effectiveness factor for species i is defined as the ratio of that species' mass flow rate entering the pellet's surface, over the calculated mass generation/consumption rate for the same species in the absence of transport limitations at the prevailing conditions at the pellet's surface. For the catalyst pellet, the effectiveness factors of all species are equal, since there is only one reaction (WGSR) taking place in the pellet with equal stoichiometric coefficients for all species. For the adsorbent pellet, there is only effectiveness factor for CO_2 as it is the only adsorbed species. The dynamic nature of the AR process suggests that the net species mass flow at the pellet's surface accommodates not only the reaction occurring in the catalyst pellet (or the adsorption occurring in the adsorbent pellet), but also helps meet the same species' accumulation needs within the pellet's pores. This suggests that early in the AR's operation, when the accumulation needs are the largest, the values of the temporal effectiveness factor may be greater than one.

Nomenclature (Mathematical Model of the AR Process)

English Symbols

$A^{\alpha}\left(m^2\right)$ Area of the control surface of domain α

$A_c^r\left(m^2\right)$ Cross section area of the tubular reactor

$B_O\left(m^2\right)$ Viscous flow parameter of domain α

$b_i\left(Pa^{-1}\right)$ Model constant for component i

$c_{\gamma,i}^{\alpha}\left(\frac{mol\ of\ species\ i}{m^3}\right)$ Species' i molar density of phase γ within domain α

$c_{\gamma}^{\alpha}\left(\frac{mol}{m^3}\right)$ Total molar density of phase γ within domain α

$C_{P,i}^{\alpha}\left(\frac{J\ of\ species\ i}{mol \cdot K}\right)$ Species' i molar specific heat at constant pressure of phase f within domain α

$C_V^{\alpha}\left(\frac{J}{mol \cdot K}\right)$ Species' i molar specific heat at constant volume of phase s within domain α

$CS^{\alpha}\left(m^2\right)$ Control surface of domain α

$CV^{\alpha}\left(m^3\right)$ Control volume of domain α

$D_{ij}^{\alpha}\left(\frac{m^2}{s}\right)$ Species' i and j binary diffusion coefficient of phase γ within domain α

$D_{ij}^{eff}\left(\frac{m^2}{s}\right)$ Species' i and j effective binary diffusion coefficient in domain α

$D_{iK}\left(\frac{total\ m^2}{s}\right)$ Species' i Knudsen diffusion coefficient in domain α

$\tilde{D}_i^r\left(\frac{m^2}{s}\right)$ Species' i thermal diffusion coefficient of phase f within domain r

$D_z\left(\frac{m^2}{s}\right)$ Axial dispersion coefficient in domain r

$d_p\,(m)$ Diameter of the pellet

$d_{pore}^{p}\,(m)$ Mean pore diameter in domain α

$d^r\,(m)$ Diameter of the tubular reactor

$h^{\alpha}\left(\frac{J}{m^2 \cdot K \cdot s}\right)$ Interfacial heat transfer coefficient between phase f within domain α and phase s within domain α.

$H_{\gamma}^{\alpha}\left(\frac{J}{kg}\right)$ Mass specific enthalpy of phase γ within domain α

$\tilde{H}_{i}^{0}\left(\frac{J}{mole}\right)$ Species' i standard molar enthalpy of formation

$\tilde{h}_{\gamma,i}^{\alpha}\left(\frac{J}{mole}\right)$ Species' i molar enthalpy of phase γ within domain α

$\lambda_{\gamma}^{\alpha}\left(\frac{J}{m \cdot K \cdot s}\right)$ Thermal conductivity of phase γ within domain α

$\overrightarrow{j_{\gamma,i}^{\alpha}}\left(\frac{kg}{m^2 \cdot s}\right)$ i^{th} species diffusion molar flux in phase γ within domain α

$\overrightarrow{J_{\gamma,i}^{\alpha}}\left(\frac{kg\ of\ species\ i}{m^2 \cdot s}\right)$ i^{th} species combined diffusion-convection molar flux in phase γ within domain

K_{eq} Equilibrium constant of WGSR

$k_a\left(s^{-1}\right)$ Adsorption mass transfer coefficient

$k_m\left(\frac{m}{s}\right)$ Interfacial mass transfer coefficient between phase f within domain α and phase s within domain α

$L^r\ (m)$ Length of the tubular reactor

$M_i\ (kg\ of\ i/mole\ of\ i)$ i^{th} species molar mass

$m_i\ (mol/kg)$ Model constant for component i

$\vec{n}\left(dimensionless\right)$ Unit vector direction of the differential area dA of the CS.

$\overrightarrow{n_{\gamma,i}^{\alpha}}\left(\frac{kg}{m^2 \cdot s}\right)$ i^{th} species diffusion mass flux in phase γ within domain α

$\overrightarrow{N_{\gamma,i}^{\alpha}}\left(\frac{kg}{m^2 \cdot s}\right)$ i^{th} species combined diffusion-convection mass flux in phase γ within domain

Nu Nusselt number

$p_{\gamma}^{\alpha}\left(\frac{J}{m^3}\right)$ Pressure of phase γ within domain α

P_r Prandtl number

$\overrightarrow{Q_{\gamma}^{\alpha}}\left(\frac{J}{m^2 \cdot s}\right)$ Heat flux into phase γ within domain α

$\overrightarrow{q_{f\to s}^{\alpha}}\left(\frac{J}{m^3 \cdot s}\right)$ Heat transferred from phase f to s within domain α

$q_i\left(\frac{mole\ i}{kg}\right)$ Solid phase concentration of component i on domain α

$q_i^{eq}\left(\frac{mole\ i}{kg}\right)$ Equilibrium solid phase concentration of component i on domain α

$R_{\gamma,i}^{\alpha}\left(\frac{mole\,of\ species\,i}{m^3 \cdot s}\right)$ i^{th} species volumetric generation rate in phase γ within domain α

$\bar{R}_{f,i}^{\alpha}\left(\frac{mols\,of\ species\,i}{kg \cdot s}\right)$ i^{th} species specific generation rate

$\tilde{R}(J/mol.K)$ Universal gas constant

R_e Reynold Number

$r(m\,of\ domain\,\alpha)$ spatial variable of domain α

$r^{\alpha}(m)$ Radius of the pellet

$\overrightarrow{S_{\gamma}^{\alpha}}\left(\frac{kg}{m^2 \cdot s^2}\right)$ Momentum source term of phase γ within domain α

$\tilde{S}_{\gamma\to\gamma'}^{\alpha}\left(\frac{J}{m^3 \cdot s^2}\right)$ Interphase energy transfer source term in domain α

$\overrightarrow{S_{f-per,i}^{\alpha}}\left(\frac{kg}{m^2 \cdot s^2}\right)$ Interphase mass transfer source term in domain α

$T_{\gamma}^{\alpha}(K)$ Temperature of phase γ within domain α

$T^{\alpha}(K)$ Temperature of the composite phase in domain α

$T^{fur}(K)$ Temperature of the furnace

$\overrightarrow{\overrightarrow{\mathrm{T}}_{\gamma}^{\alpha}}\left(\frac{kg}{m \cdot s^2}\right)$ Viscous momentum flux tensor of phase γ within domain α

$U^r\left(\frac{J}{\left(m^2\cdot K\right)\cdot s}\right)$ Global heat transfer coefficient between the furnace and domain r

$V^\alpha\left(m^3\right)$ Total volume of domain α

$\overrightarrow{v_\gamma^\alpha}\left(m/s\right)$ Mass average velocity of the phase γ within domain α

$\overrightarrow{v_{\gamma,i}^\alpha}\left(m/s\right)$ i^{th} species velocity in phase γ within domain α

$w_{\gamma,i}^\alpha\left(\frac{kg\ of\ species\ i}{kg}\right)$ i^{th} species mass fraction in phase γ within domain α .

$x_{\gamma,i}^\alpha\left(\frac{mol\ of\ species\ i}{mol}\right)$ i^{th} species molar fraction in phase γ within domain α

Greek symbols:

$\varepsilon_{\gamma,V}^\alpha\left(\frac{m^3}{total\ m^3}\right)$ Volumetric fraction of phase γ within domain α

$\varepsilon_{\gamma,A}^\alpha\left(\frac{m^2}{total\ m^2}\right)$ Surface fraction of phase γ within domain α

$\varepsilon_{c-s,V}^r\left(\frac{m^3}{total\ m^3}\right)$ Volumetric fraction of domain c within domain r

$\varepsilon_{a-s,V}^r\left(\frac{m^3}{total\ m^3}\right)$ Volumetric fraction of domain a within domain r

$\rho_\gamma^\alpha\left(\frac{kg}{m^3}\right)$ Mass density of phase γ within domain α

$\rho_{\gamma,i}^\alpha\left(\frac{kg\ of\ species\ i}{m^3}\right)$ i^{th} species mass concentration in phase γ within domain α

τ Tortuosity factor

$\mu_f^\alpha\left(\frac{kg\ of\ species\ i}{m\cdot s}\right)$ Viscosity of phase γ within domain α

$\Phi_\gamma^\alpha\left(\frac{J}{kg}\right)$ Mass specific potential energy of phase γ within domain α

$\lambda^\alpha\left(J/m^2\cdot K\cdot s\right)$ Conductivity within domain α

References (Mathematical Model of the AR Process)

[1] Wakao, N. and Smith, J. M. Diffusion in catalyst pellets. Chemical Engineering Science. 1962; 17(11): 825-834.

[2] Chen, O. T. and Rinker, R. G. Modification of the dusty-gas equation to predict mass transfer in general poruos media. Chemical Engineering Science. 1979; 34(1): 51-61.

[3] Coppens, M. O. and Froment, G. F. Diffusion and reaction in a fractal catalyst pore—I. Geometrical aspects. Chemical engineering science. 1995; 50(6): 1013-1026.

[4] Coppens, M. O. and Froment, G. F. Diffusion and reaction in a fractal catalyst pore—II. Diffusion and first-order reaction. Chemical engineering science. 1995; 50(6): 1027-1039.

[5] Keil, F. J. Diffusion and reaction in porous networks. Catalysis Today. 1999; 53(2): 245-258.

[6] Mason, E. A., Malinauskas, A. P. Gas transport in porous media: the dusty-gas model. Amsterdam ; New York : Elsevier, 1983.

[7] Lim, J. Y. and Dennis, J. S. Modeling reaction and diffusion in a spherical catalyst Industrial & Engineering Chemistry Research. 2012; 51(49): 15901-15911.

[8] Kuzeljevic, Z. V. and Dudukovic, M. P. Computational modeling of trickle bed reactors. Industrial & Engineering Chemistry Research. 2012; 51(4): 1663-1671.

[9] Jakobsen, H. A. Chemical reactor modeling. Multiphase Reactive Flows. Berlin, Germany: Springer-Verlag, 2008.

[10] da Cruz, F. E., Karagöz, S. and Manousiouthakis, V. I. Parametric studies of steam methane reforming using a multiscale reactor model. Industrial & Engineering Chemistry Research. 2017; 56(47):14123-14139.